STRUCTURAL, MAGNETIC, THERMAL AND THERMOELECTRICAL PROPERTIES OF MONONUCLEAR AND DIMERIC COBALT(II) AND IRON(II) COMPLEXES WITH EXTENDED π-CONJUGATED BIPYRIDYL LIGANDS

NIK MUHD JAZLI BIN NIK IBRAHIM

FACULTY OF SCIENCE
UNIVERSITY OF MALAYA
KUALA LUMPUR

2016

STRUCTURAL, MAGNETIC, THERMAL AND THERMOELECTRICAL PROPERTIES OF MONONUCLEAR AND DIMERIC COBALT(II) AND IRON(II) COMPLEXES WITH EXTENDED π-CONJUGATED BIPYRIDYL LIGANDS

NIK MUHD JAZLI BIN NIK IBRAHIM

DISERTATION SUBMITTED IN FULLFILMENT OF THE REQUIREMENT FOR THE DEGREE OF MASTER OF SCIENCE

FACULTY OF SCIENCE
UNIVERSITY OF MALAYA
KUALA LUMPUR

2016

UNIVERSITI MALAYA

ORIGINAL LITERARY WORK DECLARATION

Name of Candidate : **NIK MUHD JAZLI BIN NIK IBRAHIM**

I/C/Passport No

Regisration/Matric No. : **SGR140017**

Name of Degree : **MASTER OF SCIENCE**

Title of Project Paper/Research Report/Dissertation/Thesis ("this Work"):

"STRUCTURAL, MAGNETIC, THERMAL AND THERMOELECTRICAL PROPERTIES OF MONONUCLEAR AND DIMERIC COBALT(II) AND IRON(II) COMPLEXES WITH EXTENDED π-CONJUGATED BIPYRIDYL LIGANDS"

Field of Study: **INORGANIC CHEMISTRY**

I do solemnly and sincerely declare that:

(1) I am the sole author/writer of this Work,
(2) This Work is original,
(3) Any use of any work in which copyright exists was done by way of fair dealing and for permitted purposes and any excerpt or extract from, or reference to or reproduction of any copyright work has been disclosed expressly and sufficiently and the title of the Work and its authorship have been acknowledged in this Work,
(4) I do not have any actual knowledge nor do I ought reasonably to know that the making of this work constitutes an infringement of any copyright work,
(5) I hereby assign all and every rights in the copyright to this Work to the University of Malaya ("UM"), who henceforth shall be owner of the copyright in this Work and that any reproduction or use in any form or by any means whatsoever is prohibited without the written consent of UM having been first had and obtained,
(6) I am fully aware that if in the course of making this Work I have infringed any copyright whether intentionally or otherwise, I may be subject to legal action or any other action as may be determined by UM.

Candidate"s Signature Date: 08 November 2016

Subscribed and solemnly declared before,

Witness"s Signature Date: 08 November 2016

Name: **ASSOC. PROF. DR NORBANI ABDULLAH**

Designation:

ABSTRACT

This research was focused on syntheses and characterisation of Co(II) and Fe(II) complexes with four π-conjugated bipyridyl ligands (L), designed to be thermally stable and have magnetic and thermoelectric properties. A total of 16 complexes were successfully synthesized and characterised. Their general formulae were $[M_2(CH_3COO)_4(L)_2]$ and$[M(L)_3](BF_4)_2$ where M = Co(II) and Fe(II). The structures of L were ascertained by CHN elemental analyses, ^{1}H-NMR and FTIR spectroscopies, while the structures of all complexes were deduced from CHN elemental analyses and FTIR and UV-vis spectroscopies. The magnetic properties of complexes were determined at room temperature by the Gouy method, their band gaps were determined by UV-vis spectroscopy and cyclic voltammetry (CV), their thermal stability by thermogravimetry (TG) and their thermoelectrical properties deduced from their Seebeck coefficients, S_e. At room temperature, most of these complexes have both high spin and low spin Co(II) and Fe(II) atoms. Their decomposition temperatures were in the range of 170 ^oC – 265 ^oC, optical bandgaps in the range of 1.85 eV – 2.75 eV, and electrochemical bandgaps in the range of 0.32 eV – 0.55 eV. Their electrochemical bandgaps were beneficial for good thermoelectrical performance, as supported by relatively high Seebeck coefficients (-0.35 ± 0.02 mV K^{-1} – -0.62 ± 0.02 mV K^{-1}).

ABSTRAK

Penyelidikan ini berfokuskan penyediaan dan pencirian kompleks-kompleks Co(II) dan Fe(II) dengan empat ligan bipiridina terkonjugat-π (L), yang direka bentuk untuk menjadi stabil secara terma dan mempunyai sifat magnet dan termoelektrik. Sejumlah 16 kompleks berjaya disintesis dan dicirikan. Formula umum kompleks adalah $[M_2(CH_3COO)_4(L)_2]$ dan $[M(L)_3](BF_4)_2$, di mana M = Co(II) dan Fe(II). Struktur L dipastikan melalui analisis unsur CHN dan spekstroskopi ^{1}H-NMR dan FTIR, sementara struktur semua kompleks ditentukan daripada analisis unsur CHN dan spektroskopi FTIR dan UV-vis. Sifat magnet kompleks ditentukan pada suhu bilik melalui kaedah Gouy, jurang jalur ditentukan melalui spektroskopi UV-vis dan voltametri siklik (CV), kestabilan terma melalui termogravimetri (TG) dan sifat termoelektrik dideduksikan daripada pekali Seebeck, S_e. Pada suhu bilik, kebanyakan kompleks mempunyai atom Co(II) dan Fe(II) dengan spin tinggi dan spin rendah. Suhu penguraian kompleks adalah dalam julat 170 ^oC – 265 ^oC, jurang jalur optik dalam julat 1.85 eV – 2.75 eV, dan jurang jalur elektrokimia dalam julat 0.32 eV – 0.55 eV. Jurang jalur elektrokimia adalah bermanfaat untuk prestasi termoelektrik yang baik, sebagaimana disokong oleh pekali Seebeck yang agak tinggi (-0.35 ± 0.02 mV K^{-1} – -0.62 ± 0.02 mV K^{-1}).

DEDICATED TO

MY WIFE, PARENTS, FAMILY

Dr. NORBANI ABDULLAH

Dr. SUHANA MOHD SAID

ACKNOWLEDGEMENT

Alhamdulillah, praise be to Allah, His Majesty for His uncountable blessings, and best prayers and peace for His Messenger Muhammad S.A.W, his pure descendant, his family and his noble companions. Immeasurable appreciation and deepest gratitude for the help and support are extended to the following persons who have instrumentally contributed in making this study a success.

First and foremost, I would like to express my thanks to my dedicated and supportive supervisors, Assoc. Prof. Dr. Norbani binti Abdullah and Assoc. Prof. Dr. Suhana binti Mohd Said for their assistance, meticulous scrutiny, and scholarly advices. I would not be able to be at this phase without their expert guidance and encouragement.

Also, I would like to thank my lab mates of Inorganic Chemistry Research Laboratory for their supportive, cooperation and extensive help. In addition, it is a genuine pleasure for me to also deliver a huge thanks and thought to all staffs in the Department of Chemistry and Faculty of Science, University of Malaya.

Most importantly, I would like to thank the Ministry of Education (MyBrain15 - MyMaster), Fundamental Research Grant Scheme (FP011 – 2014A), University of Malaya Research Grant (RP014C – 13AET), and University of Malaya Postgraduate Grant (PG114 – 2014B) for funding this research.

Finally, my deepest appreciation and special thanks to my beloved wife, Nurul Jannah binti Mohamad Yasim for her infinite love, comfort and constant encouragement throughout my research period, and my family for their full support, understanding and patience.

TABLE OF CONTENTS

LIST OF FIGURES

LIST OF TABLES

CHAPTER 1: INTRODUCTION

Scientists have studied extensively thermoelectric materials to convert thermal energy into useful electrical energy for several decades now in order to reduce our dependence on fossil fuels and to reduce greenhouse gas emissions. In addition, a thermoelectric cell can supply continuous renewable electricity from a variety of heat energy sources. Basically, an important parameter in thermoelectric is the Seebeck coefficient (S_e), which may be determined from the gradient of a linear graph of potential difference (ΔV) *versus* temperature difference (ΔT) based on the relationship, $\Delta V = S_e \Delta T$.

Currently, research and development of higher-performance thermoelectric materials are important to suit the current market. In order to save waste heat from the exhaust to transform it into beneficial electrical energy for automotive electrical systems, thermoelectric generators have been installed in automobiles. Besides, this will also help in increasing fuel efficiency for future vehicles use. In addition, it can be applied for the electronic component cooling [1]. However, solid-state thermoelectric devices based on semiconductors have limitations due to relatively low efficiencies and poor long-term reliability [2]. Hence, research on electrochemically driven, liquid-based thermoelectric cells has become a priority. For example, Kang *et al.* reported that an aqueous solution of ferrocyanide/ferricyanide redox couple (0.4 M) has a higher $S_e$value (~1.4 mV K^{-1}) [3] than those of semiconductor system (0.1 – 0.2 mV K^{-1} at < 200 ^{o}C) [4].

Therefore, the main objectives of this research are to design, synthesise, characterize and study the thermoelectrical properties of Co(II) and Fe(II) complexes with extended π-conjugated 2,2‟-bipyridine ligands (LCn) appended with two linear alkyl chains (C_nH_{2n+1}, where n = 8, 10, 12, 14) **(Figure 1.1)**, and ethanoato (CH_3COO^-) and BF_4^- ions. The general formulae of the complexes are $[M_2(CH_3COO)_4(L)_2]$ and $[M(L)_3](BF_4)_2$, where M = Co(II) and Fe(II) **(Scheme 1.1)**.

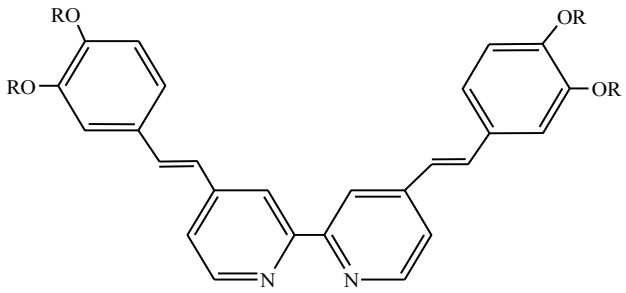

Figure 1.1 General structural formula of ligands LCn; R = C_nH_{2n+1} (n = 8, 10, 12, 14)

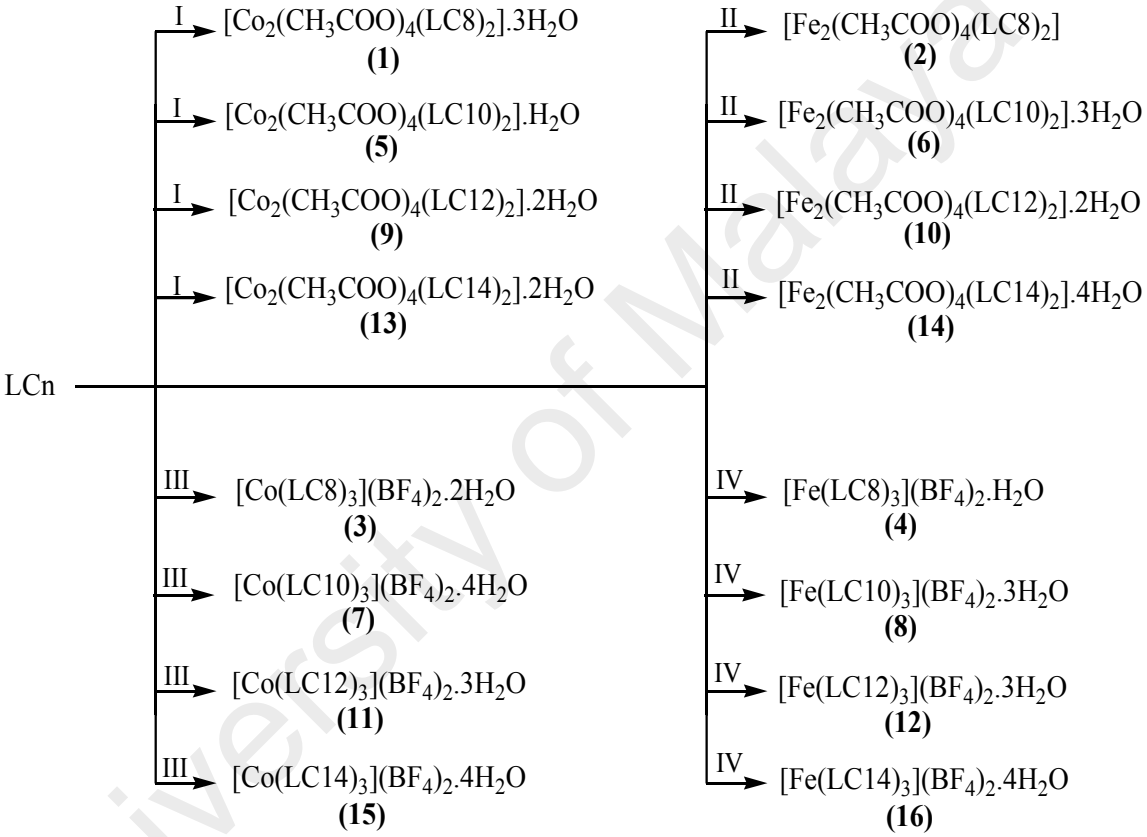

Scheme 1.1 Synthetic outline for **Complexes 1 – 16**. I = $Co(CH_3COO)_2.4H_2O$; II = $Fe(CH_3COO)_2$; III = $Co(BF_4)_2.6H_2O$; IV = $Fe(BF_4)_2.6H_2O$

The first part of this research focused on the syntheses of LCn and determination of their structural formulae by elemental analyses, ^{1}H-NMR spectroscopy and FTIR spectroscopy. This was followed by syntheses and characterization of their Co(II) and Fe(II) complexes. The structures of these complexes were deduced by elemental analyses, FTIR spectroscopy and UV-vis spectroscopy. Their magnetic susceptibilities were determined at room temperature by the Gouy method, thermal stabilities by

thermogravimetric analysis (TGA), and redox properties by cyclic voltammetry (CV) Prior to these analyses, the samples were heated in an oven at 65 ^{o}C for about a week to remove the lattice H_2O. The final part of this research was to determine their thermoelectric properties (Seebeck coefficient, S_e). The mean S_e values for all complexes were calculated as average from three heating-and-cooling cycles.

The findings of this research were accepted for publication in ISI journals and were presented in international and regional conference and seminar (**Appendix 1**), as listed below.

1. Norbani Abdullah, Mohamed Hamid Elsheikh, Nik Muhd Jazli Nik Ibrahim, Suhana Mohd Said, Mohd Faizul Mohd Sabri, Masjuki Haji Hassan and Anita Marlina, *Magnetic, Thermal, Mesomorphic and Thermoelectric Properties of Mononuclear, Dimeric and Polymeric Iron(II) Complexes with Conjugated Ligands*, RSC Adv., 50999-51007, 5, 2015.
2. Norbani Abdullah, Suhana Mohd Said, Yanti Yana Halid, Megat Muhammad Ikhsan Megat Hasnan, Naima Sharmin, Siti Amira Mat Hussin, Nik Muhd Jazli Nik Ibrahim, Abdul Rahman Nordin, Nurul Atikah Safiin and Nurul Shafinaz Anuar. *Complexes of Nickel(II) Carboxylates With Pyridine and Cyclam: Crystal Structures, Mesomorphisms and Thermoelectrical Properties*, Journal of Coordination Chemistry, Vol. 69, Iss. 19, 2016.
3. Nik Muhd Jazli Nik Ibrahim, Norbani Abdullah, Suhana Mohd Said, *Synthesis, Characterization And Thermoelectrical Properties of Complexes of Cobalt(II) with an Extended π-Conjugated Bipyridyl Ligand*. The Fifth International Conference for Young Chemists, 2015, Pulau Pinang. (Oral Presentation).
4. Nik Muhd Jazli Nik Ibrahim, Norbani Abdullah, Suhana Mohd Said, *Synthesis, Characterization And Thermoelectrical Properties of Complexes of Cobalt(II) and Iron(II) With An Extended π-Conjugated Bipyridyl Ligand*. The 28TH

Regional Symposium of Malaysian Analytical Sciences, 2015, Perak. (Oral Presentation).

This thesis contains five chapters. **Chapter 1** briefly introduces the objectives of this research, the complexes prepared, the instrumental technique involved and lists of publications and presentations of the research findings. **Chapter 2** presents the theories and literature reviews related to complexes of cobalt(II) and iron(II) with bipyridyl ligands (structural studies, cyclic voltammetry and band gaps, magnetic, thermal and thermoelectrical properties). **Chapter 3** presents the syntheses of ligands and complexes and the instrumental techniques used in the characterization of the materials prepared. **Chapter 4** contains the results and discussion for the ligands and complexes, and finally **Chapter 5** presents the conclusions and suggestions for future works. A list of references and appendices are displayed at the end of the thesis.

CHAPTER 2: THEORY AND LITERATURE REVIEW

2.1 Introduction

This research is focussed on the syntheses, structural deduction and characterisation of complexes of cobalt(II) and iron(II) with extended π-conjugated bipyridyl and CH_3COO^- ion as ligands, or BF_4^- as counterion. It includes studies on the band gaps (optical and electrochemical), magnetic, thermal and thermoelectric properties. Accordingly, this chapter focuses on the theories and literature reports relevant to these complexes.

2.2 Complexes of Cobalt(II) with Bipyridyl Ligands

2.2.1 Bipyridyl molecules

There are several types of symmetrical and asymmetrical isomers for bipyridine **(Figure 2.1)**. An example is 2,2‟-bipyridine (bpy), which is an organic compound discovered at the end of nineteenth century [5]. It may be prepared via the dehydrogenation reaction of iron(III) chloride, iodine or a nickel-alumina catalyst on pyridine in the temperature range from 300 ^oC to 400 ^oC [6].

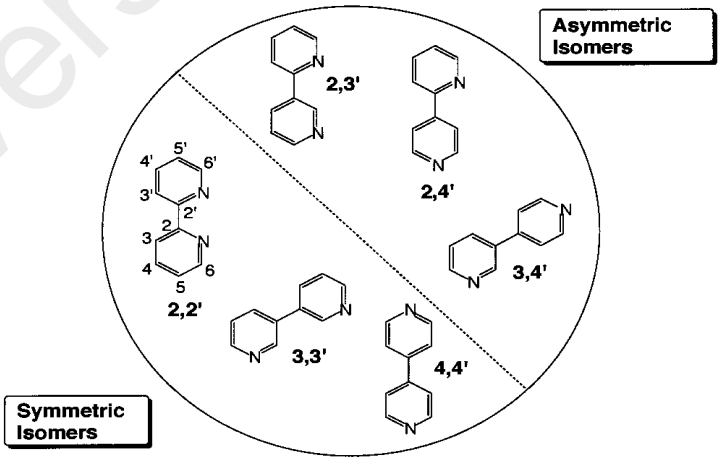

Figure 2.1 Symmetrical and asymmetrical bipyridine isomers [5]

Bpy is widely used as a ligand due to its robust redox stability and ease of functionalization. It acts as a bidentate chelating ligand with many transition metal ions [5]. It can also form octahedral complexes with metal ions, such as iron(II) and

cobalt(II), to form charged complexes. Introduction of electron-releasing groups on the aromatic ring of bpy, such as CH_3 and OCH_3, allows for delocalisation of electrons and additional stability for the complexes formed [7].

2.2.2 Bipyridyl complexes of cobalt(II)

Cobalt (Co) is a first-row transition metal ion with atomic number 27 and valence electronic configuration $4s^2 3d^7$. Its common oxidation states are Co(II) ($3d^7$) and Co(III) ($3d^6$). Sometimes, Co(II) tends to be oxidised to Co(III) when coordinated with moderate to strong field ligands, such as N- and N,O- donors. Co(II) can form octahedral, tetrahedral or square planar complexes **(Figure 2.2)**, depending on the ligands.

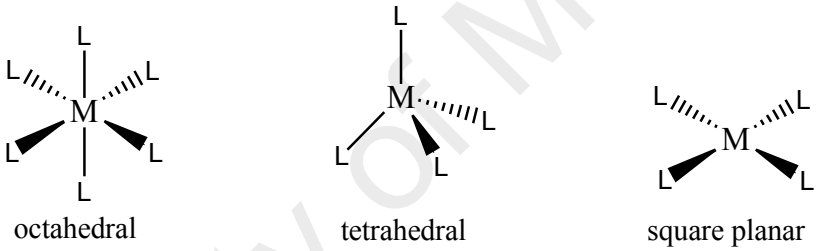

Figure 2.2 Common coordination geometries for cobalt(II) complexes

Octahedral complexes may be either high spin (HS; $t_{2g}^5 e_g^2$) or low spin (LS; $t_{2g}^6 e_g^1$), with three and one unpaired electrons, respectively. Explanation on how HS and LS complexes are formed will be explained later in this chapter.

Complexes of Co(II) with bpy as ligand have attracted many researchers' attention world wide for applications such as biosensors, antibacterial activities, designs and construction of artificial proteins, and in modelling for active sites of metalloenzymes [8, 9], and more recently, as potential thermoelectric materials in solutions [10].

(a) Structural studies

Co(II)-bpy complexes may be mononuclear or dinuclear and their structures can be deduced directly by X-ray crystallography (for crystals), or by combining data from elemental analyses, and FTIR and UV-vis spectroscopies (for non-crystals).

For example, Kumar *et al*. reported a mononuclear octahedral complex, $[CoCl_2(bpy)_2].3H_2O$, where bpy = 2,2''-bipyridine (**Figure 2.3**). The complex was prepared by adding a solution of bpy in acetone to a solution of cobalt(II) chloride in the same solvent. The yield was 90%. On recrystallization from ethanol, dark red crystals were obtained [8].

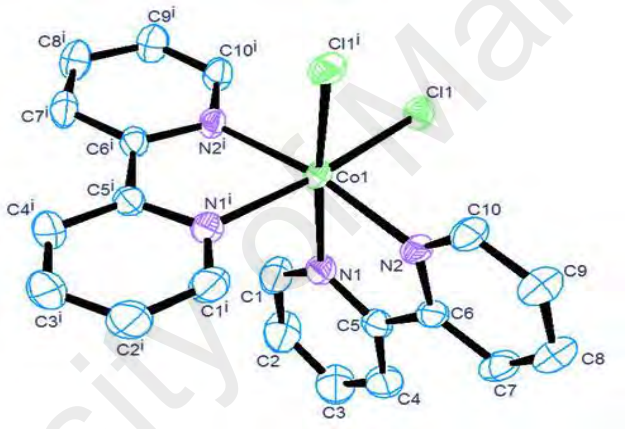

Figure 2.3 Crystal structure of $[CoCl_2(bpy)_2].3H_2O$ [8]

Elemental analyses are used to determine the mass percentage of carbon, hydrogen, nitrogen and heteroatoms (halogens and sulphur) of a sample. It can be either a qualitative (determining what elements are present) or quantitative (determining the amount of each element present) analysis. This technique involved combustion, in a furnace at about 1000 ^{o}C, which converts carbon to carbon dioxide, hydrogen to water, nitrogen to nitrogen gas or oxides, and sulphur to sulphur dioxide. These gaseous combustion products are swept out of the combustion chamber by an inert carrier gas, such as helium, and passed over heated (about 600 ^{o}C) high purity copper (to remove excess oxygen in the initial combustion and to convert any oxides of nitrogen to nitrogen gas). These gases will then pass through the absorbent traps, except for carbon

dioxide, water, nitrogen and sulphur dioxide [11]. The instrument is calibrated with blank aluminium, and acetanilide ($CH_3CONHC_6H_5$) as a quality control sample (C, 71.09 ± 0.30; H, 6.71 ± 0.30; N, 10.36 ± 0.30%). The aluminium capsules are used for solids or viscous liquid with known mass of sample (1.5 - 2.00 mg), and for liquids, sealed individual aluminium vials are used through a liquid auto sampler. The accepted error range for samples are ± 0.7% for C, ± 0.9% for H and ± 0.5% for N. For example, Agrawa *et al*. reported the values of 55.40% C, 3.71% H, 14.90% N for $[Co(bpy)(phen)_2](NO_3)_2.2H_2O$, where bpy = 2,2‟-bipyridine and phen = 1,10-phenanthroline, which were in excellent agreement with those calculated for the chemical formula $C_{34}H_{28}CoN_8O_8$ (55.51% C, 3.84% H, 15.23% N) [12].

Fourier transform infrared spectroscopy (FTIR) may be used to detect the functional groups and chemical bonds present in organic and inorganic compounds. It involves interaction of infrared light (wavenumber 4000 - 400 cm^{-1}) with matter, which changes the vibrational energy of a molecule [13, 14]. Each compound has its own absorption pattern and only certain functional groups absorbed at about the same wavelength. It can be used to characterize solid, liquid and gas samples. Traditionally, solid sample is mixed with KBr and compressed to form a transparent disk. A liquid sample may be deposited on the surface of a polished salt plate, while a gas sample is filled in an evacuated sample cell.

For metal carboxylates, FTIR spectroscopy is used to deduce the binding mode of a carboxylate ion ($RCOO^-$). This ion is a versatile ligand as it can coordinate to a metal centre as a monodentate, bidentate, chelating or bridging ligand **(Figure 2.4)**.

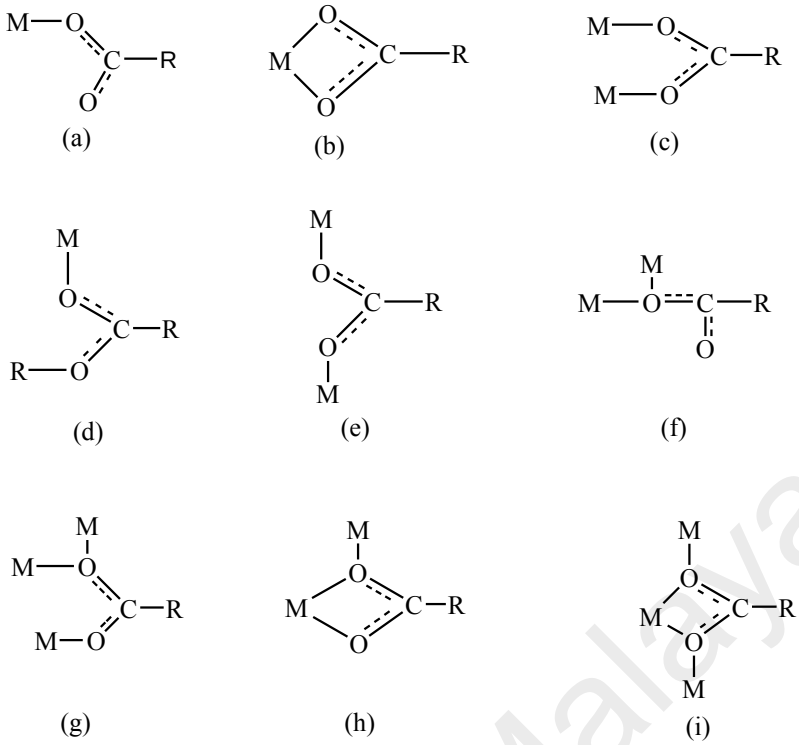

Figure 2.4 Different binding modes of carboxylate group: (a) unidentate; (b) chelating; (c) bridging bidentate (*syn-syn*); (d) bridging bidentate (*syn-anti*); (e) bridging bidentate (anti-anti); (f) monoatomic bridging; (g) monoatomic bridging; (h) additional bridging; and (i) chelating and bridging.

The IR data compiled by Deacon and Philips showed a good correlation between the difference (Δ) in wavenumbers for the asymmetric (υ_{asym}) and symmetric (υ_{sym}) stretching vibrations of COO group of the carboxylate ligand and its binding mode **(Table 2.1)** [15].

Table 2.1 The value of Δ for different binding mode of $RCOO^-$ ion

Binding mode	**$\Delta = \nu_{asym}-\nu_{sym}/cm^{-1}$**
Monodentate	>220
Chelating	<156
Bridging monodentate	~200
Bridging bidentate	~ 160
Chelating bidentate	<130

For example, Ye *et al*. reported a mononuclear Co(II) complex, $[Co(bpy)_2(OAc)](ClO_4).H_2O$, formed from the reaction of 2,2‟-bpy in methanol with $Co(CH_3COO)_2.4H_2O$, followed by $NaClO_4$. The results of its elemental analyses were 48.45% C, 3.78% H, 10.62% N, while the values calculated from its chemical formula,

$C_{22}H_{21}CoClN_4O_7$, were 48.23% H, 3.84% H, 10.23% N. Its FTIR spectrum (KBr, cm^{-1}) showed peaks at 1590 (vs), 1568 (s), 1440 (s), 1318 (m), 1164 (s), 1093 (s), 771 (s), 734 (m), 625 (s) [16]. Hence, the $\Delta\upsilon$ value was 128 cm^{-1}, indicating chelating bidentate binding mode of CH_3COO^- ligand.

Another example was $[Co_2(Pda)_2(H_2O)_5].2H_2O$, where H_2Pda = pyridine-2,6-dicarboxylic acid, reported by Siddiqi *et al.* [17]. The complex was obtained as a purple powder from the reaction of $Co(Ac)_2.4H_2O$ with pyridine-2,6-dicarboxylic acid and 3-amino-1-propanolin ethanol. Its FTIR spectrum showed strong peaks for $\upsilon_{asym}COO$ and $\upsilon_{sym}COO$ at 1632 cm^{-1} and 1322 cm^{-1}, respectively. Hence, the Δ value was 310 cm^{-1}, indicating an unsymmetrical monodentate binding mode for carboxylate ligand.

UV-visible (UV-vis) spectroscopy refers to the absorption or reflection of electromagnetic radiation in the ultraviolet-visible spectral region (approximately 200 nm to 1000 nm) by functional groups in molecules, to cause an electronic transition from the ground state (lower energy) to the excited state (higher energy). The excitation can occur between a bonding or lone pair orbital and an unoccupied non-bonding or antibonding orbital (**Figure 2.5**).

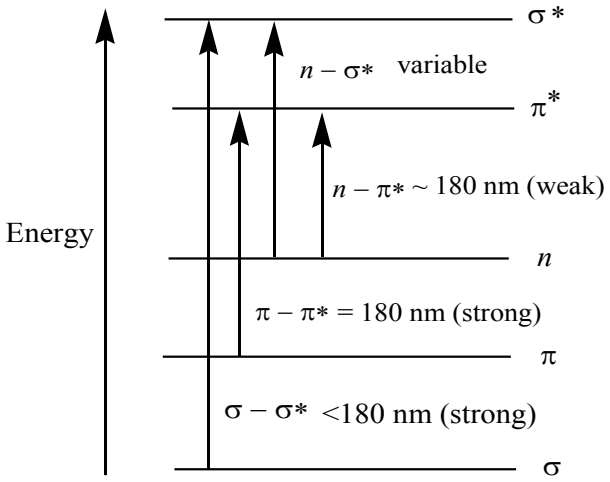

Figure 2.5 Electronic energy levels and electronic transitions

UV-vis spectroscopy may be used in quantitative analysis, such as to determine the concentration of a solution. An important equation is the Beer-Lambert law: $A = \varepsilon c l$, where A is absorbance, ε is molar absorptivity, c is concentration (mol dm^{-3}), and *l* is the optical path length (dimension of the cell or cuvette in cm). The value of ε defines how much radiation is absorbed by a molecule (a large ε value results from a strong absorption of light, while a small ε value results from a weak absorption). Different part of the molecule absorbed radiation at different wavelength. An absorption spectrum shows a number of bands corresponding to a structural group in the molecule.

This spectroscopy may also be used to probe the geometry of the transition metal ion of a complex. The sample may be a solid or in a solution. For solid samples, barium sulphate is used as a blank, while the solvent is used as a blank for solutions.

There are two types of electronic absorption transition, namely *d-d* and charge transfer. In *d-d* transition, an electron in a lower energy *d* orbital absorbs a photon and is excited to a higher energy *d* orbital. Metal-to-ligand charge transfer (MLCT) may occur for a metal in a low oxidation state (electron-rich) and a ligand possessing low-lying empty orbitals **(Figure 2.6)** [18]. MLCT causes instantaneous „oxidation" of the metal ion and „reduction" of the ligand. In contrast, ligand-to-metal charge transfer (LMCT) occurs from the filled ligand molecular orbitals to the empty or partially filled metal *d* orbitals **(Figure 2.7)** [19], causing instantaneous „reduction" of the metalion and „oxidation" of the ligand.

The different types of transition can be distinguished by ε values. The values for the spin-allowed *d-d* transition bands are 10 - 500 dm^3 mol^{-1} cm^{-1} for octahedral, and 500 - 1000 dm^3 mol^{-1} cm^{-1} for tetrahedral complexes, while the values for the spin-forbidden bands (usually cannot be seen) are less than 5 dm^3 mol^{-1} cm^{-1}. Charge transfer bands, which occur at higher energy that *d-d* band, have high ε values (normally more than 1000 dm^3 mol^{-1} cm^{-1}).

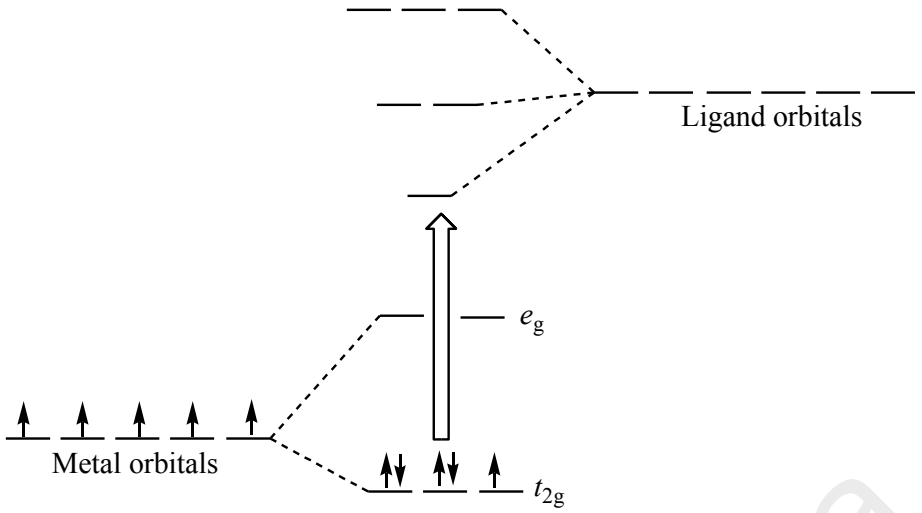

Figure 2.6 MLCT transition for a low-spin d^5 metal complex

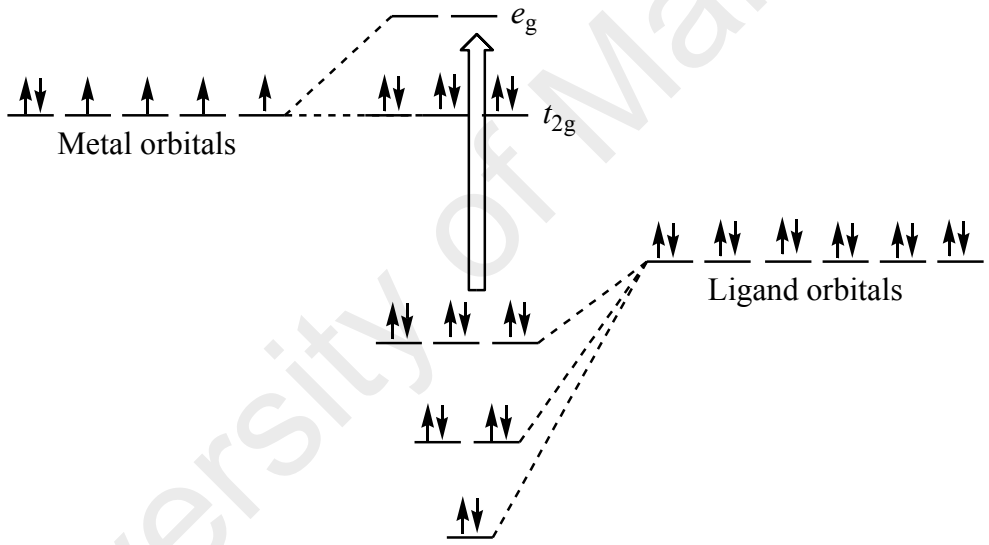

Figure 2.7 LMCT transition for a low-spin d^6 metal complex

Electronic transitions are governed by two selection rules: spin rule and Laporte rule. In the spin rule, an allowed transition involves no change in the number of unpaired electron(s) or spin state ($\Delta S = 0$), while a strongly forbidden transition involves a change in the number of unpaired electron(s) or $\Delta S \neq 0$.

Laporte selection rule determines whether a transition is allowed or forbidden. It applies to molecules or ions possessing a centre of symmetry (centrosymmetric). Transitions between orbitals of the same parity ($s \rightarrow s$; $d \rightarrow d$) are forbidden. Complexes affected by this selection rule have octahedral and square-planar geometries,

while complexes with tetrahedral geometry are not affected since they do not have a centre of symmetry (non-centrosymmetric).

A useful model for electronic structures of first-row transition metal complexes is offered by the crystal-field theory (CFT). According to this theory, there are two types of interaction in complexes: attraction between the metal cation and the anionic ligand (or lone pair(s) of a ligand), and repulsion between the *d* electrons of the metal and the electrons from the ligand, which results in the splitting of the *d* orbitals. This theory focuses on the splitting of the *d* orbitals with different energies, and uses that splitting to correlate the optical spectra, thermodynamic stability and magnetic properties of complexes [20].

For octahedral complexes, the five *d* degenerate orbitals of a free metal ion split into two sets of different energy: three degenerate orbitals at lower energy, d_{xy}, d_{xz} and d_{yz} (t_{2g} orbitals), and two degenerate orbitals at higher energy, $d_{x^2-y^2}$ and d_{z^2} (e_g orbitals) (**Figure 2.8**).The energy difference between the two energy levels is known as the octahedral crystal field splitting (Δ_o).

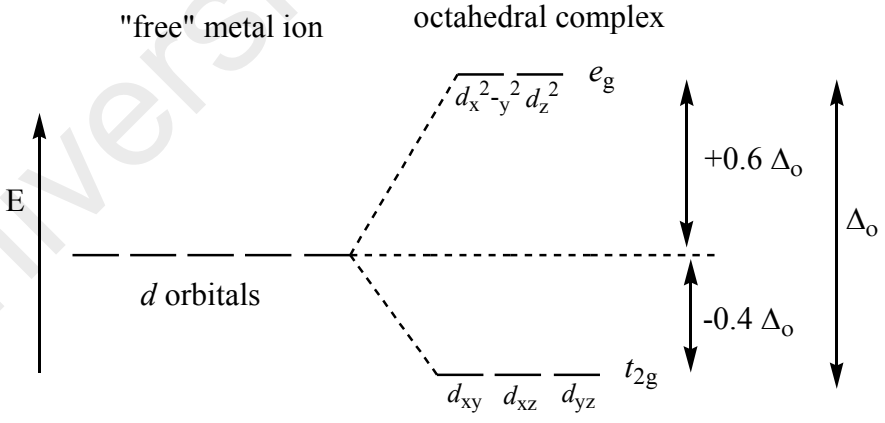

Figure 2.8 Splitting of *d* orbitals in an octahedral complex

Most transition metal ions form coloured complexes due to absorption of light in the visible region, as an electron from a *d* orbital of lower energy level is excited to a *d* orbital of higher energy level (*d-d* transition). A characteristic portion of the mixed wavelengths is absorbed when white light passes through or reflected by a coloured

substance. The remaining light will then assume the complementary colour to the wavelength(s) absorbed. The colour wheel **(Figure 2.9)** shows a relationship between the wavelength absorbed and colour. If all light is absorbed (none is transmitted), the colour of the complex is black. On the other hand, if none of the light is absorbed (all is transmitted), the colour of the complex is white (if solid) or colourless (in solution).

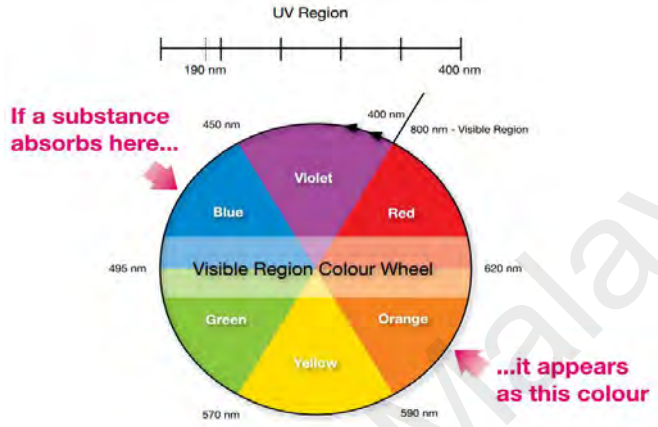

Figure 2.9 Colour wheel [21]

The magnitude of Δ_o depends on the metal ion, charge on the metal ion, and on the ligands. If the geometry and ligands are the same, the Δ_o value decreases in the following sequence for a metal ion:

$$Mn^{2+} < Ni^{2+} < Co^{2+} < Fe^{2+} < Fe^{3+} < Cr^{3+} < Co^{3+} < Rh^{3+} < Ir^{3+} < Pt^{4+}$$

Weak-field ions Strong field ions

For a particular metal ion, the strength of a ligand is shown in the spectrochemical series:

$$I^- < Br^- < Cl^- < SCN^- < F^- < OH^- < H_2O < NCS^- < NH_3 < NO_2^- < CN^- \approx CO$$

Weak –field ligand Strong-field ligand

Electrons are filled into the t_{2g} and e_g orbitals according to Aufbau principle and Hund"s rule. Depending on the magnitude of Δ_o and pairing energy (p), octahedral complexes can either be low-spin (LS) or high-spin (HS). If Δ_o is larger than p, electrons will occupy the lower t_{2g} orbitals until they are full (two electrons each) before filling the higher e_g orbitals, leading to LS complexes (minimum number of unpaired

electron(s)). On the other hand, if Δ_o is smaller than *p*, electrons will occupy the lower t_{2g} orbitals singly with parallel spins, and then the higher e_g orbitals in the same manner until all orbitals are half full (one electrons each) before they are paired. This leads to HS complexes (maximum number of unpaired electron(s)). LS complexes are more stable and have stronger M-L coordination bonds compared to HS complexes.

For example, Co(II) ion has seven 3*d* electrons. It forms HS octahedral complexes (ground state electronic configuration $t_{2g}^5 e_g^2$) when the ligands are weak fields, or LS octahedral complexes (ground state electronic configuration $t_{2g}^6 e_g^1$) when the ligands are strong fields **(Figure 2.10)**. There are three unpaired electrons in HS complexes, and one unpaired electron in LS complexes. Hence, both HS and LS complexes are paramagnetic.

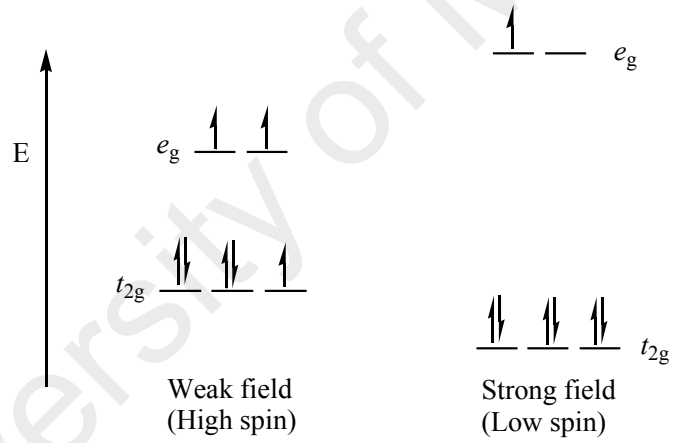

Figure 2.10 Electronic arrangement for: (a) high spin; and (b) low spin Co(II) complexes

In 1936, Hermann Jahn and Edward Teller [22] proposed that a non-linear molecule is unstable when its electronically degenerate orbitals are asymmetrically occupied. To be stable, the molecule undergoes geometrical distortion to remove the degeneracy [23]. This is now known as the Jahn-Teller theorem. In an octahedral crystal field, the triply degenerate t_{2g} orbitals do not point directly at the ligands, while the doubly-degenerate e_g orbitals point directly towards the ligands. Hence, geometrical distortion is more significant for the electronic states involving asymmetrically

occupied e_g orbitals compared to t_{2g} orbitals. The normally observed geometrical distortions for octahedral complexes are elongated and compressed **(Figure 2.11)**.

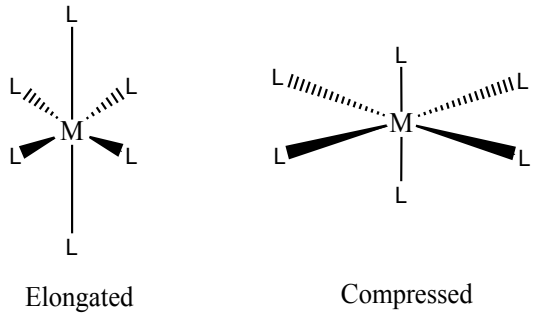

Figure 2.11 Geometrical distortions in octahedral complexes due to the Jahn-Teller effect

Generally, geometrical distortions are observed in octahedral complexes with d^4, d^5 (LS), d^6 (HS), d^7, and d^9 configurations. For example, HS Co(II) octahedral complexes experience a weaker Jahn-Teller effect compared to LS Co(II) octahedral complexes (**Figure 2.12**).

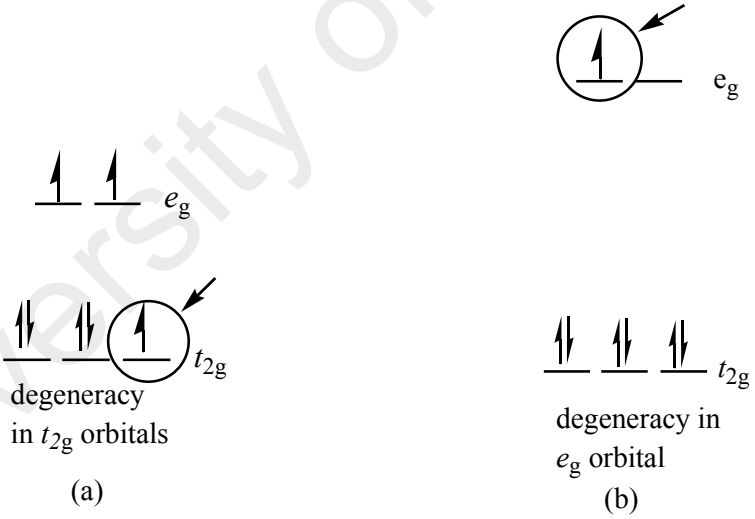

Figure 2.12 Electronic configuration of a Co(II) octahedral complex: (a) weak Jahn-Teller effect for HS, and (b) strong Jahn-Teller effect for LS

As a result of geometrical distortion, a *d-d* band in the UV-vis spectrum splits **(Figure 2.13)**.

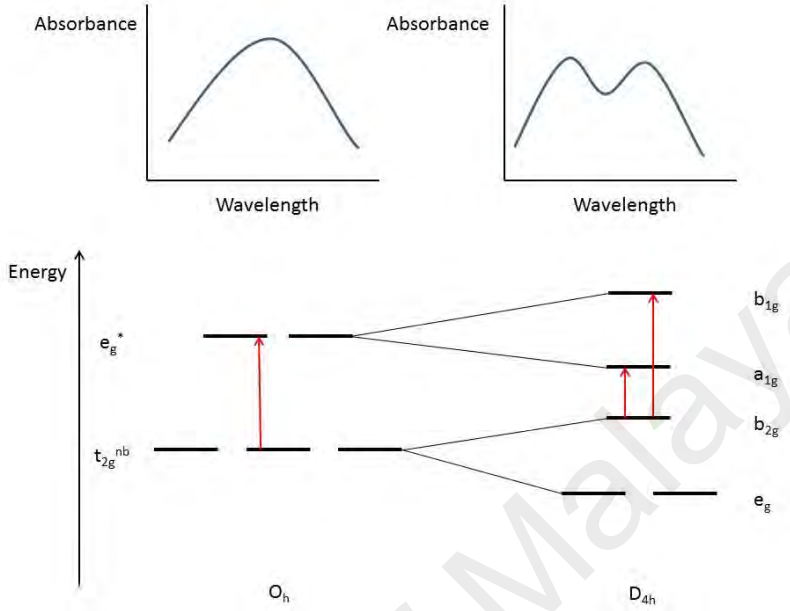

Figure 2.13 Absorption spectrum: (a) an octahedral complex (O_h symmetry); and (b) a geometrically distorted octahedral (D_{4h} symmetry)

As an example, Lehleh *et al.* reported a slightly distorted octahedral Co(II) complex, $[Co(dmbpy)_3][CoCl_4].7H_2O$, where dmbpy = 4,4‟-dimethyl-2,2‟-bipyridine **(Figure 2.14)**. The complex was obtained as green crystals in good yield (41.06%) from the reaction of cobalt(II) chloride hexahydrate with 4,4‟-dimethyl-2,2‟-bipyridine in methanol solution containing L-cysteic acid and sodium azide. The cobalt atom of the cation (Co1)was coordinated to six nitrogen atoms which belong to three different bipyridyl ligands, forming a distorted octahedron (bond length: Co1-N1 = 1.937 Å, Co1-N2 = 1.947 Å, Co1-N3 = 1.930 Å, Co1-N4 = 1.936 Å, Co1-N5 = 1.925 Å, Co1-N6 = 1.925 Å), while the $[CoCl_4]^-$ anion exhibited tetrahedral geometry, with the Co(2) ion surrounded by four Cl atoms (bond length: Co2-Cl1 = 2.298 Å, Co2-Cl2 = 2.267 Å, Co2-Cl3 = 2.279 Å, Co2-Cl4 = 2.258 Å). Accordingly, this complex experienced a weak Jahn-Teller effect [24].

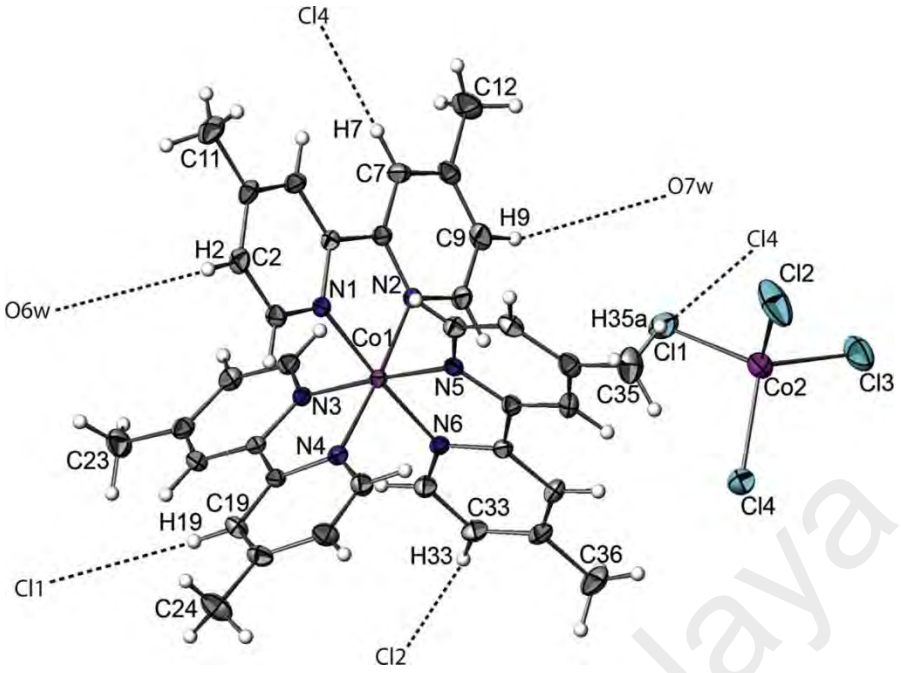

Figure 2.14 Crystal structure of $[Co(dmbpy)_3][CoCl_4].7H_2O$ [24]

Another example was reported by Cortes *et al.* for a HS cobalt(II) dimeric complex, $K[Co_2(OH)_2(Ac)_3(bipy)_2].2H_2O$, where Ac = acetate ion, and bipy = 2,2‟-bipyridine **(Figure 2.15)**. This complex was obtained as single crystals from the reaction of cobalt(II) acetate with 2,2‟-bipyridine in ethanol, followed by $KClO_4$. The geometry at both cobalt(II) centres was distorted octahedral with the O atoms of monodentate and bridging acetato ligands occupying the apical sites, the O atoms from the hydroxo groups, and the N atoms from bipy occupying the equatorial sites (bond length: Co(1)-O(1) = 1.879 Å, Co(1)-O(2) = 1.880 Å,Co(1)-O(15) = 1.917 Å, Co(1)-O(23) = 1.899 Å; Co(1)-N(12)= 1.923 Å,Co(1)-N(22)= 1.915 Å). The results of its elemental analyses (43.32% C, 4.82% H, 7.21% N) were in good agreement with the calculated values based on its chemical formula (43.55% C, 4.36% H, 7.82% N) [25].

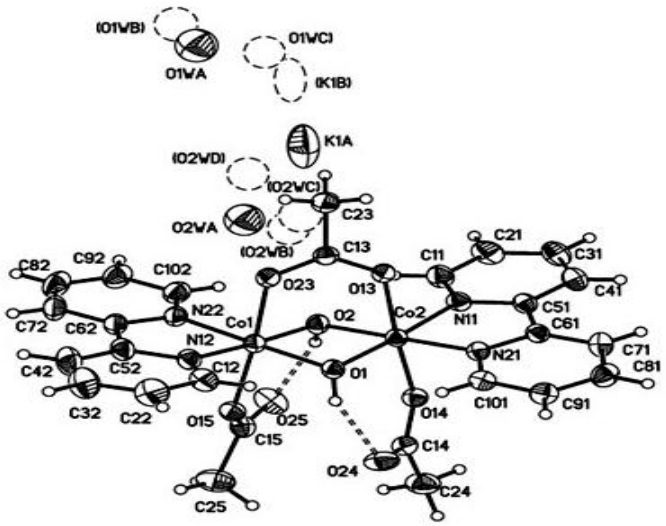

Figure 2.15 Single crystal structure of $K[Co_2(OH)_2(Ac)_3(bipy)_2].2H_2O$ [25]

Tanabe-Sugano diagrams are useful to determine the number of *d-d* bands, assign them, and predict the size of the ligand field necessary to cause HS-to-LS transition for octahedral complexes. In this diagram, the energy of electronic transitions (E) are given on the *y*-axis, denoted as E/B, and the ligand field strength increasing from left to right on the *x*-axis, denoted as Δ_o/B (B is the Racah parameter used to represent the approximation of the bond strength between the metal and ligand). The baseline (zero energy) in this diagram represents the ground state. [26].

For example, the Tanabe-Sugano diagram for Co(II) is shown in **Figure 2.16**. The diagram is divided into two regions by a vertical line. The region on the left side of the line is for electronic transitions in HS complexes, while that on the right side of the line is for electronic transitions in LS complexes. For spin-allowed transitions, the multiplicities must be the same.

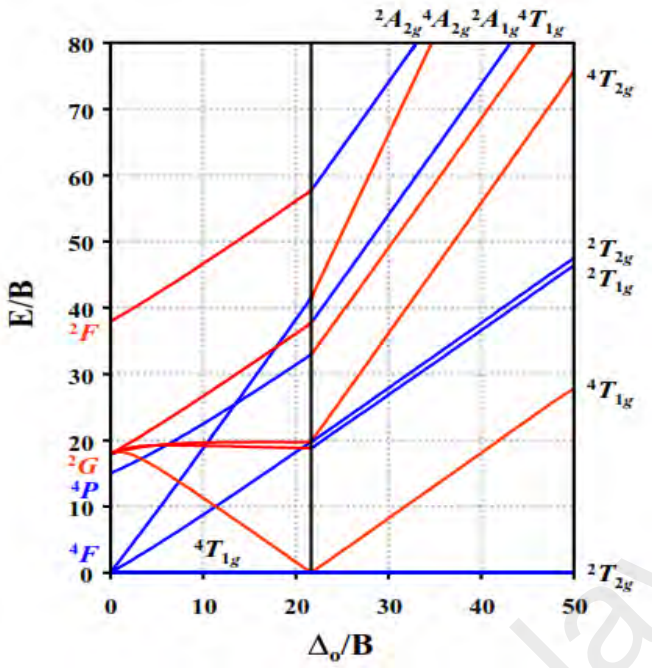

Figure 2.16 Tanabe-Sugano diagram for d^7 octahedral complexes.

For example, Santra and Lahiri reported the UV-vis spectrum of a LS Co(II) complex, $[Co(L)_3][ClO_4]_2.H_2O$, where L= 2-(phenylazo)pyridine **(Figure 2.17)**. The spectrum shows overlapping weak *d-d* bands at around 650 - 860 nm (ε_{max}, 322 - 456 M^{-1} cm^{-1}). The lowest energy band was assigned to $^2E_g \rightarrow {}^2T_{1g}$ electronic transition [27].

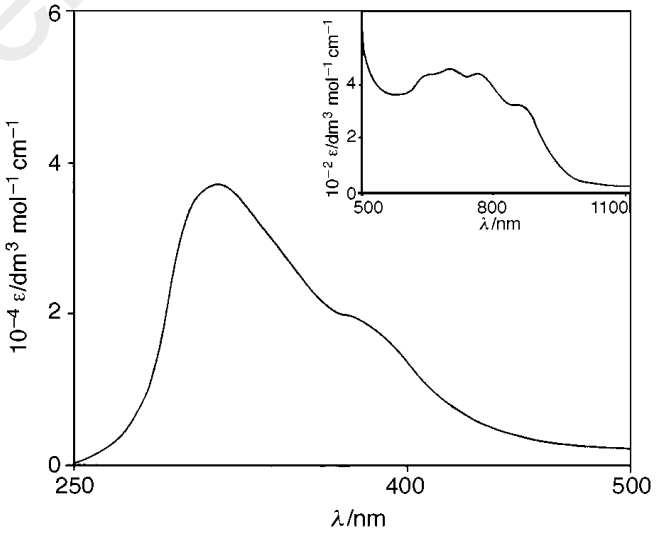

Figure 2.17 Electronic spectrum of $[Co(L)_3](ClO_4)_2.H_2O$ in acetonitrile. The inset shows low-energy *d-d* transitions [27].

Similarly, the *d-d* bands for a LS octahedral cobalt(II) complex, $[Co(terpy)2]^{2+}$, where terpy = 2,2‟:6‟,2”-terpyridine, were found at about 740 nm and 645 nm, and assigned to $^2A_{1g} \rightarrow {}^2T_{1g}$ and $^2A_{1g} \rightarrow {}^2T_{2g}$ electronic transitions, respectively [28], while the *d-d* bands for a HS cobalt(II) complex, $[Co(bipy)_3Cl_2].7H_2O$, where bipy = 2,2‟-bipyridine, were at about 920 nm and 470 nm, assigned to $^4T_{1g} \rightarrow {}^4T_{2g}$ and $^4T_{1g} \rightarrow {}^4T_{1g}(P)$ electronic transitions, respectively [29].

Czakis-Sulikowska and Czylkowska for a HS Co(II) complex, $[Co(bpy)_2(CCl_3COO)_2].H_2O$, where bpy = 2,2‟-bipyridine. Its electronic spectrum showed a band at 20800 cm^{-1} (480 nm) assigned to the $^4T_{1g}(F) \rightarrow {}^4T_{1g}(P)$ electronic transition, and a shoulder at 16000 cm^{-1} (625 nm) assigned as $^4T_{1g}(F) \rightarrow {}^4A_{2g}$ electronic transition. The charge transfer band appeared as a strong band at above 26000 cm^{-1} (385 nm) due to distorted octahedral donor environment at cobalt(II) atom [30].

(b) Cyclic voltammetry and band gaps

The study of band gap energy is important for thermoelectrical applications because it is closely related to conductivity of the metal complexes. Generally, band gap energy **(Figure 2.18**) may be defined as the difference in energy between the top of valence band and the bottom of conduction band. The unit is electron volt (eV). The valence band is the orbitals in which electrons are not free to move, while conduction band is the orbitals in which electrons are relatively free to move. The space between valence and conduction bands is called the forbidden band. Basically, electrons are able to jump from the valence band to the conduction band by acquiring an optimum amount of energy.

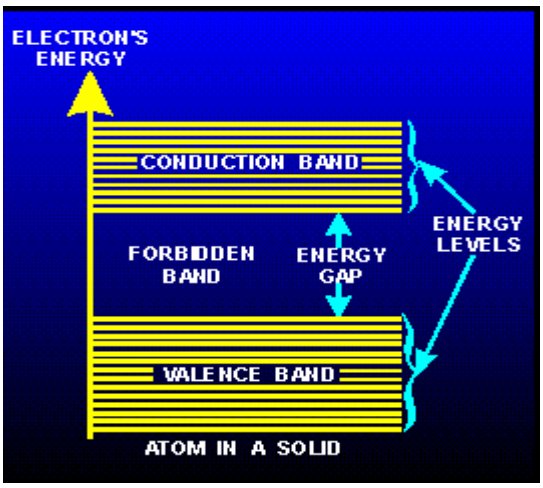

Figure 2.18 Energy arrangements of atoms in solid [31]

Based on the width of the forbidden band, a material is classed as an insulator, semiconductor or conductor **(Figure 2.19)**. Insulators have very broad energy level (E_g > 4 eV), semiconductors have smaller band gap energy (E_g < 3 eV), while conductors have very small or no band gap due to the overlap of the valence and conduction bands.

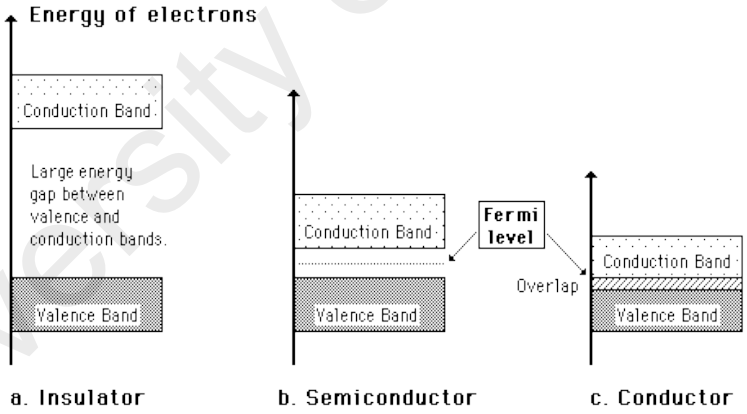

Figure 2.19 Possible energy bands for insulator, semiconductor and conductor

There are two ways in which the band gap of a material may be determined: electrochemistry (cyclic voltammetry) which measures the electrochemical band gap (E_e), and optical spectroscopy (absorption and emission) which measures the optical band gap (E_o).

Cyclic voltammetry (CV) is an electrochemical technique widely used for preliminary determination of redox properties for species. **Figure 2.20** shows a typical

CV profile exhibited by a species which undergoes a reversible electrochemical reaction.

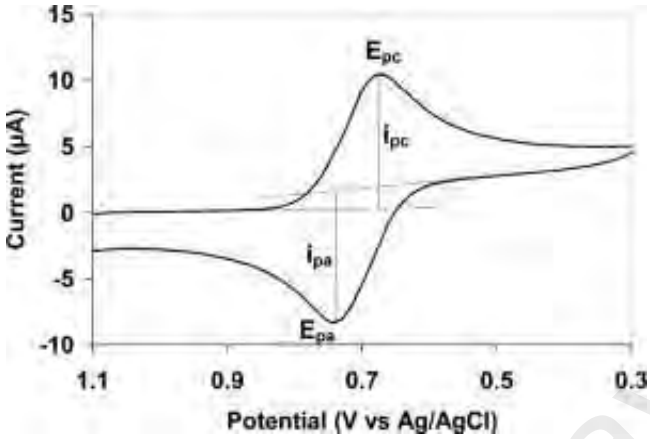

Figure 2.20 Typical CV for a reversible reaction where i_{pc} and i_{pa} are the peak cathodic and anodic current, respectively.

Normally, a CV experiment is performed using three types of electrode in a quiet solution (stationary condition): (a) working electrode (the electrochemical phenomena usually take place on this electrode). An example is glassy carbon; (b) counter or auxiliary electrode, which function as a source for electrons so that current can be flowed through the cell from the external circuit. Commonly used counter electrode is platinum due to its inert properties; and (c) reference electrode. The potential for this electrode is constant, so that it can be used as reference standard against the measurement for other electrodes present in the cell, such as silver-silver chloride electrode or calomel electrode [32]. In addition, a supporting electrolyte is added to the solution in order to increase conductivity and avoid the migration currents. An example is *tert*-butylammonium tetrafluoroborate (TBATFB) [33].

By IUPAC convention, anodic currents are positive while cathodic currents are negative [34]. If positive-going potential scan is chosen for the first cycle, starting from an initial potential, a linear potential sweep (potential ramp) is applied to this electrode until reaching at switching potential. If a peak(s) appeared in this region, the oxidation process is taking place in this species. After that, the sweep is reversed and the potential

returns linearly to its initial value [35]. If another peak(s) appeared in this region, the species is undergoing reduction process.

CV can be classified into three electrochemical reactions: reversible, irreversible and quasi-reversible reactions **(Figure 2.21)**. For reversible reaction, the reaction is fast to maintain the concentration of oxidised and reduced form in equilibrium at the electrode surface [36]. The separation between the peak potentials (ΔE_p) is approximately 59/*n* mV at 298 K, where *n* is the number of electron(s) transferred, and the ratio of the forward-to-reverse peak currents is equal to one.

$$\Delta E_p = E_{pa} - E_{pc} \approx 59 \text{ mV}/n \quad (1)$$

$$i_{pf}/i_{pr} = 1 \quad (2)$$

An irreversible process occurred when the rate of electron transfer is lower than the rate of mass transport, and the charge transfer at the electrode is extremely slow. Typically, the separation between the forward and reverse peaks is large. Lastly, a redox reaction is said to undergo a quasi-reversible process when the rate of electron transfer is in the same order of magnitude as that of mass transport. Additionally, the separation between the forward peak and reversible peak is larger than for a reversible redox reaction ($\Delta E_p > 59/n$mV) at 298 K.

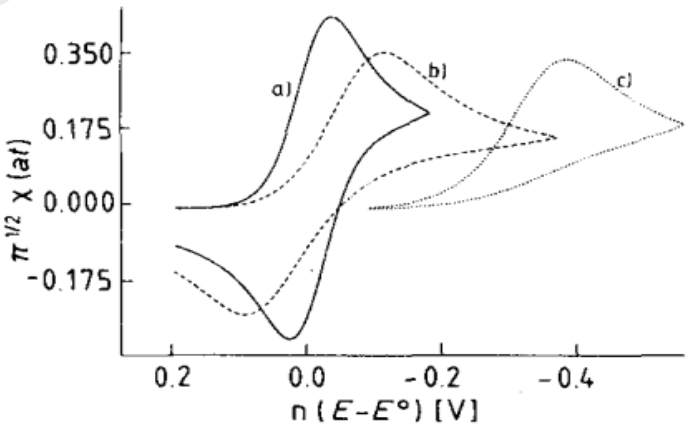

Figure 2.21 Cyclic voltammogram of three electrochemical reactions: (a) reversible; (b) quasi-reversible; and (c) irreversible

For example, Cabral *et al*. reported the CV for a 10 mmol dm^{-3} solution of $[Co(bpy)_3]^{2+}$, where bpy = 2,2‟-bipyridine, in 1-butyl-1-methylpyrrolidinium bis(trifluoromethanesulfonyl)amide (C_4mpyr NTf_2). The complex underwent two different reversible redox reactions **(Figure 2.22)**. However, the CV of this complex in acetonitrile showed irreversible redox (only one reduction peak appeared) [37].

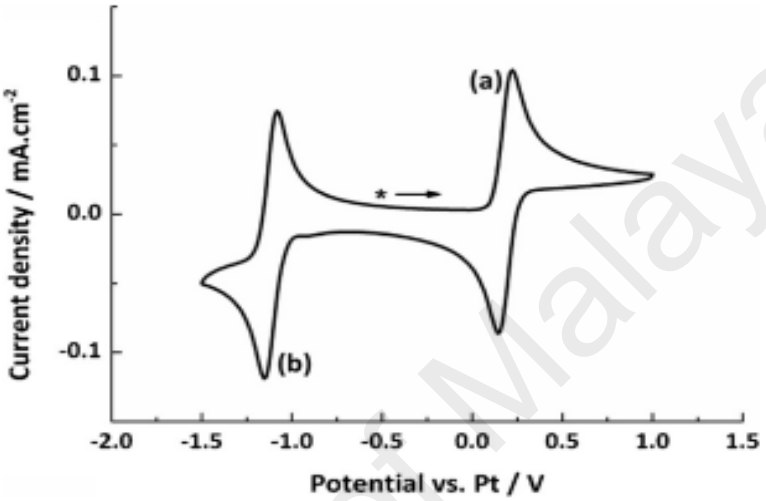

Figure 2.22 Cyclic voltammogram of reversible redox reaction for $[Co(bpy)_3]^{2+}$ [37]

Santra and Lahiri reported the CV for a LS octahedral cobalt(II) complex, prepared from the reaction of 2-(arylazo)pyridine with cobalt(II) perchlorate hexahydrate in ethanol. The voltammogram **(Figure 2.23)** showed a quasi-reversible oxidative program (ΔE_p ~ 1 V)**,** assigned to cobalt(II) to cobalt(III) oxidation, and six sequential ligand reduction processes (N=N groups) in the range 0.2 V – 1.8 V (*versus* standard calomel electrode, SCE) [27].

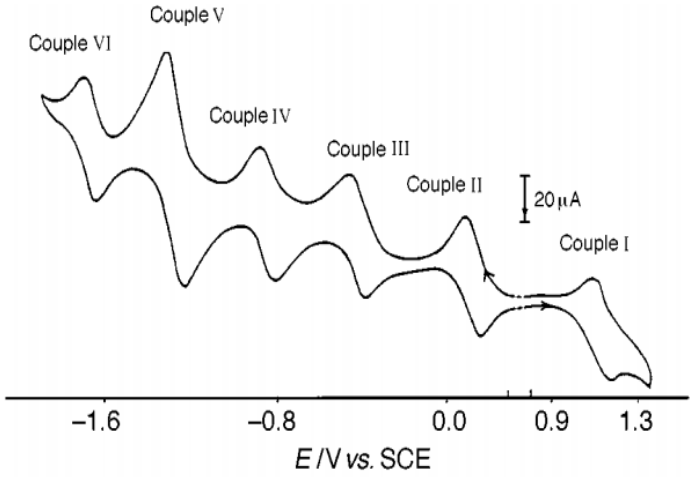

Figure 2.23 Cyclic voltammogram of quasi-reversible redox reaction for a LS octahedral Co(II) complex [27].

E_e is calculated from the equation: E_e = (HOMO – LUMO), where HOMO is the highest occupied molecular orbital, and LUMO is the lowest unoccupied molecular orbital. The value of 4.4 eV is added to each HOMO and LUMO in order to convert the calculated value into the eV unit [38]. For example, Kaya and Koyuncu reported the E_e value of 3.06 eV for O-2-PIMP-Co, where O-2-PIMP is oligo-2-[(phenyllimino) methyl)]phenol (E_{LUMO} = -2.68 eV and E_{HOMO} = -5.74 eV) [39].

The optical band gap (E_g) is calculated using the formula: $E_g = hc/\lambda$, where c = velocity of light (3.0 x 10^8 m s^{-1}), h = Planck constant (6.626 x 10^{-34} J s^{-1}), and λ (absorption edge or onset of CT band). The value in joule (J) is converted to electron volt (eV) using the conversion factor: 1 J = 1.60 x 10^{-19} eV. For example, Zhang *et al.* reported that $[Co_2(bpy)_6(W_6O_{19})_2]$, where bpy = 4,4‟-bipyridine, has an optical band gap of 2.2 eV [40].

(c) Magnetic properties

Transition metal complexes with one or more unpaired electrons (S > 0) are paramagnetic (attracted towards magnetic field), while those with no unpaired electrons (S = 0) are diamagnetic (repelled out of magnetic field).

An important parameter for magnetism is magnetic susceptibility. It is a measure of the ability of a material or sample to be magnetized. For solid sample, the value can be easily obtained by the Gouy method at room temperature. In this method, the Gouy balance gives directly the value of gram susceptibility (χ_g). The mass magnetic susceptibility (χ_M), the molar susceptibility corrected at certain temperature in Kelvin ($\chi_M T$) and the percentage of HS and LS of the samples were calculated using the following equations:

$$\chi_M = \chi_g \text{ x } MW$$

$$\chi_M^{corr} = \chi_M - \chi_D$$

$$\chi_M T = \chi_M^{corr} \text{ x } T$$

$$\chi_M T_{(\text{found})} = [(\chi_M T)_{\text{HS(theoretical)}} \text{ x } (a/100\%)] + [(\chi_M T)_{\text{LS(theoretical)}} \text{ x } ((100\text{-}a)/100\%)]$$

where MW = formula mass of the complex, T = absolute temperature (K), χ_D = diamagnetic corrections and χ_M^{corr} is the molar susceptibility corrected for the diamagnetic components of the ligands and associated ions.

For example, Krivokapic *et al.* reported that the magnetic susceptibility for $[Co(bpy)_3]^{2+}$, where bpy = 2,2‟-bipyridine, was 3.3 cm^3 mol^{-1} K at 300 K [41]. The theoretical values for HS (S = 3/2) and LS (S = 1/2) mononuclear Co(II) complexes were 1.876 cm^3 K mol^{-1} and 0.375 cm^3 K mol^{-1}, respectively [42]. Hence, this complex has 100% HS Co(II) at this temperature, which indicates weak Co-N bonds.

(d) Thermal properties

Thermal stability may be measured by thermogravimetric analsis (TGA). In general, it involves measurements of mass loss of a material as a function of temperature or time. The mass loss may be due to evaporation such as solvents or lattice water or/and decomposition of a part of the material or breaking of chemical bonds.

Commonly, TGA is used to determine the decomposition temperatures, absorbed moisture content, and level of inorganic and organic components in materials and residues. A thermogram may also be used to estimate the formula mass of a complex from the residue formed and hence its chemical formula. The calculation is based on the gravimetric concept and only be done if the residue is identified and the ligands are completely decomposed (as assign by a plateau at high temperature). In the absence of crystal data, the TGA data may be used to support the proposed structure deduced from elemental analyses, FTIR and UV-vis spectroscopies. TGA instrument usually consist of a sample pan (platinum, aluminium or alumina) placed on a precision balance inside a furnace where the sample is heated from about 50 ^{o}C to 900 ^{o}C. The sample is heated under nitrogen or in synthetic air with constant heat rate. During this process, the mass difference is measured. For instance, the reaction with oxygen from the synthetic air probably leads to a mass increase [43].

For example, Czakis-Sulikowska and Czylkowska reported the thermogram of $[Co(2\text{-bpy})_2(CCl_3COO)_2].H_2O$, where 2-bpy = 2,2‟-bipyridine, which showed that the hydrated complex was stable up to 100 ^{o}C. The rapid mass loss observed from 100 ^{o}C to 180 ^{o}C was due to the dehydration and decomposition of trichloroacetates. $[Co(2\text{-bpy})_2Cl_2]$ was formed from the decomposition of $[Co(2\text{-bpy})_2Cl_{1.5}(CCl_3COO)_{0.5}]$ in the temperature range of 180 - 260 ^{o}C. The intermediate compound ($[Co(2\text{-bpy})_2Cl_2]$ deaminate in two stages. In the first stage, 2-bpy was eliminated to form $[Co(2\text{-bpy})Cl_2]$ in the temperature range of 260 ^{o}C to 440 ^{o}C. In the second stage, $[Co(2\text{-bpy})Cl_2]$ decomposed via Co_3O_4 to CoO as a residue on high temperature. The oxides of Co(II) was verified by X-ray diffraction patterns registration. The step-like thermogram and scheme of this complex are shown in **Figure 2.24** and **Scheme 2.1**, respectively [30].

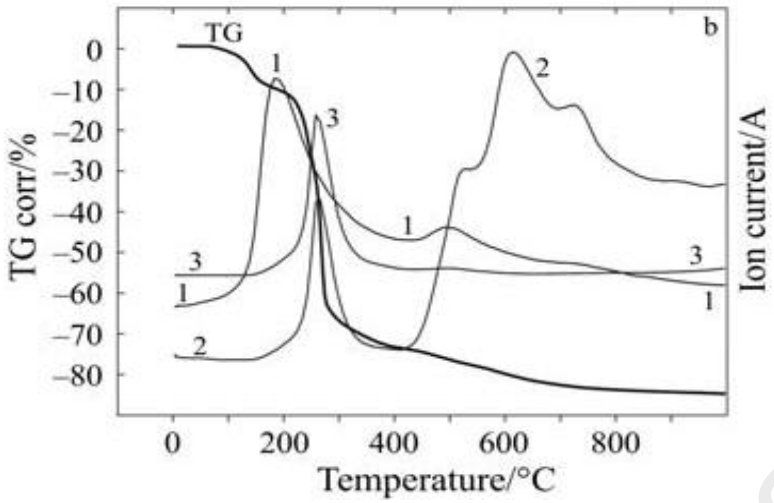

Figure 2.24 TGA trace of $[Co(2\text{-bpy})_2(CCl_3COO)_2].H_2O$

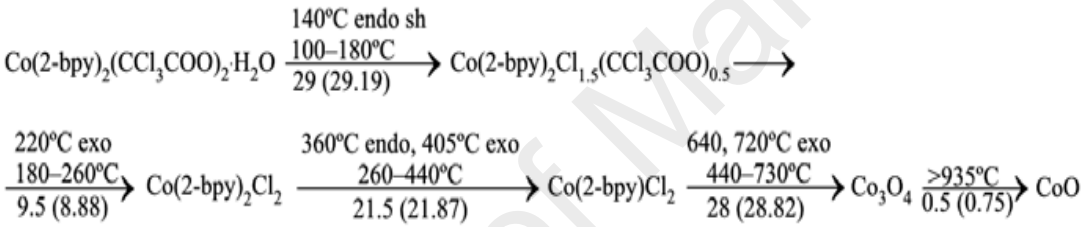

Scheme 2.1 Thermal decomposition of $[Co(2\text{-bpy})_2(CCl_3COO)_2].H_2O$

Another example, the thermal properties of a mononuclear complex, $[Co(2,2\text{-bipy})(H_2O)_2(SO_4)]_n$**(1)** and a binuclear Co(II) complex, $[Co_2(2,2\text{-bipy})_2(btec)(H_2O)_6].2H_2O$ **(2)**, where 2,2-bipy = 2,2‟-bipyridine, and btec = 1,2,4,5-benzenetetracarboxylate ion **(Figure 2.25)** were reported by Tao *et al* [44]. Complex **1** showed three stages of decomposition. The first mass loss of 10.84% in the range of 108 - 200 ^oC, due to loss of two water molecules (calc. 10.38%). The next mass loss of 45.09% from 300 ^oC to 495 ^oC due to loss of coordinated 2,2-bipy ligand (calc. 44.96%). The final mass loss of 22.30% in the range of 500 - 800 ^oC was due to loss of SO_3 (calc. 23.05%). The mass of residue was 20.85%, which responded to CoO (calc. 21.60%).

Complex **2** showed two continuous mass loss stages in the range of 30 - 570 ^oC. The first mass loss of 17.52% from 57 ^oC to 200 ^oC was due to loss of two lattice water

and six coordinated water molecules (calc. 17.47%). The second mass loss of 61.94% from 240 ^{o}C to 400 ^{o}C was due to loss of coordinated 2,2-bipy and btec ligands (calc. 62.34%). The amount of residue was 20.66% (assuming Co_2O_3) was in good agreement with the theoretical value of 20.14%.

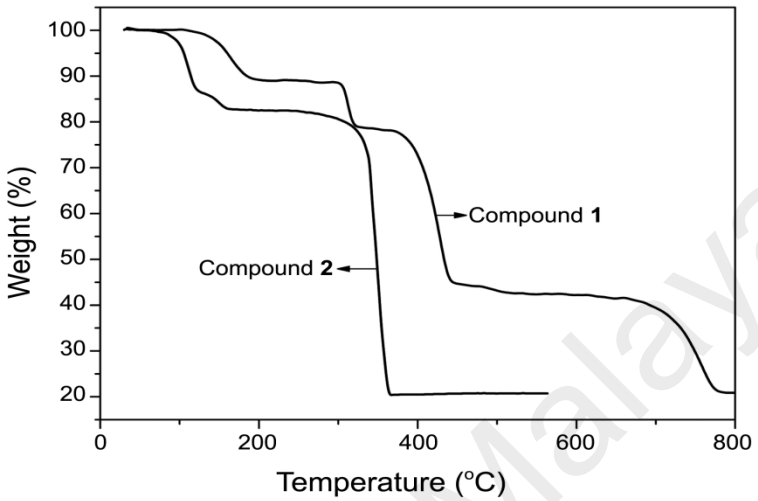

Figure 2.25 TGA trace of $[Co(2,2\text{-bipy})(H_2O)_2(SO_4)]_n$ **(1)** and $[Co_2(2,2\text{-bipy})_2(btec)(H_2O)_6].2H_2O$ **(2)**[44]

(e) Thermoelectricity

Currently, **thermoelectric** materials are intensively researched, given its potential to harvest electricity from a temperature gradient. It promises numerous applications in harvesting energy from sources of waste heat, such as industrial heat, domestic heat and automobiles. An important parameter in thermoelectricity is the Seebeck coefficient (S_e), which is a measure of electrical voltage generated per degree Kelvin.

The concept of thermoelectricity in the solid state is shown in **Figure 2.26.** The electrons in the hot side (more energetic) have a longer mean free path, higher velocities and then tend to diffuse to the cold side [1]. This creates a potential difference between both junctions. Electrons will keep moving towards the cold side until the potential established by the charge separation decreases and creates equilibrium.

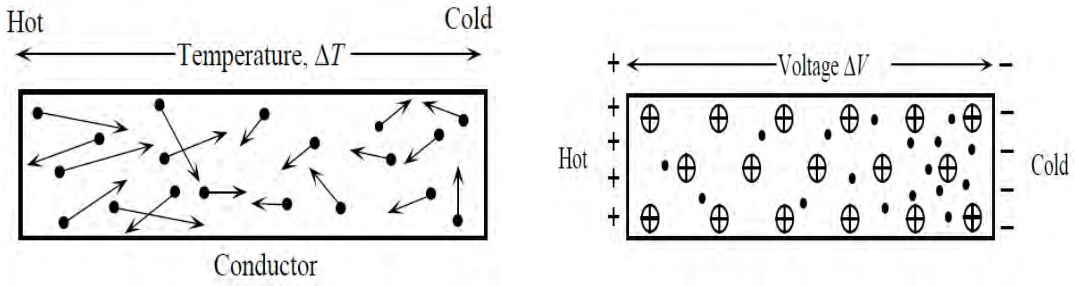

Figure 2.26 Moving of electron and carriers in the conductor

A thermoelectrical material is considered to be an *n*-type when the electrons as the majority charge carriers are diffused from the hot side to the cold side. In contrast, a material is *p*-type when the holes (vacancy of electron or acceptor atom) moved from cold side to hot side. These phenomenons are shown in **Figure 2.27**.

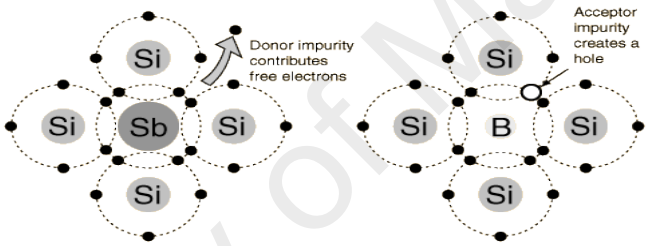

Figure 2.27 Example for the *n*-type and *p*-type materials

Semiconductor-based thermoelectric materials have drawbacks, such as high cost, difficult fabrication processes and limited raw materials. As an alternative in recent years, electrolyte solutions containing a redox couple have been proposed as an alternative thermoelectric material. These solutions demonstrate an electrochemically driven thermoelectric effect [45], which demonstrates a Seebeck coefficient in the range of 5 - 10 times higher than those of semiconductor thermoelectric materials. More recently, several complexes were found to generate electricity when subjected to a temperature gradient in solution [10, 45, 46, 47]. The measurement setup consists of a solution of these complexes with a redox couple which is then subjected to a temperature difference. The Seebeck coefficient can then be determined by the gradient

of linear graph of potential difference (ΔV) *versus* temperature difference (ΔT). The equation of S_e is shown as follow:

$$S_e = {}^{\Delta V}/_{\Delta T}$$

Theoretically, cations and anions in solution possess higher kinetic energy values when heat is supplied in the system. The ions migrate from the hot side to the cold side and at the same time, a redox process occurs. This creates a potential difference between both junctions.

Research in thermoelectrics has very recently been associated with spin crossover materials. For example, Abdullah *et al.* reported the thermoelectrical properties of $[Co(L^{12})_2](BF_4)_2$**(1)** and $[Co(L^{14})_2](BF_4)_2.H_2O$ **(2)**, where L = N_3-Schiff bases appended with linear $C_{12,14}$ carbon chains at the nitrogen atom, in 2-methoxypropionitrile (MPN) the presence of TBATBF [10]. The S_e values were 1.89 ± 0.02 mV K^{-1} for **1**, and 1.92 ± 0.08 mV K^{-1} for **2** (**Figure 2.28**). Therefore, both complexes were potential materials for thermoelectrochemical cell applications.

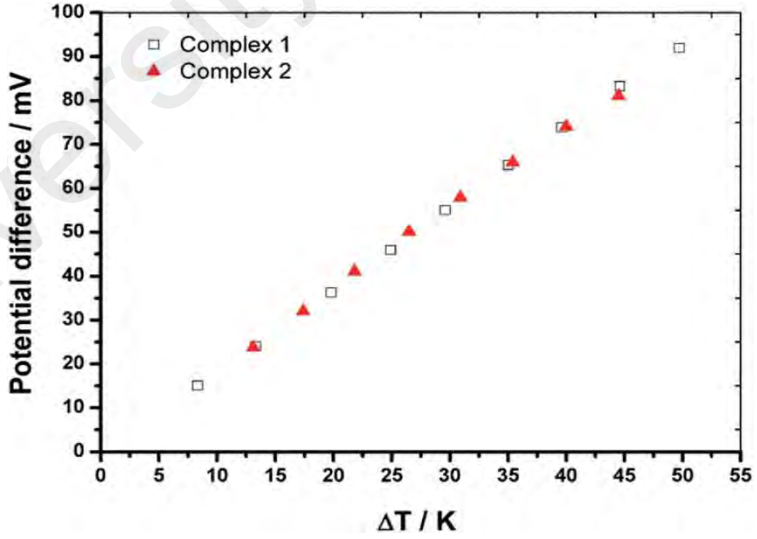

Figure 2.28 S_e measurement of $Co^{II/III}$ redox couples in MPN containing TBATFB [10]

Abraham *et al.* for their thermoelectrical studies for $Co^{II/III}(bpy)_3(NTf_2)_{2/3}$, where bpy = bipyridyl, and NTf_2 = bis(trifluoromethanesulfonyl)amide, in various ionic liquids (ILs) and MPN at different concentrations of electrolytes [45]. The graphs are shown in

Figure 2.29. The S_e and ΔS^o_{rc} values associated with the electron transfer in this complex varied with both the nature of the ions (cation and anion) of the IL, and indicate that the cation and anion were involved in associated solvent reorganization. Based on their results, MPN was the best electrolyte as it gave the highest S_e value ($+2.19 \pm 0.02$ mV K^{-1}) for this complex.

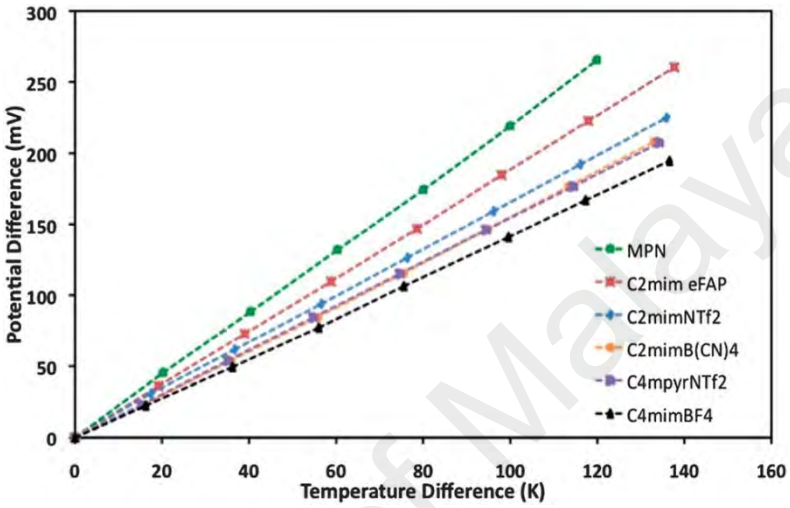

Figure 2.29 Graphs of S_e measurements of $Co^{II/III}(bpy)_3(NTf_2)_{2/3}$ in ILs and MPN electrolytes [45]

2.2.3 Bipyridyl complexes of iron(II)

Iron (Fe) is a first-row transition metal with atomic number is 26 and valence electron configuration is $4s^2d^6$. The most common oxidation states for Fe are +2 and +3 and the valence electronic of Fe(II) ion is $3d^6$, whilst for Fe(III) ion is $3d^5$. In air, most Fe(II) compounds are easily oxidise to Fe(III) and its analogs.

(a) Structural studies

Iron(II) form paramagnetic HS octahedral complexes ($t_{2g}^4e_g^2$; four unpaired electrons) with weak field ligands, and diamagnetic LS octahedral complexes (t_{2g}^6; no unpaired electron) with strong field ligands (**Figure 2.30**). Hence, HS complexes experience weak Jahn-Teller effect, while LS complexes do not experience this effect.

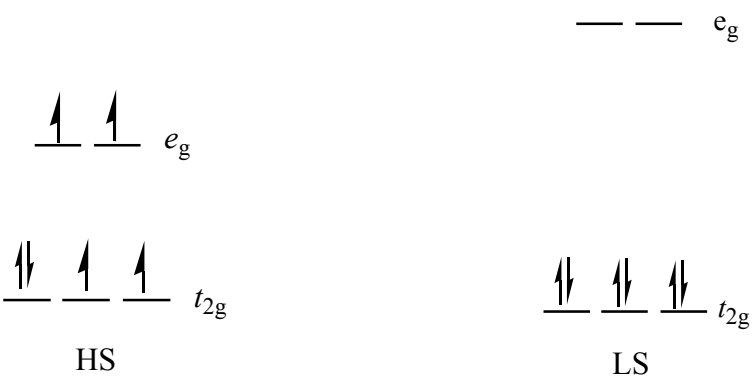

Figure 2.30 Electronic arrangement for HS and LS Fe(II) octahedral complexes

For example, Pomeranc *et al.* in 2001 reported the crystal structure of an octahedral $[Fe(L)(dmbp)](PF_6)_2$, where L = a tetradentate(bis-chelate) ligand, and dmbp = 4,4‟-dimethyl-2,2‟-bipyridine. The complex was from the reaction of $[Fe(dmbp)_3](PF_6)_2$ with L in 1,2-dicholoroethane under argon. It crystallizes in the triclinic *P*-1 space group **(Figure 2.31)** [48].

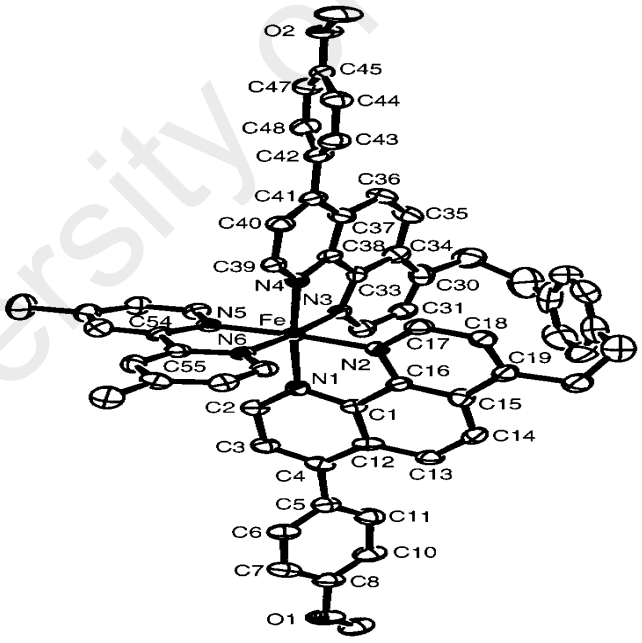

Figure 2.31 X-ray crystal structure of $[Fe(L)(dmbp)]^{2+}$ [48]

Abdullah *et al.* [49] reported the structure of a dimeric iron(II) complex, *trans*-$[Fe_2(CH_3COO)_4(L)_2]$ **(Figure 2.32)**, where L = 4,4‟-bis[3,4-bis(tetradecyloxy)styryl]-2,2‟-bipyridine, based on combined instrumental analyses and molecular modelling. This complex was obtained as a dark purple powder from the reaction of

[$Fe(CH_3COO)_2$] with L in chloroform in the presence of ascorbic acid as an antioxidant. The results of its elemental analyses (74.96% C, 11.25% H, 1.84% N) were in good agreement with the calculated values for $FeC_{86}H_{138}N_2O_8$ (74.29% C, 10.48% H, 2.01% N). From its FTIR spectrum, the Δ values for CH_3COO^- ligand were 130 cm^{-1} and 206 cm^{-1}, which suggesting bidentate chelating and monodentate bridging binding modes, respectively. This proposed structure was supported by IR spectral simulation **(Figure 2.33)**.

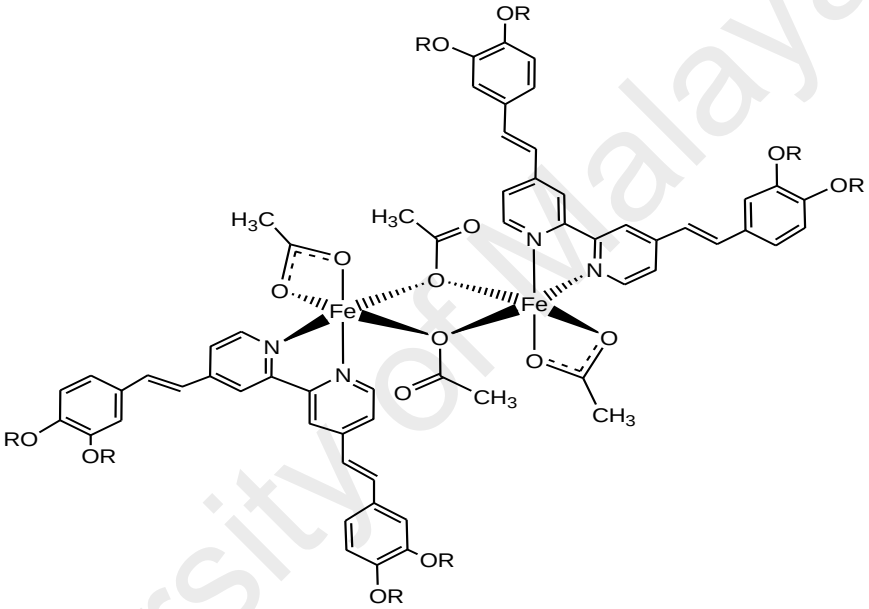

Figure 2.32 The proposed structure for *trans*-[$Fe_2(CH_3COO)_4(L)_2$] [49]

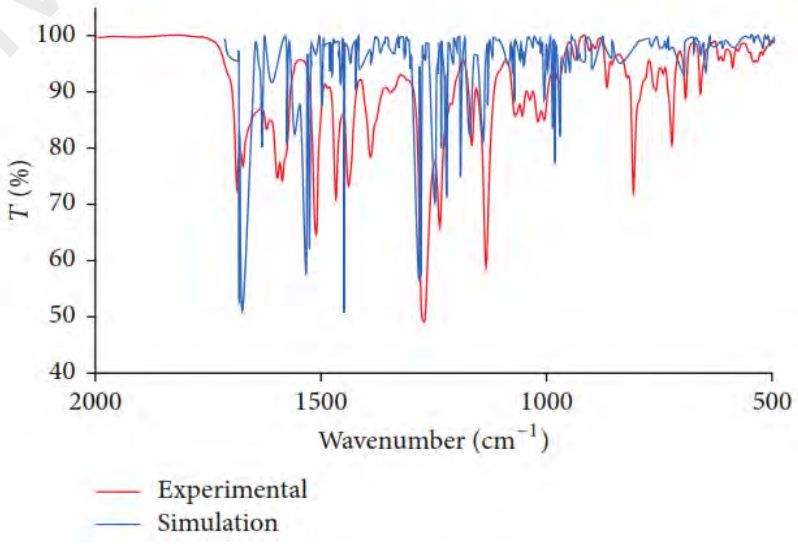

Figure 2.33 The experimental and simulated IR spectra for *trans*-[$Fe_2(CH_3COO)_4(L)_2$] [49]

The UV-vis spectrum for the above complex showed a strong singlet MLCT peak at 544 nm (ε_{max} = 2194 cm^{-1}), two weak *d-d* peaks at 1412 nm (ε_{max} = 25.6 cm^{-1}) and 1755 nm (ε_{max} = 25.6 cm^{-1}), and another *d-d* peak which appeared as a shoulder on the strong MLCT band was assigned to $t_{2g} \rightarrow \pi^*$ electronic transition for a LS Fe(II) atom, while the *d-d* bands were assigned to the $^5T_{2g} \rightarrow {}^5E_g$ electronic transition for HS Fe(II) and $^1A_{1g} \rightarrow {}^1T_{1g}$ electronic transition for LS Fe(II), respectively, based on the Tanabe-Sugano diagram **(Figure 2.34)**. The authors explained that the splitting of the *d-d* peaks for HS Fe(II) may be attributed to distorted octahedral N_2O_4 coordination core at metal centre due to weaker Fe-N and Fe-O bonds.

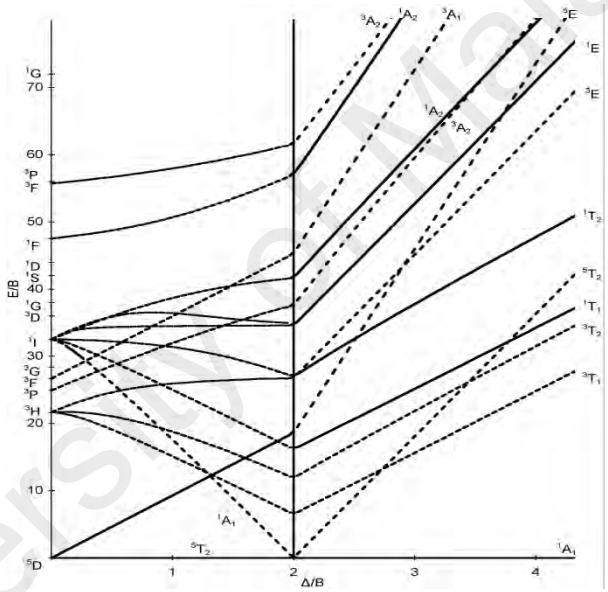

Figure 2.34 Tanabe-Sugano diagram of d^6

Braterman *et al.* [50] reported the electronic absorption spectrum for an iron(II) complex, $[Fe(bpy)_3]^{2+}$, where bpy = 2,2‟-bipyridine. The highest energy absorption at about 33000 cm^{-1} (300 nm) was associated with $\pi \rightarrow \pi^*$ transition of the coordinated bpy ligand, and an intense band at around 20000 cm^{-1} (500 nm) was assigned to MLCT transition.

In 2012, Bushuev *et al.* [51] reported the electronic spectra for Fe(II) complexes with the chemical formulae $[Fe(L^1)_2](ClO_4)_2.H_2O$ (**1a**), HS $[Fe(L^1)_2](ClO_4)_2.H_2O$ (**1b**),

$[Fe(L^2)_2](ClO_4)_2.EtOH$ (**2**) and $[Fe(L^2)_2](CF_3SO_3]_2$(**3**), where L^1 = 4-methyl-2,6-bis(1H-pyrazol-1-yl)pyrimidine, and L^2 = 2,4-bis(3,5-dimethyl-1H-pyrazol-1-yl)-6-methylpyrimidine (**Figure 2.35**). The spectra showed two maximum of a broad absorption band in the region 600 - 1400 nm, assigned to the $^5T_{2g} \rightarrow {}^5E_g$ electronic transition in weak distorted octahedral ligand fields. The splitting of this band may be due to the strong distortion of the octahedral coordination core FeN_6 in these complexes.

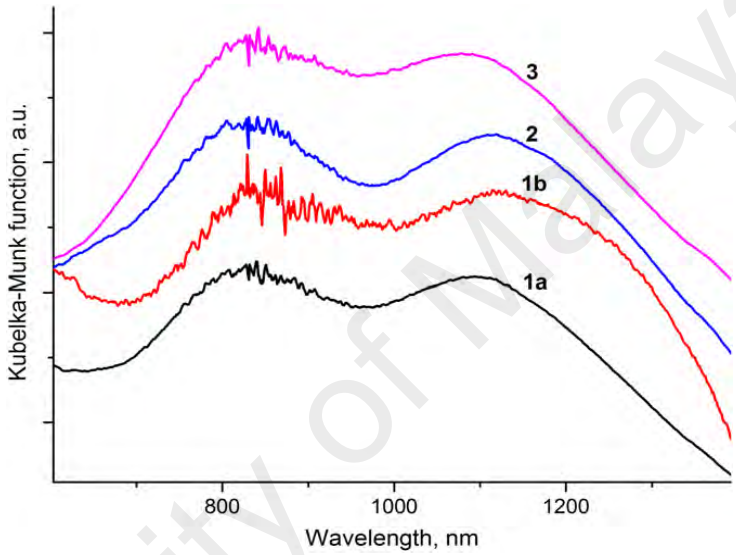

Figure 2.35 Electronic spectra of **1a, 1b, 2**, and **3** [51]

(b) Cyclic voltammetry and band gaps

Braterman *et al*. [50] reported CV scans for four Fe(II) complexes, $[Fe(bpy)_3]^{2+}$, $[Fe(bpym)_3]^{2+}$, $[Fe(phen)_3]^{2+}$ and $[Fe(terpy)_2]^{2+}$, where bpy = 2,2‟-bipyridine, bpym = 2,2‟-bipyrimidine, phen = 1,10-phenanthroline, terpy = 2,2‟:6‟2”-terpyridine. All complexes showed a single one-electron reversible oxidation in the range +0.785 V to +1.036 V, assigned to oxidation of [Fe(II)] to [Fe(III)], followed by several reversible one-electron reduction process at potentials between -1.276 V and -1.970 V, assigned to ligand-based reduction process. The sequence of increasing ease of oxidation and decreasing ease of reduction follows the order: bpym > terpy > bpy ≥ phen. The

reduction of terpy was easier than bpy, and probably was due to the more extended ligand π-system in the former ligand.

Ferrere reported the CV scans for $[Fe(L)_2(CN)_2]$, where L = 4,4‟-dimethyl-2,2‟-bipyridine, 4,4‟-bis(hydroxymethyl)-2,2‟-bipyridine and 4,4‟-dicarboxylate-2,2‟-bipyridine, showed reversible reaction for all complexes in ethanol **(Figure 2.36)**. The author suggested that electron withdrawing groups destabilize Fe^{III}, making the $Fe^{III/II}$ potential more positive, while electron donating groups show the opposite effect, resulting in a more negative $Fe^{III/II}$ process. For example, the oxidation potential of [Fe(4,4‟-bis(hydroxymethyl)-2,2‟-bipyridine)$_2$(CN)$_2$] was similar to [Fe(4,4‟-dimethyl-2,2‟-bipyridine)$_2$(CN)$_2$], while the oxidation of [Fe(4,4‟-dicarboxylate-2,2‟-bipyridine(CN)$_2$] occurred at a more positive potential [52].

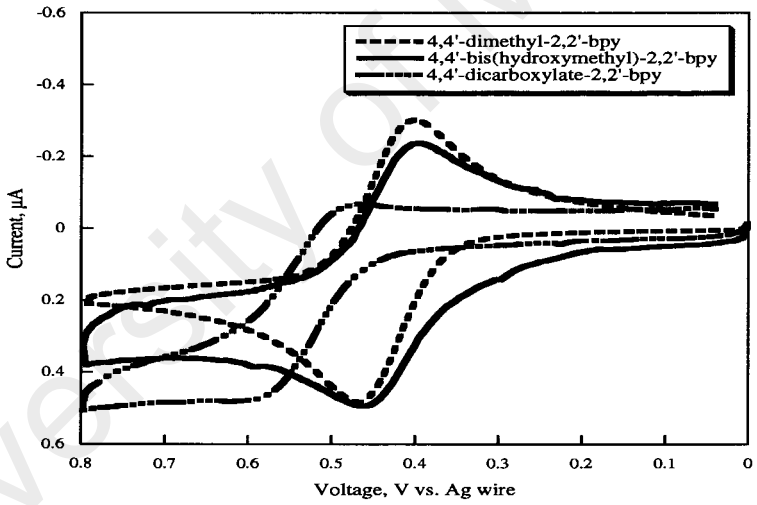

Figure 2.36 Cyclic voltammograms of $[Fe(L)_2(CN)_2]$ [52]

Abdullah *et al.*, reported the optical band gap *(E_o)* of 1.9 eV for a dimeric iron(II) complex, *trans*-$[Fe_2(CH_3COO)_4(L)_2]$, where L = 4,4‟-bis[3,4-bis(tetradecyloxy)styryl]-2,2‟-bipyridine, calculated from the onset from absorption spectrum (λ = 643 nm). The CV scan for the complex **(Figure 2.37)** shows a weak anodic peak at +1.2 V assigned to oxidation of Fe(II) to Fe(III) and two weak cathodic peaks at +0.05 V and -0.56 V assigned to reduction of Fe(III) to Fe(II) and L1 to $L1^-$, respectively. The electrochemical band gap (E_e) was 0.83 eV [49].

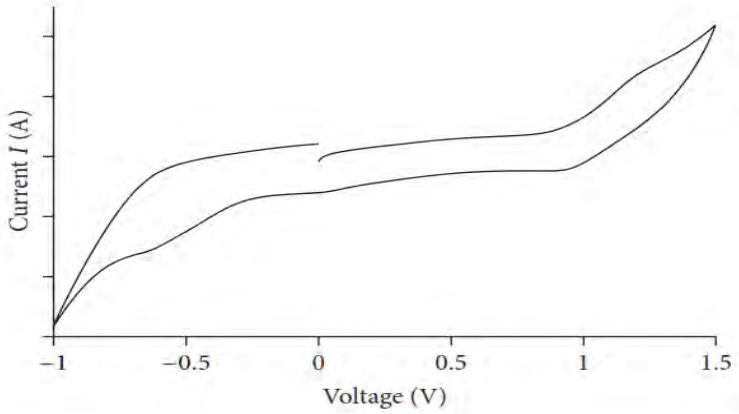

Figure 2.37 Cyclic voltammogram of *trans*-$[Fe_2(CH_3COO)_4(L1)_2]$ [49]

(c) Magnetic properties

Osowole *et al.* [53] published a paper for iron(II) complex, $[FeSO_4(L)(L^1)]$, where L = riboflavin, and L^1 = 2,2‟-bipyridine. The $\chi_M T$ value for the complex was 1.66 cm^3 K mol^{-1} (μ_{eff} = 3.66 BM) at 303 K, which indicates spin equilibrium between the HS and LS octahedral geometry. Hence, this complex has a mixture of HS Fe(II) and LS Fe(II) atoms at this temperature in the solid state.

Bushuev *et al.* [51] reported their magnetic study for $[Fe(L)_2](ClO_4)_2.H_2O$, where L = 4-methyl-2,6-bis(1H-pyrazol-1-yl)pyrimidine. The $\chi_M T$ value for this complex was 3.45 cm^3 K mol^{-1} at 300 K, which indicates 100% HS Fe(II) atom. Hence, the Fe(II)-N coordination bonds are weak for this complex.

(d) Thermal stability

Czakis-Sulikowska and Ka uzna-Czapli ska [54] TG for $[Fe(4\text{-bipy})_2(NCS)_2].2H_2O$, where 4-bipy = 4,4‟-bipyridine. The trace **(Figure 2.38)** showed an initial weight loss of 7.0% from 70 - 135 ^oC due to evaporation of two moles of water molecules (calc. 6.9%). This was followed by 30.0% from 142 - 250 ^oC due to loss of one mol of 4-bipy (calc. 30%), 31.0% from 275 - 360 ^oC due to loss of another one mole of 4-bipy (calc. 31.0%), and 9.5% from 360 - 475 ^oC due to the decomposition of iron(II) thiocyanates

to $Fe_2O_3.SO_3$ (calc. 10.0%). The amount of residue was 7.5% from 570 - 660 ^oC (assuming pure Fe_2O_3, calc. 7.7%).

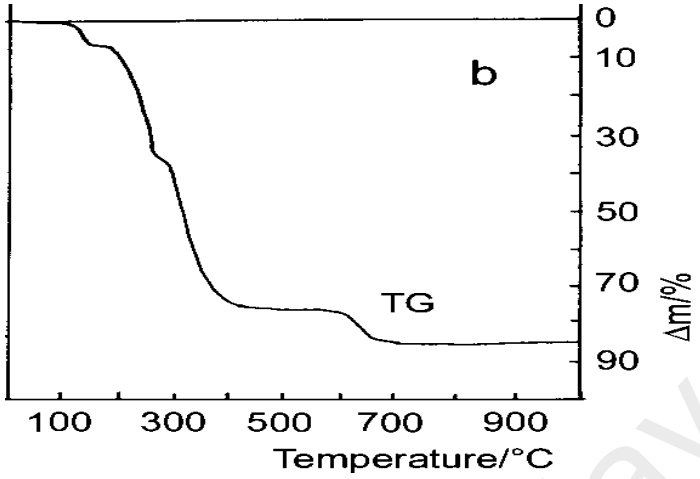

Figure 2.38 TGA trace of $[Fe(4\text{-bipy})_2(NCS)_2].2H_2O$ [54]

Lawandy *et al.* [55] studied the thermal properties of $[FeCl_2(bpy)]$, where bpy = 4,4‟-bipyridine. Its TGA trace (**Figure 2.39**) showed a three-step decomposition process involving loss of 4,4‟-bipyridine and chlorine in the temperature range of 400 - 800 ^oC. Subsequent powder XRD analysis identified elemental metal (Fe) as the only residue. Therefore, this complex was thermally stable on heating up to 400 ^oC, and this was attributed to the π-π interactions among the compounds containing aromatic rings and also between adjacent parallel bipyridine rings.

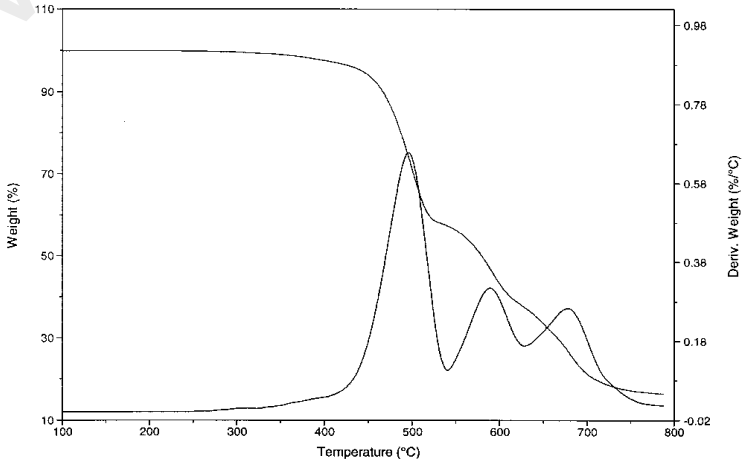

Figure 2.39 TGA trace of $[FeCl_2(bpy)]$[55]

(e) Thermoelectricity

Thermoelectric studies (Seebeck coefficient) for Fe complexes in solutions are intensively studied in recent years. For instance, Kang *et al.* [3] reported their study for ferro/ferricyanide ($Fe(CN)_6^{4-}/Fe(CN)_6^{3-}$) redox couple used as an electrolyte in thermocells. This redox couple has a relatively high thermoelectric power, in which its Seebeck value (S_e) was ~1.4 mV K^{-1} **(Figure 2.40)**. Additionally, the redox couple also has a large exchange current density which allows high currents to be drawn from the cell.

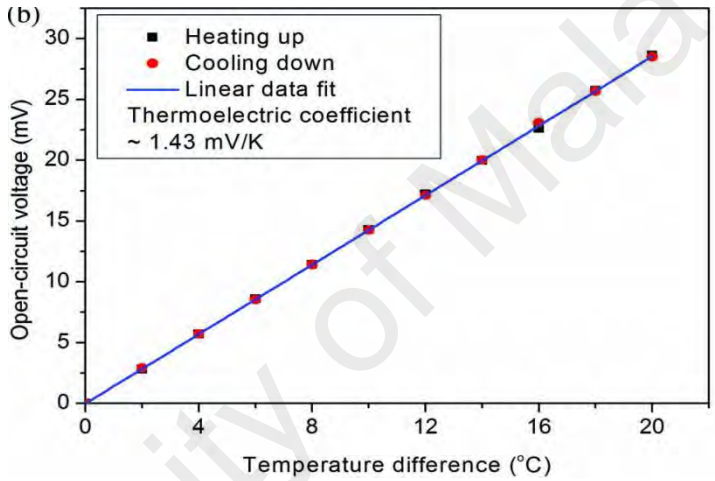

Figure 2.40 Graphs of $S_e$measurements for $Fe(CN)_6^{4-}/Fe(CN)_6^{3-}$ (heating and cooling) [3]

More recently, Abdullah *et al.* reported the thermoelectric studies (Seebeck coefficient) in solutions for three Fe(II) complexes, $[Fe(CH_3COO)_4(L1)_2]$ **(1)**, $[Fe(L1)_3](BF_4)_2.4H_2O$ **(2)** and $\{[Fe_2(CH_3COO)_4(L2)].2H_2O\}_n$**(3)**, where L1 and L2 = conjugated multidonor ligands [46]. The proposed structures for these complexes are shown in **Figure 2.41.**

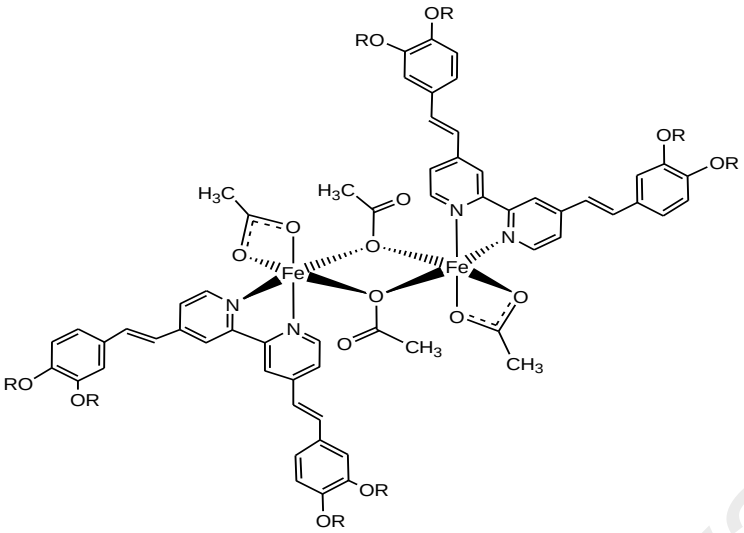

(a)

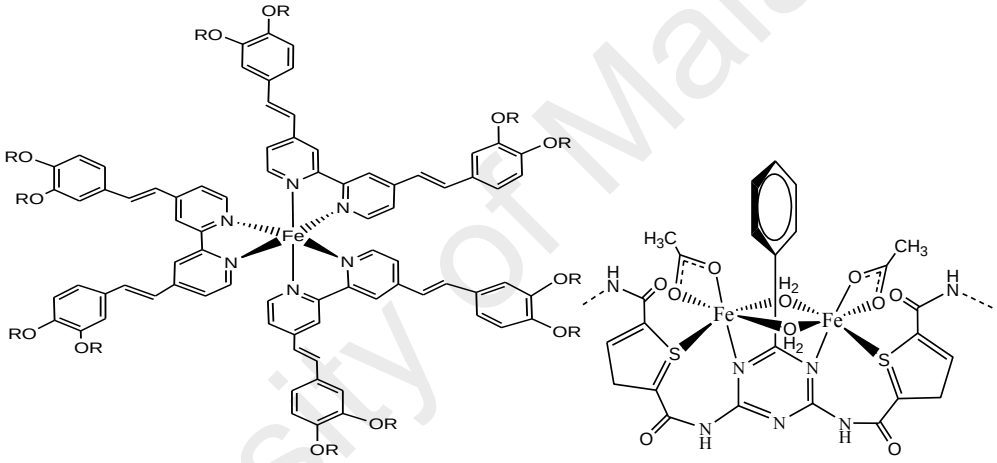

(b) (c)

Figure 2.41 Structural formulae of: (a) $[Fe(CH_3COO)_4(L1)_2]$ (**1**), (b) $[Fe(L1)_3](BF_4)_2.4H_2O$ (**2**); and (c) $\{[Fe_2(CH_3COO)_4(L2)].2H_2O\}_n$(**3**)[46]; R = $CH_3(CH_2)_{13}$

The S_e values (mV K^{-1}), calculated as an average of six readings from heating-and-cooling cycles (**Figure 2.42**), were -0.65 ± 0.02 for **1**, -0.54 ± 0.02 for **2** and +0.25 ± 0.05 for **3**. The authors suggested that the negative S_e values for **1** and **2** might be due to the CH_3COO^- and BF_4^- anions, respectively, which were more mobile than the larger and sterically demanding cationic complexes. For **3**, the Fe(II) cation was the charge carrier since Fe(II) ion was smaller and carries a higher charge compared to CH_3COO^- ion, and expected to move faster in the solution.

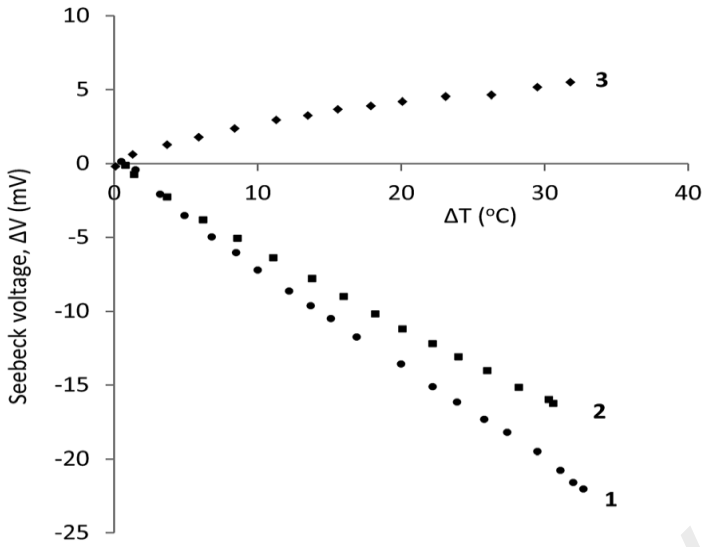

Figure 2.42 S_e measurements for $[Fe(CH_3COO)_4(L1)_2]$ (**1**), $[Fe(L1)_3](BF_4)_2.4H_2O$ (**2**) and $\{[Fe_2(CH_3COO)_4(L2)].2H_2O\}_n$ (**3**) [46]

CHAPTER 3: EXPERIMENTAL

3.1 Introduction

This chapter presents the synthesis and characterisation of complexes of general formulae $[M_2(CH_3COO)_4(LCn)_2]$ and $[M(LCn)_3](BF_4)_2$, where M = Co(II) and Fe(II), and LCn = extended π-conjugated 2,2'-bipyridine ligands (LCn) appended with two linear alkyl chains (**Figure 1.1**). The materials were analysed by CHN elemental analyses, ^{1}H-NMR spectroscopy (for LCn), FTIR spectroscopy, and UV-vis spectroscopy, cyclic voltammetry (CV), room-temperature effective magnetic moment by the Gouy method, thermal stability by thermogravimetry and thermoelectric properties (Seebeck coefficient).

3.2 Chemicals

The chemicals used in this research **(Table 3.1)** were AnalaR reagents obtained commercially, and were used as received.

Table 3.1 List of chemicals used in this research, arranged alphabetically

Name	Structural formula	Formula weight	Supplier
Aniline	$C_6H_5NH_2$	93.13	Aldrich
1-Bromooctane	$CH_3(CH_2)_7Br$	193.12	Merck
1-Bromodecane	$CH_3(CH_2)_9Br$	221.17	Merck
1-Bromododecane	$CH_3(CH_2)_{11}Br$	249.23	Merck
1-Bromotetradecane	$CH_3(CH_2)_{13}Br$	277.28	Merck
3,4-Dihydroxybenzaldehyde	$3,4\text{-}(HO)C_6H_3CHO$	138.12	Merck
4,4‟-Dimethyl-2,2‟-bipyridine	$4,4\text{‟-}(CH_3)_2\text{-}2,2\text{‟-}(C_5H_3N)_2$	184.24	Aldrich
Cobalt(II) acetate tetrahydrate	$Co(CH_3COO)_2.4H_2O$	249.08	Acros
Cobalt(II) tetrafluoroborate hexahydrate	$Co(BF_4)_2.6H_2O$	340.63	Aldrich
Iron(II) acetate	$Fe(CH_3COO)_2$	173.93	Aldrich
Iron(II) tetrafluoroborate hexahydrate	$Fe(BF_4)_2.6H_2O$	337.55	Aldrich

3.3 Syntheses

3.3.1 Ligand LC8 and its Cobalt(II) and Iron(II) Complexes

(a) Ligand LC8

(i) 3,4-Bis(octyloxy)benzaldehyde

1-Bromooctane (13.9819 g, 72.4 mmol) was added portion wise to a magnetically stirred suspension of 3,4-dihydroxybenzaldehyde (5.0012 g, 36.2 mmol), potassium carbonate (12.2570 g, 88.7 mmol) and potassium iodide (0.3602 g, 2.2 mmol) in dimethylformamide (100 cm^3) in a round-bottomed flask at room temperature. The reaction mixture was then heated under reflux for 24 hours, and left to cool to room temperature. Distilled water (70 cm^3) was added, and the solid formed was filtered by suction, washed with distilled water followed by ethanol, and purified using hot acetone. The product was a pale brown powder. The yield was 10.46 g (79.7%).

(ii) 3,4-Bis(octyloxybenzylidene)phenylamine

3,4-Bis(octyloxy)benzaldehyde (4.5323 g, 12.5 mmol) was dissolved in hot ethanol (50 cm^3) in a round-bottomed flask. Aniline (1.3970 g, 15.0 mmol) was added to the hot solution followed by a few crystals of *para*-toluenesulfonic acid. The reaction mixture was cooled to room temperature overnight. The white solid formed was filtered and washed with ethanol. The yield was 3.79 g (69.3%).

(iii) Ligand LC8

3,4-Bis(octyloxybenzylidene)phenylamine (3.0176 g, 6.9 mmol) was dissolved in dimethylformamide (50 cm^3) at 50^{o}C. 4,4‟‟-Dimethyl-2,2‟‟-bipyridine (0.6122 g, 3.3 mmol) was added to the magnetically-stirred reaction mixture, followed by flushing with nitrogen gas for 30 minutes. Potassium *tert*-butoxide (3.2494 g, 28.9 mmol) was added portionwise, the reaction mixture was again flushed with nitrogen gas, and then heated under reflux for 3 hours. It was cooled to room temperature, and hydrochloric acid (10%) was added dropwise until pH = 7 (litmus paper), followed by distilled water

(70 cm^3) and dichloromethane (100 cm^3). The organic layer was washed with saturated solution of sodium bicarbonate (70 cm^3), then distilled water (70 cm^3). The organic layer yang dried using anhydrous sodium sulphate for 1 to 2 hours. The solvent was removed by rotary evaporator, and the solid obtained was purified with hexane to give a white powder. The yield was 2.05 g (71.2%).

(b) $[Co_2(CH_3COO)_4(LC8)_2].3H_2O$

Cobalt(II) acetate tetrahydrate (0.2852 g, 1.1 mmol) was dissolved in methanol (50 cm^3) at room temperature. Nitrogen gas was passed through the solution for about 30 minutes, followed by gradual addition of a solution of LC8 (1.0018 g, 1.1 mmol) in chloroform. The reaction mixture was stirred magnetically under nitrogen gas at room temperature overnight, and then the solvents were removed on a rotary evaporator. The solid product formed was successively washed with aqueous methanol (distilled water:methanol, 1:1 v/v), methanol and dried in a warm oven overnight. The product was a reddish-orange powder, and its yield was 0.76 g (65.1%).

(c) $[Fe_2(CH_3COO)_4(LC8)_2]$

Iron(II) acetate (0.1992 g, 1.1 mmol) and ascorbic acid as antioxidant (0.3227 g, 1.8 mmol) were dissolved in methanol (50 mL) at room temperature. Nitrogen gas was passed to the immediately formed black solution for about 30 minutes. A solution of LC8 (1.0021 g, 1.1 mmol) in chloroform (25 cm^3) was gradually added to the black solution. The reaction mixture was stirred magnetically under nitrogen gas overnight, and then the solvents were removed using rotary evaporator. The product formed was successively washed with distilled water, aqueous methanol (distilled water:methanol, 1:1 v/v), a minimum volume of methanol, and dried in a warm oven for overnight. The product was a black powder, and its yield was 0.68 g (59.1%).

(d) $[Co(LC8)_3](BF_4)_2.2H_2O$

The procedure was the same as in **Section 3.3.1(b),** using cobalt(II) tetrafluoroborate hexahydrate (0.1302 g, 0.4 mmol) and LC8 (1.0017 g, 1.1 mmol). The product was a dark red powder, and its yield was 0.81 g (70.1%).

(e) $[Fe(LC8)_3](BF_4)_2.H_2O$

The procedure was the same as in **Section 3.3.1(c)**, using iron(II) tetrafluoroborate hexahydrate (0.1291 g, 0.4 mmol), ascorbic acid (0.1078 g, 0.6 mmol) and LC8 (1.0020 g, 1.1 mmol). The product was a black powder, and its yield was 0.81 g (70.5%).

3.3.2 Ligand LC10 and its Cobalt(II) and Iron(II) complexes

(a) Ligand LC10

The procedure was the same as **Section 3.3.1(a)**, using 3,4-dihydroxybenzaldehyde (4.5005 g, 32.6 mmol), potassium carbonate (11.0311 g, 79.8 mmol), potassium iodide (0.3237 g, 2.0 mmol), 1-bromodecane (14.4121 g, 65.2 mmol), 3,4-bis(decyloxy)benzaldehyde (9.5236 g, 22.7 mmol), aniline (2.5424 g, 27.3 mmol), 3,4-bis(decyloxybenzylidene)phenylamine (5.0244 g, 10.2 mmol), 4,4‟‟-dimethyl-2,2‟‟-bipyridine (0.9035 g, 4.9 mmol), and potassium *tert*-butoxide (4.7957 g, 42.7 mmol).

The yield of 3,4-bis(decyloxy)benzaldehyde was 12.25 g (89.8%), 3,4-bis(decyloxybenzylidene)phenylamine was 9.25 g (82.6%), and LC10 (white powder) was 3.76 g (77.9%).

(b) $[Co_2(CH_3COO)_4(LC10)_2].H_2O$

The procedure was the same as in **Section 3.3.1(b)**, using cobalt(II) acetate tetrahydrate (0.2703 g, 1.1 mmol) and LC10 (1.0030 g, 1.1 mmol). The product was a dark red powder, and its yield was 0.78 g (60.8%).

(c) $[Fe_2(CH_3COO)_4(LC10)_2].3H_2O$

The procedure was the same as in **Section 3.3.1**(**c**), using iron(II) acetate (0.1887 g, 1.1 mmol), ascorbic acid (0.3058 g, 1.7 mmol) and LC10 (1.0033 g, 1.1 mmol). The product was a black powder, and its yield was 0.82 g (63.0%).

(d) $[Co(LC10)_3](BF_4)_2.4H_2O$

The procedure was the same as in **Section 3.3.1**(**b**)**,** using cobalt(II) tetrafluoroborate hexahydrate (0.1155 g, 0.3 mmol) and LC10 (1.0022 g, 1.0 mmol). The product was a dark red powder, and its yield was 0.82 g (84.0%).

(e) $[Fe(LC10)_3](BF_4)_2.3H_2O$

The procedure was the same as in **Section 3.3.1**(**c**), using iron(II) tetrafluoroborate hexahydrate (0.1143 g, 0.3 mmol), ascorbic acid (0.0954 g, 0.5 mmol) and LC10 (1.0012 g, 1.0 mmol). The product was a black powder, and its yield was 0.94 g (96.2%).

3.3.3 Ligand LC12 and its Cobalt(II) and Iron(II) complexes

(a) Ligand LC12

The procedure was the same as **Section 3.3.1**(**a**), using 3,4-dihyroxybenzaldehyde (5.0012 g, 36.2 mmol), potassium carbonate (12.2570 g, 88.7 mmol), potassium iodide (0.3602 g, 2.2 mmol), 1-bromododecane (18.0443 g, 72.4 mol), 3,4-bis(dodecyloxy)benzaldehyde (11.0023 g, 23.2 mmol), aniline (2.5890 g, 27.8 mmol), 3,4-bis(dodecyloxybenzylidene)phenylamine (5.0011 g, 9.1 mmol), 4,4‟-dimethyl-2,2‟-bipyridine (0.8074 g, 4.4 mmol), and potassium *tert*-butoxide (4.2854 g, 38.2 mmol).

The yield of 3,4-bis(decyloxy)benzaldehyde was 16.16 g (94.0%), 3,4-bis(decyloxybenzylidene)phenylamine was 10.56 g (82.8%), and LC12 (white powder) was 3.99 g (82.5%).

(b) $[Co_2(CH_3COO)_4(LC12)_2].2H_2O$

The procedure was the same as in **Section 3.3.1(b),** using cobalt(II) acetate tetrahydrate (0.2269 g, 0.9 mmol) and LC12 (1.0025 g, 0.9 mmol). The product was a dark yellow powder, and its yield was 0.82 g (70.2%).

(c) $[Fe_2(CH_3COO)_4(LC12)_2].2H_2O$

The procedure was the same as in **Section 3.3.1(c)**, using iron(II) acetate (0.1585 g, 0.9 mmol), ascorbic acid (0.2567 g, 1.5 mmol) and LC12 (1.0009 g, 0.9 mmol). The product was a black powder, and its yield was 0.89 g (77.0%).

(d) $[Co(LC12)_3](BF_4)_2.3H_2O$

The procedure was the same as in **Section 3.3.1(b)**, using cobalt(II) tetrafluoroborate hexahydrate (0.1036 g, 0.3 mmol) and LC12 (1.0019 g, 0.9 mmol). The product was a dark red powder, and its yield was 0.84 g (78.1%).

(e) $[Fe(LC12)_3](BF_4)_2.3H_2O$

The procedure was the same as in **Section 3.4(a)**, using iron(II) tetrafluoroborate hexahydrate (0.1028 g, 0.3 mmol), ascorbic acid (0.0857 g, 0.5 mmol) and LC12 (1.0017 g, 0.9 mmol). The product was a black powder, and its yield was 0.94 g (87.6%).

3.3.4 Ligand LC14 and its Cobalt(II) and Iron(II) complexes

(a) Ligand LC14

The procedure was the same as **Section 3.3.1(a)**, using 3,4-dihyroxybenzaldehyde (5.0018 g, 36.2 mmol), potassium carbonate (12.2570 g, 88.7 mmol), potassium iodide (0.3602 g, 2.2 mmol), 1-bromotetradecane (20.0751 g, 72.4 mmol), 3,4-bis(tetradecyloxy)benzaldehyde (12.0033 g, 22.6 mmol), aniline (2.4670 g, 26.5 mmol), 3,4-bis(tetradecyloxybenzylidene)phenylamine (7.0021 g, 11.6 mmol),

4,4‟-dimethyl-2,2‟-bipyridine (1.0257 g, 5.6 mmol), and potassium *tert*-butoxide (5.4442 g, 48.5 mmol).

The yield of 3,4-bis(decyloxy)benzaldehyde was 17.92 g (93.3%), 3,4-bis(decyloxybenzylidene)phenylamine was 11.35 g (82.9%), and LC14 (white powder) was 5.94 g (87.6%).

(b) $[Co_2(CH_3COO)_4(LC14)_2].2H_2O$

The procedure was the same as in **Section 3.3.1(b),** using cobalt(II) acetate tetrahydrate (0.2059 g, 0.8 mmol) and LC14 (1.0035 g, 0.8 mmol). The product was a dark red powder, and its yield was 0.83 g (73.7%).

(c) $[Fe_2(CH_3COO)_4(LC14)_2].4H_2O$

The procedure was the same as in **Section 3.3.1(c)**, using iron(II) acetate (0.1438 g, 0.80 mmol), ascorbic acid (0.2330 g, 1.3 mmol) and LC14 (1.0005 g, 0.80 mmol). The product was a black powder, and its yield was 0.88 g (77.8%).

(d) $[Co(LC14)_3](BF_4)_2.4H_2O$

The procedure was the same as in **Section 3.3.1(b),** using cobalt(II) tetrafluoroborate hexahydrate (0.0941 g, 0.3 mmol) and LC14 (1.0029 g, 0.8 mmol). The product was a dark red powder, and its yield was 0.84 g (71.4%).

(e) $[Fe(LC14)_3](BF_4)_2.4H_2O$

The procedure was the same as in **Section 3.3.1(c)**, using iron(II) tetrafluoroborate hexahydrate (0.0932 g, 0.3 mmol), ascorbic acid (0.0778 g, 0.4 mmol) and LC14 (1.0022 g, 0.8 mmol). The product was a black powder, and its yield was 0.94 g (80.1%).

3.4 Instrumental Analyses

3.4.1 ^{1}H-NMR spectroscopy

The ^{1}H-NMR spectrum was recorded on a JEOL FT-NMR lambda 400 MHz spectrometer. A small amount of the sample was dissolved in $CDCl_3$ and placed to a height of about 4 cm in an NMR tube. The chemical shifts were reported in ppm using the residual protonated solvent as the reference.

3.4.2 Elemental analyses

Perkin-Elmer PE 2400 Series II CHNS/O analyzer and Thermo-Finnigan Flash EA 110 were used for the elemental analyses (carbon, hydrogen, nitrogen). An accurately known mass of a sample (1.5 - 2.0 mg) was placed in a tin capsule (5 mm x 8 mm), folded into a small piece and placed into the analyser and heated to a maximum temperature of 1000 ^{o}C. Acetanilide ($CH_3CONHC_6H_5$) was used as a calibrant prior to the analysis.

3.4.3 FTIR spectroscopy

The FTIR spectra were obtained for neat samples from 4000 – 400 cm^{-1} on a Perkin-Elmer Frontier FTIR Spectrometer equipped with a diamond attenuated total reflectance (ATR) attachment.

3.4.4 UV-vis spectroscopy

The UV-vis spectra were recorded from 1500 nm to 300 nm on a Shimadzu UV-vis-NIR 3600 spectrophotometer. An exactly known mass of a sample (about 0.0020 g and 0.01 g) was dissolved in chloroform in a 10-mL volumetric flask, and then placed into a 1-cm quartz cuvette. The molar absorptivity (ε) was calculated using the Beer-Lambert Law: $A = \varepsilon cl$, where A is the absorbance, c is the molarity, and l is the path length (1 cm).

3.4.5 Cyclic voltammetry

The cyclic voltammograms (CV) were recorded on a Gamry Instrument Reference 600 potentiostat/galvanostat/ZRA. Tetrabutylammoniumtetrafluoroborate (TBATFB) was used as a supporting electrolyte. The molarity of the samples and electrolyte were 0.001 M and 0.3 M, respectively. The sample was dissolved in dried chloroform, and nitrogen gas was bubbled through the solution for about 5 minutes. A three-electrode cell, consisting of a glassy carbon electrode as the working electrode, saturated calomel electrode (SCE) as the reference electrode, and the platinum wire as the counter electrode, were used. The initial potential range was +1.5 V to -1.5 V, and the scan rate was 20 – 50 mV s^{-1}.

3.4.6 Magnetic susceptibility

The room-temperature magnetic susceptibility measurements were done a Sherwood Auto Magnetic Susceptibility by the Gouy method. The solid sample was finely ground and then packed properly into an empty glass tube to the calibration mark (approximately 2.5 – 3.7 cm). The tube was inserted into the balance. After recording the length and weight, the value of gram magnetic susceptibility (χ_g) was read directly from the instrument. The molar magnetic susceptibility (χ_M), and percentages of HS (a%) and LS ((100 - a)%) metal(II) atoms were calculated using the following equations:

$$\chi_M = \chi_g \times MW$$

$$\chi_M^{corr} = \chi_M - \chi_D$$

$$\chi_M T_{\text{experimental}} = [\chi_M T_{\text{HS theoretical}} \times (a/100\%)] + [\chi_M T_{\text{LS theoretical}} \times (100-a)/100\%)]$$

where MW = formula mass, T = absolute temperature (K), χ_M^{corr} = corrected molar susceptibility, and χ_D = diamagnetic corrections calculated using Pascal‟s constants **(Appendices)**.

3.4.7 Thermogravimetric analyses

Thermogravimetric analyses (TGA) were done on a Perkin-Elmer Pyris Diamond TG/DTA Thermal instrument. An accurately known mass of a sample (4-8 mg) was placed inside the pan and heated under N_2 at a flow rate of 10 cm^3 min^{-1} from 50 ^oC to 900 ^oC at the scan rate 20 ^oC min^{-1}.

3.4.8 Thermoelectricity (Seebeck coefficient)

The experimental set-up is shown in **Figure 3.1**. The concentration of the samples and tetra-*n*-butylammonium tetrafluoroborate (TBATFB) as a supportive electrolyte were 0.001 M and 0.3 M, respectively. KI-KI_3 (0.01 g) was added as the redox couple. The solvent used was chloroform. The solution was placed in two compartments connected by a solution bridge. Each compartment contained a thermometer anda platinum wire electrode precleaned with dilute HCl followed by distilled water. The compartments were placed in two separate water baths and one of them was heated on a hot plate (hot side) while the other was left at room temperature (cold side). The potential difference between the hot side and cold side was measured at 2-3^oC interval within the temperature range 25-55 ^oC using an Agilent 34461A Digital Multimeter. This measurement was done for three heating-and-cooling cycles. Controlled thermoelectric measurements were done for the solutions of KI-KI_3 and a mixture of KI-KI_3 and TBATFB under similar conditions.

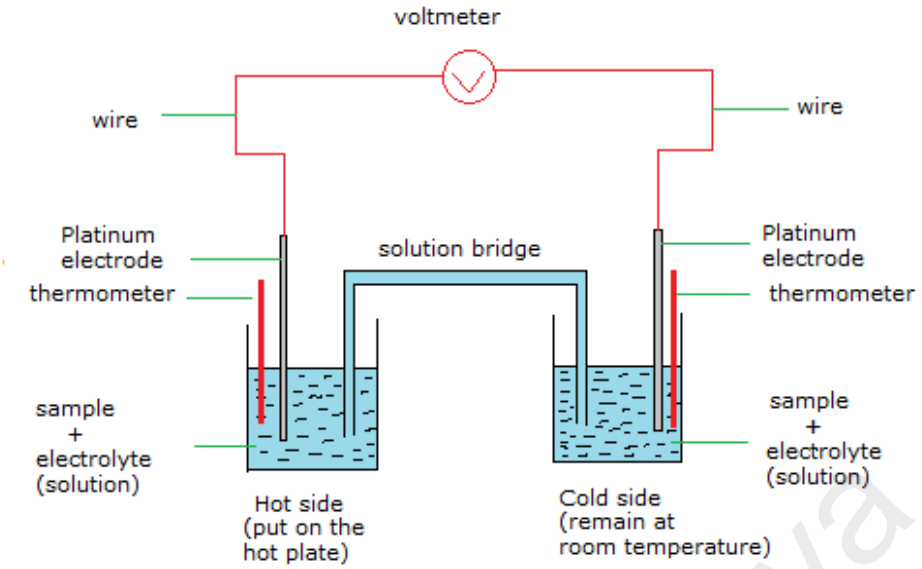

Figure 3.1 Experimental set-up for thermoelectrical measurement

CHAPTER 4: RESULTS AND DISCUSSION

4.1 Introduction

In this work, the neutral ligands were 2,2‟‟-bipyridyl with extended conjugation and appended at each aromatic ring with two long alkyloxy chains, labelled LC8 – LC14 (**Figure 1.1**). These ligands were used in order to study the effect of varying the alkyl chain on the properties of complexes. The anions were CH_3COO^- ion, chosen due to its variability in its binding modes to the metal centre, such as chelating and bridging [15], and expected to lead to multinuclear molecular complexes, while BF_4^- ion was non-coordinating and expected to form ionic mononuclear complexes. Complexes of Co(II) and Fe(II) ions were reported to exhibit spin crossover (SCO) properties with ligands of intermediate field strength (N- and O- donors) [56, 57, 58]. The low spin (LS) to high spin (HS) transition was proposed as a favourable factor in thermoelectric properties (direct conversion of heat energy to electricity) of such complexes due to an increase in entropy on heating [2, 59].

4.2 Ligand LC8 and its Cobalt(II) and Iron(II) Complexes

4.2.1 Ligand LC8

The steps involved in the synthesis of LC8 are shown in **Scheme 1.1**. It was obtained as a white powder and its yield was 71.2%. The result of **elemental analyses** (79.30% C, 9.98% H, 3.54% N) were in a good agreement with those calculated for the chemical formula $C_{58}H_{84}N_2O_4$ (79.77% C, 9.70% H, 3.21% N; formula weight, 873.3 g mol^{-1}).

Its **^{1}H-NMR** spectrum, recorded in $CDCl_3$ **(Figure 4.1)**, shows peaks (in ppm) at 0.8 (triplet, CH_3, 12 H), 1.2 – 1.8 (multiplet, CH_2, 48 H), 3.9 (triplet, OCH_2, 8 H), 6.80 – 7.40 (multiplet, aromatic C-H and HC=CH, 12 H), 8.5 (singlet, aromatic C-H, 2 H), 8.6 (doublet, aromatic C-H, 2 H). The peak assignments are given in **Table 4.1**.

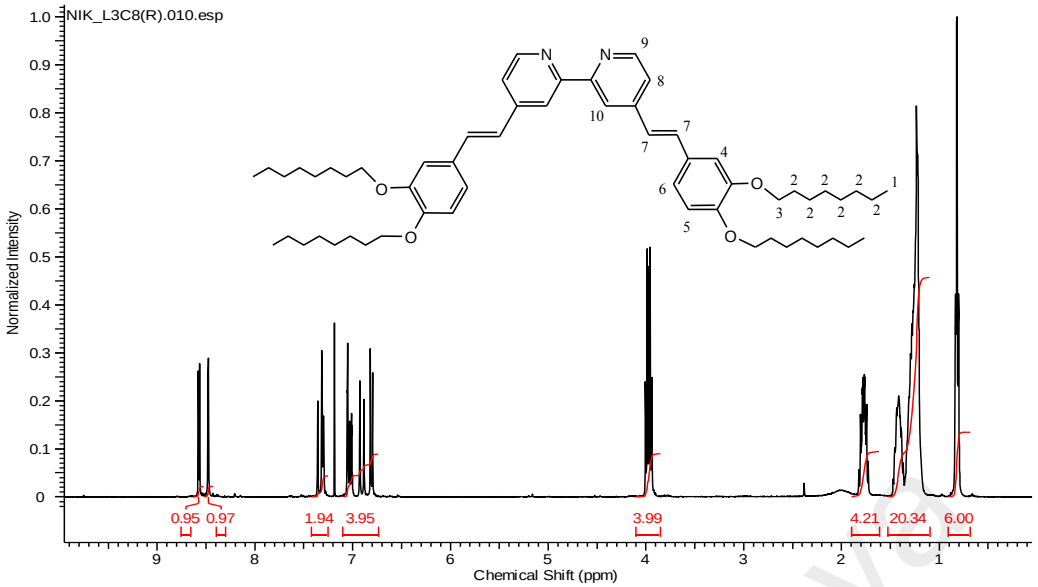

Figure 4.1 ^{1}H-NMR spectrum of LC8

Table 4.1 The ^{1}H-NMR peak assignments for LC8

Chemical shift (ppm)	**Integral**	**Multiplicity**	**Assignment**
0.8	6.00	Triplet	H-1
1.2 – 1.8	24.55	Multiplet	H-2
3.9	3.99	Triplet	H-3
6.8 – 7.4	5.89	Multiplet	H-4, H-5, H-6, H-7, H-8
8.5	0.97	Singlet	H-10
8.6	0.95	Doublet	H-9

The structural formula of LC8 was further supported by its **FTIR** spectrum **(Figure 4.2)**. The peak assignments are given in **Table 4.2** (which also includes the data for the corresponding metal(II) complexes for later discussion). The results shows two strong peaks at 2918 cm^{-1} and 2849 cm^{-1} for CH_2 asymmetric and symmetric vibrations respectively, a medium peak at 1660 cm^{-1} for C=N, a strong peak at 1585 cm^{-1} for aromatic C=C, and a strong peak at 1262 cm^{-1} for C-O stretch [60].

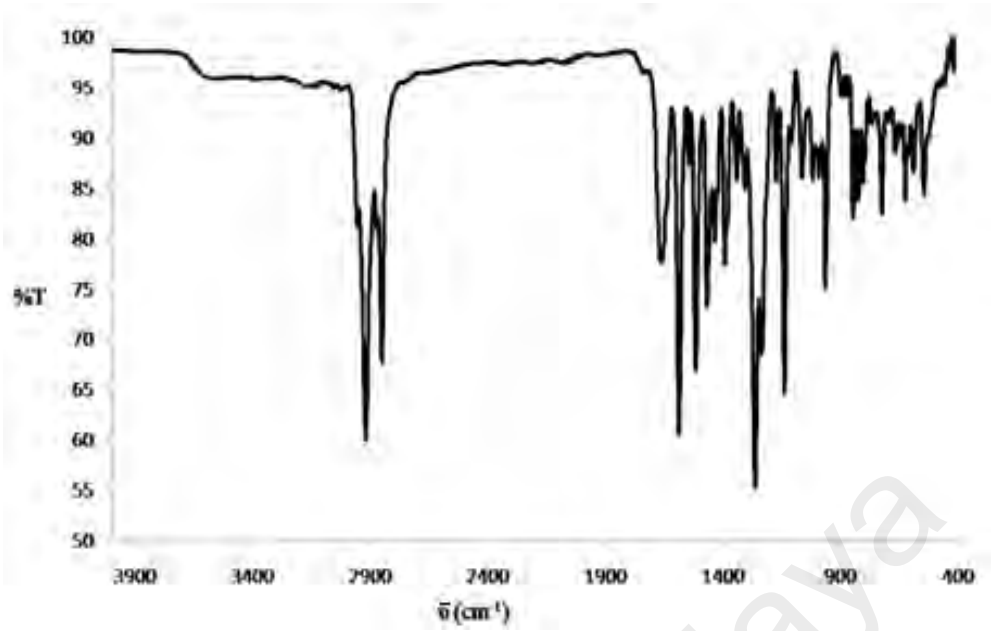

Figure 4.2 FTIR spectrum of LC8

Table 4.2 The FTIR data (in cm^{-1}) of LC8 and its metal complexes

	Assignment								
	CH_2 (asym)	CH_2 (sym)	C=N	C=C (ar)	COO (asym)	COO (sym)	BF_4^-	M-N	M-O
LC8	2918s	2849s	1660m	1585s	-	-	-	-	-
1	2923s	2854m	1610m	1593s	1575m	1468m 1339m	-	553w	444w
2	2923s	2854m	1608s	1592s	1673m 1632m	1467m 1510s	-	550w	479w
3	2923s	2854m	1607s	1588s	-	-	1053s, br	551w	-
4	2922s	2854m	1609m	1591s	-	-	1040s, br	556w	-

s = strong; m = medium; w = weak; br = broad

4.2.2 $[Co_2(CH_3COO)_4(LC8)_2].3H_2O$

Ligand LC8 reacted with cobalt(II) acetate tetrahydrate, $Co(CH_3COO)_2.4H_2O$, in a mole ratio of 1:1, to form a reddish-orange powder **(Complex 1)**, and the yield was 65.1%. It was readily soluble in dichloromethane and chloroform, but insoluble in other common organic solvents.

(a) Deduction of structural formula

The proposed structure of **Complex 1 (Figure 4.3)** was deduced based on combined results of elemental analyses, FTIR and UV-vis spectroscopies.

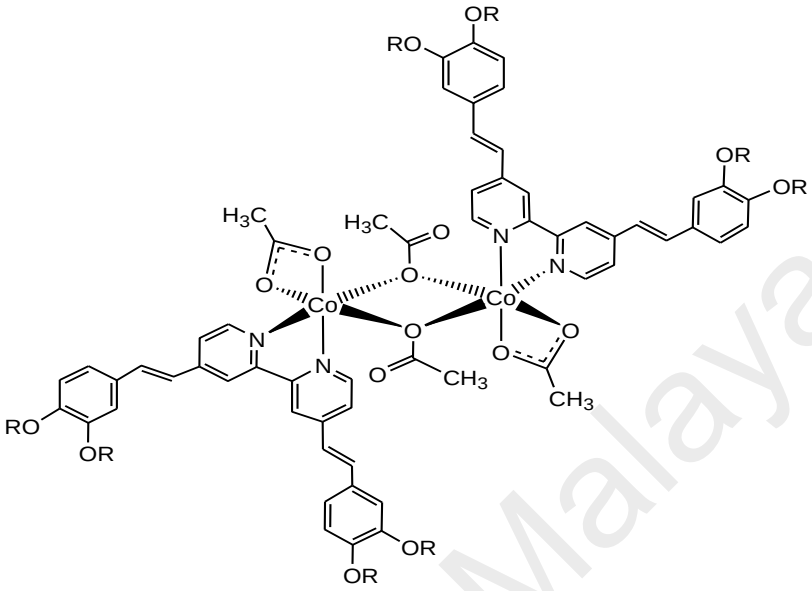

Figure 4.3 Proposed structure of **Complex 1**; R = $CH_3(CH_2)_7$

The result from the **elemental analyses** (68.95% C, 8.80% H, 2.96% N) were in good agreement with those calculated for the chemical formula $C_{124}H_{186}Co_2N_4O_{19}$ (69.12% C, 8.70% H, 2.60% N; formula weight, 2154.7 g mol^{-1}).

Its **FTIR** spectrum (**Figure 4.4**) shows two strong peaks at 2923 cm^{-1} and 2854 cm^{-1} for the asymmetric and symmetric of CH_2 of the long alkyloxy chain, respectively, a strong peak at 1610 cm^{-1} for C=N (aromatic), shifted to lower energy compared to LC8 (1660 cm^{-1}), suggesting the coordination of nitrogen atoms to Co(II) centre [61, 62], a strong peak at 1593 cm^{-1} for aromatic C=C, a medium peak at 1575 cm^{-1} for $\upsilon_{asym}COO$, two medium peaks at 1468 cm^{-1} and 1339 cm^{-1} for $\upsilon_{sym}COO$, respectively, a strong peak at 1263 cm^{-1} for C-O stretch, and two weak peaks at 553 cm^{-1} and 444 cm^{-1} for Co-N and Co-O bonds, respectively [63, 64] **(Table 4.2)**. The Δ values ($\Delta = \upsilon_{asym}COO - \upsilon_{sym}COO$) were 236 cm^{-1} and 107 cm^{-1}, suggesting monodentate bridging and bidentate chelating binding modes for the CH_3COO^- ligand, respectively [15, 49], hence indicating a dinuclear complex.

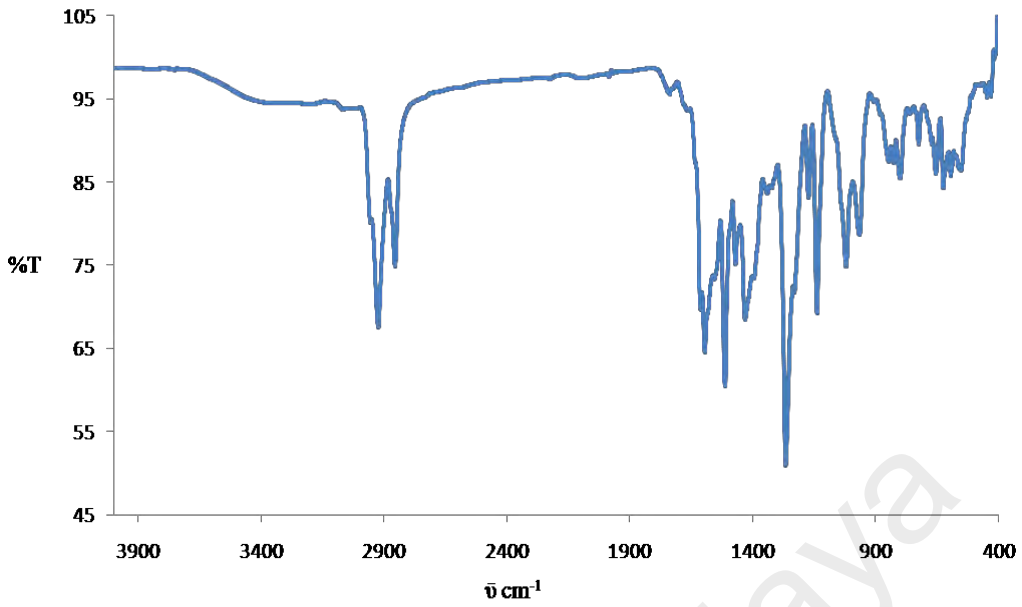

Figure 4.4 FTIR spectrum of **Complex 1**

Its **UV-vis** spectrum (**Figure 4.5**), recorded for a dark red solution in $CHCl_3$ shows a broad *d-d* band at 1150 nm (ε_{max}, 30.5 M^{-1} cm^{-1}; inset) assigned to the $^4T_{1g} \rightarrow {}^4T_{2g}$ electronic transition for high-spin (HS) Co(II) [29], and two strong overlapping metal-to-ligand charge transfer (MLCT) bands at 385 nm (ε_{max}, 7.5 x 10^4 M^{-1} cm^{-1}) and 316 nm (ε_{max}, 6.2 x 10^4 M^{-1} cm^{-1}). The molarities of the solutions were 2.4 x 10^{-2} mol dm^{-3} for the *d-d* band and 2.9 x 10^{-5} mol dm^{-3} for the MLCT bands.

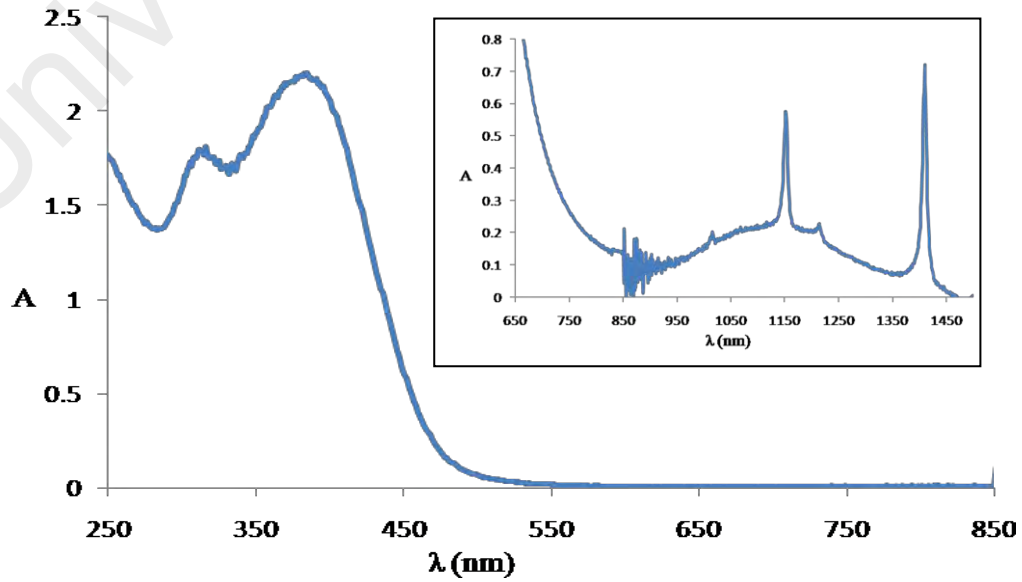

Figure 4.5 UV-vis spectrum of **Complex 1**

(b) Band gap

UV-vis spectrum and cyclic voltammetry (CV) may be used to calculate the optical *(E_o)* and electrochemical *(E_o)* bandgaps, respectively. For E_o, the equation is $E_o = hc/\lambda$, where c = velocity of light (3.0 x 10^8 ms^{-1}), h = Planck constant (6.626 x 10^{-34} Js^{-1}), and λ (absorption edge or onset of CT band [65]). The calculated value in joule (J) is converted to electronvolt (eV) using the conversion factor: 1 J = 1.60 x 10^{-19} eV. For **Complex 1**, the onset wavelength of the MLCT band was 475 nm. Hence, its E_o value was 2.61 eV which was similarly reported for cobalt(II) oxide (E_o = 2.48 – 2.76 eV) [66].

The **CV** for **Complex 1** was recorded in $CHCl_3$, which was the same solvent used in recording its UV-vis spectrum. The scan was recorded anodically from 0 V within the potential window of -1.5 V to +1.5 V at room temperature under nitrogen gas. The scan rate was 20 - 50 mV/s, and the supporting electrolyte was tetra-*n*-butylammonium tetrafluoroborate (TBATFB) [33]. The voltammogram **(Figure 4.6)** shows overlapping anodic peaks at +0.85 V assigned to the oxidation of [Co(II)Co(II)] to [Co(II)Co(III)], [Co(II)] to [Co(III)] and LC8 to $LC8^+$, as a result of dissociation of dimer [67]. These were followed by three overlapping cathodic peaks at -0.05 V, -0.80 V and -0.90 V for the reduction of [Co(II)Co(III)] to [Co(II)Co(II)], [Co(III)] to [Co(II)] and $LC8^+$ to LC8, respectively. The metal-based peak separation (ΔE_p) was 950 mV, hence suggesting a quasireversible redox reaction (ΔE_p> 59 mV at 30 ^oC [68]), due to extensive structural distortion of the oxidised complex. The redox reaction is shown below.

$$[Co(II)Co(II)] \underset{-0.10\ V}{\overset{+0.85\ V}{\rightleftharpoons}} [Co(II)Co(III)]$$

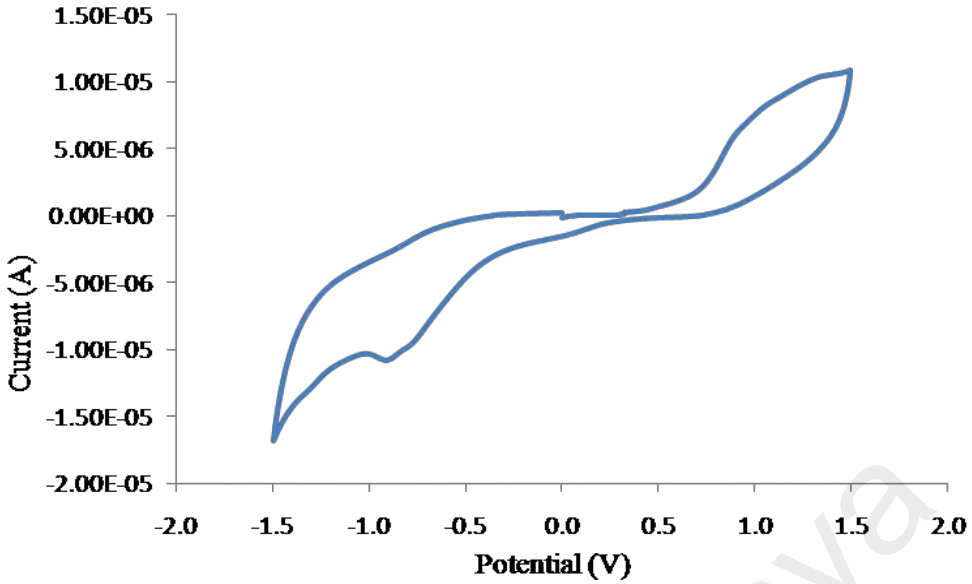

Figure 4.6 Cyclic voltammetry of **Complex 1**

The electrochemical bandgap *(E_e)* was calculated using the formula: E_e = HOMO – LUMO (HOMO = highest occupied molecular orbital; LUMO = lowest unoccupied molecular orbital). E_{HOMO} and E_{LUMO} were calculated by adding +4.4 V (the standard electrode potential of saturated calomel electrode (SCE) to the onset oxidation potential and reduction potential, respectively [69]. The E_e for **Complex 1**, calculated from the onset potentials for oxidation (+0.70 V) and reduction (+0.20 V), the values for E_{HOMO} (5.10 eV) and E_{LUMO} (4.60 eV), was 0.50 eV.

(c) Magnetic properties

The $\chi_M T$ value for **Complex 1**, calculated from its proposed chemical formula (FW = 2190.7 g mol^{-1}), χ_g (5.40 x 10^{-6} cm^3 g^{-1}), χ_M (1.18 x 10^{-2} cm^3 mol^{-1}, χ_D (-1.38 x 10^{-3} cm^3 mol^{-1}) and χ_M^{corr} (1.32 x 10^{-2} cm^3 mol^{-1}), was 3.96 cm^3 K mol^{-1} at 298 K. Since the theoretical value for a high-spin (HS) dinuclear Co(II) octahedral complex (S = 3/2) is 3.752 cm^3 K mol^{-1}, and for a low-spin (LS) dinuclear Co(II) octahedral complex (S = 1/2) is 0.75 cm^3 K mol^{-1} [42], it may be suggested that both Co(II) atoms in **Complex 1** were HS at this temperature. The result indicates weak Co-N and Co-O bonds in the complex. Additionally, its proposed structure was

expected to be tetragonally-compressed octahedron due to the Jahn-Teller effect [25, 70].

(d) Thermal properties

The **TGA** trace for **Complex 1** (**Figure 4.7**) shows a total mass loss of 93.9% from 180 ^{o}C to 740 ^{o}C due to the decomposition of CH_3COO^- ions and LC8 (calculated, 94.3 %). The amount of residue at temperatures above 740 ^{o}C was 6.1% (calculated, 5.7% assuming pure CoO [30]). Hence, **Complex 1** was thermally stable up to 180 ^{o}C. Also, the good agreement between the found and calculated values further support its proposed formula and indicate high purity of the sample.

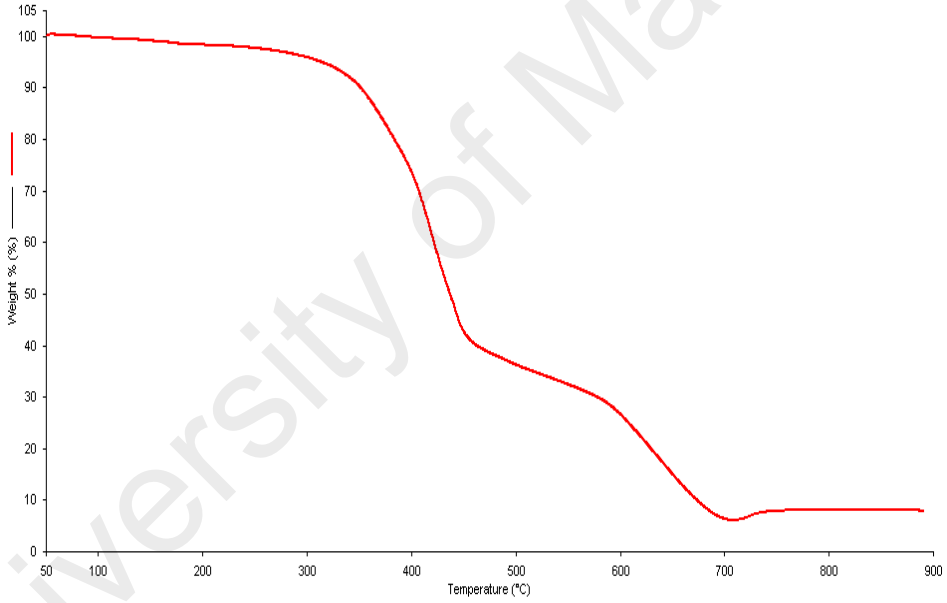

Figure 4.7 TGA trace of **Complex 1**

(e) Thermoelectric properties

An important parameter in thermoelectricity is the Seebeck coefficient (S_e). Its value can be determined by the gradient of a linear graph of potential difference (ΔV) *versus* temperature difference (ΔT), based on the equation: $S_e = \Delta V/\Delta T$. The S_e value is directly proportional to the entropy of the reaction ($S_e = \Delta S/nF$), and can be a function of several factors within the solution, such as solvent reorganization, solvation factors [59] and micelle-like-structure formed by the long alkyl chains.

For **Complex 1,** graphs of ΔV *versus* ΔT **(Figure 4.8**) were in general linear, indicating good thermoelectric behaviour. The mean S_e value, calculated from six readings made up of three heating-and-cooling cycles, was -0.58 ± 0.03 mV K^{-1}. Comparing this with the values for KI-KI_3 in $CHCl_3$ (-0.03 mV K^{-1}) and a mixture of KI-KI_3 and TBATFB in $CHCl_3$ (+0.57 mV K^{-1}) [47], it may be inferred that **Complex 1** was functioning as a thermoelectric material in $CHCl_3$.

However on closer inspection, it is noted that the graph for the second heating (**Figure 4.8**(**b**)) was less satisfactory compared to those of other heating-and-cooling cycles. Recalling that the dimer has weak Co-N and Co-O bonds, it is postulated that this was due to the dissociation of the dimer to monomer [46], which was significant in the second heating due to the slow process. However, the thermoelectric behaviours of the dimer and monomer were similar since good linear graphs were again obtained in the third cycle.

The negative S_e values are proposed to arise from the oxidation of I^- ion at the hot electrode since it has a lower potential (oxidation potential = +0.15 V) compared to Co(II) (oxidation potential = +0.85 V). In addition, **Complex 1** formed micelle-like structures in $CHCl_3$, trapping the ions from KI-KI_3 and TBATFB, and increased the mobility of the ions in the solution. On heating, the micelle-like-structures absorbed the heat and expanded in size, allowing the trapped ions to escape. Therefore, the increased entropy of the solution accounted for the S_e effect.

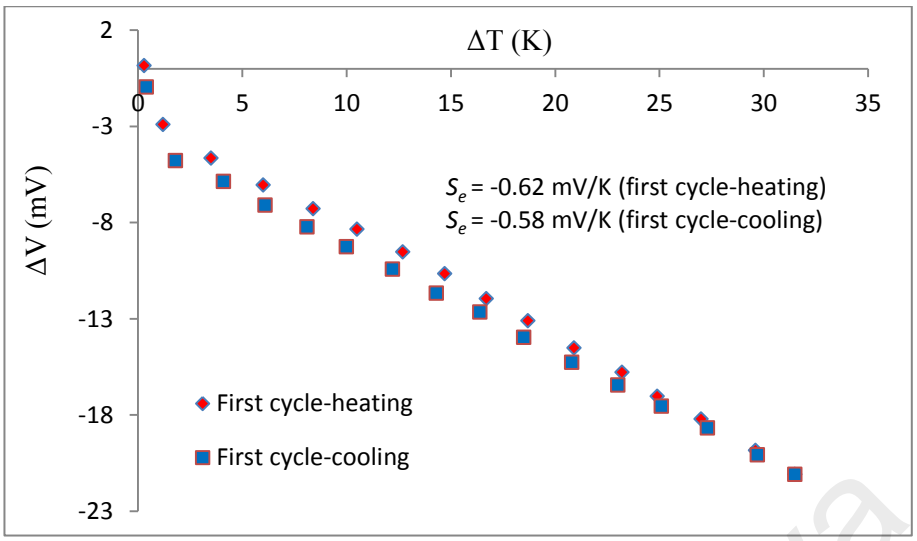

(a)

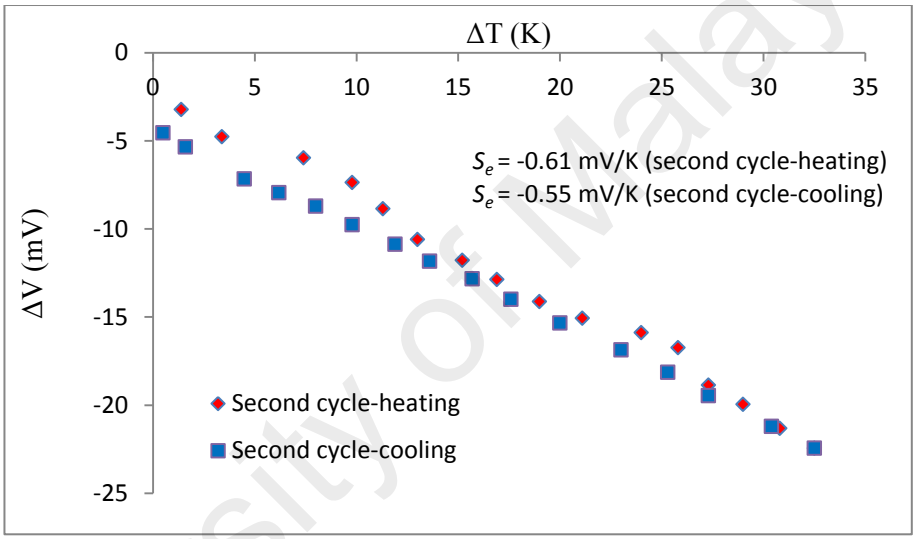

(b)

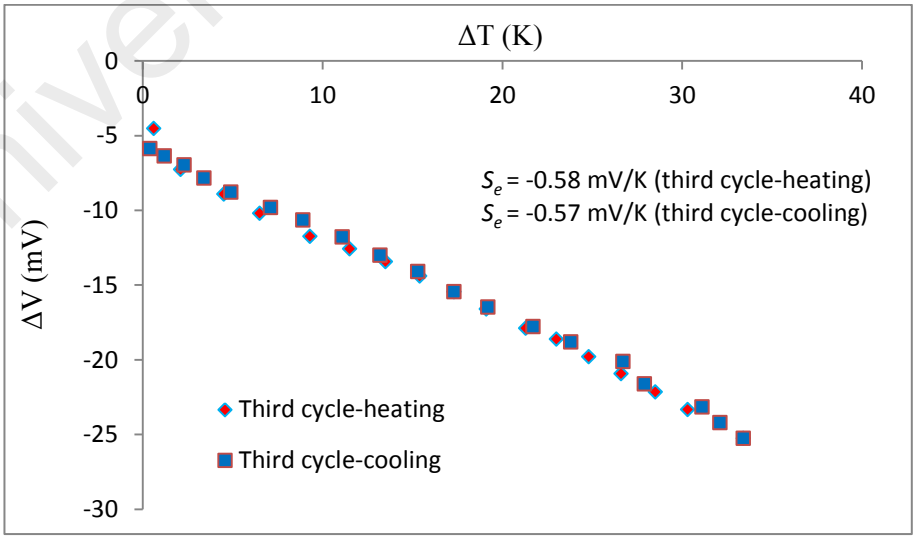

(c)

Figure 4.8 Graphs of ΔV *versus* ΔT for **Complex 1**: (a) first; (b) second; and (c) third heating-and-cooling cycles

4.2.3 [$Fe_2(CH_3COO)_4(LC8)_2$]

Ligand LC8 reacted with iron(II) acetate, $Fe(CH_3COO)_2$, in a mole ratio of 1:1 to form a black powder (**Complex 2**), and its yield was 59.1%. Its solubility was similar to **Complex 1**.

(a) Deduction of structural formula

The structural formula of **Complex 2**, $[Fe_2(CH_3COO)_4(LC8)_2]$, is proposed based on combined data from elemental analyses and FTIR and UV-vis spectroscopies. Hence, its structure is similar to **Complex 1** ($[Co_2(CH_3COO)_4(LC8)_2].3H_2O$; **Figure 4.3**).

Its **elemental analytical** data (70.95% C, 9.03% H, 2.33% N) were in good agreement with those calculated for the chemical formula $C_{124}H_{180}Fe_2N_4O_{16}$ (71.11% C, 8.66% H, 2.67% N; formula weight: 2094.5 g mol^{-1}).

Its **FTIR** spectrum **(Figure 4.9)** shows similar peaks as found for **Complex 1**, and may be similarly assigned and explained **(Table 4.2)**. The values of Δ for CH_3COO^- ligand were 206 cm^{-1} and 122 cm^{-1}, suggesting monodentate bridging and bidentate chelating binding modes, respectively [15, 49].

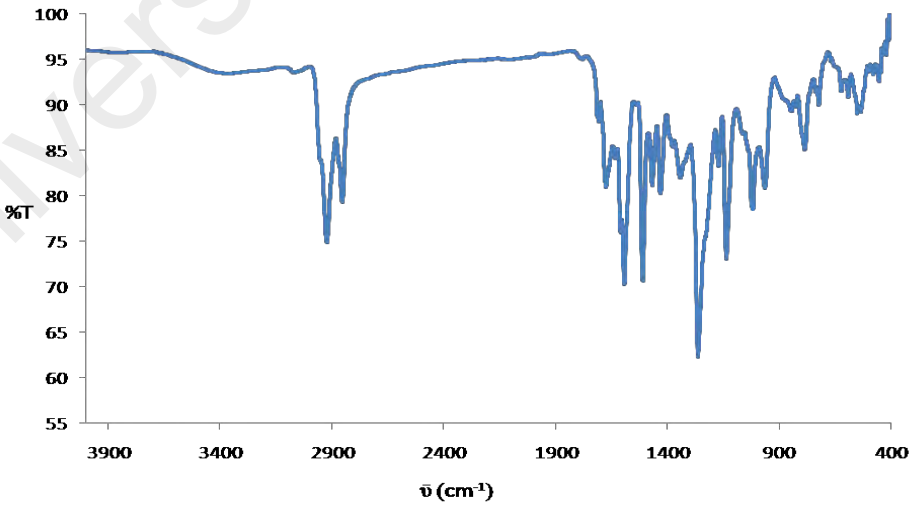

Figure 4.9 FTIR spectrum of **Complex 2**

Its **UV-vis** spectrum in $CHCl_3$ (**Figure 4.10**) shows two weak *d-d* bands at 1410 nm (ε_{max}, 68.7 M^{-1} cm^{-1}; inset) and 1152 nm (ε_{max}, 43.1 M^{-1} cm^{-1}; inset) for

$^5T_{2g} \rightarrow {}^5E_g$ electronic transition for HS Fe(II) in the solution [49, 51], and a broad peak at 571 nm (ε_{max}, 1.3 x 10^4 M^{-1} cm^{-1}) assigned to the MLCT band. The molarities of the solutions were 9.6 x 10^{-3} mol $dm^{-3}$for the *d-d* band and 8.3 x 10^{-5} mol dm^{-3} for the MLCT bands.

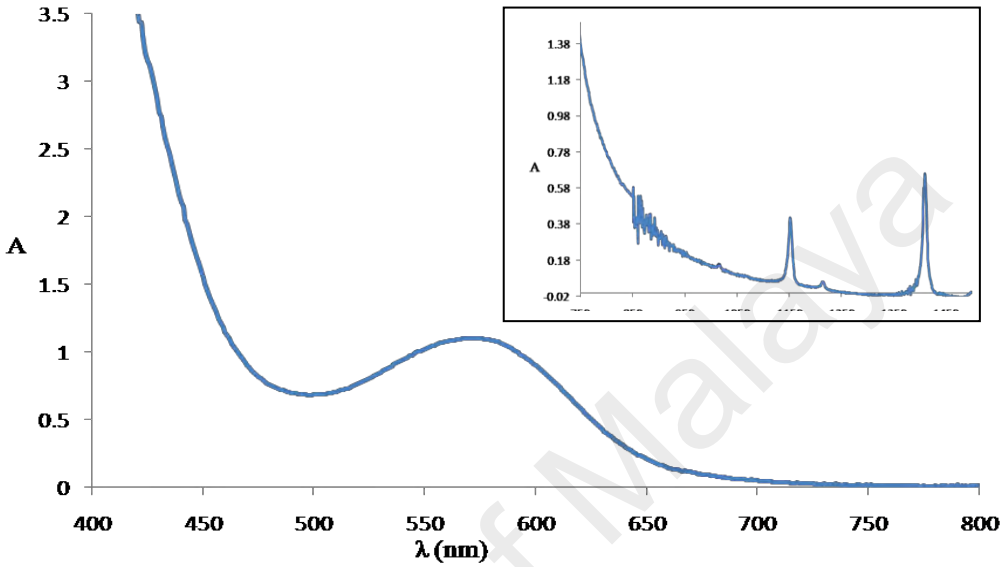

Figure 4.10 UV-visible spectrum of **Complex 2**

(b) Band gap

The E_o of **Complex 2** was similarly calculated as for **Complex 1**. From the value of λ_{onset} (660 nm), its E_o was 1.87 eV which was similarly reported for $[Fe(L1)_2](BF_4)$, where L1 = neutral N_3-donor Schiff base (E_o = 1.80 eV) [72]. This value was lower than **Complex 1** ($[Co_2(CH_3COO)_4(LC8)_2].3H_2O$; E_o = 2.61 eV), indicating a less stable (higher energy) antibonding orbitals (E_g) of Fe(II) compared to Co(II). As a result, the photonic excitation of electron from Fe(II) to the ligand was easier.

The **CV** scan for **Complex 2 (Figure 4.11)** shows two overlapping anodic peaks at +0.75 V and +1.05 V, assigned to oxidation of [Fe(II)Fe(II)] to [Fe(II)Fe(III)] and [Fe(II)] to [Fe(III)], respectively, as a result of dissociation of dimer [67]. These were followed by three cathodic peaks at +0.10, -0.75 V and -0.90 V, assigned to reduction of [Fe(II)Fe(III)] to [Fe(II)Fe(II)], [Fe(III)] to [Fe(II)] and LC8 to $LC8^-$, respectively. The

metal-based ΔE_p was 650 mV, suggesting a quasireversible redox for the complex [68]. The redox reaction is as follows.

$$[Fe(II)Fe(II)] \underset{+0.10\ V}{\overset{+0.75\ V}{\rightleftharpoons}} [Fe(II)Fe(III)]$$

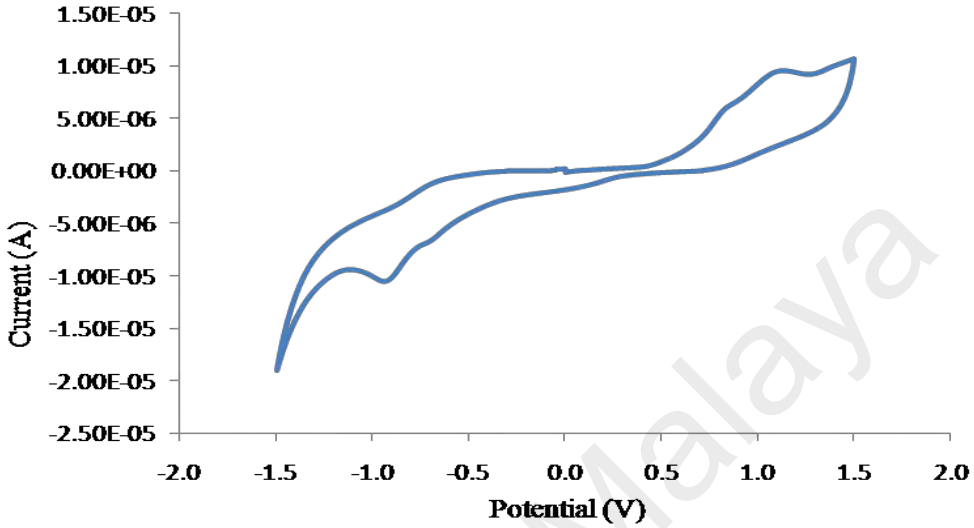

Figure 4.11 Cyclic voltammetry of **Complex 2**

Its E_e value, similarly calculated as previously done from the onset potentials for oxidation (+0.65 V) and reduction (+0.20 V), the values for E_{HOMO} (5.05 eV) and E_{LUMO} (4.60 eV), was 0.45 eV. It is noted that this was the same as **Complex 1** ($[Co_2(CH_3COO)_4(LC8)_2].3H_2O$; E_e = 0.50 eV).

(c) Magnetic susceptibility

The $\chi_M T$ value for **Complex 2**, calculated from its proposed chemical formula (FW = 2094.5 g mol^{-1}), χ_g (5.95 x 10^{-6} cm^3 g^{-1}), χ_M (1.25 x 10^{-2} cm^3 mol^{-1}), χ_D (-1.31 x 10^{-3} cm^3 mol^{-1}) and χ_M^{corr} (1.38 x 10^{-2} cm^3 mol^{-1}), was 4.11 cm^3 K mol^{-1} at 298 K. Since the theoretical $\chi_M T$ values for HS dinuclear Fe(II) octahedral complex (S = 2) is 6.002 cm^3 K mol^{-1}, while LS Fe(II) is diamagnetic [42], it may be inferred that this complex was made up of 68.5% HS and 31.5% LS Fe(II) atoms at this temperature in the solid state.

(d) Thermal properties

TGA trace for **Complex 2 (Figure 4.12)** shows a total mass loss of 90.6% from 175 ^{o}C to 885 ^{o}C, due to decomposition of CH_3COO^- ions and LC8 (calculated 91.5%). However, the amount of residue could not be ascertained as there was no plateau in the thermogram at the temperatures above 885 ^{o}C (instrumental limitation). Hence, its decomposition temperature was 175 ^{o}C, which was slightly lower than **Complex 1** ($[Co_2(CH_3COO)_4(LC8)_2].3H_2O$; T_{dec} = 180 ^{o}C).

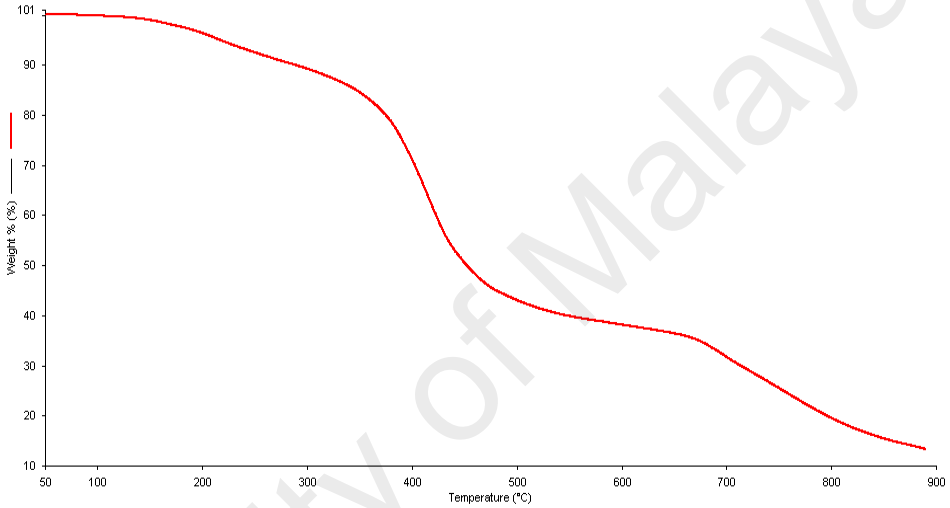

Figure 4.12 TGA trace of **Complex 2**

(e) Thermoelectric properties

The thermoelectric experiment for **Complex 2** was similarly conducted as for **Complex 1**. Graphs of ΔV *versus* ΔT (**Figure 4.13**) were linear, indicating a good thermoelectric behaviour.

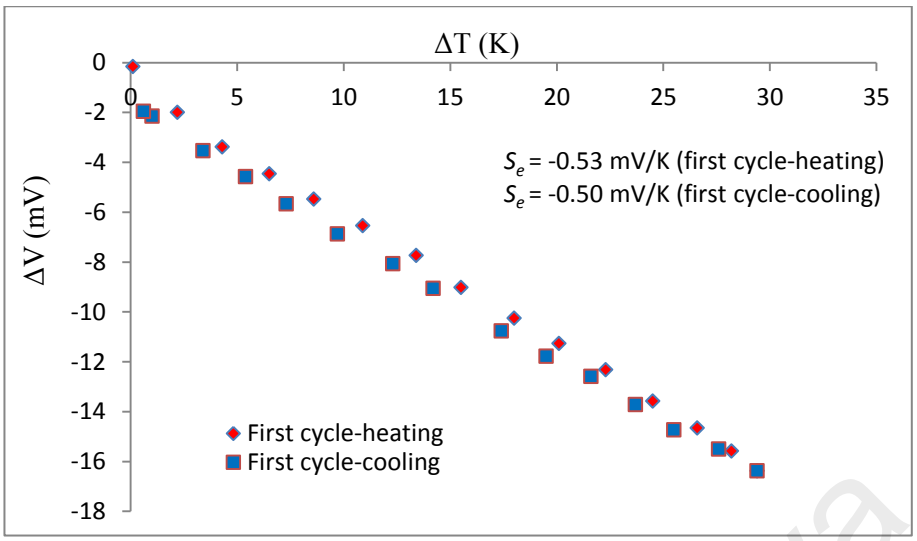

(a)

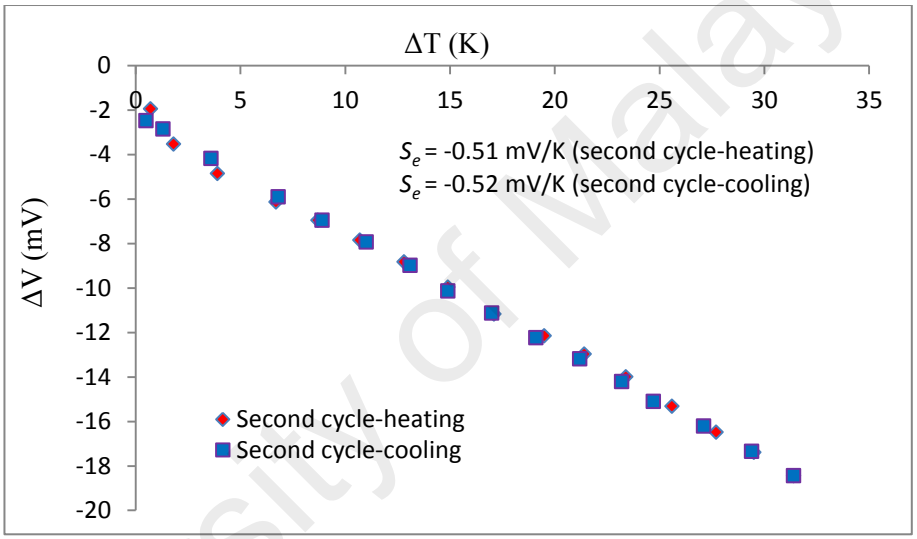

(b)

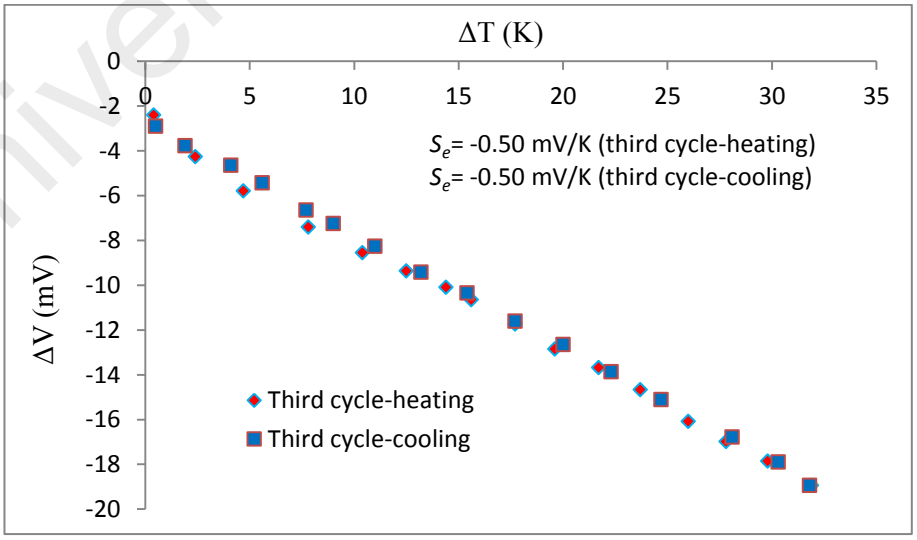

(c)

Figure 4.13 Graphs of ΔV *versus* ΔT for **Complex 2**: (a) first; (b) second; and (c) third heating-and-cooling cycles

Its mean S_e value was -0.51 ± 0.01 mV K^{-1}, which was similar to **Complex 1** ($[Co_2(CH_3COO)_4(LC8)_2].3H_2O$; S_e = -0.58 ± 0.03 mV K^{-1}), and most likely due to the similarity in their structures, and may be similarly explained. The only different between the two complexes was that **Complex 2** showed a better thermoelectric behaviour during all three heating-and-cooling cycles, and this may be due to the stronger Fe-N and Fe-O bonds in the dimer (it has a higher percentage of LS Fe(II) atom), and hence has a lesser tendency to dissociate.

4.2.4 $[Co(LC8)_3](BF_4)_2.2H_2O$

Cobalt(II) tetrafluoroborate hexahydrate, $Co(BF_4)_2.6H_2O$, reacted with LC8 in a mole ratio of 1:3 to form a brick red powder **(Complex 3)**, and its yield was 70.1%. Its solubility was similar to the previously discussed complexes.

(a) Deduction of structural formula

As previously done, the structure of **Complex 3**, $[Co(LC8)_3](BF_4)_2.2H_2O$ **(Figure 4.14)**, was proposed based on combined results of elemental analyses, FTIR spectroscopy and UV-vis spectroscopy.

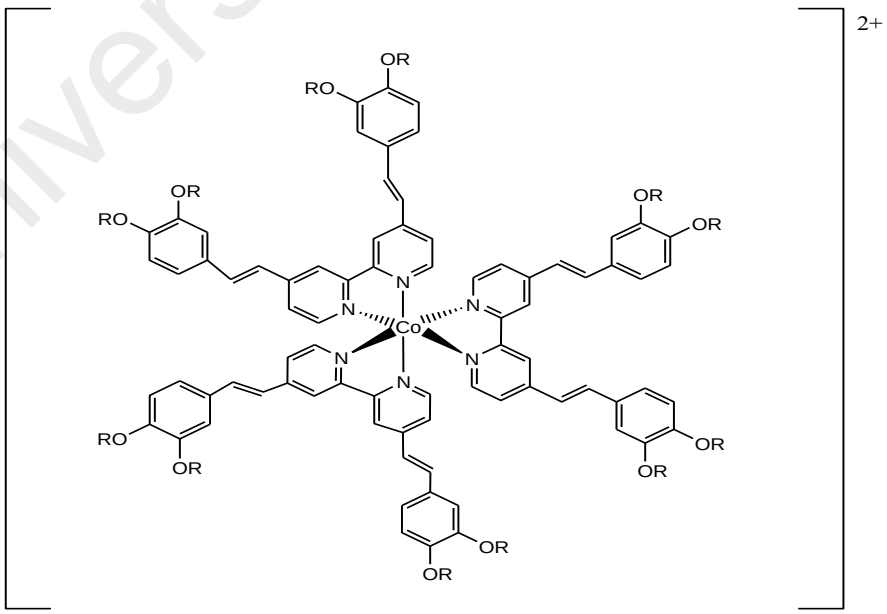

Figure 4.14 Proposed structure of $[\mathbf{3}]^{2+}$; R = $CH_3(CH_2)_7$

The results of its **elemental analyses** (71.98% C, 9.25% H, 3.02% N) were in good agreement with those calculated for the chemical formula $C_{174}H_{256}B_2CoF_8N_6O_{14}$ (72.35% C, 8.93% H, 2.91% N; formula weight: 2888.5 g mol^{-1}).

Its **FTIR** spectrum (**Figure 4.15**) shows the presence of the expected functional groups and may be similarly assigned and explained as for **Complex 1** ($[Co_2(CH_3COO)_4(LC8)_2].3H_2O$). In addition, there were two strong overlapping peaks at 1053 cm^{-1} for C-N and BF_4^- ion [72], and a weak peak at 551 cm^{-1} for Co-N bonds [63] **(Table 4.2)**.

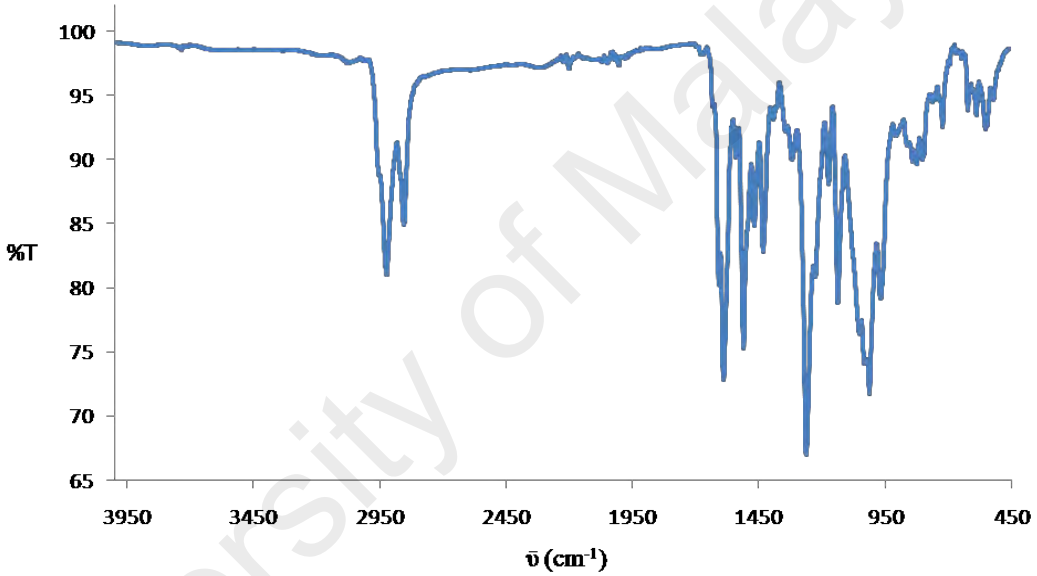

Figure 4.15 FTIR spectrum of **Complex 3**

Its **UV-vis** spectrum **(Figure 4.16)** was recorded as a solution in $CHCl_3$. It shows two sharp *d-d* bands at 1410 nm (ε_{max}, 93.8 M^{-1} cm^{-1}; inset) and 1152 nm (ε_{max}, 51.6 M^{-1} cm^{-1}; inset) assigned to the $^4T_{1g} \rightarrow {}^4T_{2g}$ and $^4T_{1g} \rightarrow {}^4A_{2g}$ electronic transitions for HS Co(II), respectively. Also seen was a strong MLCT band at 414 nm (ε_{max}, 8.5 x 10^4 M^{-1} cm^{-1}). The molarities of the solutions were 7.1 x 10^{-3} mol dm^{-3} for the *d-d* band and 1.6 x 10^{-5} mol dm^{-3} for the MLCT bands.

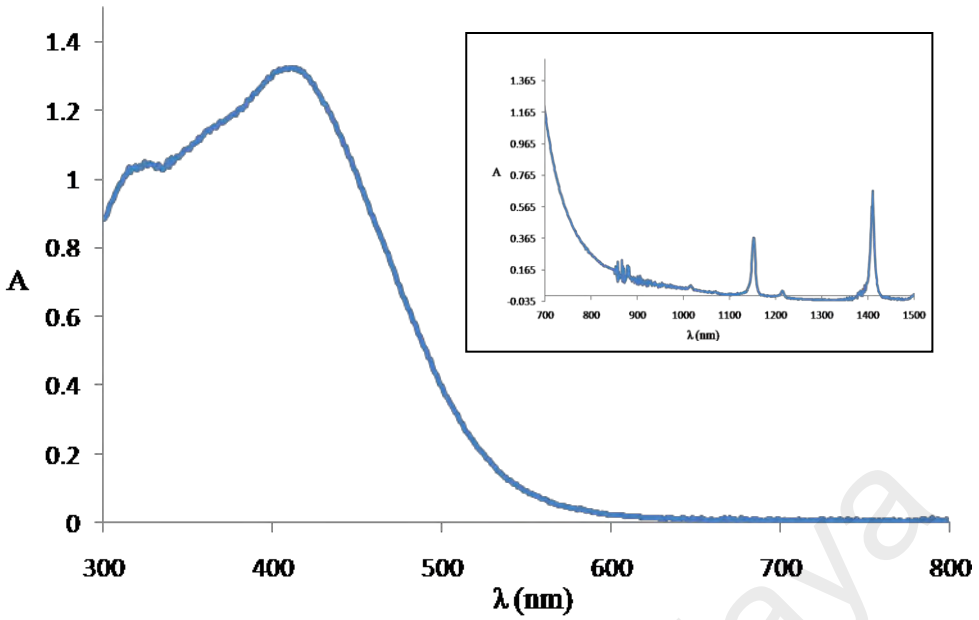

Figure 4.16 UV-vis spectrum of **Complex 3**

(b) Band gap

Its E_o, calculated as before, was 2.33 eV (λ_{onset} = 530 nm). This value was slightly lower than **Complex 1** ($[Co_2(CH_3COO)_4(LC8)_2].3H_2O$; E_o = 2.61 eV).

The **CV** scan for **Complex 3 (Figure 4.17)** shows two overlapping anodic peaks at +0.85 V and +1.15 V, assigned to the oxidation of [Co(II)] to [Co(III)] and LC8 to $LC8^+$, respectively. On the reversed scan, there were two cathodic peaks at +0.20 V and -0.95 V, assigned to the reduction of [Co(III)] to [Co(II)] and $LC8^+$ to LC8, respectively. The metal-based ΔE_pvalue was 650 mV, indicating a quasireversible redox reaction [68]. The redox reaction is as follows:

$$[Co(II)] \underset{+0.20\ V}{\overset{+0.85\ V}{\rightleftharpoons}} [Co(III)]$$

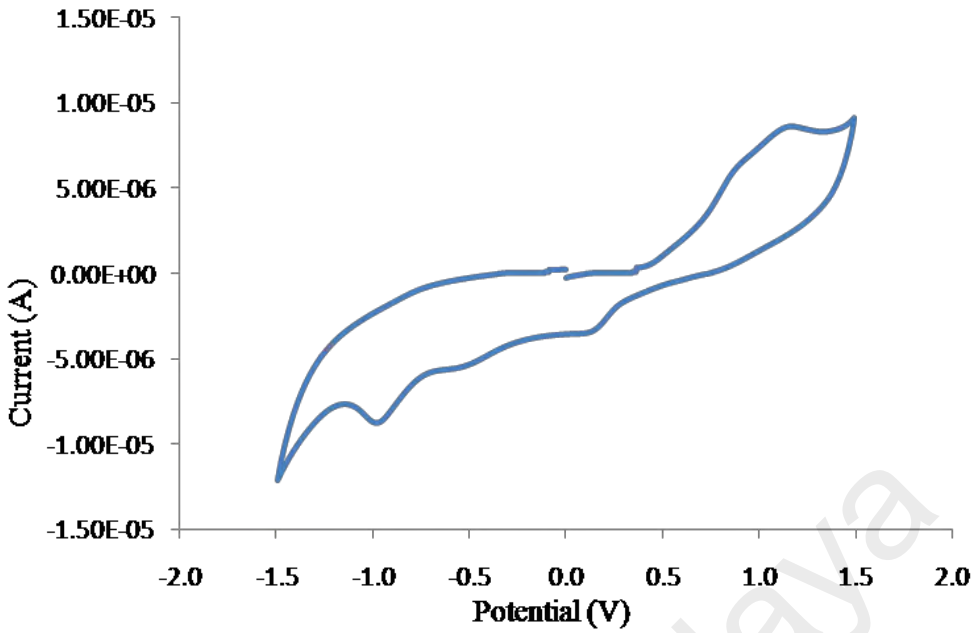

Figure 4.17 Cyclic voltammetry of **Complex 3**

Its E_e value, similarly calculated as previously done from the onset potentials for oxidation (0.70 V) and reduction (+0.35 eV), the values for E_{HOMO} (5.10 eV) and E_{LUMO} (4.75 eV), was 0.35 eV. The value was lower than **Complex 1** ($[Co_2(CH_3COO)_4(LC8)_2].3H_2O$, E_e = 0.50 eV), indicating that the mononuclear complex was easier to be oxidised and reduced compared to the dinuclear complex.

(c) Magnetic properties

The $\chi_M T$ value for **Complex 3**, similarly calculated as for previously discussed complexes, from its proposed chemical formula (FW = 2888.5 g mol^{-1}), χ_g (1.80 x 10^{-6} cm^3 g^{-1}), χ_M (5.26 x 10^{-3} cm^3 mol^{-1}), χ_D (-2.00 x 10^{-3} cm^3 mol^{-1}) and χ_M^{corr} (7.26 x 10^{-3} cm^3 mol^{-1}), was 2.18 cm^3 K mol^{-1} at 298 K. The theoretical value for a HS mononuclear Co(II) octahedral complex (S = 3/2) is 1.876 cm^3 K mol^{-1} [42]. Accordingly, it is inferred that **Complex 3** was HS at this temperature, which is similar with **Complex 1** ($[Co_2(CH_3COO)_4(LC8)_2].3H_2O$; 100% HS).

(d) Thermal properties

The **TGA** trace for **Complex 3 (Figure 4.18)** shows a total mass loss of 94.5% from 265 ^{o}C to 825 ^{o}C due to the loss of BF_3 (from BF_4^- ions) and decomposition of LC8 (calculated 96.5%). The amount of residue at temperatures above 825 ^{o}C was 5.5% while the calculated amount was 3.5% (assuming pure CoF_2) [73]. Hence, its decomposition temperature was 265 ^{o}C, which was higher than **Complex 1** ($[Co_2(CH_3COO)_4(LC8)_2].3H_2O$; T_{dec} = 180 ^{o}C) and **Complex 2** ($[Fe_2(CH_3COO)_4(LC8)_2]$; T_{dec} = 175 ^{o}C). This was likely due to the breaking of the stronger B-F bond of BF_4^- ion [10] compared to CH_3-COO bond [74] of **Complexes 1** and **2**, respectively.

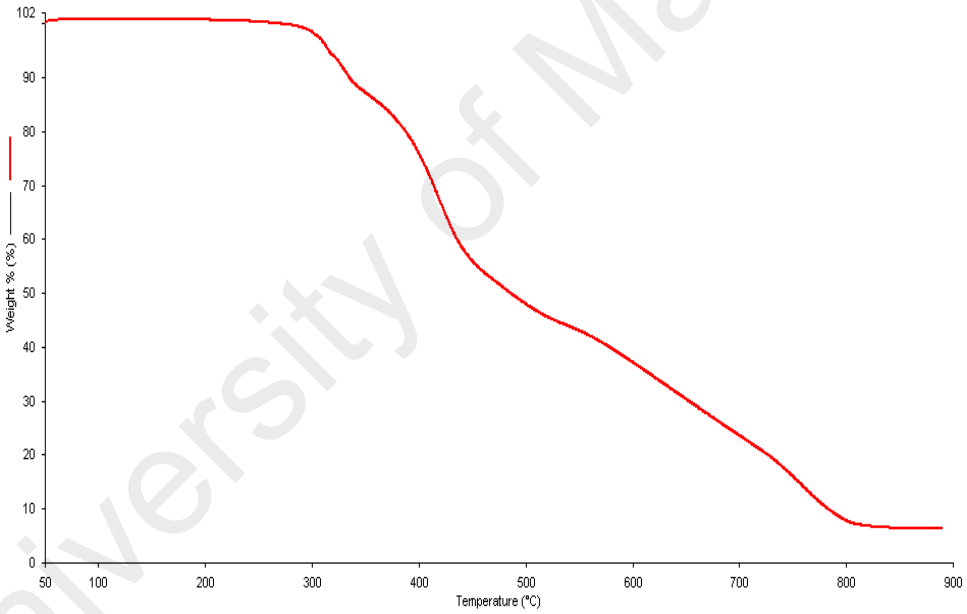

Figure 4.18 TGA trace of **Complex 3**

(e) Thermoelectric properties

The thermoelectric experiment for **Complex 3** was carried out similarly as for previous complexes. It is noted that its graphs of ΔV *versus* ΔT in the heating cycles were less satisfactory than in the cooling cycles **(Figure 4.19).** Its mean S_e value, calculated for the cooling cycles only, was -0.45 ± 0.01 mV K^{-1}, which was lower than **Complex 1** ($[Co_2(CH_3COO)_4(LC8)_2].3H_2O$; S_e = -0.58 ± 0.03 mV K^{-1}. The negative values mean that both complexes have similar majority charge carriers. Both complexes have 100%

HS Co(II) atoms, but their difference was that **Complex 1** was dimeric and molecular (but dissociated to monomers on heating), while **Complex 3** was mononuclear and ionic. Hence, the proposed micelle-like structure formed from the latter complex may have slower mobility in $CHCl_3$ and/or the complex cation less readily released the trapped I^- ion due to the stronger coulombic attraction.

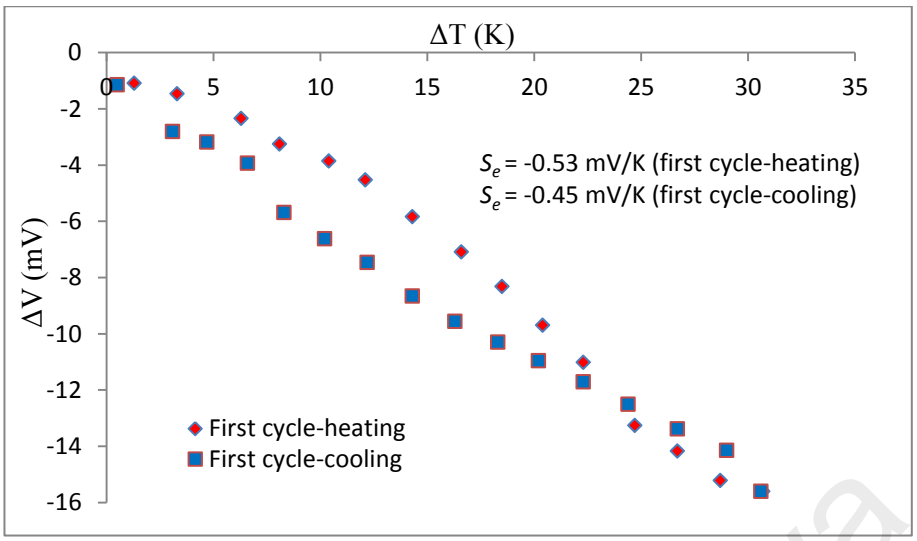

(a)

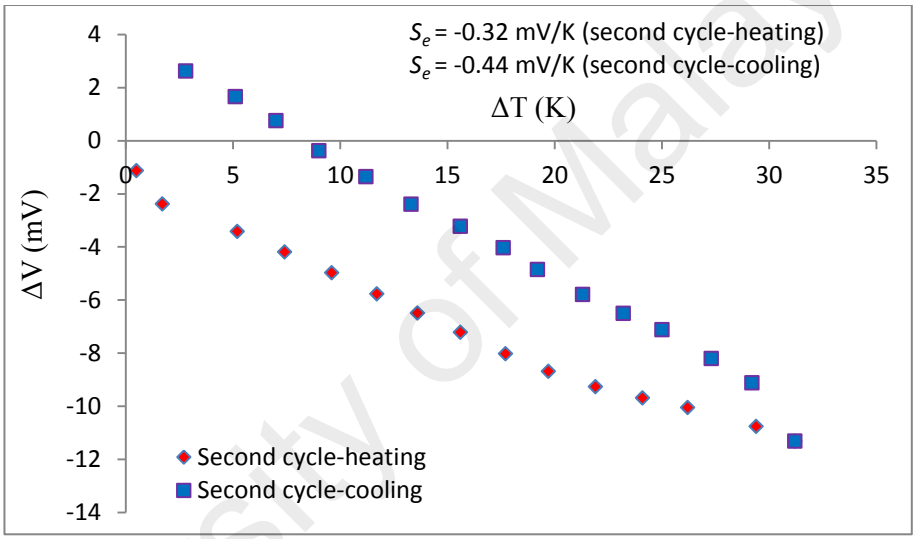

(b)

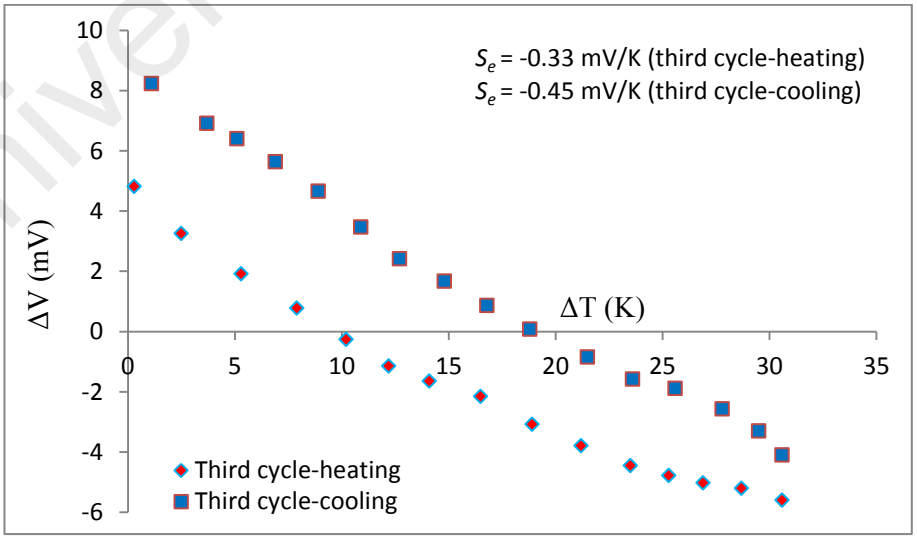

(c)

Figure 4.19 Graphs of ΔV *versus* ΔT for **Complex 3**: (a) first; (b) second; and (c) third heating-and-cooling cycles

4.2.5 $[Fe(LC8)_3](BF_4)_2.H_2O$

Iron(II) tetrafluoroborate hexahydrate, $Fe(BF_4)_2.6H_2O$, reacted with LC8 in a mole ratio of 1:3 to form a black powder (**Complex 4**), and its yield was 70.5%. Its solubility was similar to **Complexes 1 – 3**.

(a) Deduction of structural formula

The structure of **Complex 4** was deduced based on the same instrumental data as previously discussed. From the results discussed below, it is proposed that its structural formula was $[Fe(LC8)_3](BF_4)_2.H_2O$, which was similar to **Complex 3** ($[Co(LC8)_3](BF_4)_2.2H_2O$; **Figure 4.14**).

The results of its **elemental analyses** (72.90% C, 9.23% H, 3.27% N) were in good agreement with those calculated for the chemical formula $C_{174}H_{254}B_2F_8FeN_6O_{13}$ (72.88% C, 8.93% H, 2.93% N; formula weight: 2867.4 g mol^{-1}).

Its **FTIR** spectrum **(Figure 4.20)** shows peaks (in cm^{-1}) indicating the presence of the expected functional groups at 2922, 2854, 1609, 1591, 1040 and 556 (**Table 4.2**). These peaks may be similarly assigned as for **Complex 3**.

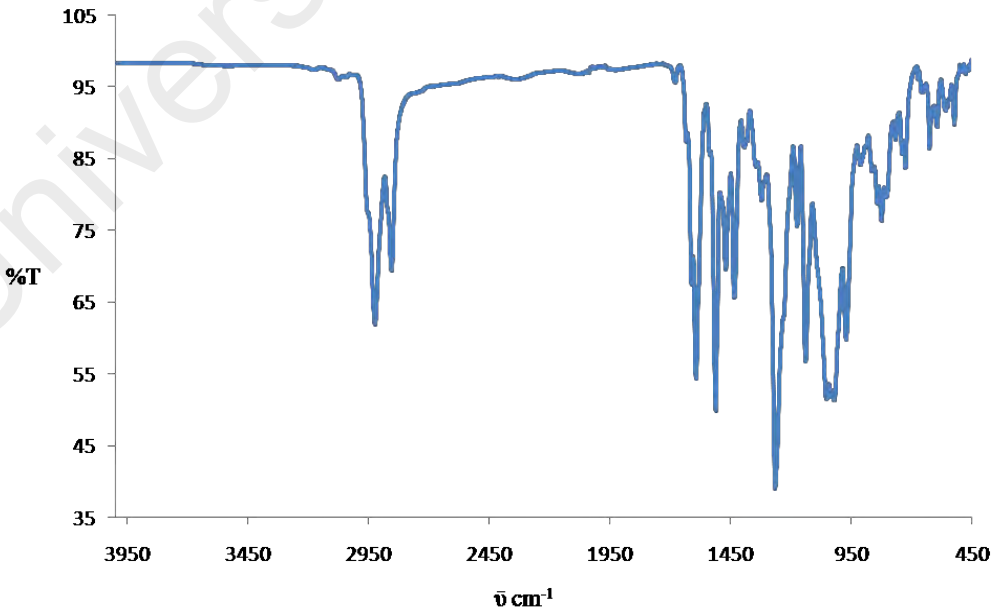

Figure 4.20 FTIR spectrum of **Complex 4**

Its **UV-vis** spectrum (**Figure 4.21**) in $CHCl_3$ shows sharp *d-d* peaks at 1410 nm (ε_{max}, 94.6 M^{-1} cm^{-1}; inset) and 1152 nm (ε_{max}, 54.2 M^{-1} cm^{-1}; inset) as well as three broad MLCT peaks at 570 nm (ε_{max}, 2.9 x 10^4 M^{-1} cm^{-1}), 401 nm (ε_{max}, 9.9 x 10^4 M^{-1} cm^{-1}) and 314 nm (ε_{max}, 7.5 x 10^4 M^{-1} cm^{-1}). The *d-d* bands are assigned to $^5T_{2g} \rightarrow {}^5E_g$ electronic transition for HS Fe(II) in the solution [49, 51]. The molarities of the solutions were 7.0 x 10^{-3} mol dm^{-3} for the *d-d* band and 3.5 x 10^{-5} mol dm^{-3} for the MLCT bands.

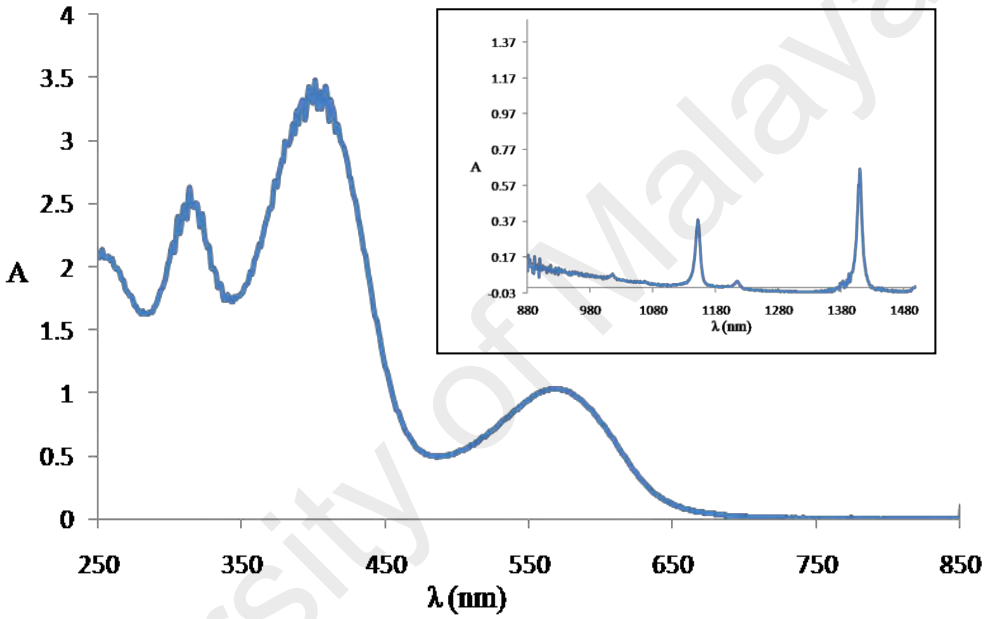

Figure 4.21 UV-vis spectrum of **Complex 4**

(b) Band gap

The E_o for **Complex 4** was similarly calculated as previous complexes. The E_o was 1.90 eV (λ_{onset} = 650 nm). This value was significantly lower than **Complex 3** ($Co(LC8)_3(BF_4)_2.2H_2O$; E_o = 2.33 eV).

Its **CV** scan **(Figure 4.22)** shows two overlapping anodic peaks at +0.78 V and +1.20 V and also two cathodic peaks appeared at +0.15 V and -0.95 V. These are assigned to the oxidation of [Fe(II)] to [Fe(III)] and LC8 to $LC8^+$, followed by reduction of [Fe(III)] to [Fe(II)] and $LC8^+$ to LC8, respectively. The metal-based ΔE_p was

630 mV, indicating a quasireversible redox reaction [68]. The redox reaction is shown below.

$$[Fe(II)] \underset{+0.20\ V}{\overset{+0.78\ V}{\rightleftharpoons}} [Fe(III)]$$

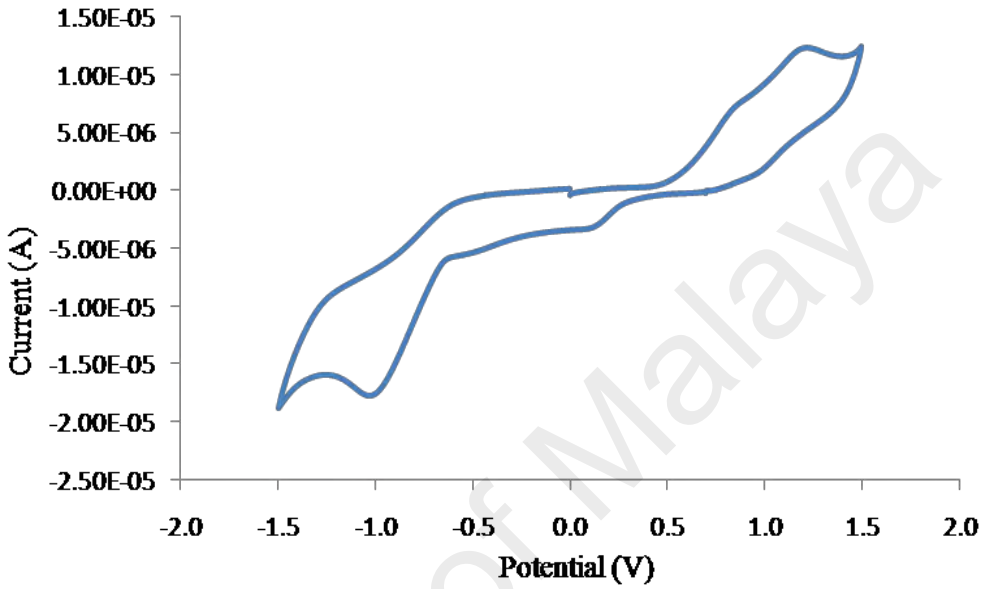

Figure 4.22 Cyclic voltammetry of **Complex 4**

Its $E_o$value, similarly calculated as previously done from the onset potentials for oxidation (+0.55 V) and reduction (+0.22 V), the values for E_{HOMO} (4.95 eV) and E_{LUMO} (4.62 eV), was 0.33 eV. This value was similar to **Complex 3** ($[Co(LC8)_3](BF_4)_2.2H_2O$; E_e = 0.35 eV), may be due to the similarities of proposed structures for both complexes.

(c) Magnetic properties

The value of χ_g for **Complex 4** was -2.7 x 10^{-7} cm^3 g^{-1} at room temperature. The negative value means that this complex was diamagnetic. Accordingly, it is inferred that its Fe(II) atom was LS at room temperature as a result of strong Fe-N bonds. Additionally, may be the Fe-N covalent bond in the solid state is shorter than in the solution, resulting higher LS in this complex.

(d) Thermal properties

The **TGA** trace for **Complex 4 (Figure 4.23)** shows a total mass loss of 91.4% from 265 ^{o}C to 884 ^{o}C due to loss of BF_3 (from BF_4^- ions) and decomposition of LC8 (calculated, 96.6%). However, the amount of residue could not be calculated as there was no plateau in the thermogram at temperatures above 884 ^{o}C (instrumental limitation). Hence, its thermal stability (T_{dec} = 265 ^{o}C) was similar to **Complex 3** ($[Co(LC8)_3](BF_4)_2.2H_2O$; T_{dec} = 265 ^{o}C), and may be similarly explained.

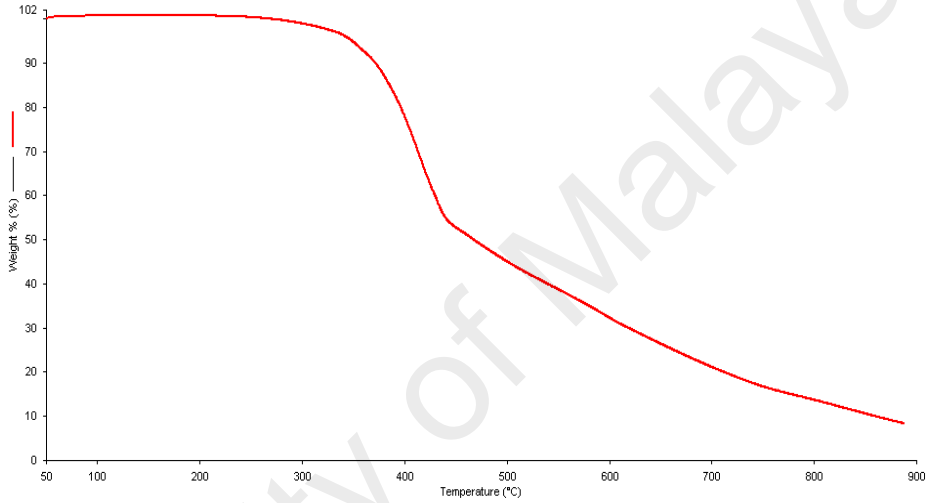

Figure 4.23 TGA trace of **Complex 4**

(e) Thermoelectric properties

Graphs of ΔV *versus* ΔT for **Complex 4** (**Figure 4.24**) were linear, indicating good thermoelectric behaviour. However, it is noted that the graphs on heating were satisfactory, while those on cooling were only linear in the ΔT range of about 7 K to 30 K for all cycles. Its mean S_e value was -0.57 ± 0.01 mV K^{-1} (calculated for the linear parts on the graphs only), was higher than **Complex 3** ($[Co(LC8)_3](BF_4)_2.2H_2O$; S_e = -0.45 ± 0.01 mV K^{-1} (cooling cycles).

Both complexes were mononuclear and ionic. However, **Complex 3** has 100% HS Co(II) atom (weaker Co-N bonds) and its geometry was subjected to distortion (tetragonally compressed octahedron) due to Jahn-Teller effect, while **Complex 4** has 100% LS Fe(II) atom (stronger Fe-N bonds) and its geometry was octahedral since it

was not subjected to Jahn-Teller effect. On heating, some of the LS Fe(II) atoms in **Complex 4** changed to HS Fe(II) atoms (weaker Fe-N bonds), and its octahedral geometry became more tetragonally compressed. The higher entropy explained the higher S_e value for this complex compared to **Complex 3**. On cooling, the reverse HS-to-LS transition occurred and completed at ΔT less than about 7 K, which explains the lower gradients of the cooling graphs below this value.

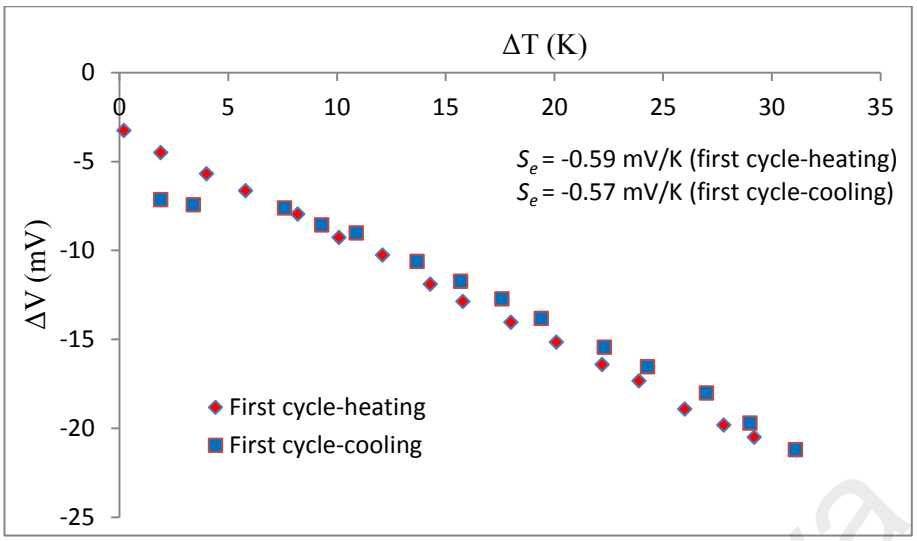

(a)

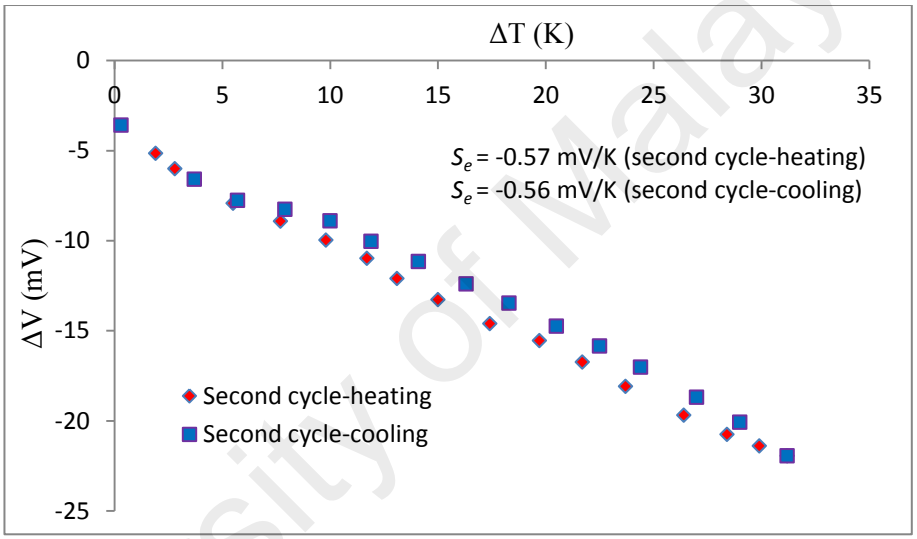

(b)

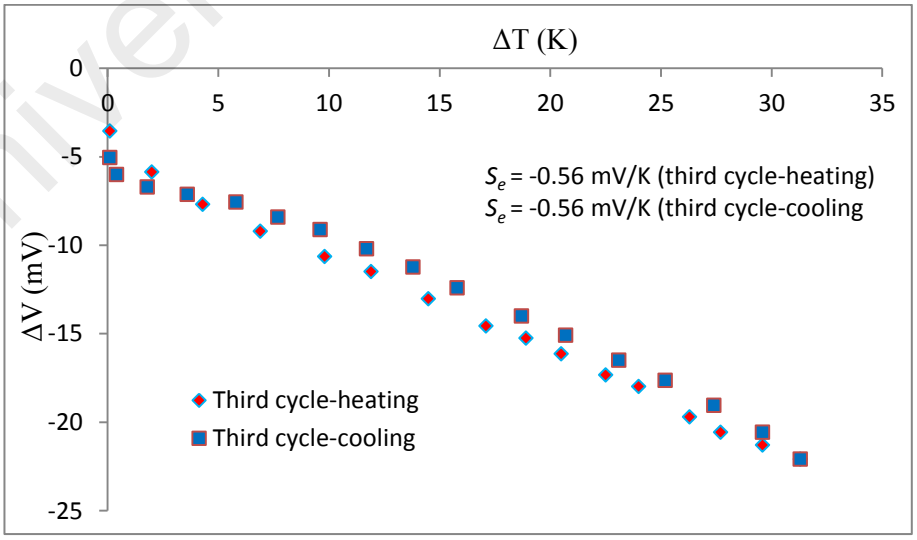

(c)

Figure 4.24 Graphs of ΔV *versus* ΔT for **Complex 4**: (a) first; (b) second; and (c) third heating-and-cooling cycles

4.2.6 Summary

The results from analytical data for **Complexes 1 - 4** are summarised in **Table 4.3**.

Table 4.3 Summary of results for **Complexes 1 - 4**

Chemical Formula	**Band gap (eV)**		$\chi_M^{corr}T$ **(cm^3 K mol^{-1})**	T_{dec} **C**	S_e **(mV K^{-1})**
	E_o	E_e			
$[Co_2(CH_3COO)_4(LC8)_2].3H_2O$ (**Complex 1**)	2.61	0.50	3.96 100% HS	180	-0.58 ± 0.03
$[Fe_2(CH_3COO)_4(LC8)_2]$ (**Complex 2**)	1.87	0.45	4.11 68.5% HS	175	-0.51 ± 0.01
$[Co(LC8)_3](BF_4)_2.2H_2O$ (**Complex 3**)	2.33	0.35	2.18 100% HS	265	-0.45 ± 0.01 (cool)
$[Fe(LC8)_3](BF_4)_2.H_2O$ (**Complex 4**)	1.90	0.33	diamagnetic 100% LS	265	-0.57 ± 0.01

Complexes 1 and **2** were dinuclear and molecular, while **Complexes 3** and **4** were mononuclear and ionic. All complexes have octahedral geometry at the metal(II) centre, and soluble only in lipophilic solvents, such as chloroform and dichloromethane.

The optical band gap (E_o) for the Co(II) complexes were higher compared to Fe(II) complexes. This is may be due to the more stable (lower energy) antibonding orbitals (E_g) of Co(II) compared to Fe(II). Hence, the photonic excitation of electron from Co(II) to the ligand required more energy.

For the electrochemical band gap (E_e) for the molecular complexes **(Complexes 1** and **2)** were higher than the ionic complexes **(Complexes 3** and **4)**. All complexes have electrochemical band gap (E_e = 0.33 eV – 0.50 eV) within the semiconductor band which were good for thermoelectrical properties (Seebeck coefficient) [75].

At room temperature, **Complexes 1** and **3** have 100% HS Co(II) atoms indicating weak M-L bonds. It is likely due to geometrical distortion as a result of weak Jahn-Teller effect in these complexes. Instead, **Complex 4** has 100% LS Fe(II) atom

indicating strong Fe-N bonds, while for **Complex 2** has a mixture of HS (68.5%) and LS (31.5%) of Fe(II) atoms.

From TGA data, the molecular complexes **(Complexes 1** and **2)** have lower thermal stability compared to the ionic complexes **(Complexes 3** and **4)**. This maybe because the decomposition process for the former complexes arose from the decarboxylation of CH_3COO^- ion due to the breaking of C-COO bond [74], while the decomposition process for the latter complexes was due to the breaking of the stronger B-F bond in BF_4^- ion.

Finally, all complexes have negative Seebeck coefficient (S_e) values. Based on their S_e values, these complexes are potential thermoelectrical materials in chloroform. **Complex 1** has the highest value (S_e = -0.58 ± 0.03 mV K^{-1}) while **Complex 3** has the lowest value (S_e = -0.45 ± 0.01 mV K^{-1}). The difference in their thermoelectric behaviours arose from the differences in their structures and spin states.

4.3 LC10 and its Cobalt(II) and Iron(II) Complexes

4.3.1 Ligand LC10

The steps involved in the synthesis of LC10 were similar as for LC8 (**Scheme 1.1**). The ligand was obtained as a white powder and its yield was 77.9%. Its structure was ascertained by elemental analyses, ^{1}H-NMR spectroscopy, and FTIR spectroscopy.

The result of its **elemental analyses** (80.10% C, 9.92% H, 3.10% N) were in a good agreement with those calculated for the chemical formula $C_{66}H_{100}N_2O_4$ (80.44% C, 10.23% H, 2.84% N; formula weight: 985.5 g mol^{-1}).

Its **^{1}H-NMR** spectrum **(Figure 4.25)** shows peaks (in ppm) at 0.8 (triplet, CH_3, 12 H), 1.2 - 1.9 (multiplet, CH_2, 64 H), 4.0 (triplet, O-CH_2-, 8 H), 6.80 - 7.50 (multiplet, aromatic C-H and HC=CH, 12 H), 8.6 (singlet, aromatic C-H, 2 H), and 8.7 (doublet, aromatic C-H, 2 H). The peak assignments are given in **Table 4.4**.

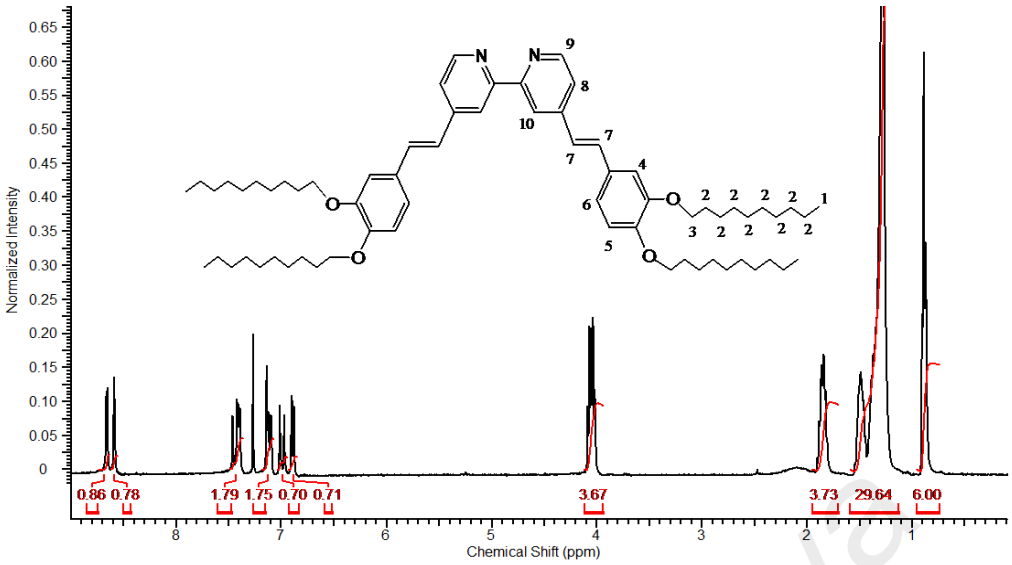

Figure 4.25 ^{1}H-NMR spectrum of LC10

Table 4.4 The ^{1}H-NMR data and peak assignments for LC10

Chemical shift (ppm)	**Integral**	**Multiplicity**	**Assignment**
0.8 - 0.9	6.00	Triplet	H-1
1.2 - 1.9	33.37	Multiplet	H-2
4.0	3.67	Triplet	H-3
6.8 - 7.5	4.95	Multiplet	H-4, H-5, H-6, H-7, H-8
8.6	0.76	Singlet	H-10
8.7	0.86	Doublet	H-9

Its **FTIR** spectrum **(Figure 4.26)** shows peaks (in cm^{-1}) indicating the presence of the expected functional groups at 2919, 2850, 1657, 1588 and 1264, as previously discussed for LC8. The peak assignments are shown in **Table 4.5** (which also includes peaks for the corresponding complexes for later discussion).

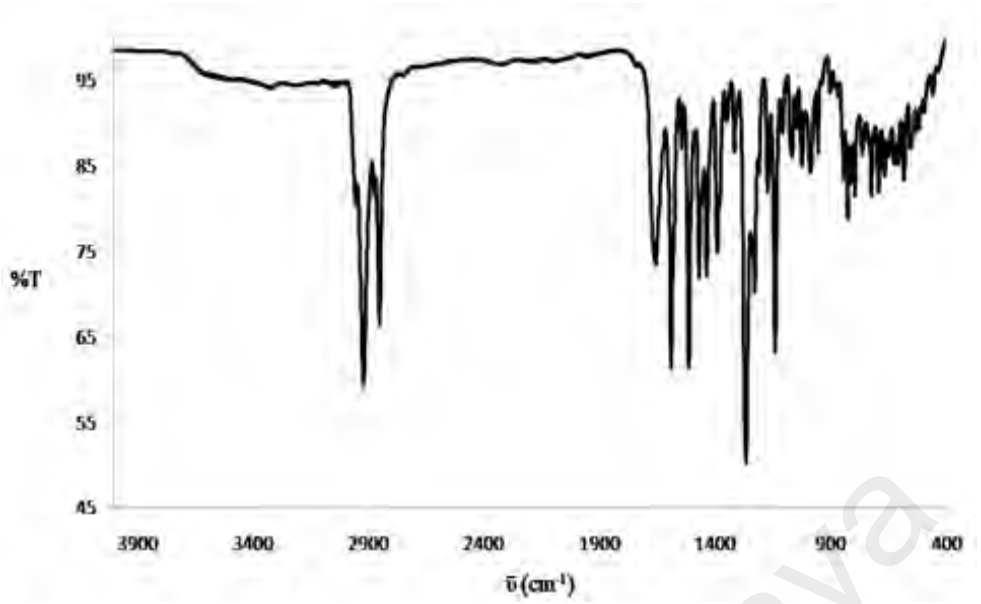

Figure 4.26 FTIR spectrum of LC10

Table 4.5 The FTIR data (in cm^{-1}) of LC10 and its complexes

	Assignment								
	CH_2 (asym)	CH_2 (sym)	C=N	C=C (ar)	COO (asym)	COO (sym)	BF_4^-	M-N	M-O
LC10	2919s	2850s	1657m	1588s	-	-	-	-	-
5	2921s	2852m	1611m	1593s	1663w 1511m	1467m 1392m	-	558w	452w
6	2920s	2850m	1610m	1595s	1673m 1509m	1457m 1391m	-	586w	445w
7	2921s	2853m	1609s	1589s	-	-	1031s,br	557w	-
8	2921s	2852m	1609m	1592s	-	-	1051s, br	544w	-

s = strong; m = medium; w = weak; br = broad

4.3.2 $[Co_2(CH_3COO)_4(LC10)_2].H_2O$

Ligand LC10 reacted with cobalt(II) acetate tetrahydrate, $Co(CH_3COO)_2.4H_2O$, in a mole ratio of 1:1 to form a dark red powder **(Complex 5),** and its yield was 60.8%. Its solubility was similar to the previously discussed complexes.

(a) Deduction of structural formula

From the elemental analyses data, FTIR spectroscopy and UV-vis spectroscopy discussed below, it is proposed that the structural formula of **Complex 5** was $[Co_2(CH_3COO)_4(LC10)_2].H_2O$, which was similar as **Complex 1** ($[Co_2(CH_3COO)_4(LC8)_2].3H_2O$; **Figure 4.3**).

The result of the **elemental analyses** (71.43% C, 9.57% H, 2.41% N) were in excellent agreement with those calculated for the chemical formula $C_{140}H_{214}Co_2N_4O_{17}$ (71.76% C, 9.21% H, 2.39% N; formula weight, 2343.1 g mol^{-1}).

Its **FTIR** spectrum **(Figure 4.27)** shows peaks (in cm^{-1}) at 2921, 2852, 1663, 1611, 1593, 1511, 1467, 1392, 1263, 558 and 452 **(Table 4.5).** These peaks may be similarly assigned as for **Complexes 1** ($[Co_2(CH_3COO)_4(LC8)_2].3H_2O$) and **2** ($[Fe_2(CH_3COO)_4(LC8)_2]$). The Δ values for CH_3COO^- ligand were 196 cm^{-1} and 119 cm^{-1}, suggesting monodentate bridging and bidentate chelating binding modes [15, 49], respectively.

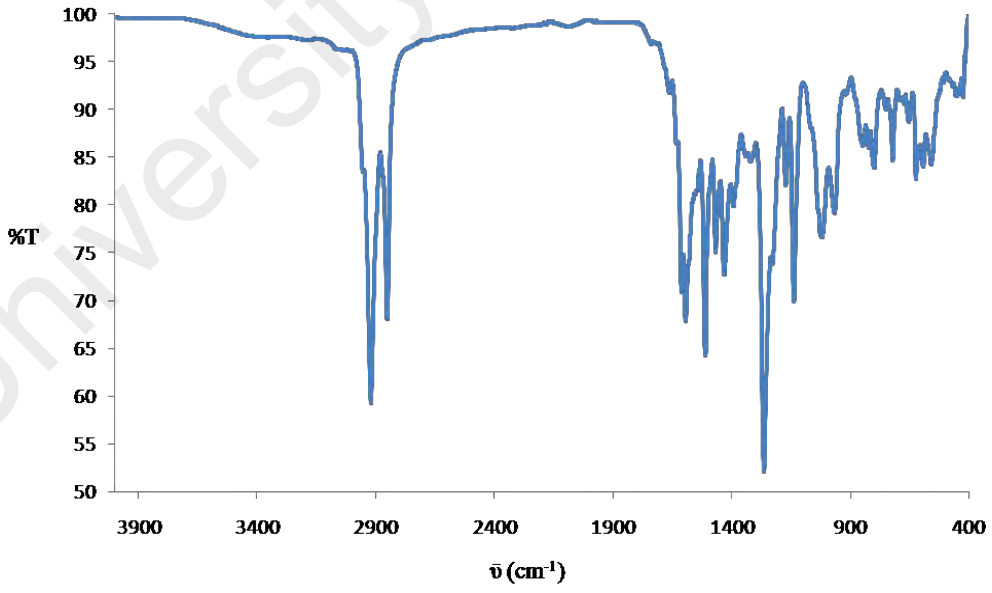

Figure 4.27 FTIR spectrum of **Complex 5**

Its **UV-vis** spectrum in $CHCl_3$ **(Figure 4.28)** shows a broad *d-d* band at 1192 nm (ε_{max}, 9.5 M^{-1} cm^{-1}; inset). The electronic transition may be similarly assigned as for **Complex 1**. Also seen were two intense overlapping MLCT peaks at 388 nm

(ε_{max}, 8.8 x 10^4 M^{-1} cm^{-1}) and 320 nm (ε_{max}, 7.1 x 10^4 M^{-1} cm^{-1}). The molarities of the solutions were 1.0 x 10^{-2} mol dm^{-3} for the *d-d* band and 2.1 x 10^{-5} mol dm^{-3} for the MLCT bands.

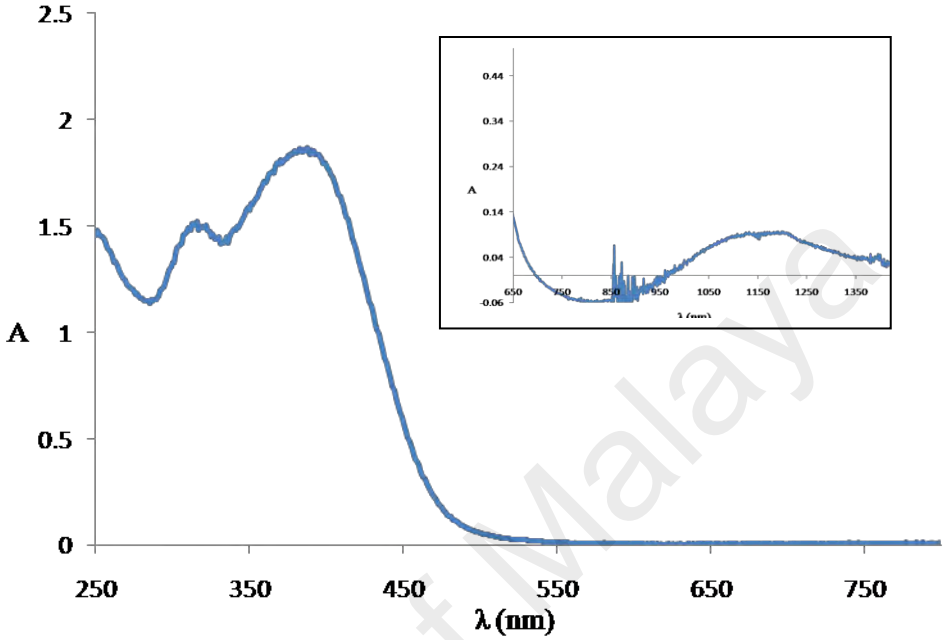

Figure 4.28 UV-vis spectrum of **Complex 5**

(b) Band gap

Its E_o value, similarly calculated as for previously discussed complexes, was 2.61 eV (λ_{onset} = 475 nm). The value was the same as **Complex 1** ($[Co_2(CH_3COO)_4(LC8)_2].3H_2O$; E_o = 2.61 eV).

The **CV** scan **(Figure 4.29)** shows overlapping anodic peaks at +0.86 V and two cathodic peaks at -0.05 V and -1.10 V. These peaks are assigned to the oxidation of [Co(II)Co(II)] to [Co(II)Co(III)] and LC10 to $LC10^+$, followed by the reduction of [Co(II)Co(III)] to [Co(II)Co(II)] and $LC10^+$ to LC10, respectively. Accordingly, the metal-based ΔE_p was 910 mV, suggesting a quasireversible redox reaction [68]. Hence, its redox behaviour was similar to **Complex 1**.

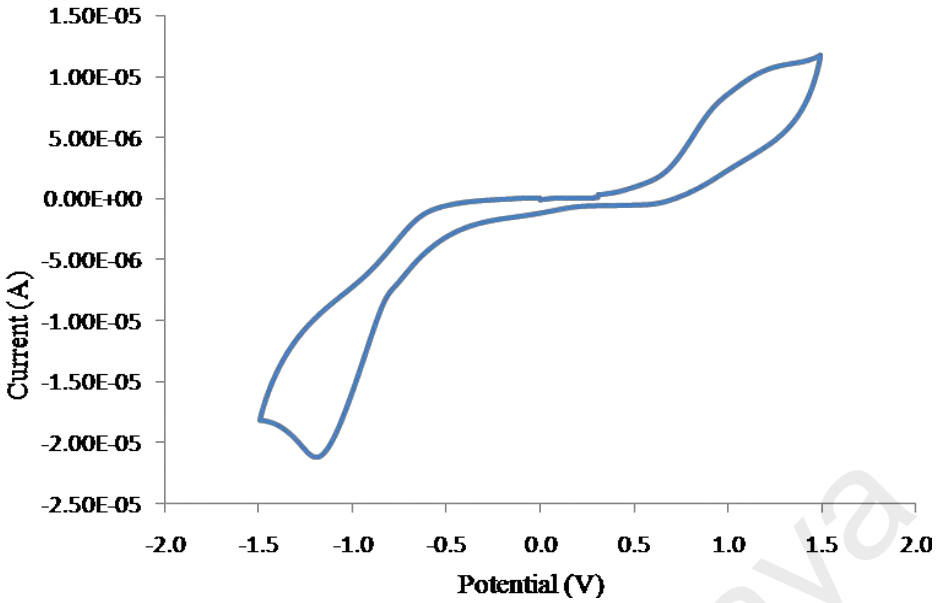

Figure 4.29 Cyclic voltammetry of **Complex 5**

Its E_e value, similarly calculated as previously done from the onset potentials for oxidation (+0.70 V) and reduction (+0.15 V), the values for E_{HOMO} (5.10 eV) and E_{LUMO} (4.55 eV) was 0.55 eV. This value was similar to **Complex 1** ($[Co_2(CH_3COO)_4(LC8)_2].3H_2O$; E_o = 0.50 eV).

(c) Magnetic properties

The $\chi_M T$ value for **Complex 5**, calculated from its proposed chemical formula (FW = 2343.1 g mol^{-1}), χ_g (4.79 x 10^{-6} cm^3 g^{-1}), χ_M (1.12 x 10^{-2} cm^3 mol^{-1}), χ_D (-1.55 x 10^{-3} $cm^3 mol^{-1}$) and χ_M^{corr} (1.28 x 10^{-2} cm^3 mol^{-1}), was 3.81 cm^3 K mol^{-1} at 298 K. Hence, this complex has 100% HS Co(II) atom at this temperature, which was similar to **Complex 1** and may be similarly explained.

(d) Thermal properties

The **TGA** trace of **Complex 5 (Figure 4.30)** shows almost similar thermal behaviour as **Complex 1**. It suffered a total mass loss of 94.5% from 178 ^oC to 720 ^oC, due to the decomposition of CH_3COO^- ions and LC10 (calculated, 94.9%). The amount of residue at temperatures above 720 ^oC was 5.5%, which was in a good agreement with the

calculated amount of 5.1% (assuming pure CoO [30]). Hence, the decomposition temperature of the complex was 178 ^{o}C, which was similar as **Complex 1** ($[Co_2(CH_3COO)_4(LC8)_2].3H_2O$; T_{dec} = 180 ^{o}C).

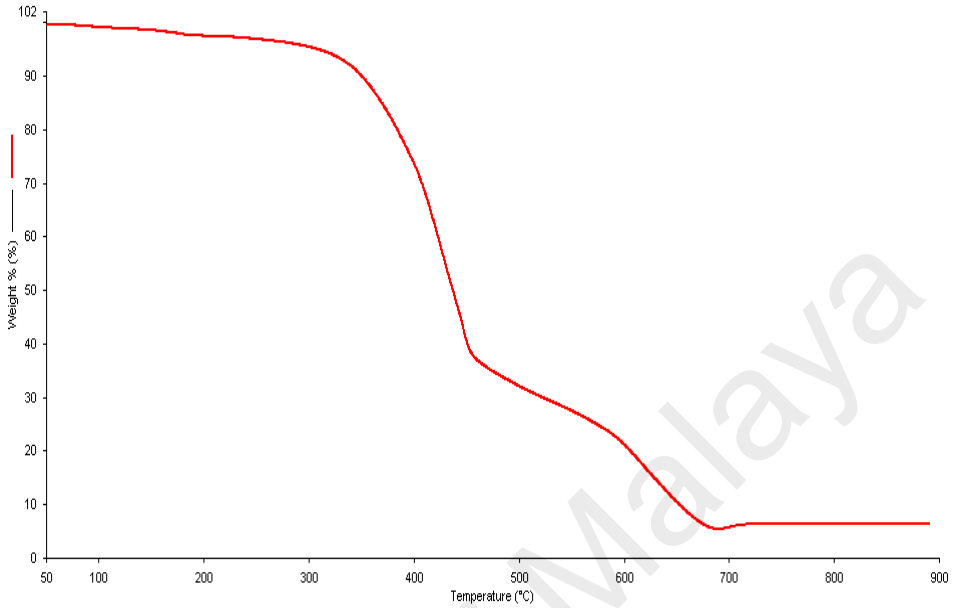

Figure 4.30 TGA trace of **Complex 5**

(e) Thermoelectric properties

Graphs of ΔV *versus* ΔT for **Complex 5 (Figure 4.31)** were linear up to ΔT of about 25 K for all three heating-and-cooling cycles. Its mean S_e value was -0.62 ± 0.01 mV K^{-1} for the heating cycles, and -0.55 ± 0.01 mV K^{-1} for the cooling cycles. Hence, its mean S_e values were similar to **Complex 1** ($[Co_2(CH_3COO)_4(LC8)_2].3H_2O$; S_e = -0.58 ± 0.03 mV K^{-1}). However, its thermoelectric behaviour was better than **Complex 1**. Since both complexes were dimeric and molecular with 100% Co(II) atoms, the better thermoelectric behavior of **Complex 5** may arose from its longer alkyloxy chains, resulting in a more stable micelle-like structures, hence lower dimeric dissociation in $CHCl_3$ at ΔT lower than about 25 K. The higher gradients at above this ΔT value may be due to dimer-monomer equilibrium.

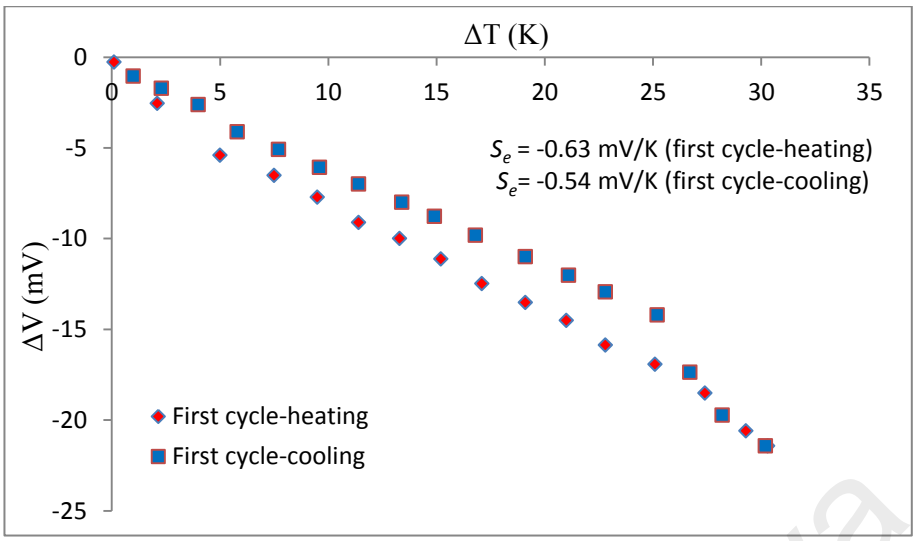

(a)

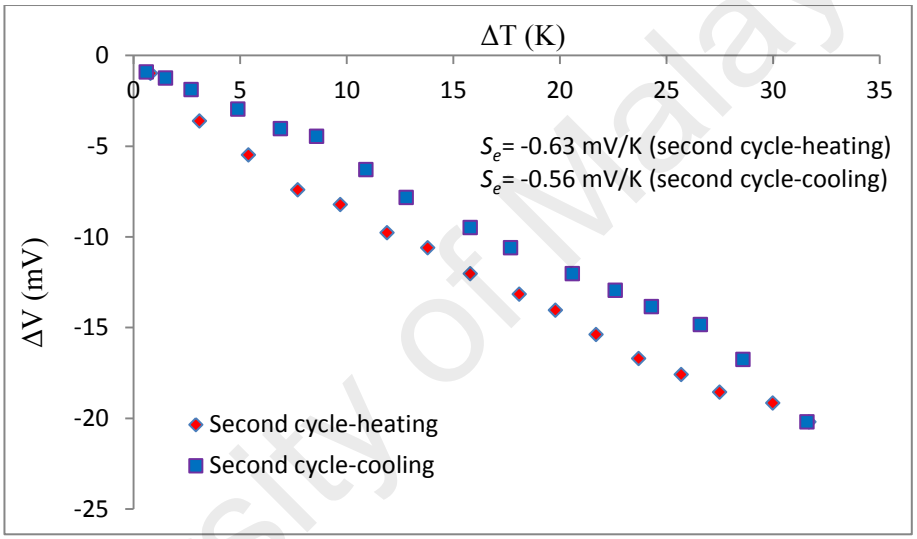

(b)

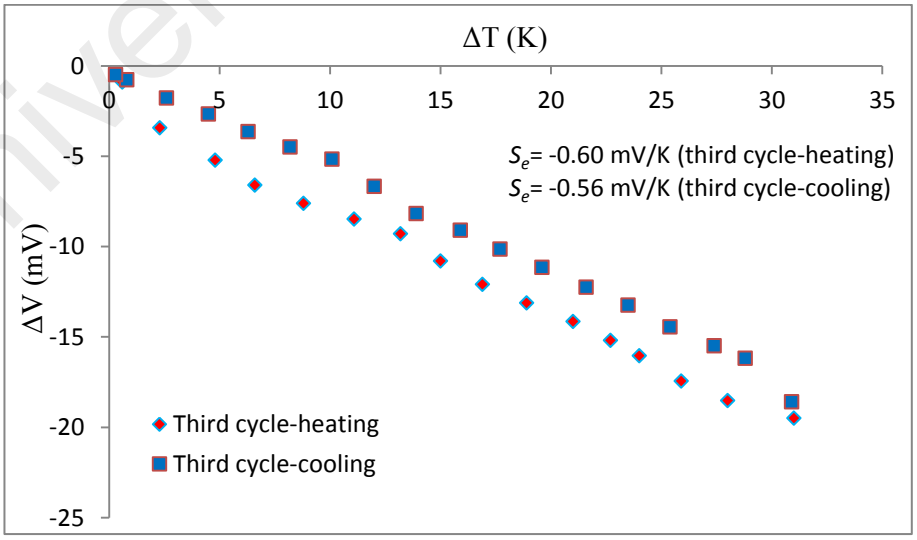

(c)

Figure 4.31 Graphs of ΔV *versus* ΔT for **Complex 5**: (a) first; (b) second; and (c) third heating-and-cooling cycles

4.3.3 $[Fe_2(CH_3COO)_4(LC10)_2].3H_2O$

Ligand LC10 reacted with iron(II) acetate, $Fe(CH_3COO)_2$, in a mole ratio of 1:1 to form a black powder (**Complex 6**), and its yield was 63.0%. Its solubility was similar to the previously discussed complexes.

(a) Deduction of structural formula

The proposed structure of **Complex 6** was deduced from combined instrumental analyses as done before. It is proposed that **Complex 6** ($[Fe_2(CH_3COO)_4(LC10)_2].3H_2O$) has similar structure as **Complex 1** ($[Co_2(CH_3COO)_4(LC8)_2].3H_2O$; **Figure 4.3**).

The result of the **elemental analyses** (70.55% C, 9.08% H, 1.96% N) were in excellent agreement with those calculated for the chemical formula $C_{140}H_{218}Fe_2N_4O_{19}$ (70.86% C, 9.26% H, 2.36% N; formula weight, 2372.9 g mol^{-1}).

Its **FTIR** spectrum **(Figure 4.32)** shows peaks (in cm^{-1}) at 2920, 2852, 1673, 1610, 1595, 1509, 1457, 1391, 1267, 586 and 445 **(Table 4.5)**. These peaks may be similarly assigned as for **Complexes 1** ($[Co_2(CH_3COO)_4(LC8)_2].3H_2O$), **2** ($[Fe_2(CH_3COO)_4(LC8)_2]$) and **5** ($[Co_2(CH_3COO)_4(LC10)_2].H_2O$). The Δ values for CH_3COO^- ligand were 216 cm^{-1} and 118 cm^{-1}, suggesting monodentate bridging and bidentate chelating binding modes, respectively [15, 49].

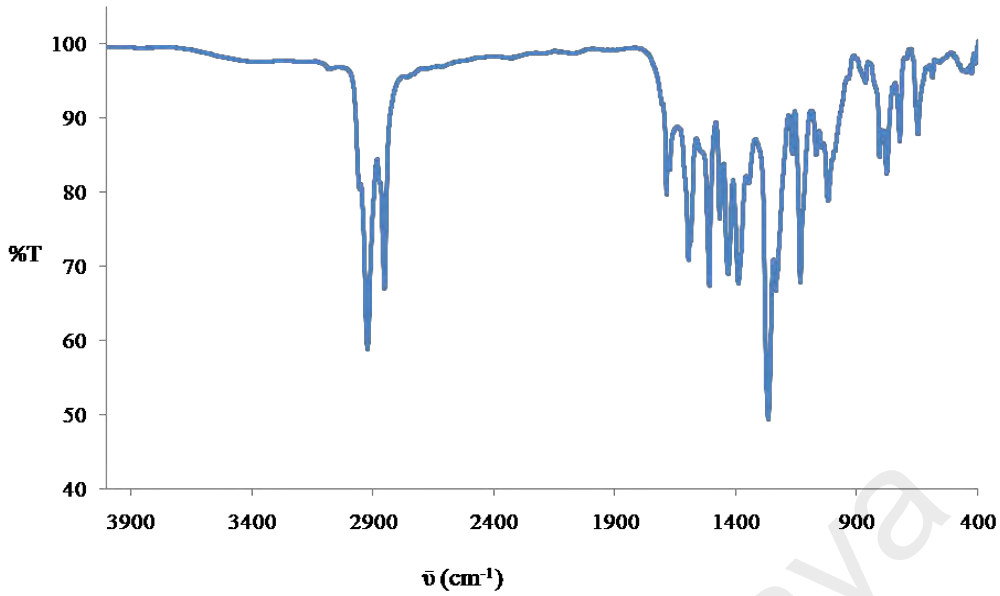

Figure 4.32 FTIR spectrum of **Complex 6**

Its **UV-vis** spectrum recorded in $CHCl_3$ **(Figure 4.33;** 4.2 x 10^{-4} mol dm^{-3}**)** shows a weak *d-d* band which appeared as a shoulder at about 640 nm (ε_{max}, 4.0 x 10^2 M^{-1} cm^{-1}) and three MLCT bands at 571 nm (ε_{max}, 1.5 x 10^3 M^{-1} cm^{-1}), 381 nm (ε_{max}, 6.8 x 10^3 M^{-1} cm^{-1}) and 312 nm (ε_{max}, 7.1 x 10^3 M^{-1} cm^{-1}). The *d-d* band may be assigned for $^1A_{1g} \rightarrow {}^1T_{1g}$ electronic transition for LS Fe(II) complex [76]. The spectrum did not show distinct peak for *d-d* bands due to the hidden under MLCT bands and it is mainly LS in the solution.

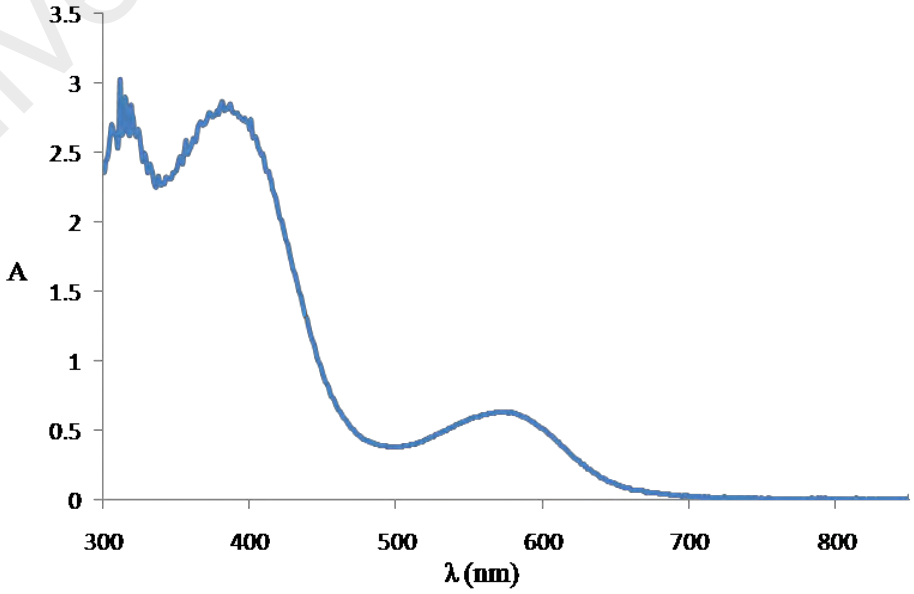

Figure 4.33 UV-vis spectrum of **Complex 6**

(b) Band gap

Its E_o value, similarly calculated as for previously discussed complexes, was 1.90 eV (λ_{onset} = 650 nm). The value was similar as **Complex 2** ($[Fe_2(CH_3COO)_4(LC8)_2]$; E_o = 1.87 eV).

Its **CV** scan **(Figure 4.34)** shows overlapping anodic peaks at +0.86 V, assigned to the oxidation of [Fe(II)Fe(II)] to [Fe(II)Fe(III)], [Fe(II)] to [Fe(III)] and LC10 to $LC10^+$, as a result of the dissociation of dimer. These were followed by and three cathodic peaks at -0.10 V, -0.70 V and -0.90 V, assigned to the reduction of [Fe(II)Fe(III)] to [Fe(II)Fe(II)], [Fe(III)] to [Fe(II)] and $LC10^+$ to LC10, respectively. Accordingly, the metal-based ΔE_p was 960 mV, suggesting a quasireversible redox reaction [68]. Hence, its redox behaviour was similar to **Complex 2**.

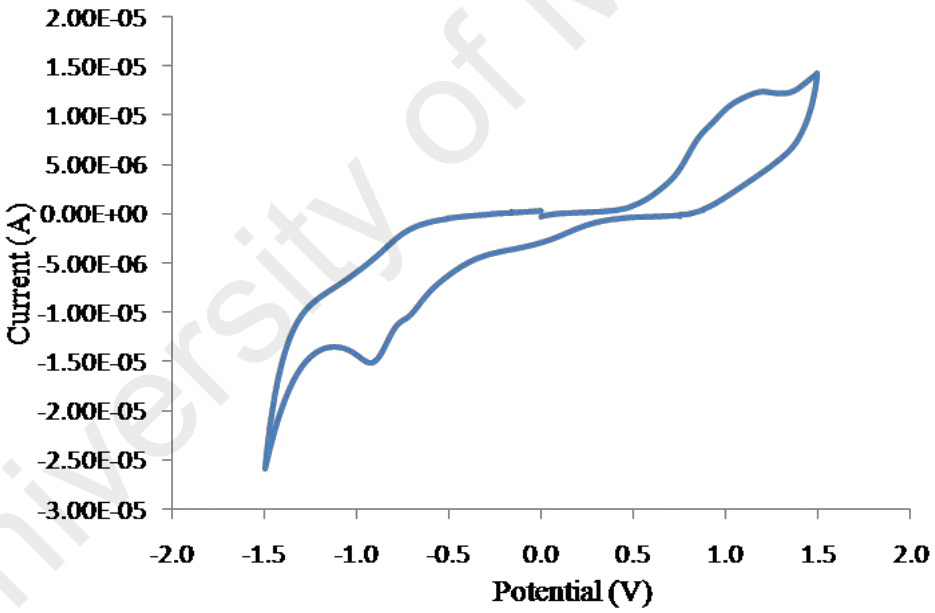

Figure 4.34 Cyclic voltammetry of **Complex 6**

Its E_e, similarly calculated as previously done from onset potentials for oxidation (+0.74 V) and reduction (+0.25 V), the values for E_{HOMO} (5.14 eV) and E_{LUMO} (4.65 eV), was 0.49 eV. This value was similar to **Complex 2** ($[Fe_2(CH_3COO)_4(LC8)_2]$; E_e = 0.45 eV).

(c) Magnetic properties

The value of $\chi_M T$ of **Complex 6,** calculated from its proposed chemical formula (FW = 2372.9 g mol^{-1}), χ_g (6.99 x 10^{-6} cm^3 g^{-1}), χ_M (1.68 x 10^{-2} cm^3 mol^{-1}), χ_D (-1.56 x 10^{-3} cm^3 mol^{-1}) and χ_M^{corr} (1.82 x 10^{-2} cm^3 mol^{-1}), was 5.46 cm^3 K mol^{-1} at 298 K. Accordingly, this complex was made up of 91.0% of HS and 9.0% of LS Fe(II) at this temperature. Hence, it has a higher percentage of HS Fe(II) atom compared to **Complex 2** ($[Fe_2(CH_3COO)_4(LC8)_2]$; 71.0% HS, 29.0% LS), indicating weaker Fe-N and Fe-O coordinate bonds in the former complex in solid state.

(d) Thermal properties

Its **TGA** trace **(Figure 4.35)** shows that the complex was thermally stable up to 172 ^oC. It suffered a total mass loss of 92.8% from 172 ^oC to 787 ^oC due to the decomposition of CH_3COO^- ions and LC10 (calculated, 94.0%). The amount of residue at temperatures above 787 ^oC was 7.2% (calculated, 6.0 %, assuming pure FeO). Therefore, the data was in good agreement with its proposed structure. It is noted the thermal stability of **Complex 6** (T_{dec} = 172 ^oC) was similar to **Complex 2** ($[Fe_2(CH_3COO)_4(LC8)_2]$; T_{dec} = 175 ^oC). Therefore, the thermal stability of these complexes was independent on the chain length of the ligand.

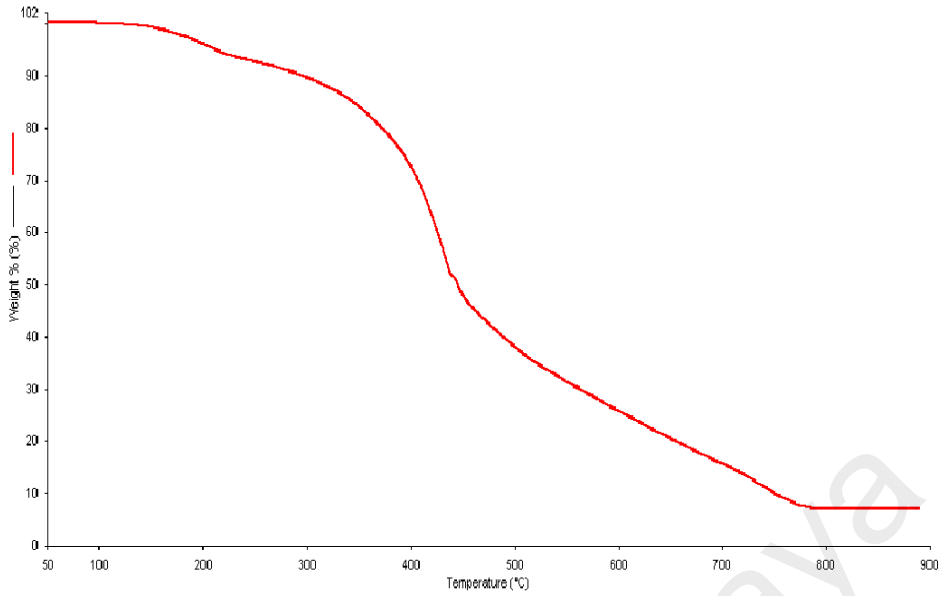

Figure 4.35 TGA trace of **Complex 6**

(e) Thermoelectric properties

Graphs of ΔV *versus* ΔT for **Complex 6** (**Figure 4.36)** were linear for all three heating-and-cooling cycles, indicating a good thermoelectric behaviour. Its mean S_e value was -0.56 ± 0.02 mV K^{-1}. Hence, its S_e value and thermoelectric behavior were similar to **Complex 2** (-0.51 ± 0.01 mV K^{-1}), and may be similarly explained. This is consistent with their similar structures and spin states (both complexes have higher percentages of HS Fe(II) atoms).

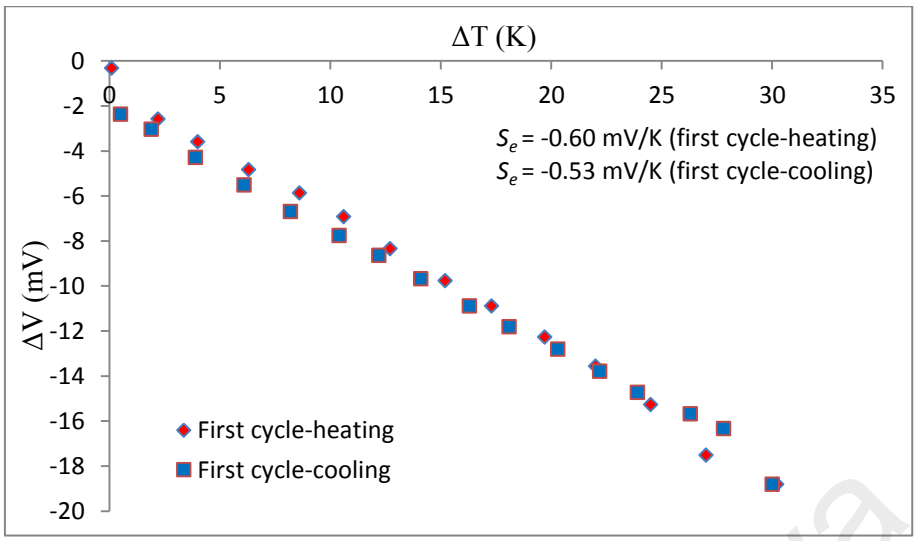

(a)

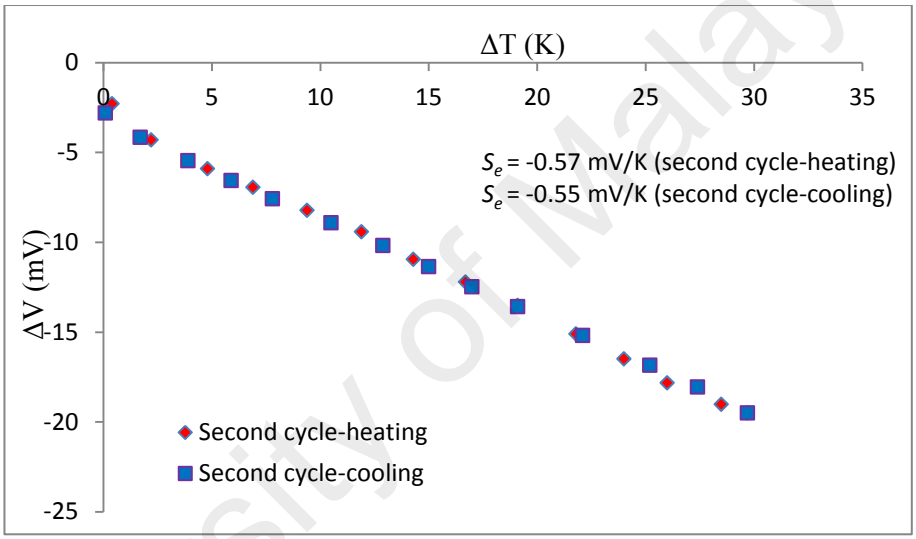

(b)

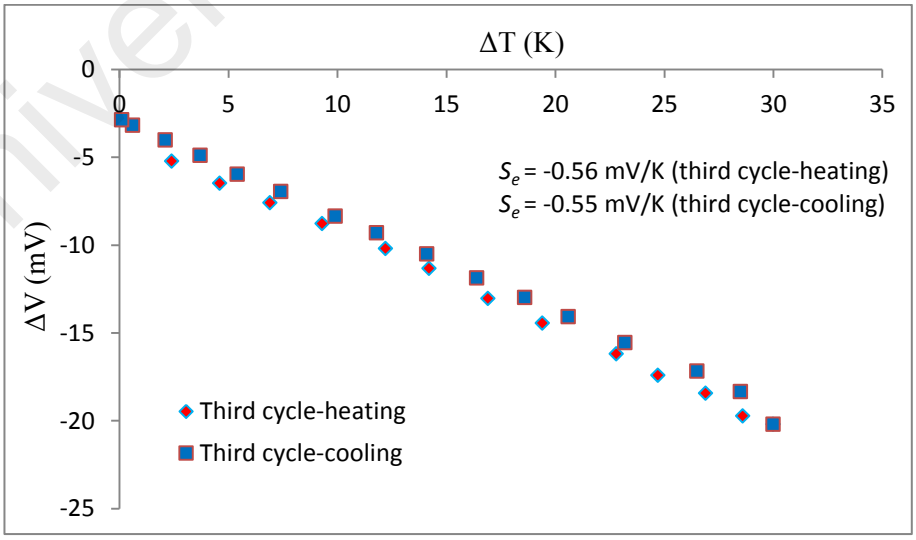

(c)

Figure 4.36 Graphs of ΔV *versus* ΔT for **Complex 6**: (a) first; (b) second; and (c) third heating-and-cooling cycles

4.3.4 $[Co(LC10)_3](BF_4)_2.4H_2O$

Cobalt(II) tetrafluoroborate hexahydrate, $Co(BF_4)_2.6H_2O$, reacted with LC10 in a mole ratio of 1:3 to form a dark red powder (**Complex 7**), and its yield was 84.0%. Its solubility was similar as the previously discussed complexes.

(a) Deduction of structural formula

Based on combined results of elemental analyses, FTIR spectroscopy and UV-vis spectroscopy discussed below, it is proposed that the structure of **Complex 7** ($[Co(LC10)_3](BF_4)_2.4H_2O$) was similar to **Complex 3** ($[Co(LC8)_3](BF_4)_2.2H_2O$; **Figure 4.14**).

The results of its **elemental analyses** (72.79% C, 9.31% H, 2.71% N) were in excellent agreement with those calculated for the chemical formula $C_{198}H_{308}B_2CoF_8N_6O_{16}$ (72.92% C, 9.52% H, 2.58% N; formula weight, 3261.1 g mol^{-1}).

Its **FTIR** spectrum **(Figure 4.37)** shows peaks (in cm^{-1}) indicating the presence of the expected functional groups at 2921, 2853, 1609, 1589, 1031, and 557 **(Table 4.5)**. These peaks may be similarly assigned as for **Complex 3** ($[Co(LC8)_3](BF_4)_2.2H_2O$)**.**

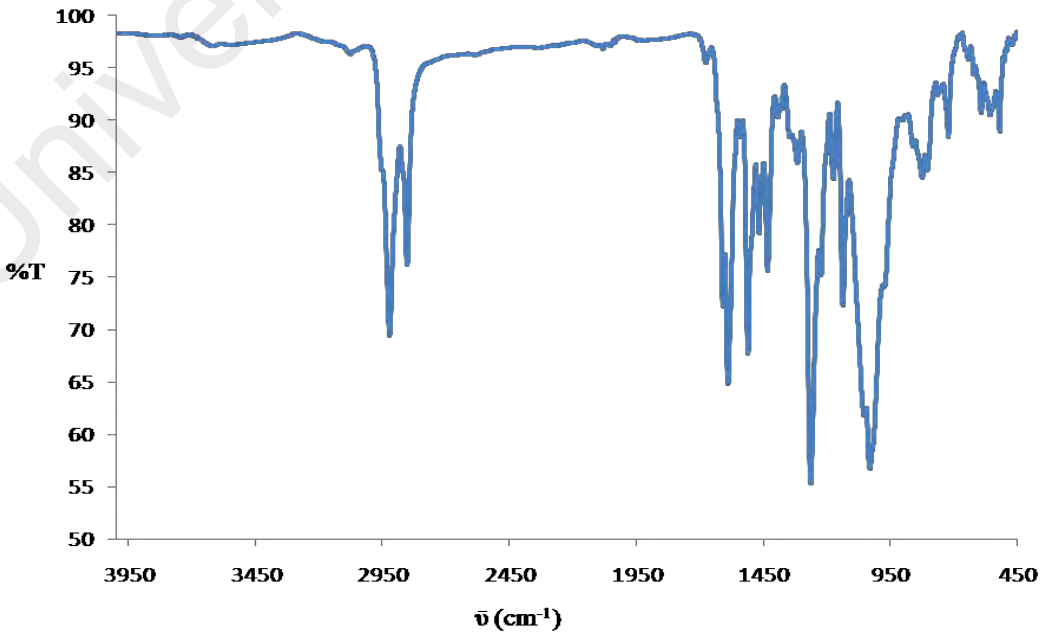

Figure 4.37 FTIR spectrum of **Complex 7**

Its **UV-vis** spectrum in $CHCl_3$ **(Figure 4.38)** shows a weak *d-d* band at 1202 nm (ε_{max}, 6.8 M^{-1} cm^{-1}; inset) and a broad MLCT band at 445 nm (ε_{max}, 1.4 x 10^4 M^{-1} cm^{-1}). The electronic transition may be similarly assigned as **Complexes 1** ($[Co_2(CH_3COO)_4(LC8)_2].3H_2O$) and **5** ($[Co_2(CH_3COO)_4(LC10)_2].H_2O$). The molarities of the solutions were 1.6 x 10^{-2} mol dm^{-3} for the *d-d* band and 2.8 x 10^{-5} mol dm^{-3} for the MLCT bands.

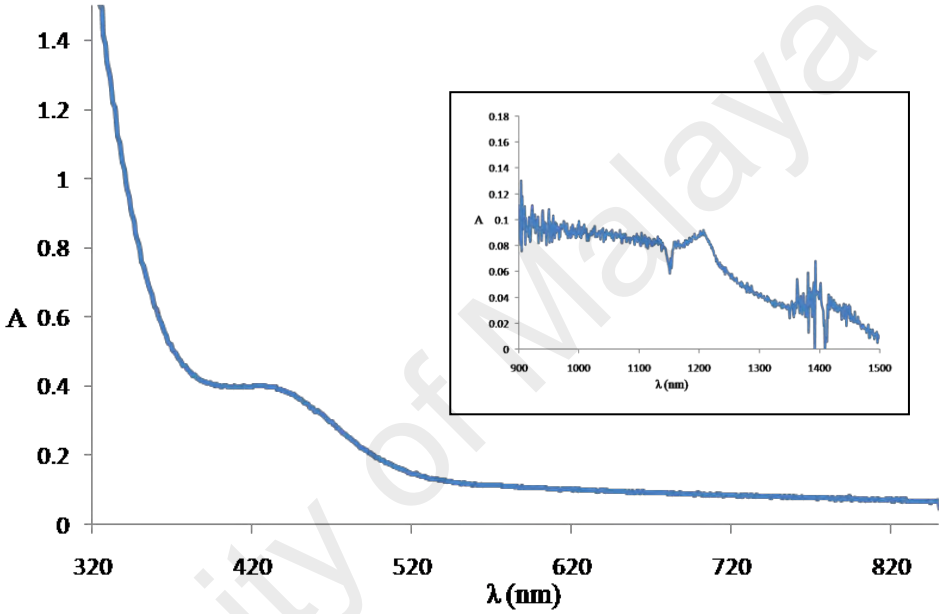

Figure 4.38 UV-vis spectrum of **Complex 7**

(b) Band gap

Its E_o value, calculated similarly as before, was 2.43 eV (λ_{onset} = 510 nm). This value was similar as **Complex 3** ($[Co(LC8)_3](BF_4)_2.2H_2O$; E_o = 2.33 eV).

Its **CV**scan **(Figure 4.39)** shows two overlapping anodic peaks at +0.85 V and +1.20 V, assigned as oxidation of [Co(II)] to [Co(III)] and LC10 to $LC10^+$, respectively. This was followed by two cathodic peaks at +0.15V and -1.05 V, assigned as reduction of [Co(III)] to [Co(II)] and $LC10^+$ to LC10, respectively. Accordingly, the metal-based ΔE_p was 700 mV, suggesting a quasireversible redox reaction [68]. Hence, its redox behaviour was similar to **Complex 3**.

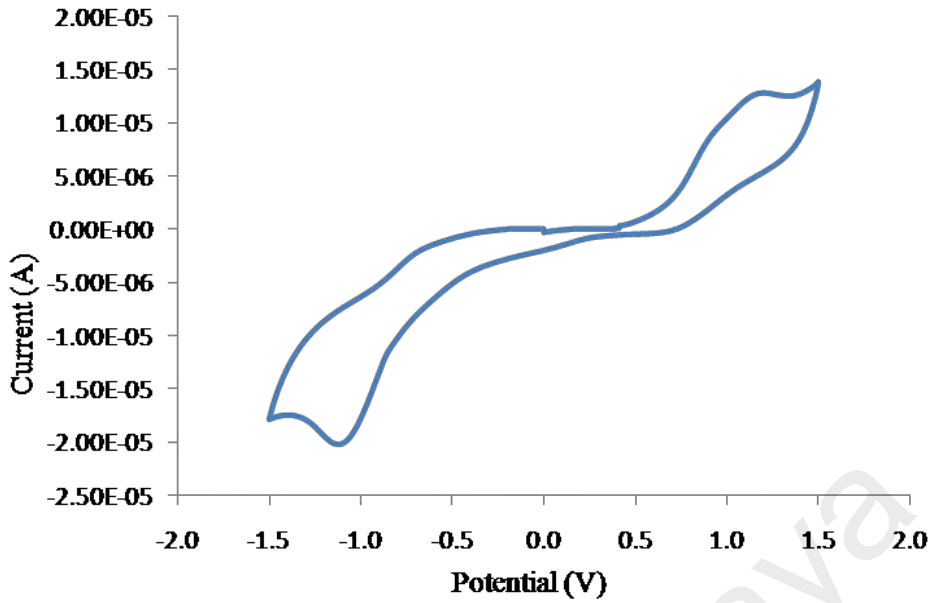

Figure 4.39 Cyclic voltammetry of **Complex 7**

Its E_e value, similarly calculated as previously done from the onset potentials for oxidation (+0.67 V) and reduction (+0.30 V), the values for E_{HOMO} (5.07 eV) and E_{LUMO} (4.70 eV), was 0.37 eV. This value was similar to **Complex 3** ($[Co(LC8)_3](BF_4)_2.2H_2O$; E_e = 0.35 eV), may be similarly explained.

(c) Magnetic properties

The $\chi_M T$ value for **Complex 7**, calculated from its proposed chemical formula (FW = 3261.1 g mol^{-1}), χ_g (1.10 x 10^{-6} cm^3 g^{-1}), χ_M (3.59 x 10^{-3} cm^3 mol^{-1}), χ_D (-2.28 x $10^{-3}$$cm^3$ mol^{-1}) and χ_M^{corr} (5.87 x 10^{-3} cm^3 mol^{-1}), was 1.76 cm^3 K mol^{-1} at 298 K. Accordingly, the complex was made up of 92.3% HS and 7.7% LS Co(II) atoms at this temperature. Hence, the complex has a lower percentage of HS Co(II) compared to **Complex 3** ($[Co(LC8)_3](BF_4)_2.2H_2O$; 100% HS). This suggests a stronger Co-N bond in the former complex.

(d) Thermal properties

Its **TGA** trace **(Figure 4.40)** shows that the complex suffered a total mass loss of 95.0% in the temperature range of 260 ^oC – 831 ^oC due to the loss of BF_3 (from BF_4^- ions) and decomposition of LC10 (calculated, 96.9%). The amount of residue at temperatures

above 831 ^{o}C was 5.0% (calculated, 3.1%; assuming pure CoF_2 [73]). Hence, its decomposition temperature was 260 ^{o}C, which was similar to **Complex 3** ($[Co(LC8)_3](BF_4)_2.2H_2O$; T_{dec} = 265 ^{o}C).

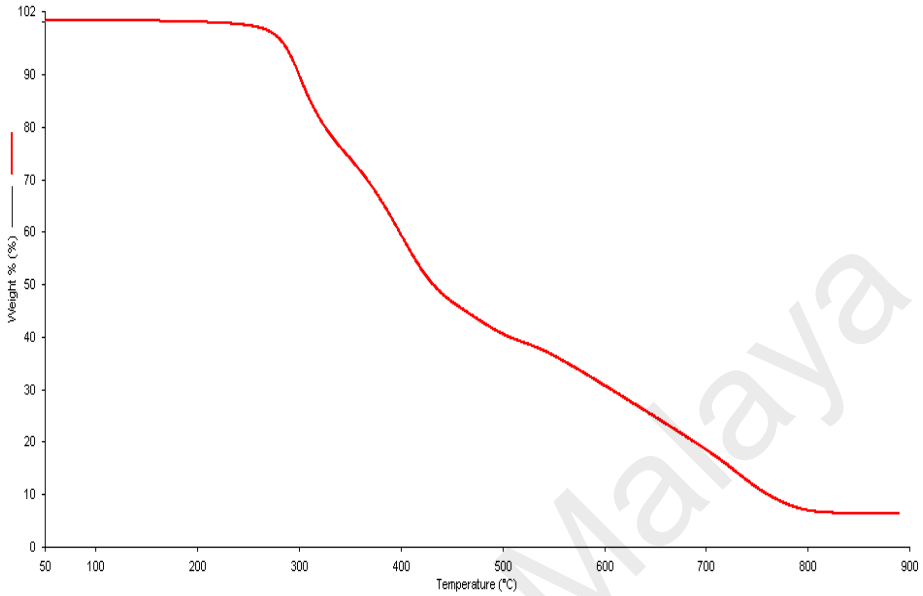

Figure 4.40 TGA trace of **Complex 7**

(e) Thermoelectric properties

It is noted that its graphs of ΔV *versus* ΔT in the heating cycles were less satisfactory than in the cooling cycles (**Figure 4.41**). Its mean S_e value, calculated for the cooling cycles only, was -0.40 ± 0.01 mV K^{-1}. Hence, its S_e value and thermoelectric behaviour were similar to **Complex 3** ($[Co(LC8)_3](BF_4)_2.2H_2O$; S_e = -0.45 ± 0.01 mV K^{-1}), and may be similarly explained. This is consistent with their similar structures and spin states (both complexes have higher percentages of HS Co(II) atoms).

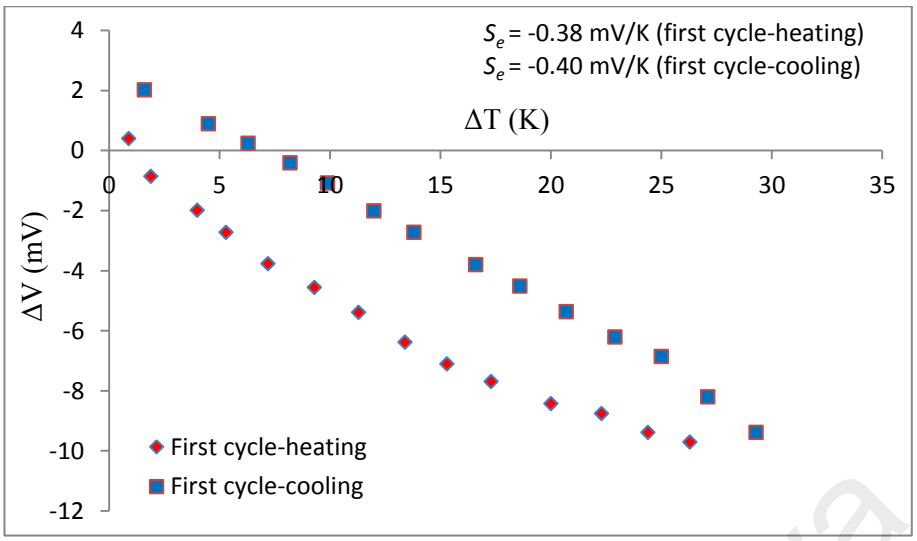

(a)

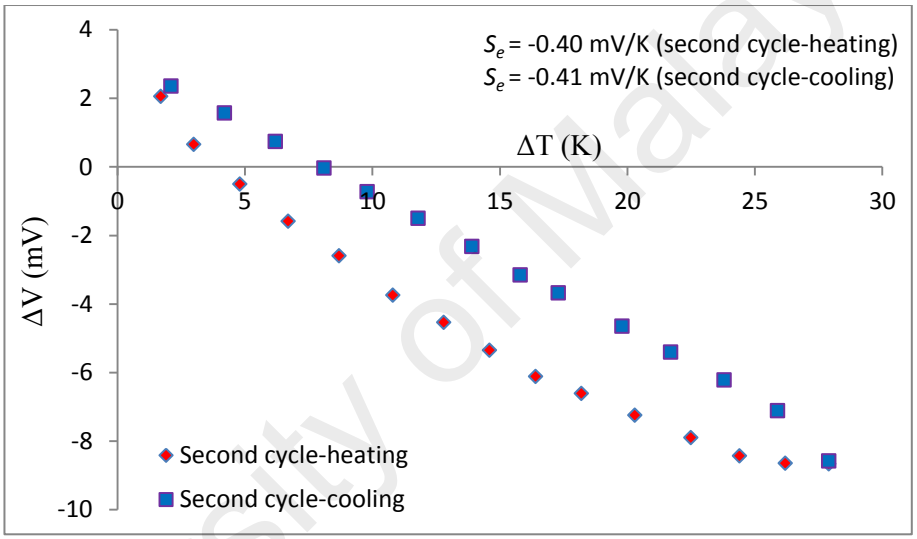

(b)

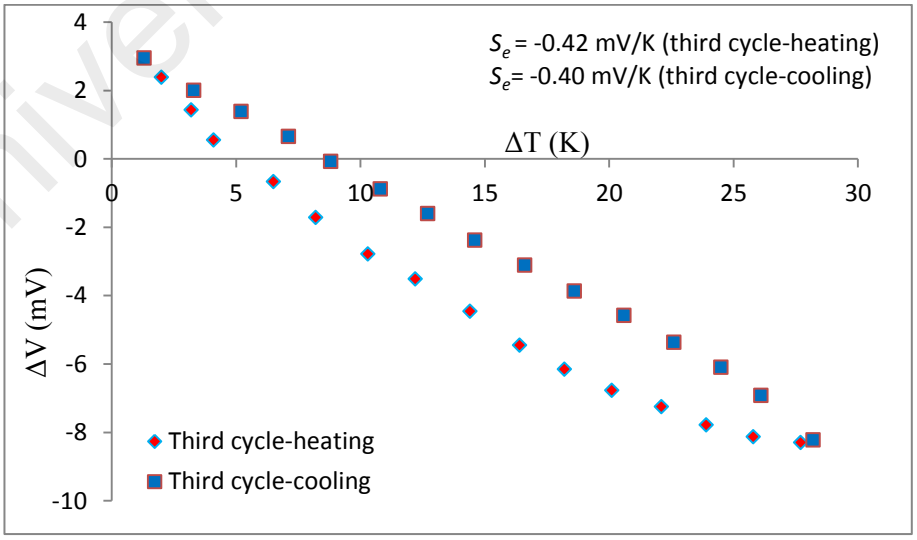

(c)

Figure 4.41 Graphs of ΔV *versus* ΔT for **Complex 7**: (a) first; (b) second; and (c) third heating-and-cooling cycles

4.3.5 [Fe(LC10)$_3$](BF$_4$)$_2$.3H$_2$O

Iron(II) tetrafluoroborate hexahydrate, $Fe(BF_4)_2.6H_2O$, reacted with LC10 in a mole ratio of 1:3 to form a black powder (**Complex 8**), and its yield was 96.2%. Its solubility was similar to the previously discussed complexes.

(a) Deduction of structural formula

Based on combined analytical data discussed below, it is proposed that the structural formula for **Complex 8** was $[Fe(LC10)_3](BF_4)_2.3H_2O$, which was similar as **Complex 3** ($[Co(LC8)_3](BF_4)_2.2H_2O$; **Figure 4.14**).

The results of the **elemental analyses** (73.12% C, 9.84% H, 2.85% N) were in a good agreement with those calculated for the chemical formula $C_{198}H_{306}B_2F_8FeN_6O_{15}$ (73.40% C, 9.52% H, 2.59% N; formula weight: 3240.0 g mol^{-1}).

Its **FTIR** spectrum **(Figure 4.42)** shows peaks (in cm^{-1}) indicating the presence of the expected functional groups at 2921, 2852, 1609, 1592, 1051 and 544 (**Table 4.5**). These peaks may be similarly assigned as for **Complex 3** ($[Co(LC8)_3](BF_4)_2.2H_2O$)**.**

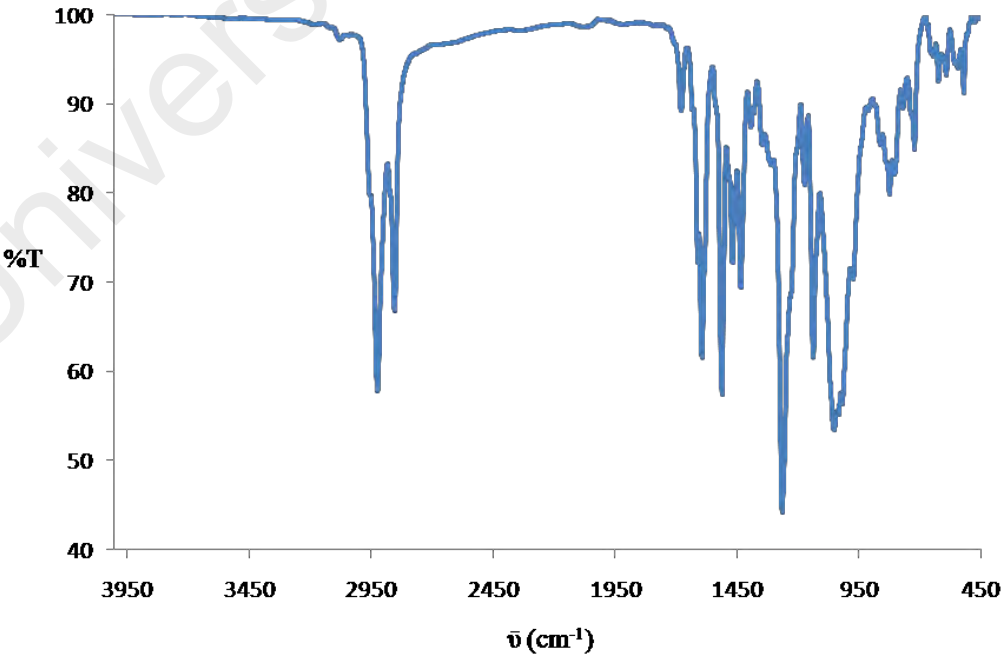

Figure 4.42 FTIR spectrum of **Complex 8**

Its **UV-vis** spectrum in $CHCl_3$ **(Figure 4.43)** shows a weak *d-d* band at 1192 nm (ε_{max}, 6.2 M^{-1} cm^{-1}; inset), and a broad MLCT peak at 570 nm (ε_{max}, 3.7 x 10^4 M^{-1} cm^{-1}). These electronic transitions may be similarly assigned as for **Complex 4** ($[Fe(LC8)_3](BF_4)_2.H_2O$). The molarities of the solutions were 6.2 x 10^{-3} mol dm^{-3} for the *d-d* band and 5.9 x 10^{-5} mol dm^{-3} for the MLCT bands.

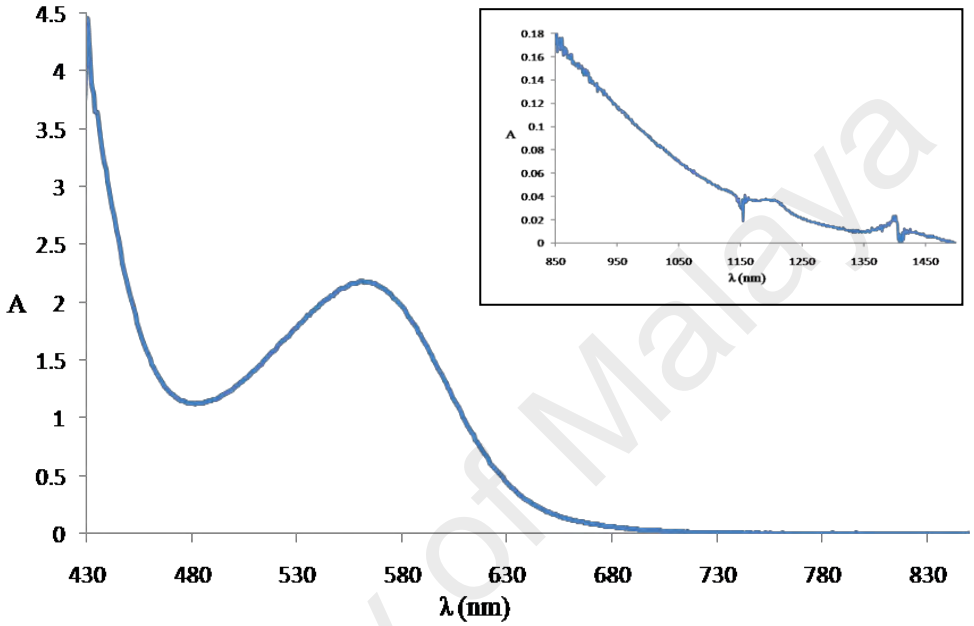

Figure 4.43 UV-vis spectrum of **Complex 8**

(b) Band gap

The $E_o$value for **Complex 8**, similarly calculated as previous discussed complexes, was 1.93 eV (λ_{onset} = 650 nm). This value was similar to **Complex 4** ($[Fe(LC8)_3](BF_4)_2.H_2O$; E_o = 1.90 eV).

Its **CV** scan **(Figure 4.44)** shows two overlapping anodic peaks at +0.80 V and +1.10 V, assigned as oxidation of [Fe(II)] to [Fe(III)] and LC10 to $LC10^+$, respectively. These were followed by two reduction peaks at +0.20 V and -0.95 V, assigned to reduction of [Fe(III)] to [Fe(II)] and $LC10^+$ to LC10, respectively. Accordingly, the metal-based ΔE_p was 600 mV, indicating a quasireversible redox reaction [68]. Hence, its redox behaviour was similar to **Complex 4** ($[Fe(LC8)_3](BF_4)_2.H_2O$).

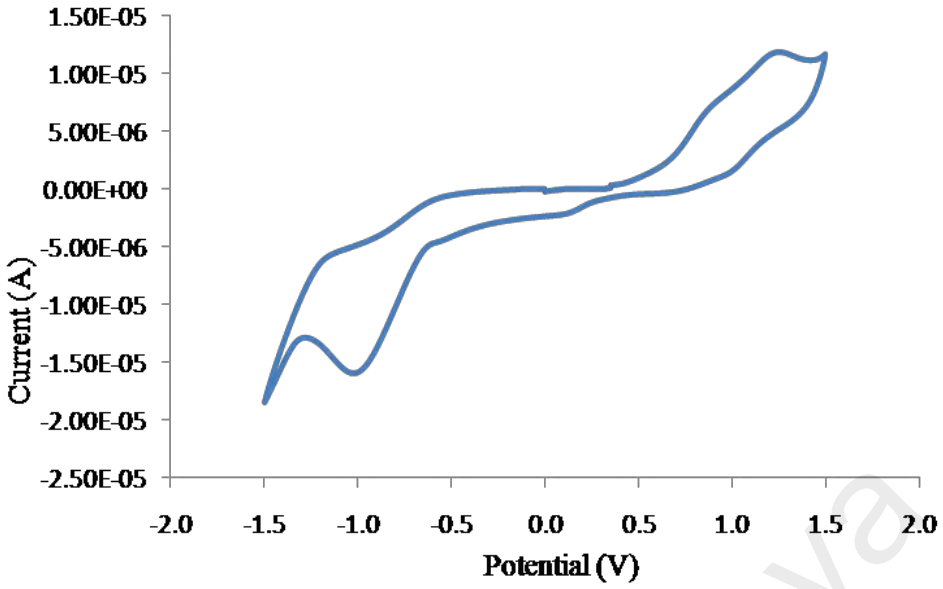

Figure 4.44 Cyclic voltammetry of **Complex 8**

Its E_e value, similarly calculated as previously done from the onset potentials for oxidation (+0.65 V) and reduction (+0.30 V), the values for E_{HOMO} (5.05 eV) and E_{LUMO} (4.70 eV), was 0.35 eV. This value was similar to **Complex 4** ($[Fe(LC8)_3](BF_4)_2.H_2O$; E_e = 0.33 eV), and may be similarly explained.

(c) Magnetic properties

The χ_g value for **Complex 8** was -2.7 x 10^{-7} cm^3 g^{-1} at room temperature. The negative value means that the complex was diamagnetic. Hence, it was made up of 100% LS Fe(II) atom at room temperature, as similarly found and explained for **Complex 4** ($[Fe(LC8)_3](BF_4)_2.H_2O$).

(d) Thermal properties

Its **TGA** trace **(Figure 4.45)** shows it suffered a total mass loss of 93.9% from the 259 ^oC to 887 ^oC due to the loss of BF_3 (from BF_4^- ions) and decomposition of LC10 (calculated, 97.0%). However, the amount of residue could not be calculated as there was no plateau in this thermogram at temperatures above 887 ^oC (instrumental limitation). Hence, the decomposition temperature of **Complex 8** was 259 ^oC, which was similar to **Complex 4** ($[Fe(LC8)_3](BF_4)_2.H_2O$; T_{dec} = 265 ^oC).

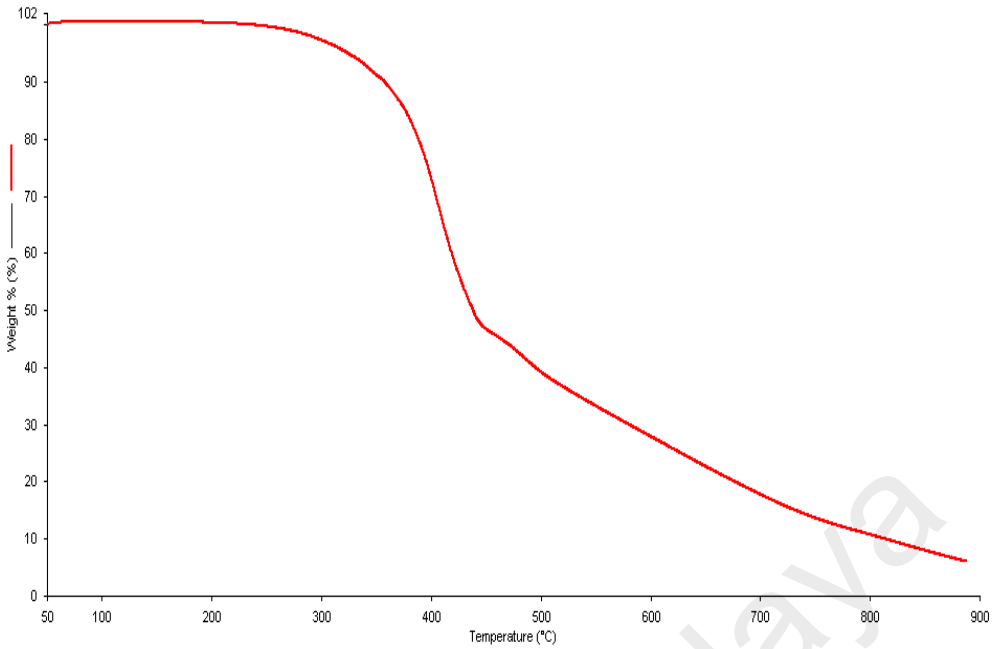

Figure 4.45 TGA trace of **Complex 8**

(e) Thermoelectric properties

Graphs of ΔV *versus* ΔT for **Complex 8** (**Figure 4.46)** were linear, indicating good thermoelectric behaviour for all three heating-and-cooling cycles. Its mean S_e value was -0.51 ± 0.01 mV K^{-1}, which was similar to **Complex 4** (S_e = -0.57 ± 0.01 mV K^{-1}), and may be similarly explained. However, its thermoelectric behaviour was better than **Complex 4**, which showed good thermoelectric behaviour on heating cycles only. Since both complexes were mononuclear and ionic with 100% LS Fe(II) atoms, the better thermoelectric behavior of **Complex 8** may arose from its longer alkyloxy chains, resulting in a more stable micelle-like structures, as similarly suggested for **Complex 5**.

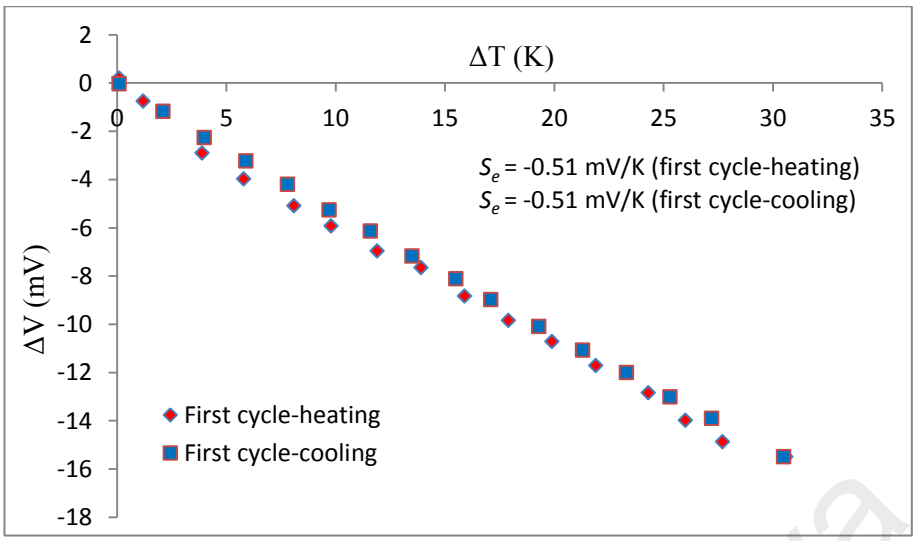

(a)

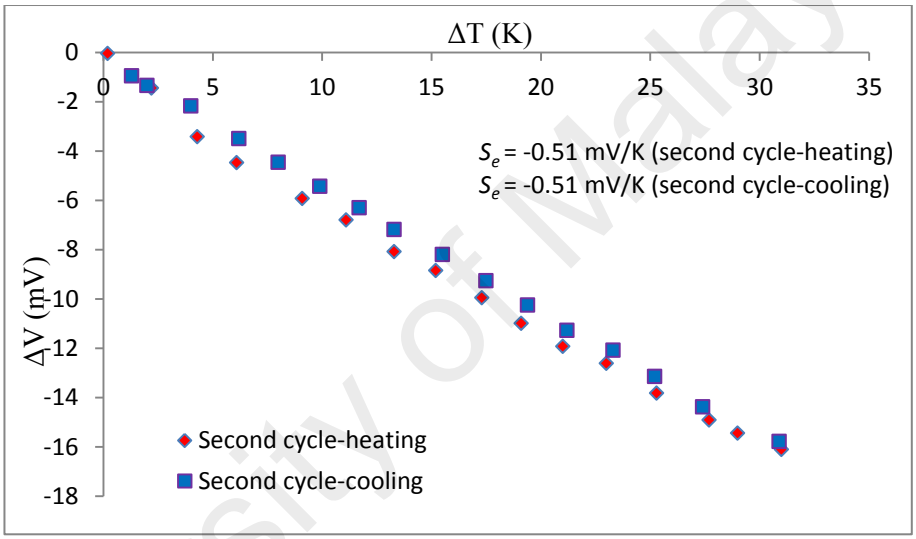

(b)

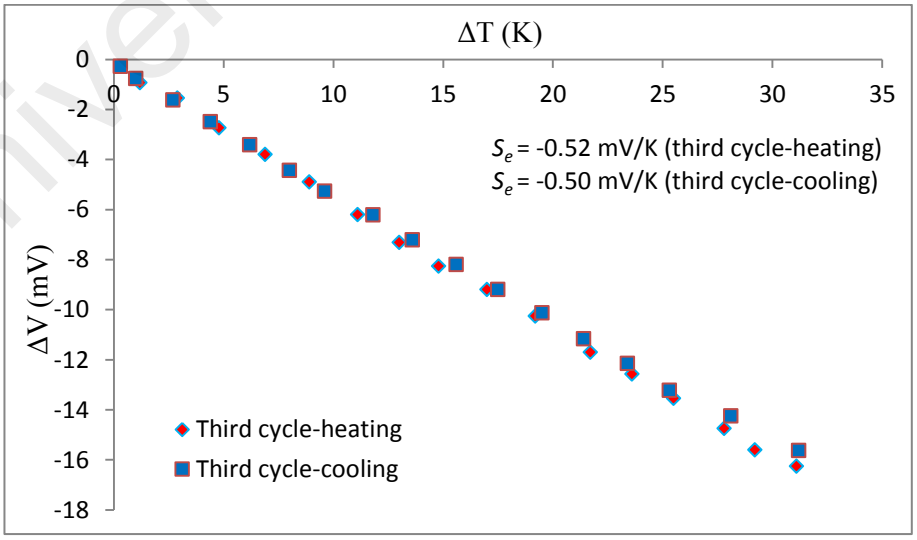

(c)

Figure 4.46 Graphs of ΔV *versus* ΔT for **Complex 8**: (a) first; (b) second; and (c) third heating-and-cooling cycles

4.3.6 Summary

The results from the analytical data for **Complexes 5 – 8** are summarised in **Table 4.6**. These results were similar with those for **Complexes 1 – 4 (Table 4.3)** and may be similarly explained. However, **Complexes 5 – 8** showed better thermoelectric behaviours due to the presence of longer alkyloxy chains in their bipyridyl ligands, resulting in more stable micelle-like structures in $CHCl_3$.

Table 4.6 Summary of results for **Complexes 5 - 8**

Chemical Formula	**Band gap (eV)**		**$\chi_M^{corr}T$ (cm^3 K mol^{-1})**	**T_{dec} C**	***S_e*** **(mV K^{-1})**
	E_o	***E_e***			
$[Co_2(CH_3COO)_4(LC10)_2].H_2O$ **(Complex 5)**	2.61	0.55	3.81 100% HS	178	-0.61 ± 0.01 (heat) -0.55 ± 0.01 (cool)
$[Fe_2(CH_3COO)_4(LC10)_2].3H_2O$ **(Complex 6)**	1.90	0.49	5.46 91.0% HS	172	-0.56 ± 0.02
$[Co(LC10)_3](BF_4)_2.4H_2O$ **(Complex 7)**	2.43	0.37	1.76 92.3% HS	260	-0.40 ± 0.01 (cool)
$[Fe(LC10)_3](BF_4)_2.3H_2O$ **(Complex 8)**	1.93	0.35	diamagnetic 100% LS	259	-0.51 ± 0.01

4.4 Ligand LC12 and its Cobalt(II) and Iron(II) complexes

4.4.1 Ligand LC12

The steps involved in the synthesis of LC12 were similar to the previously discussed ligands, as shown in **Scheme 1.1**. It was obtained as a white powder, and its yield was 82.5%. The structure of LC12 was ascertained from the results of elemental analyses, ^{1}H-NMR spectroscopy and FTIR spectroscopy, discussed below.

The result of **elemental analyses** (80.51% C, 10.27% H, 2.07% N) were in a good agreement with those calculated for the chemical formula $C_{74}H_{116}N_2O_4$ (80.97% C, 10.65% H, 2.55% N; formula weight: 1097.7 g mol^{-1}).

Its **^{1}H-NMR** spectrum **(Figure 4.47)** shows peaks (in ppm) at 0. 8 (triplet, CH_3, 12 H), 1.2 - 1.9 (multiplet, CH_2, 80 H), 4.0 (triplet, O-CH_2-, 8 H), 6.8 - 7.5 (multiplet, aromatic C-H and HC=CH, 12 H), 8.6 (singlet, aromatic C-H, 2 H), 8.7 (doublet, aromatic C-H, 2 H). The peaks assignments are shown in **Table 4.7**.

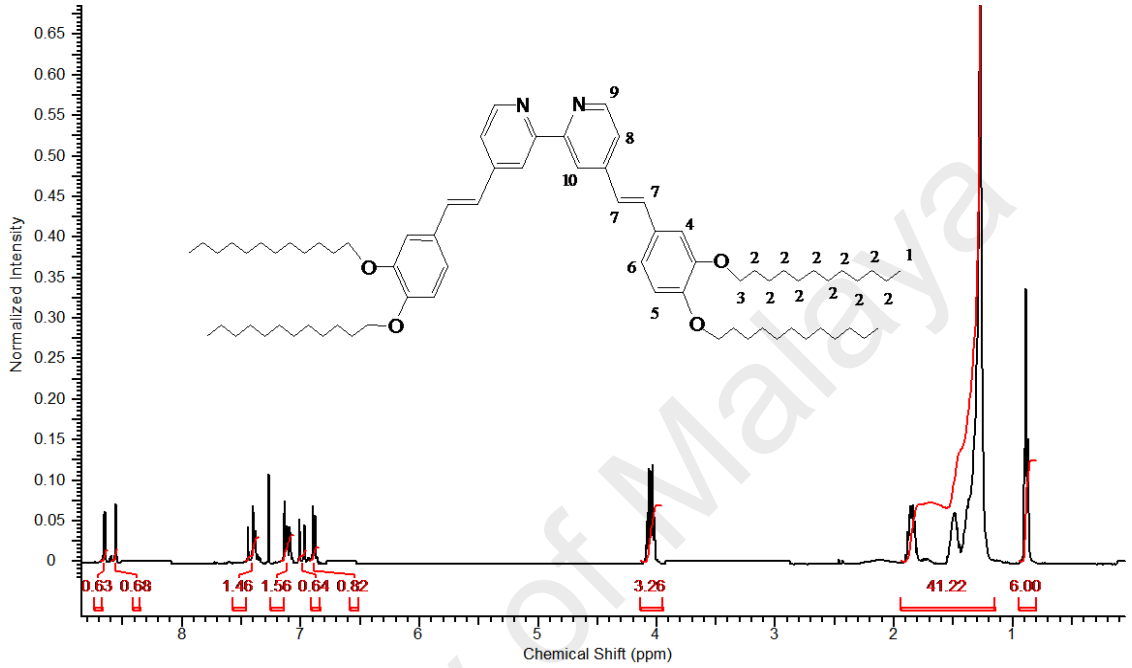

Figure 4.47 ^{1}H-NMR spectrum of LC12

Table 4.7 The ^{1}H-NMR peak assignments of LC12

Chemical shift (ppm)	**Integral**	**Multiplicity**	**Assignment**
0.8	6.00	Triplet	H-1
1.2 - 1.9	41.22	Multiplet	H-2
4.0	3.26	Triplet	H-3
6.8 - 7.5	4.48	Multiplet	H-4, H-5, H-6, H-7, H-8
8.6	0.68	Singlet	H-10
8.7	0.63	Doublet	H-9

Its **FTIR** result shows the presence of the expected functional groups. The peak assignments are shown in **Table 4.8** (which also includes peaks for the corresponding

metal(II) complexes for later discussion). The spectrum **(Figure 4.48)** shows expected peaks (cm^{-1}) at 2917, 2849, 1669, 1589 and 1269. These peaks are similarly assigned as for LC8.

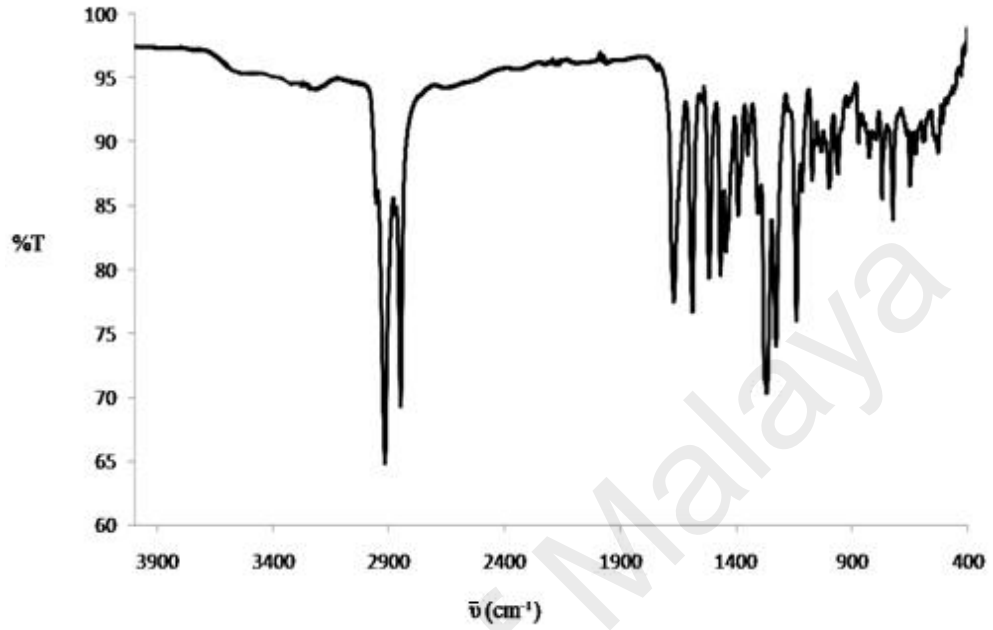

Figure 4.48 FTIR spectrum of LC12

Table 4.8 The FTIR data (in cm^{-1}) of LC12 and its metal complexes

	Assignment								
	CH_2 (asym)	CH_2 (sym)	C=N	C=C (ar)	COO (asym)	COO (sym)	BF_4^-	M-N	M-O
LC12	2917s	2849s	1669m	1589m	-	-	-	-	-
9	2920s	2851m	1610m	1591s	1686w 1511s	1467m 1392m	-	550w	480w
10	2921s	2852m	1608m	1592s	1630m 1509s	1431m 1380m	-	543w	475w
11	2921s	2852m	1607s	1591s	-	-	1052s, br	549w	-
12	2919s	2849s	1609m	1594m	-	-	1057m,br	590w	-

s = strong; m = medium; w = weak; br = broad

4.4.2 $[Co_2(CH_3COO)_4(LC12)_2].2H_2O$

Ligand LC12 reacted with cobalt(II) acetate tetrahydrate, $Co(CH_3COO)_2.4H_2O$, in a mole ratio 1:1, to form a dark yellow powder (**Complex 9**), and its yield was 70.2%. Its solubility was similar to the previously discussed complexes.

(a) Deduction of structural formula

According to the elemental analyses data, FTIR spectroscopy and UV-vis spectroscopy, the proposed structure for **Complex 9** was $[Co_2(CH_3COO)_4(LC12)_2].2H_2O$, which was similar to **Complex 1** ($[Co_2(CH_3COO)_4(LC8)_2].3H_2O$; **Figure 4.3**).

The result of the **elemental analyses** (72.66% C, 9.59% H, 1.98% N) were in excellent agreement with those calculated for the chemical formula $C_{156}H_{248}Co_2N_4O_{18}$ (72.47% C, 9.67% H, 2.17% N; formula weight, 2585.5 g mol^{-1}).

Its **FTIR** spectrum **(Figure 4.49)** shows peaks (in cm^{-1}) at 2920, 2851, 1686, 1610, 1591, 1511, 1467, 1392, 1263, 550 and 480 **(Table 4.8)**. These peaks may be similarly assigned as **Complexes 1** ($[Co_2(CH_3COO)_4(LC8)_2].3H_2O$) and **5** ($[Co_2(CH_3COO)_4(LC10)_2].H_2O$). The values of Δ for CH_3COO^- ligand were 219 cm^{-1} and 119 cm^{-1}, suggesting monodentate bridging and bidentate chelating binding modes, respectively [15, 49].

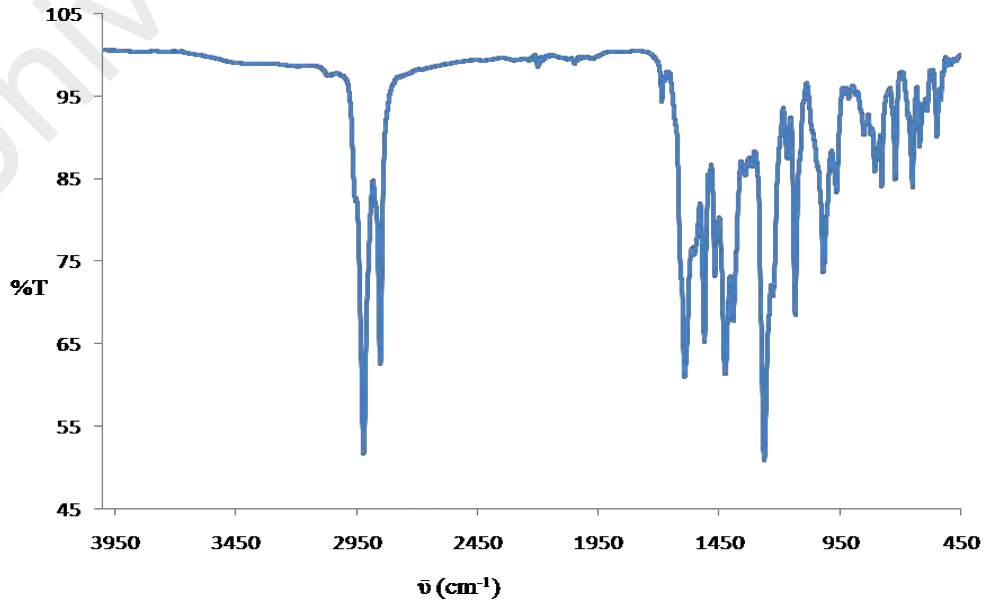

Figure 4.49 FTIR spectrum of **Complex 9**

The **UV-vis** spectrum for **Complex 9** in $CHCl_3$ **(Figure 4.50)**, shows a broad *d-d* band at 1098 nm (ε_{max}, 15.6 M^{-1} cm^{-1}; inset) and an intense MLCT peak at 372 nm (ε_{max}, 3.0 x 10^4 M^{-1} cm^{-1}). The electronic transition may be similarly assigned as for **Complex 1** ($[Co_2(CH_3COO)_4(LC8)_2].3H_2O$). The molarities of the solutions were 7.9 x 10^{-3} mol dm^{-3} for the *d-d* band and 4.6 x 10^{-5} mol dm^{-3} for the MLCT bands.

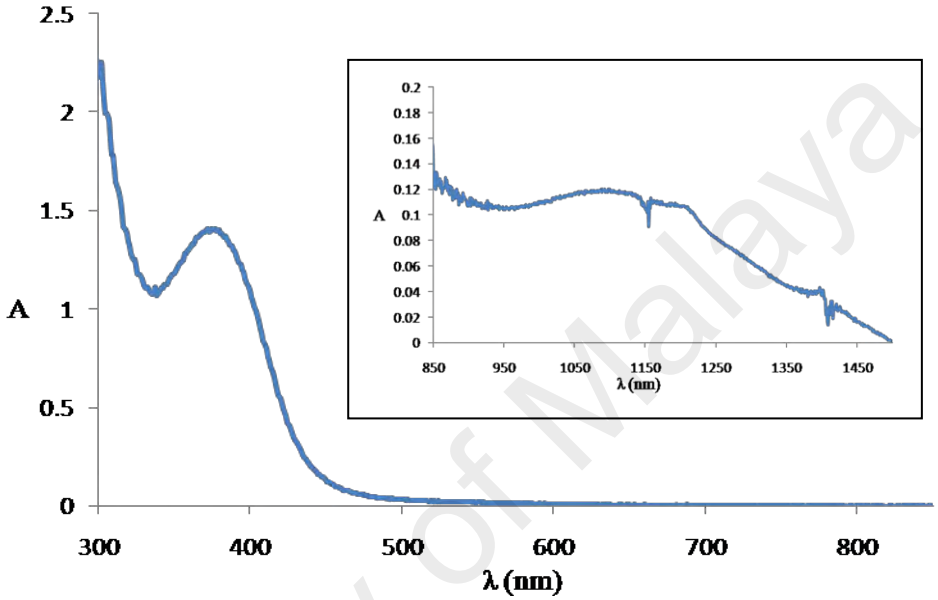

Figure 4.50 UV-vis spectrum of **Complex 9**

(b) Band gap

The E_o value for **Complex 9**, calculated as for previously discussed complexes, was 2.61 eV (λ_{onset} = 475 nm). Hence, the value was the same as **Complex 1** ($[Co_2(CH_3COO)_4(LC8)_2].3H_2O$; E_o = 2.61 eV) and **Complex 5** ($[Co_2(CH_3COO)_4(LC10)_2].H_2O$; E_o = 2.61 eV), which supported the similarity in their structures.

Its **CV** scan (**Figure 4.51**) shows overlapping anodic peaks at +1.25 V, assigned to the oxidation of [Co(II)Co(II)] to [Co(II)Co(III)], [Co(II)] to [Co(III)] and LC12 to $LC12^+$, as a result of the dissociation of the dimer. These were followed by three cathodic peaks at -0.10 V, -0.60 V and -1.00 V, assigned to the reduction of [Co(III)Co(II)] to [Co(II)Co(II)], [Co(III)] to [Co(II)] and $LC12^+$ to LC12, respectively.

The metal-based ΔE_p was 1350 mV, suggesting a quasireversible redox reaction [68]. Hence, the redox behaviour of this complex was similar to **Complex 1**.

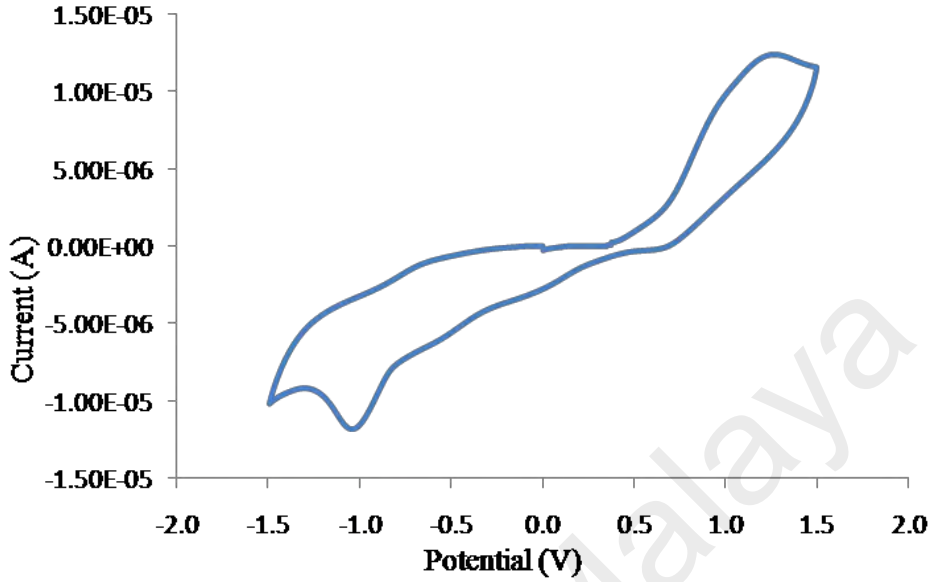

Figure 4.51 Cyclic voltammetry of **Complex 9**

By taking the onset potentials for oxidation (+0.70), reduction (+0.20 V), and the values for E_{HOMO} (5.10 eV) and E_{LUMO} (4.60 eV), the E_e value for **Complex 9** was 0.50 eV. This value was similar to **Complex 5** ($[Co_2(CH_3COO)_4(LC10)_2].H_2O$; E_e = 0.55 eV), which further support the similarity in their structures.

(c) Magnetic properties

The $\chi_M T$ value for **Complex 9**, similarly calculated as for previously discussed complexes from its proposed chemical formula (FW = 2585.5 g mol^{-1}), χ_g (6.93 x 10^{-6} cm^3 g^{-1}), χ_M (1.79 x 10^{-2} cm^3 mol^{-1}), χ_D (-1.67 x 10^{-3} cm^3 mol^{-1}) and χ_M^{corr} (1.95 x 10^{-2} cm^3 mol^{-1}), was 5.41 cm^3 K mol^{-1} at room temperature (298 K). Therefore, it may be inferred that both Co(II) atoms in this complex were HS at this temperature. This is similar with **Complex 5** ($[Co_2(CH_3COO)_4(LC10)_2].H_2O$)**.**

(d) Thermal properties

TGA trace **Complex 9** (**Figure 4.52**) shows that the complex suffered a total mass loss of 93.2% from 182 ^oC to 675 ^oC due to the decomposition of CH_3COO^- ions and LC12

(calculated, 95.4%). The amount of residue for the temperatures above 675 ^{o}C was 6.8%, which was in a good agreement with the calculated value of 5.8% (assuming pure CoO [30]). Therefore, the decomposition temperature for this complex was 182 ^{o}C, which was as thermally stable as **Complex 5** ($[Co_2(CH_3COO)_4(LC10)_2].H_2O$; T_{dec} = 178 ^{o}C).

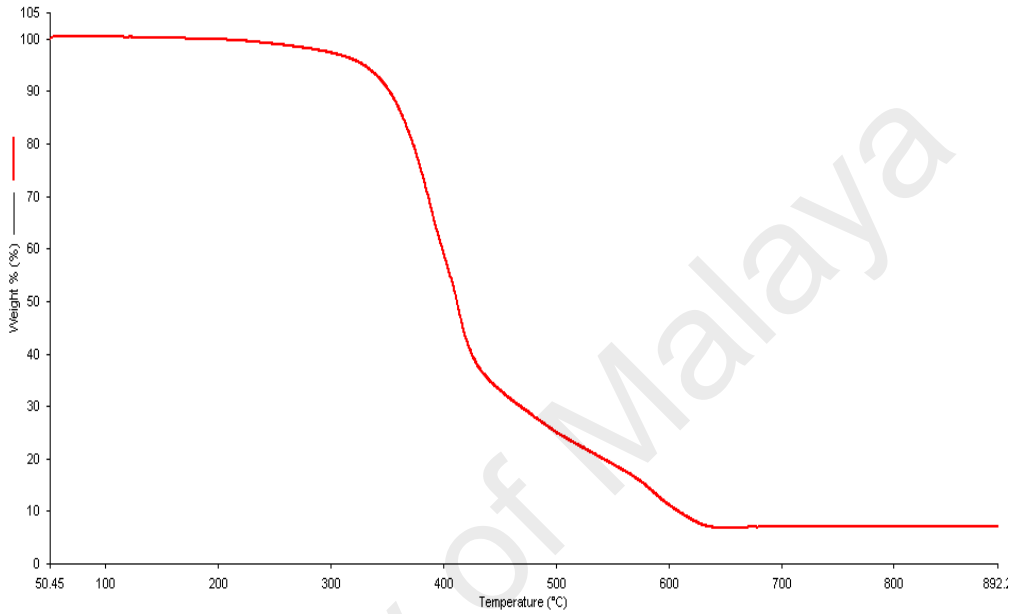

Figure 4.52 TGA trace of **Complex 9**

(e) Thermoelectric properties

Graphs of ΔV *versus* ΔT for **Complex 9 (Figure 4.53)** were almost linear for all three heating-and-cooling cycles, indicating satisfactory thermoelectric behaviour. It is noted that during the first heating cycle, a good linear graph was obtained up to ΔT of about 25 K. In contrast, the second and third heating cycles showed better linearity compared to the cooling cycles. Its mean S_e value was -0.53 ± 0.01 mV K^{-1} (calculated for the second and third heating cycles only). The value was similar to **Complex 1** ($[Co_2(CH_3COO)_4(LC8)_2].3H_2O$; S_e = -0.58 ± 0.03 mV K^{-1}) and **Complex 5** ($[Co_2(CH_3COO)_4(LC10)_2].H_2O$; S_e = -0.55 ± 0.01 mV K^{-1} for the cooling cycles), in agreement with the similarity in their structures and same spin states (100% HS Co(II) atoms).

However, **Complex 9** showed good thermoelectric behavior during the second and third heating cycles only. In contrast, **Complex 1** showed unsatisfactory thermoelectric behavior during the second heating cycle (due to dissociation of the dimer to its monomers), while **Complex 5** showed good behaviour in all three heating and cooling cycles. This may be due to the longer alkyloxy chains in **Complex 9**, which resulted in the formation of less stable micelle-structures in $CHCl_3$, hence a higher tendency for the dimer to dissociate to its monomers. Accordingly, the observed thermoelectric behavior in the second and third heating cycles for **Complex 9** was that of its monomer.

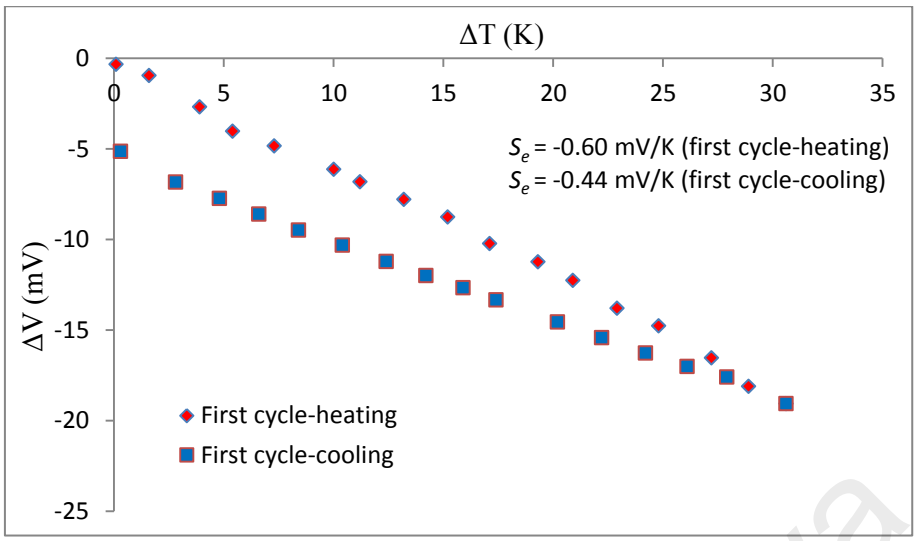

(a)

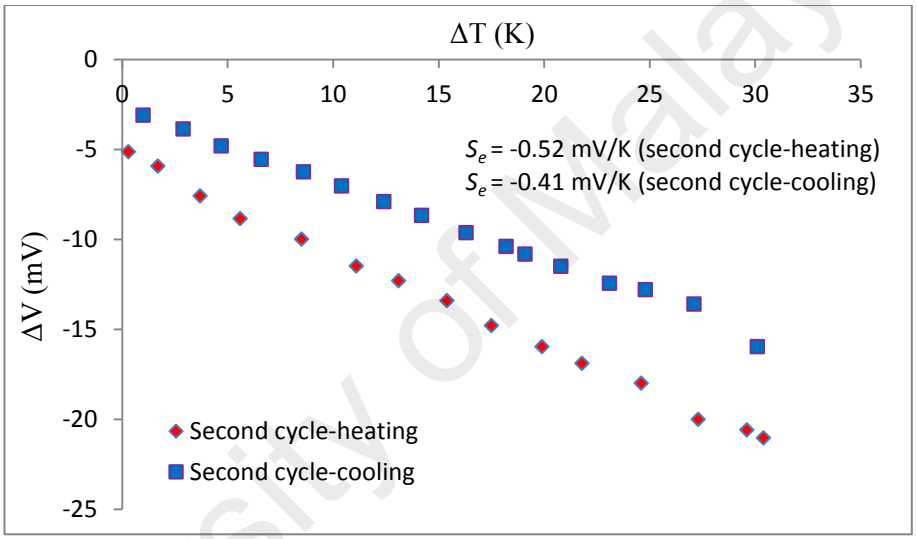

(b)

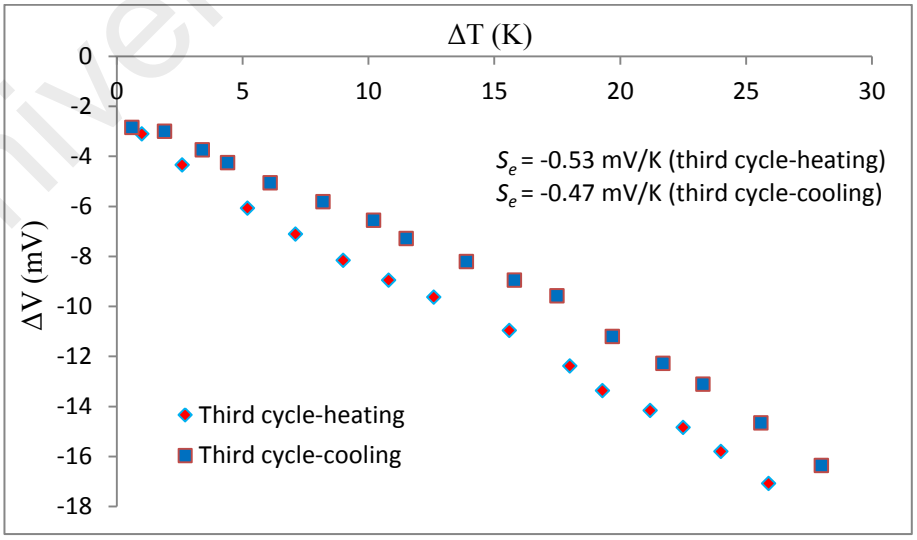

(c)

Figure 4.53 Graphs of ΔV *versus* ΔT for **Complex 9**: (a) first; (b) second; and (c) third heating-and-cooling cycles

4.4.3 [$Fe_2(CH_3COO)_4(LC12)_2$].2H_2O

Ligand **LC12** reacted with iron(II) acetate, $Fe(CH_3COO)_2$, in a mole ratio of 1:1, to form a black powder (**Complex 10**), and its yield was 77.0%. Its solubility was similar to the previously discussed complexes.

(a) Deduction of structural formula

As previously done, the structure for **Complex 10** ($[Fe_2(CH_3COO)_4(LC12)_2].2H_2O$) was proposed based on combined results of instrumental analyses discussed below. The proposed structure was similar to **Complex 1** ($[Co_2(CH_3COO)_4(LC8)_2].3H_2O$; **Figure 4.3)**.

The result of the **elemental analyses** (72.49% C, 9.28% H, 2.20% N) were in excellent agreement with those calculated for the chemical formula $C_{156}H_{248}Fe_2N_4O_{18}$ (72.64% C, 9.69% H, 2.17% N; formula weight, 2579.4 g mol^{-1}).

Its **FTIR** spectrum **(Figure 4.54)** shows peaks (in cm^{-1}) at 2921, 2852, 1630, 1608, 1592, 1509, 1431, 1380, 1261, 543 and 475 **(Table 4.8)**. These peaks may be similarly assigned as for **Complex 1** ($[Co_2(CH_3COO)_4(LC8)_2].3H_2O$). The values of Δ for CH_3COO^- ligand were 199 cm^{-1} and 129 cm^{-1}, suggesting monodentate bridging and bidentate chelating binding modes [15, 49], respectively.

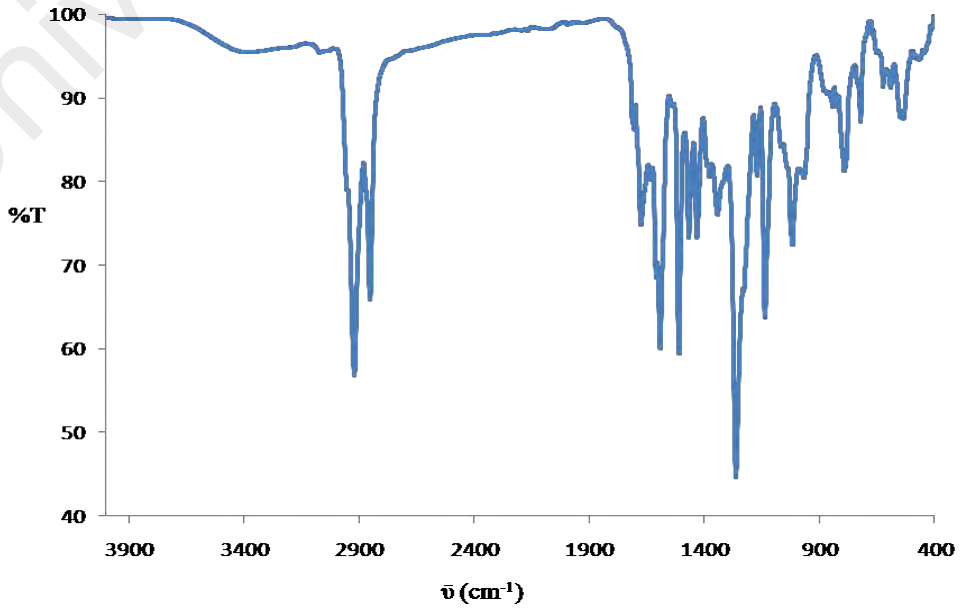

Figure 4.54 FTIR spectrum of **Complex 10**

Its **UV-vis** spectrum recorded in $CHCl_3$ (**Figure 4.55**; 6.5 x 10^{-4} mol dm^{-3}) shows a weak *d-d* band which appeared as a shoulder at about 660 nm (ε_{max}, 1.2 x 10^2 M^{-1} cm^{-1}) and a MLCT peak at 572 nm (ε_{max}, 1.3 x 10^3 M^{-1} cm^{-1}). The electronic transition was similarly assigned as **Complex 6** (**[**$Fe_2(CH_3COO)_4(LC10)_2].3H_2O$) and may be similarly explained.

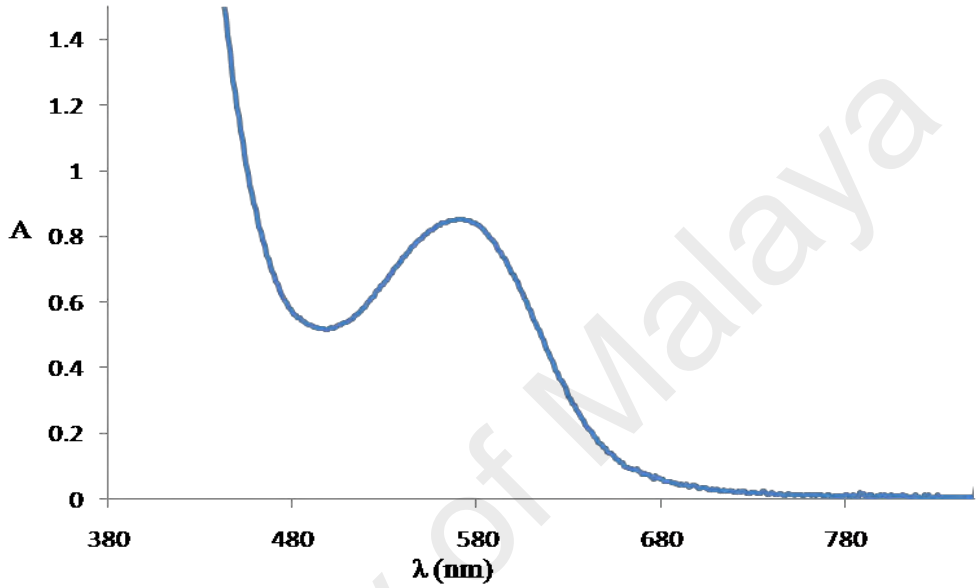

Figure 4.55 UV-vis spectrum of **Complex 10**

(b) Band gap

Using the same equation as previously shown, the E_o value for **Complex 10** was 1.85 eV (λ_{onset} = 670 nm). This value was similar to **Complexes 2** ([$Fe_2(CH_3COO)_4(LC8)_2$]; E_o = 1.87 eV) and **6** ([$Fe_2(CH_3COO)_4(LC10)_2].3H_2O$; E_o = 1.90 eV).

Its **CV** scan **(Figure 4.56)** shows two overlapping anodic peaks at +0.82 V and +1.10 V assigned as the oxidation of [Fe(II)Fe(II)] to [Fe(II)Fe(III)] and LC12 to $LC12^+$, respectively. These were followed by two cathodic peaks at +0.10 V and -0.90 V assigned as the reduction of [Fe(II)Fe(III)] to [Fe(II)Fe(II)] and $LC12^+$ to LC12, respectively. Hence, the metal-based ΔE_p value was 720 mV, indicating a quasireversible redox reaction [68]. The redox behaviour was similar to **Complex 2**.

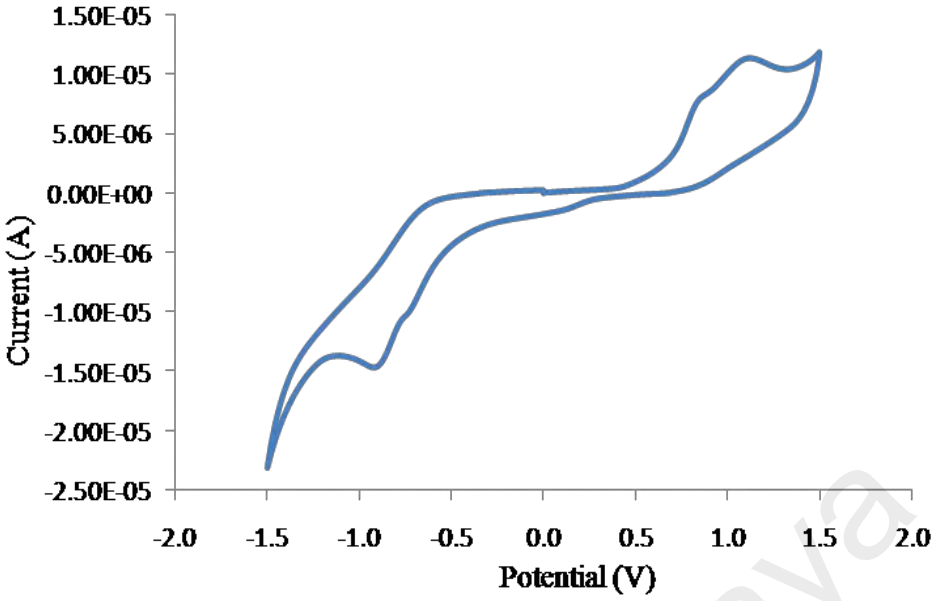

Figure 4.56 Cyclic voltammetry of **Complex 10**

Its E_e value, similarly calculated as previously done from the onset potentials for oxidation (+0.71 V) and reduction (+0.23 V), and the values of E_{HOMO} (5.11 eV) and E_{LUMO} (4.63 eV), was 0.48 eV. This value was similar to **Complex 6** ($[Fe_2(CH_3COO)_4(LC10)_2].3H_2O$; E_e = 0.49 eV).

(c) Magnetic properties

The value of $\chi_M T$ of **Complex 10,** calculated as previously discussed from its proposed chemical formula (FW = 2579.4 g mol^{-1}), χ_g (7.26 x 10^{-6} cm^3 g^{-1}), χ_M (1.87 x 10^{-2} cm^3 mol^{-1}), χ_D (-1.77 x 10^{-3} cm^3 mol^{-1}) and χ_M^{corr} (2.05 x 10^{-2} cm^3 mol^{-1}), was 6.11 cm^3 K mol^{-1} at 298 K. Hence, it may be concluded that both Fe(II) atoms of this complex were HS at this temperature, indicating weak Fe-O and Fe-N bonds.

(d) Thermal properties

TGA trace for **Complex 10** (**Figure 4.57**) shows a total mass loss of 94.1% from 170 ^oC to 768 ^oC due to the decomposition of CH_3COO^- ions and LC12 (calculated, 94.4%). The amount of residue at temperatures above 768 ^oC was 5.9% (calculated, 5.6% assuming pure FeO). These data further support the proposed structure for this

complex. Hence, this complex was thermally stable up to 170 ^{o}C, which was similar to **Complex 6** ($[Fe_2(CH_3COO)_4(LC10)_2].3H_2O$; T_{dec} = 172 ^{o}C).

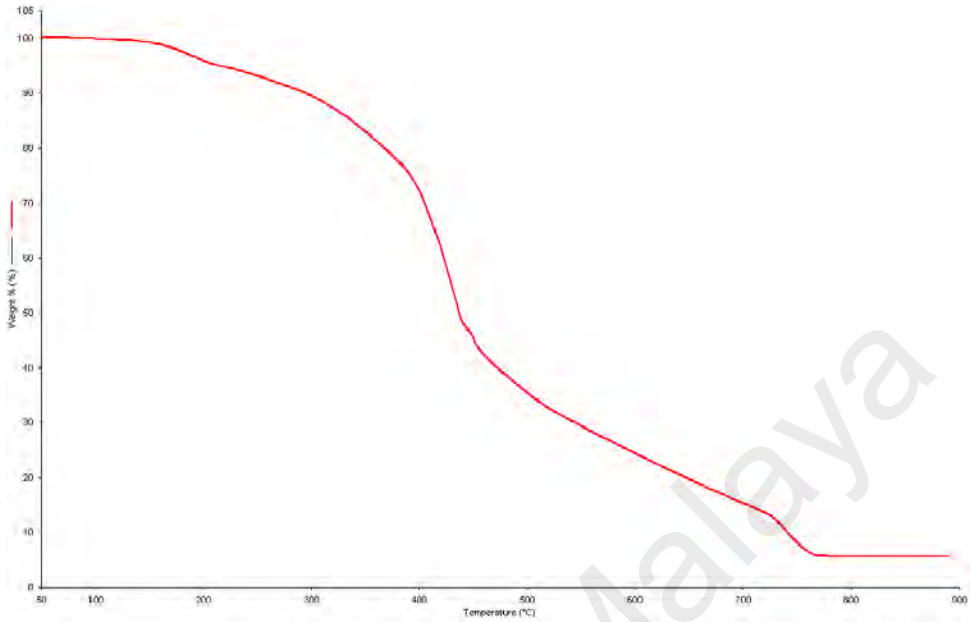

Figure 4.57 TGA trace of **Complex 10**

(e) Thermoelectric properties

Graphs of ΔV *versus* ΔT for **Complex 10** (**Figure 4.58)** were linear for all three heating-and-cooling cycles, indicating a good thermoelectric behaviour. Its mean S_e value was -0.61 ± 0.02 mV K^{-1}. This value was similar to **Complex 2** ($[Fe_2(CH_3COO)_4(LC8)_2]$; S_e = -0.51 ± 0.01 mV K^{-1}) and **Complex 6** (S_e = -0.56 ± 0.02 mV K^{-1}), and may be similarly explained. This is consistent with their similar structures and spin states (these complexes have higher percentages of HS Fe(II) atoms).

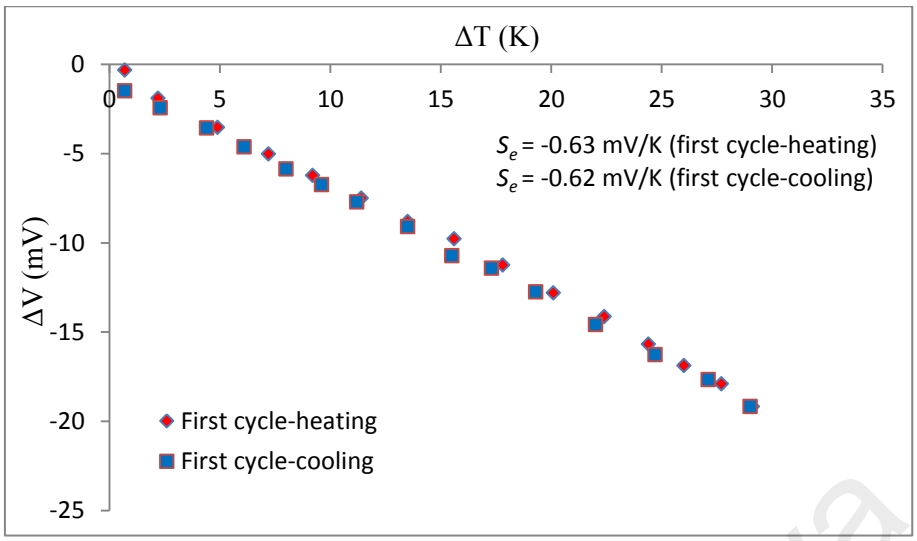

(a)

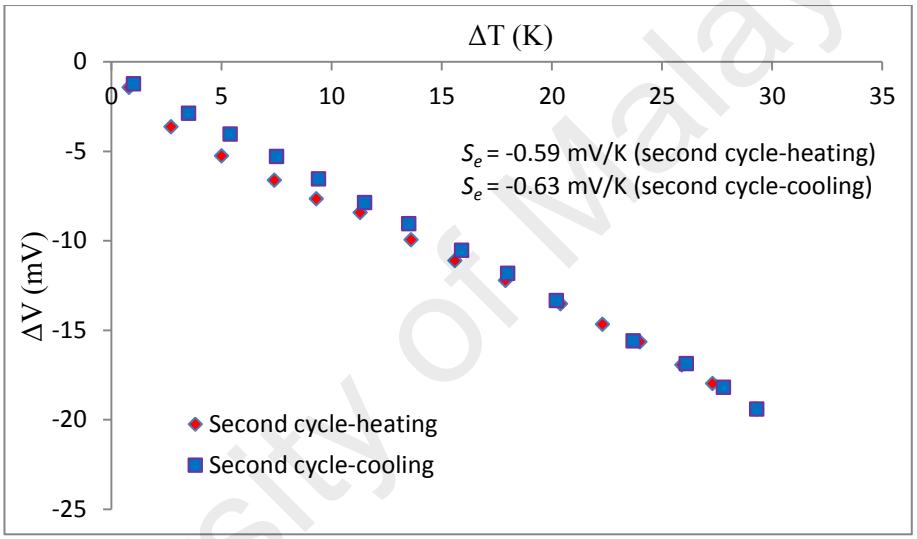

(b)

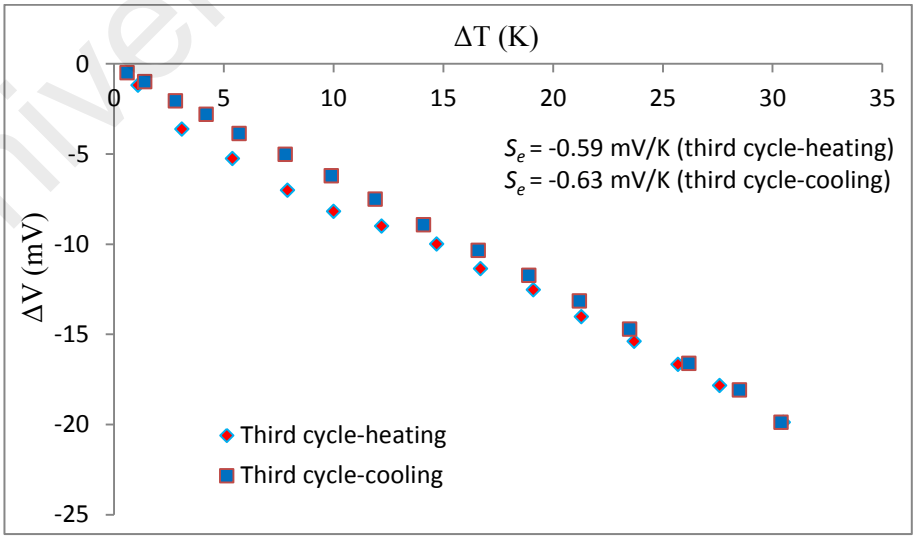

(c)

Figure 4.58 Graphs of ΔV *versus* ΔT for **Complex 10**: (a) first; (b) second; and (c) third heating-and-cooling cycles

4.4.4 $[Co(LC12)_3](BF_4)_2.3H_2O$

Cobalt(II) tetrafluoroborate hexahydrate, $Co(BF_4)_2.6H_2O$, reacted with **LC12** in a mole ratio of 1:3 to form a dark red powder (**Complex 11**), and its yield was 78.1%. Its solubility was similar as previously discussed complexes.

(a) Deduction of structural formula

As previously done, the proposed structure of **Complex 11** ($[Co(LC12)_3](BF_4)_2.3H_2O$) was based on combined results of elemental analyses, FTIR spectroscopy and UV-vis spectroscopy, discussed below. Hence, its proposed was similar to **Complex 3** ($[Co(LC8)_3](BF_4)_2.2H_2O$; **Figure 4.14**).

The results for **elemental analyses** (74.49% C, 9.65% H, 2.17% N) were in excellent agreement with those calculated for the chemical formula $C_{222}H_{354}B_2CoF_8N_6O_{15}$ (74.48% C, 9.97% H, 2.35% N; formula weight: 3579.8 g mol^{-1}).

Its **FTIR** spectrum (**Figure 4.59**) shows the presence of the expected peaks (cm^{-1}) at 2921, 2852, 1607, 1591, 1052 and 549 **(Table 4.8)**. These peaks may be similarly assigned as for **Complex 3**.

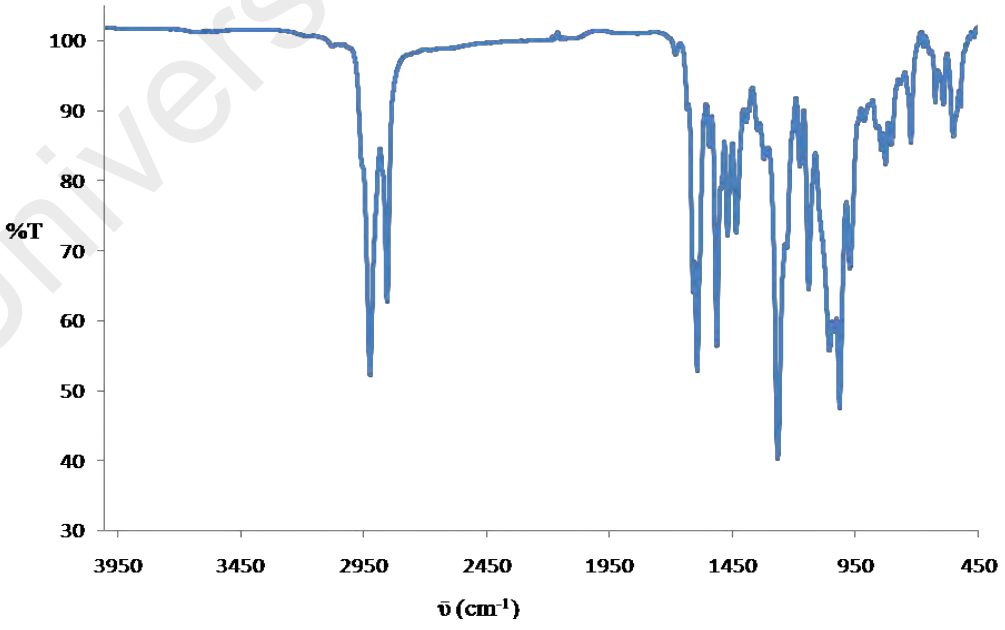

Figure 4.59 FTIR spectrum of **Complex 11**

The **UV-vis** spectrum of **Complex 11 (Figure 4.60)** shows a weak *d-d* bands at 1204 nm (ε_{max}, 6.8 M^{-1} cm^{-1}; inset), and an MLCT band at 396 nm (ε_{max}, 6.8 x 10^4 M^{-1} cm^{-1}). The electronic transitions may be similarly assigned as **Complex 1** ($[Co_2(CH_3COO)_4(LC8)_2].3H_2O$). The molarities of the solutions were 5.6 x 10^{-3} mol dm^{-3} for the *d-d* band and 2.5 x 10^{-5} mol dm^{-3} for the MLCT bands.

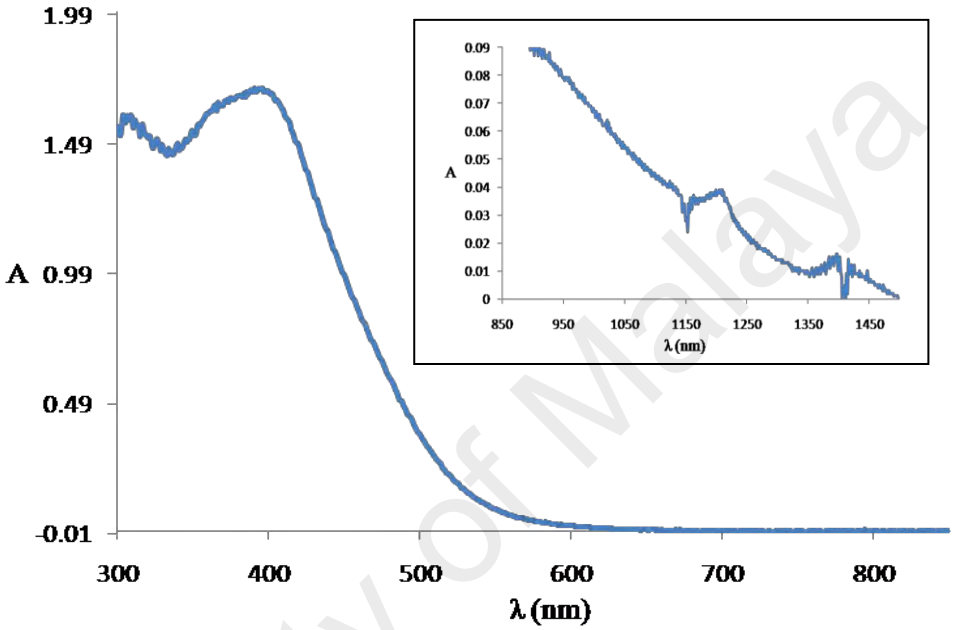

Figure 4.60 UV-vis spectrum of **Complex 11**

(b) Band gap

As before, by taking the onset wavelength of the MLCT band, the E_o value for **Complex 11** was 2.25 eV (λ = 550 nm). This value was similar to **Complex 7** ($[Co(LC10)_3](BF_4)_2.4H_2O$; E_o =2.33 eV).

Its **CV** scan (**Figure 4.61**) shows two overlapping anodic peaks at +0.85 V and +1.20 V, assigned to the oxidation of [Co(II)] to [Co(III)] and LC12 to $LC12^+$, respectively. These were followed by two the cathodic peaks at +0.10 V and -1.05 V which assigned reduction of [Co(III)] to [Co(II)] and $LC12^+$ to LC12. Hence, the metal-based ΔE_p was 750 mV, suggesting a quasireversible redox reaction [68]. The redox behaviour was similar to **Complex 3** ($[Co(LC8)_3](BF_4)_2.2H_2O$).

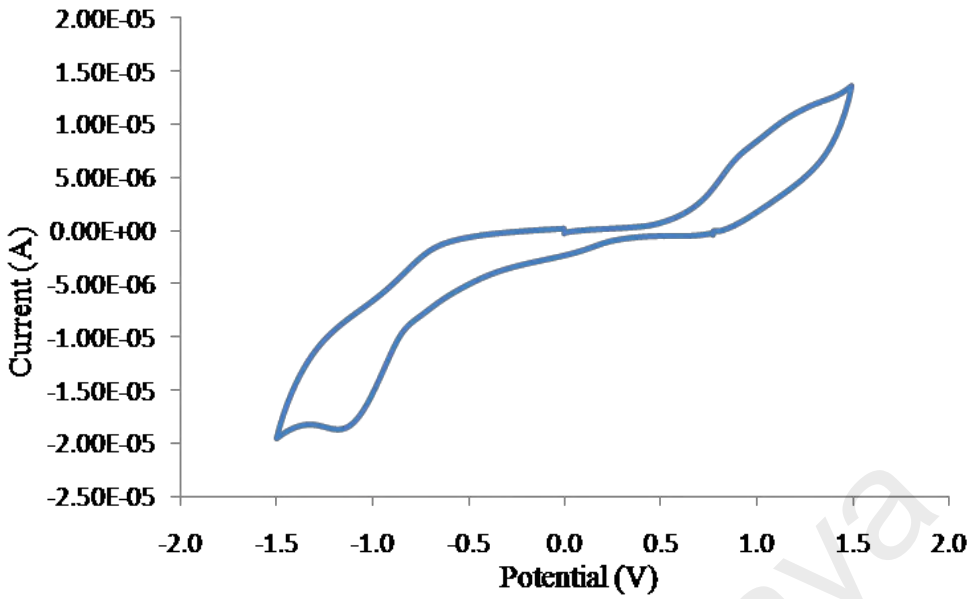

Figure 4.61 Cyclic voltammetry of **Complex 11**

Its E_e value, similarly calculated as previously done from the onset potentials for oxidation (+0.60 V) and reduction (+0.25), the values of E_{HOMO} (5.00 eV) and E_{LUMO} (3.64 eV), was 0.35 eV which was similar to **Complex 7** ($[Co(LC10)_3](BF_4)_2.4H_2O$; E_e = 0.37 eV).

(c) Magnetic properties

The $\chi_M T$ value for **Complex 11**, calculated as previously done from its proposed chemical formula (FW = 3579.8 g mol^{-1}), χ_g (1.65 x 10^{-6} cm^3 g^{-1}), χ_M (5.91 x 10^{-3} cm^3 mol^{-1}), χ_D (-2.48 x 10^{-3} cm^3 mol^{-1}) and χ_M^{corr} (8.39 x 10^{-3} cm^3 mol^{-1}), was 2.50 cm^3 K mol^{-1} at 298 K. Thus, it may be inferred that this complex has HS Co(II) at this temperature, hence weak Co-N bonds.

(d) Thermal properties

TGA trace for **Complex 11 (Figure 4.62)** shows that it suffered a total mass loss of 96.4% from 260 ^oC to 770 ^oC due to the loss of BF_3 (from BF_4^- ions) and decomposition of LC12 (calculated, 97.2 %). The amount of residue at temperatures above 770 ^oC was 3.6%, which was in a good agreement with the calculated amount of 2.8%, assuming it was pure CoF_2 [73]. Hence, the complex was thermally stable on heating up to 260 ^oC.

Its thermal stability was similar to **Complex 7** ($[Co(LC10)_3](BF_4)_2.4H_2O$; T_{dec} = 260 ^oC), supporting the similarity of their proposed structures.

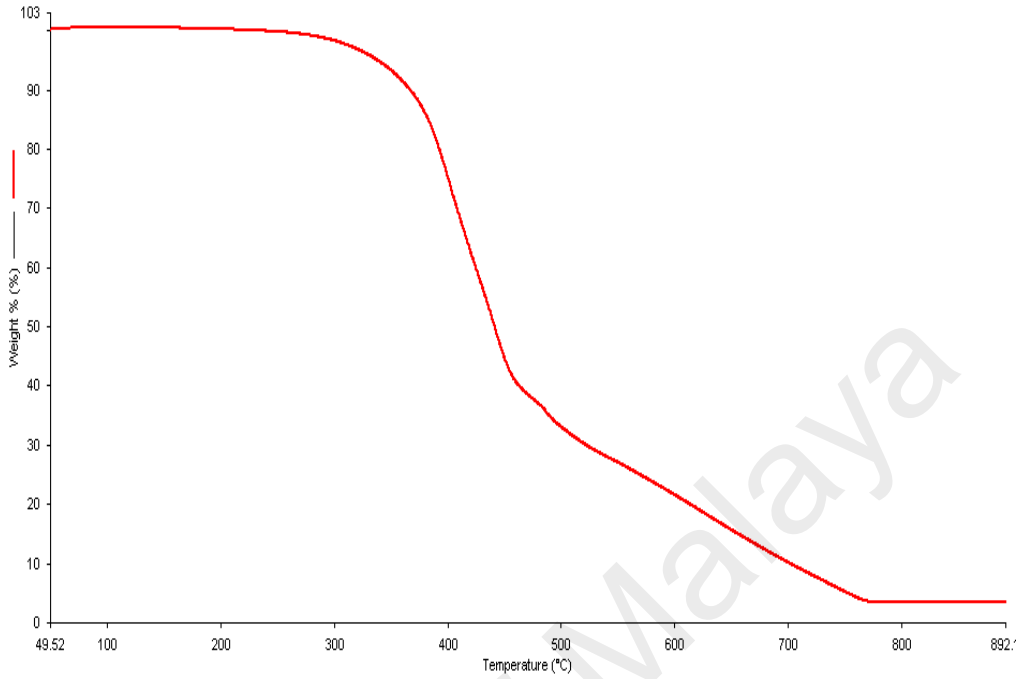

Figure 4.62 TGA trace of **Complex 11**

(e) Thermoelectric properties

Graphs of ΔV *versus* ΔT for **Complex 11 (Figure 4.63)** were almost linear indicating good thermoelectric behaviour. Its mean S_e value was -0.48 ± 0.03 mV K^{-1} for the heating cycles, and -0.44 ± 0.01 mV K^{-1} for the cooling cycles. This value was similar to **Complex 3** ($[Co(LC8)_3](BF_4)_2.2H_2O$; S_e = -0.42 ± 0.08 mV K^{-1}) and **Complex 7** ($[Co(LC10)_3](BF_4)_2.4H_2O$; S_e = -0.40 ± 0.01 mV K^{-1}), due to the similarity in their structures and same spin states (100% cobalt(II) atoms).

The negative values mean that these complexes have similar majority charge carriers (I^- ion), as previously discussed. However, the thermoelectric behavior of **Complex 11** was better than **Complexes 3** and **7**, which showed satisfactory behavior during the cooling cycles only. This is likely due to the longer alkyoxy chains in the former complex, resulting in more stable micelle-like structures in $CHCl_3$.

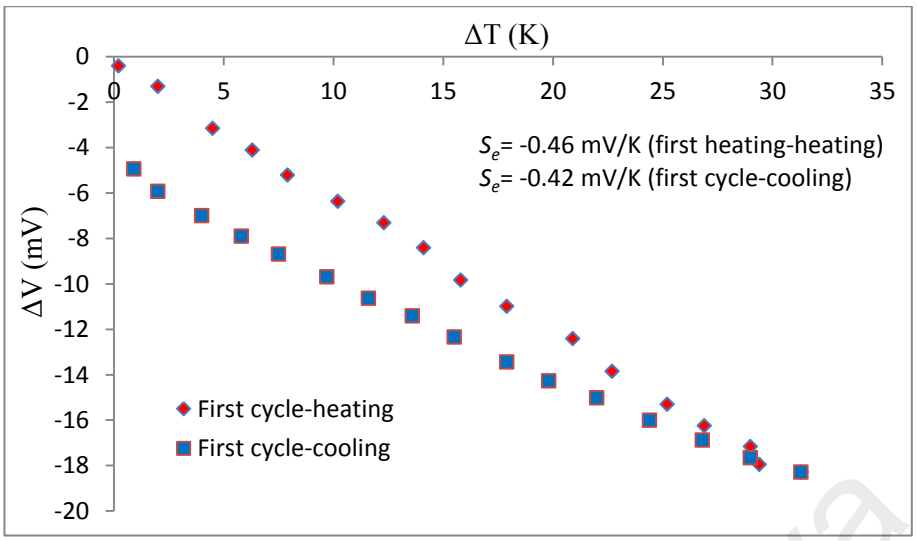

(a)

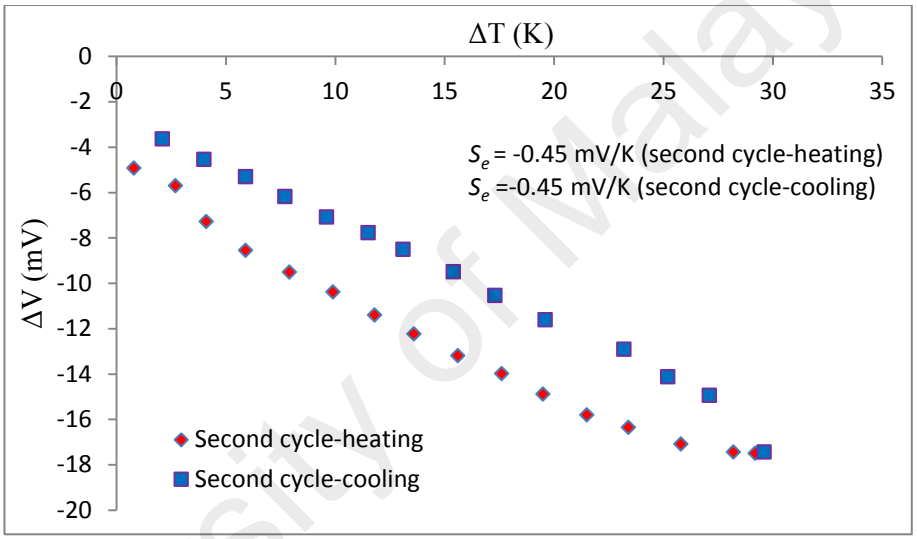

(b)

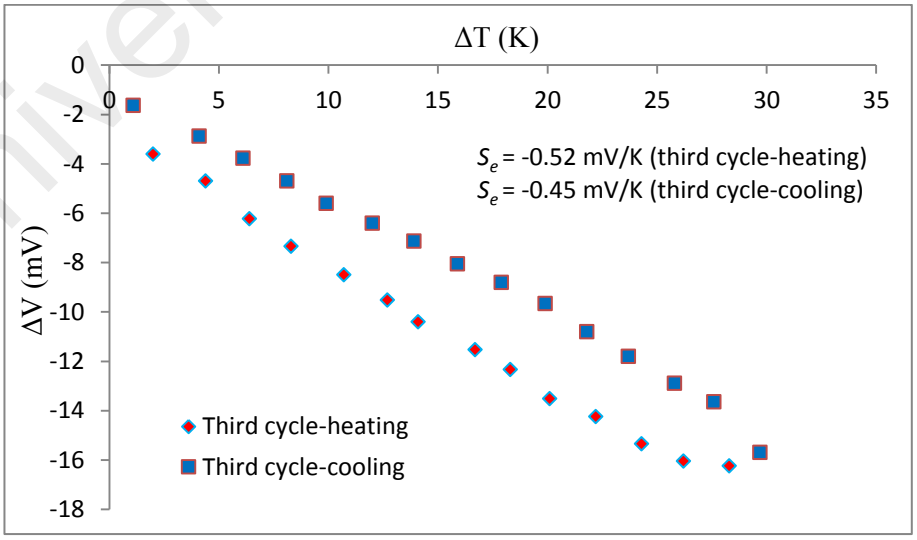

(c)

Figure 4.63 Graphs of ΔV *versus* ΔT for **Complex 11**: (a) first; (b) second; and (c) third heating-and-cooling cycles

4.4.5 [Fe(LC12)$_3$](BF$_4$)$_2$.3H$_2$O

Iron(II) tetrafluoroborate hexahydrate, $Fe(BF_4)_2.6H_2O$, reacted with **LC12** in a mole ratio of 1:3, to form a black powder (**Complex 12**), and its yield was 87.6%. Its solubility was similar to the previously discussed complexes.

(a) Deduction of structural formula

Based on combined instrumental analytical data discussed below, it is proposed that the structural formula for **Complex 12** was $[Fe(LC12)_3](BF_4)_2.3H_2O$. Hence, its structure was similar to **Complex 3** ($[Co(LC8)_3](BF_4)_2.2H_2O$; **Figure 4.14**).

The results of the **elemental analyses** (74.22% C, 10.24% H, 1.95% N) were in good agreement with those calculated for the chemical formula $C_{222}H_{354}B_2F_8FeN_6O_{15}$ (74.55% C, 9.98% H, 2.35% N; formula weight: 3576.7 g mol^{-1}).

Its **FTIR** spectrum **(Figure 4.64)** shows a presence of the expected peaks (cm^{-1}) at 2919, 2849, 1609, 1594, 1057 and 590 **(Table 4.8)**. These peaks may be similarly assigned as for **Complex 3.**

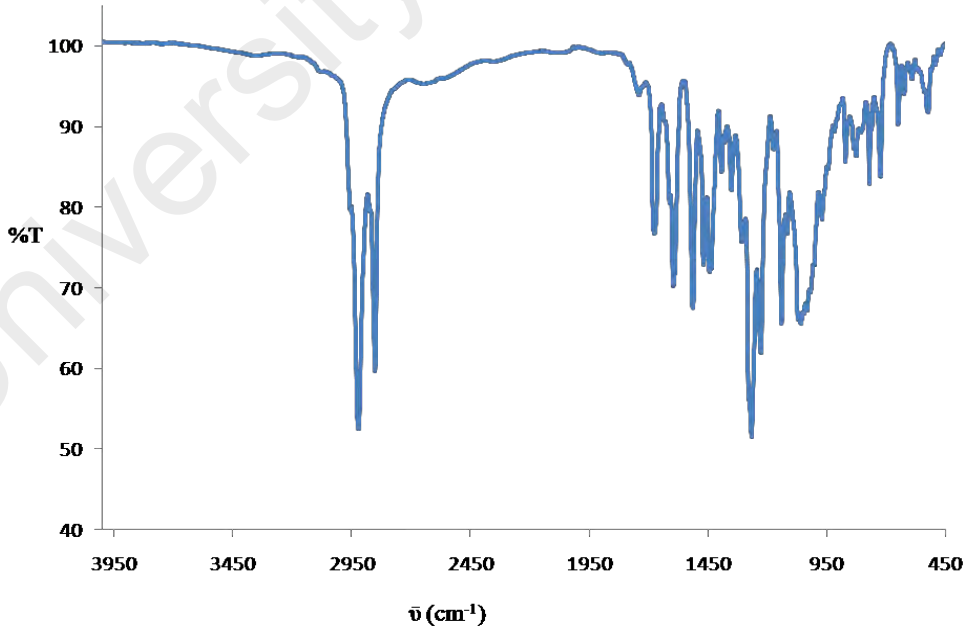

Figure 4.64 FTIR spectrum of **Complex 12**

Its **UV-vis** spectrum recorded in $CHCl_3$ **(Figure 4.65;** 1.4 x 10^{-4} mol dm^{-3}**)** shows a weak *d-d* band which appeared as a shoulder at about 640 nm

(ε_{max}, 2.1 x 10^2 M^{-1} cm^{-1}) and four MLCT peaks 557 nm (ε_{max}, 1.8 x 10^3 M^{-1} cm^{-1}), 394 nm (ε_{max}, 5.5 x 10^3 M^{-1} cm^{-1}), 302 nm (ε_{max}, 6.3 x 10^3 M^{-1} cm^{-1}) and 261 nm (ε_{max}, 6.4 x 10^3 M^{-1} cm^{-1}). The *d-d* electronic transition was similarly assigned as for **Complex 6** ($[Fe_2(CH_3COO)_4(LC10)_2].3H_2O$) and **Complex 10** ($[Fe_2(CH_3COO)_4(LC12)_2].2H_2O$), and may be similarly explained.

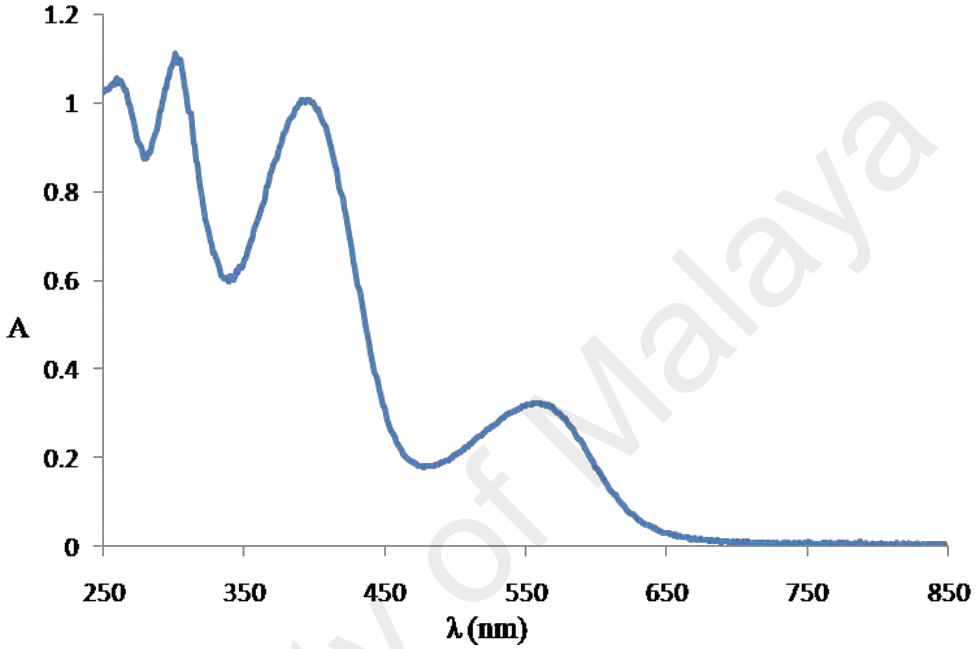

Figure 4.65 UV-vis spectrum of **Complex 12**

(b) Band gap

The E_o value for **Complex 12** was 1.93 eV (λ_{onset} = 640 nm). This value was the same as **Complex 8** ($[Fe(LC10)_3](BF_4)_2.3H_2O$; E_e = 1.93 eV), as expected from the similarity of their structures..

Its **CV** scan **(Figure 4.66)** shows two overlapping anodic peaks at +0.80 V and +1.10 V, assigned to the oxidation of [Fe(II)] to [Fe(III)] and LC12 to $LC12^+$ respectively. On the reversed scan, these were followed by two cathodic peaks at +0.18 V and -0.90 V, assigned to the reduction of [Fe(III)] to [Fe(II)] and $LC12^+$ to LC12, respectively. The metal-based ΔE_p was 620 mV, suggesting a quasireversible redox reaction [68]. Hence, the redox behaviour was similar to **Complex 4** ($[Fe(LC8)_3](BF_4)_2.H_2O$).

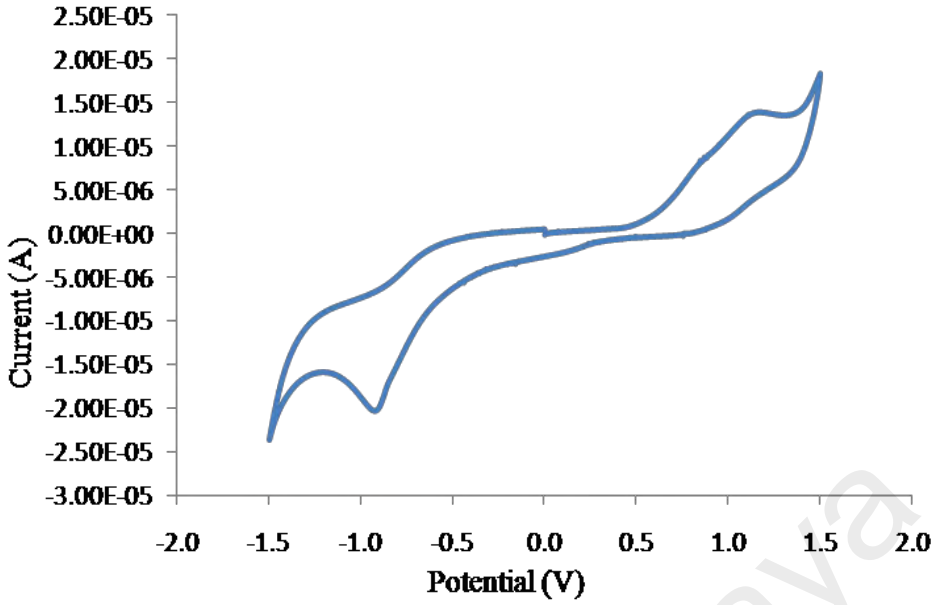

Figure 4.66 Cyclic voltammetry of **Complex 12**

Its E_e value, similarly calculated as previously done from the onset potentials for oxidation (+0.60 V) and reduction (-0.24 V), and the values for E_{HOMO} (5.00 eV) and E_{LUMO} (4.64 eV), was 0.36 eV, which was similar to **Complex 8** ($[Fe(LC10)_3](BF_4)_2.3H_2O$; E_e = 0.35 eV).

(c) Magnetic properties

The value of χ_g for **Complex 12** was 0 at 298 K. This means that this complex was diamagnetic at this temperature. Therefore, it is inferred that the complex has LS Fe(II), as similarly found and explained for **Complexes 4** ($[Fe(LC8)_3](BF_4)_2.H_2O$) and **8**.

(d) Thermal properties

TGA trace for **Complex 12 (Figure 4.67)** shows that it suffered a total mass loss of 97.1% from 262 ^oC to 742 ^oC due to the loss of BF_3 (from BF_4^- ions) and decomposition of LC12 (calculated, 97.3%). The amount of residue at temperatures above 742 ^oC was 2.9% (calculated, 2.7% assuming pure FeF_2 [73]). Hence, its decomposition temperature was 262 ^oC, which was similar to **Complex 8** (T_{dec} = 259 ^oC).

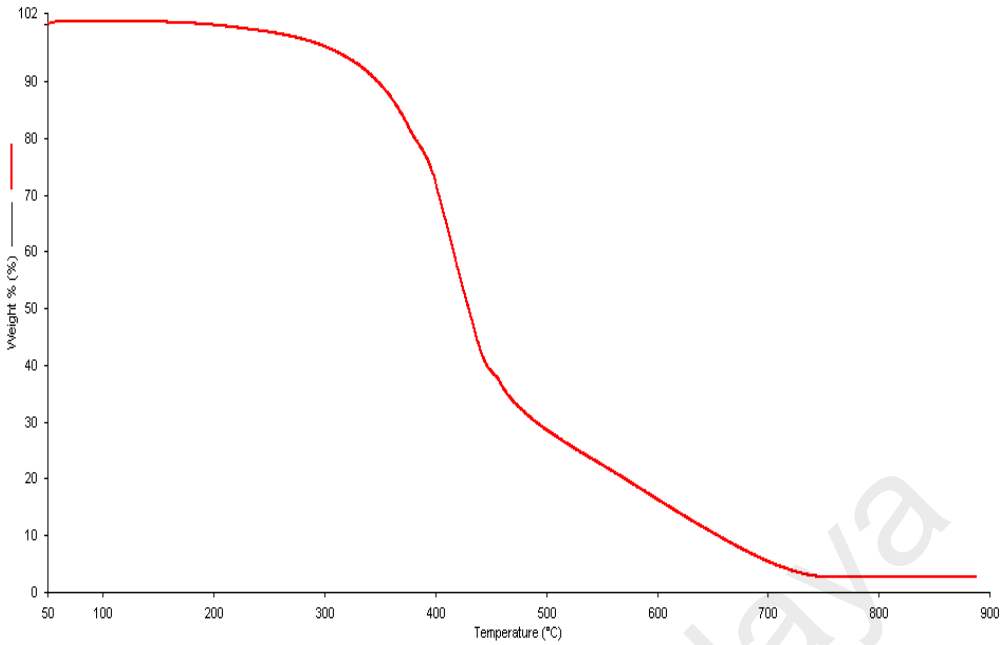

Figure 4.67 TGA trace of **Complex 12**

(e) Thermoelectric properties

Graphs of ΔV *versus* ΔT for **Complex 12 (Figure 4.68)** were linear, indicating good thermoelectric behaviour. Its mean S_e value was -0.52 ± 0.01 mV K^{-1}. This value was similar to **Complex 4** ($[Fe(LC8)_3](BF_4)_2.H_2O$; S_e = -0.55 ± 0.03 mV K^{-1}) and **Complex 8** ($[Fe(LC10)_3](BF_4)_2.3H_2O$; S_e = -0.51 ± 0.01 mV K^{-1}), and may be similarly explained. Therefore, the S_e values for these complexes were independent on the alkyloxychain length of the bipyridyl ligands.

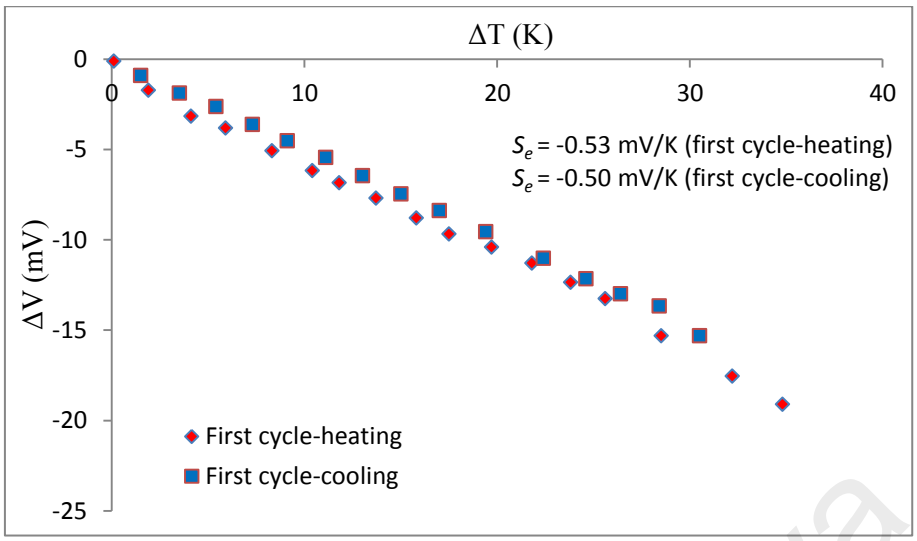

(a)

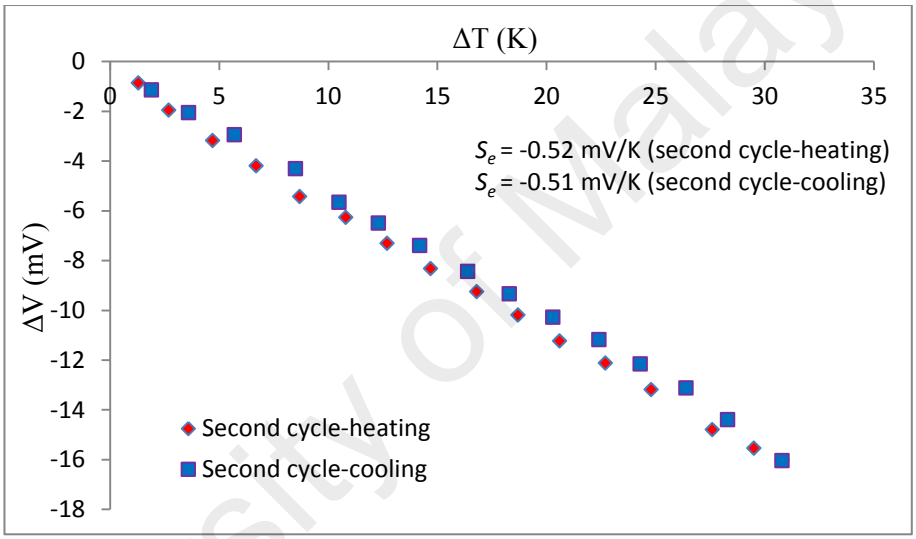

(b)

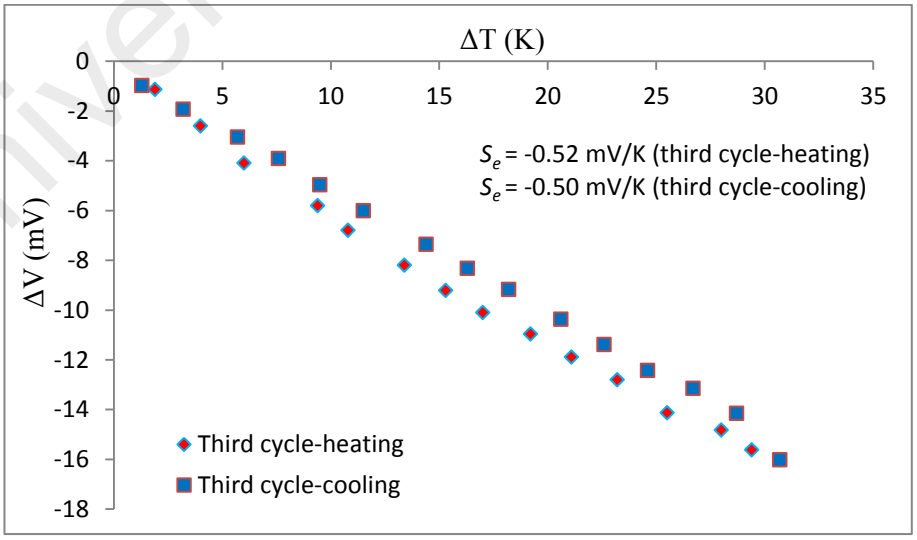

(c)

Figure 4.68 Graphs of ΔV *versus* ΔT for **Complex 12**: (a) first; (b) second; and (c) third heating-and-cooling cycles

4.4.6 Summary

The results of the analytical data for **Complexes 9 - 12** are summarised in **Table 4.9**. These results were similar with those for **Complexes 1 - 4 (Table 4.3)** and **Complexes 5 – 8 (Table 4.6)**, and may be similarly explained. It is noted that the dimeric molecular complexes **(Complexes 9** and **10)** formed less stable micelle-like structures, while the mononuclear ionic complexes **(Complexes 11** and **12)** formed more stable micelle-like structures, compared to their analogs with shorter alkyoxyl chains for the bipyridyl ligands.

Table 4.9 Summary of results for **Complexes 9 - 12**

Chemical Formula	**Band gap (eV)**		$\chi_M^{corr}T$ (cm^3 K mol^{-1})	T_{dec} C	S_e (mV K^{-1})
	E_o	E_e			
$[Co_2(CH_3COO)_4(LC12)_2].2H_2O$ **(Complex 9)**	2.61	0.50	5.41 100% HS	182	-0.53 ± 0.01(Heat)*
$[Fe_2(CH_3COO)_4(LC12)_2].2H_2O$ **(Complex 10)**	1.85	0.48	6.11 100% HS	170	-0.62 ± 0.02
$[Co(LC12)_3](BF_4)_2.3H_2O$ **(Complex 11)**	2.25	0.35	2.50 100% HS	260	-0.48 ± 0.03 (Heat) -0.44 ± 0.01 (Cool)
$[Fe(LC12)_3](BF_4)_2.3H_2O$ **(Complex 12)**	1.93	0.36	0 100% LS	262	-0.52 ± 0.01

*Second and third cycles only

4.5 LC14 and its Cobalt(II) and Iron(II)

4.5.1 Ligand LC14

The steps involved in the synthesis of ligand LC14 were similar to the previously discussed ligands, as shown in Scheme 1.1. It was obtained as a white powder, and its yield was 87.6%. The structure of LC14 was determined by elemental analyses, ^{1}H-NMR, and FTIR spectroscopies.

The result of **elemental analyses** (81.04% C, 11.11% H, 2.02% N) were in good agreement with those calculated for the chemical formula $C_{82}H_{132}N_2O_4$ (81.40% C, 11.00% H, 2.32% N; formula weight: 1209.9 g mol^{-1}).

Its ^{1}H-NMR spectrum **(Figure 4.69)** shows peaks (in ppm) at 0.8 (triplet, CH_3, 12 H), 1.3 - 2.2 (multiplet, CH_2, 96 H), 4.1 (triplet, O-CH_2-, 8 H), 6.8 - 7.5 (multiplet, aromatic C-H and HC=CH, 12 H), 8.6 – 8.7 (multiplet, aromatic C-H, 4 H). The peaks assignments are shown in **Table 4.10**.

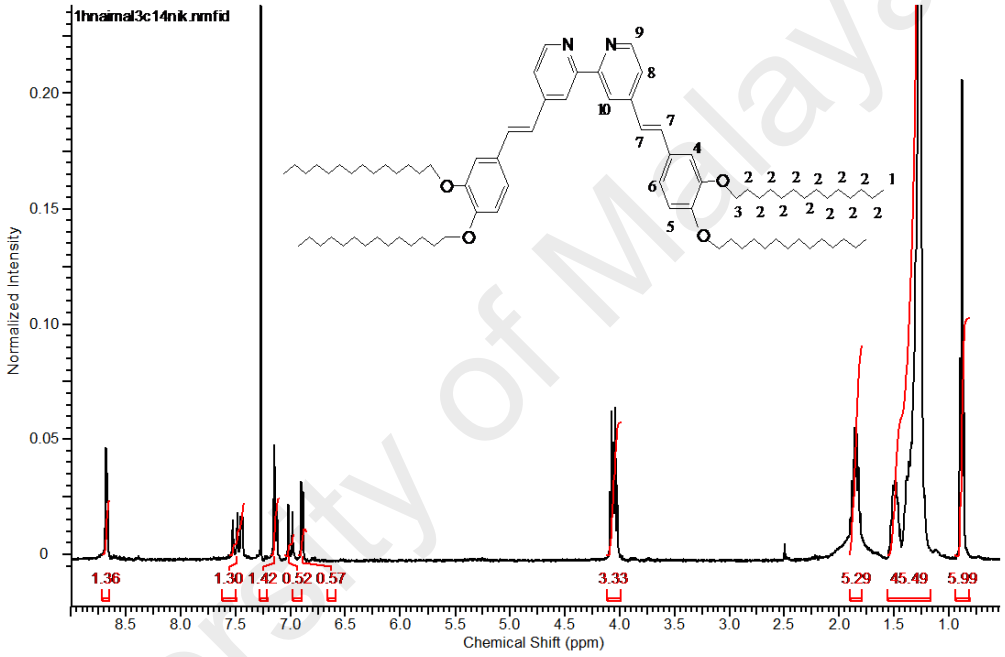

Figure 4.69 ^{1}H-NMR spectrum of LC14

Table 4.10 The ^{1}H-NMR peak assignments for LC14

Chemical shift (ppm)	**Integral**	**Multiplicity**	**Assignment**
0.8	5.99	Triplet	H-1
1.3 - 2.2	50.78	Multiplet	H-2
4.1	3.33	Triplet	H-3
6.8 - 7.5	3.81	Multiplet	H-4, H-5, H-6, H-7, H-8
8.6 - 8.7	1.36	Singlet Doublet	H-10 H-9

Its **FTIR** spectrum is shown in **Figure 4.87** and the peak assignments are shown in **Table 4.11** (which also includes peaks for the corresponding metal(II) complexes for later discussion). It shows peaks (in cm^{-1}) at 2916, 2849, 1662, 1589 and 1265. These peaks are similarly assigned as for ligand LC8.

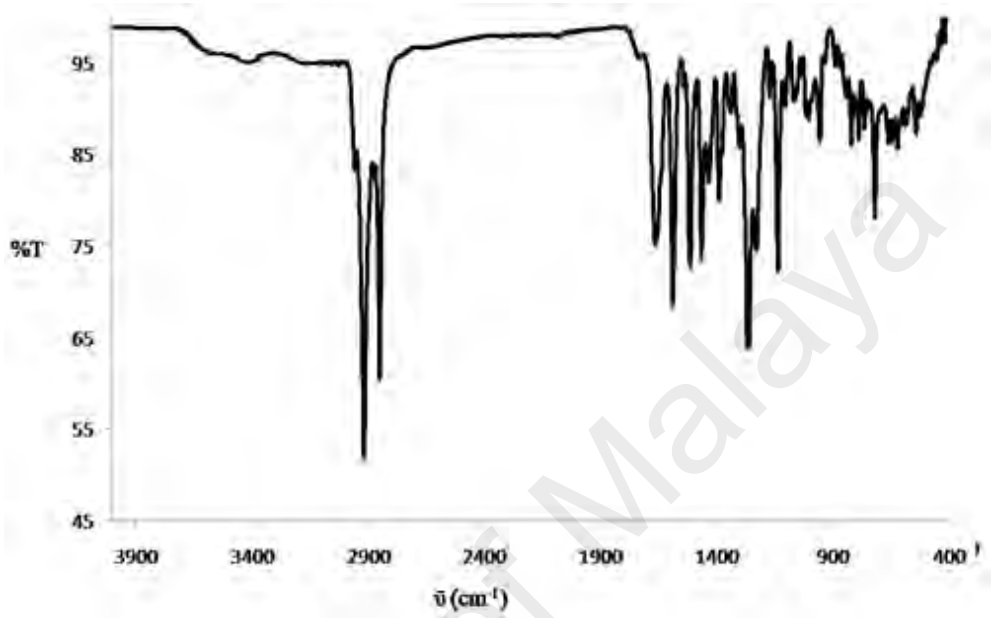

Figure 4.70 FTIR spectrum of LC14

Table 4.11 The FTIR data (in cm^{-1}) of LC14 and its metal complexes

	Assignment								
	CH_2 (asym)	CH_2 (sym)	C=N	C=C(ar)	COO (asym)	COO (sym)	BF_4^-	M-N	M-O
LC14	2916s	2849s	1662m	1589m	-	-	-	-	-
13	2918s	2850s	1610m	1595m	1686w 1553m	1467m 1428m	-	553w	478w
14	2918s	2850s	1610m	1594m	1672m 1510m	1467m 1389m	-	531w	481w
15	2918s	2849m	1609m	1590m	-	-	1056m, br	592w	-
16	2917s	2849s	1610m	1594m	-	-	1054m, br	589w	-

s = strong; m = medium; w = weak; br = broad

4.5.2 $[Co_2(CH_3COO)_4(LC14)_2].2H_2O$

Ligand LC14 reacted with cobalt(II) acetate tetrahydrate, $Co(CH_3COO)_2.4H_2O$, in a 1:1 mole ratioto form a dark red powder **(Complex 13)**, and its yield was 73.7%. Its solubility was similar to the previously discussed complexes.

(a) Deduction of structural formula

Based on combined instrumental analytical data discussed below, it is proposed that the structural formula for **Complex 13** was $[Co_2(CH_3COO)_4(LC14)_2].2H_2O$, which was similar to **Complex 1** ($[Co_2(CH_3COO)_4(LC8)_2].3H_2O$; **Figure 4.3)**.

The results of the **elemental analyses** (73.84% C, 10.24% H, 2.02% N) were in good agreement with those calculated for the chemical formula $C_{172}H_{280}Co_2N_4O_{18}$ (73.52% C, 10.04% H, 1.99% N; formula weight, 2809.9 g mol^{-1}).

Its **FTIR** spectrum **(Figure 4.71)** shows peaks (in cm^{-1}) for the expected functional groups and bonds at 2918, 2850, 1686, 1610, 1595, 1553, 1467, 1428, 1266, 533 and 478 **(Table 4.11)**. These peaks may be similarly assigned as for **Complex 1** ($[Co_2(CH_3COO)_4(LC8)_2].3H_2O$). The Δ values for CH_3COO^- ligand were 219 cm^{-1} and 125 cm^{-1}, suggesting monodentate bridging and bidentate chelating binding modes [15, 49], respectively.

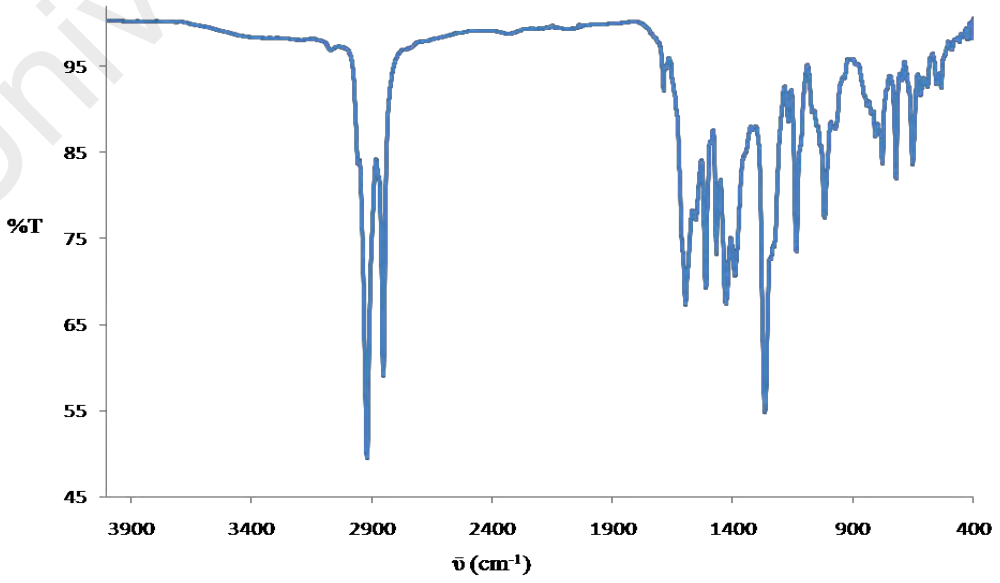

Figure 4.71 FTIR spectrum of **Complex 13**

Its **UV-vis** spectra in $CHCl_3$ (1.1 x 10^{-2} mol dm^{-3} for the *d-d* band, and 7.1 x 10^{-5} mol dm^{-3} for the MLCT bands) are shown in **Figure 4.72**. The spectra show a broad *d-d* band at 1200 nm (ε_{max}, 9.7 M^{-1} cm^{-1}; inset) and two MLCT peaks at 372 nm (ε_{max}, 3.9 x 10^4 M^{-1} cm^{-1}) and 296 nm (ε_{max}, 4.9 x 10^4 M^{-1} cm^{-1}). The *d-d* electronic transition is similarly assigned as for **Complex 1** ($[Co_2(CH_3COO)_4(LC8)_2].3H_2O$), suggesting a HS Co(II) complex.

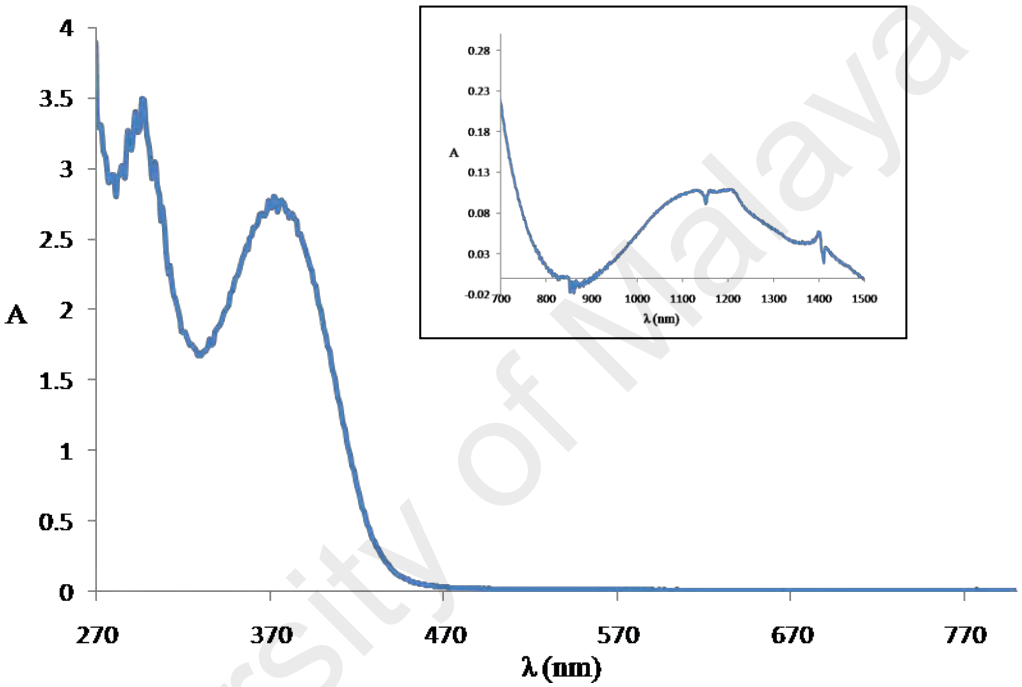

Figure 4.72 UV-vis spectrum of **Complex 13**

(b) Band gap

The E_o value for **Complex 13** was 2.75 eV (λ_{onset} = 450 nm). This was slightly higher compared to **Complex 9** ($[Co_2(CH_3COO)_4(LC12)_2].2H_2O$; E_o = 2.61 eV).

Its **CV** scan (**Figure 4.73**) shows overlapping anodic peaks at +0.90 V assigned to oxidation of [Co(II)Co(II)] to [Co(II)Co(III)] and LC14 to $LC14^+$, and two corresponding cathodic peaks at -0.10 V and -0.85 V assigned to reduction of [Co(II)Co(III)] to [Co(II)Co(II)] and $LC14^+$ to LC14, respectively. The metal-based ΔE_p was 1000 mV, suggesting a quasireversible redox reaction [68]. Hence, its redox behaviour was similar with **Complex 1** ($[Co_2(CH_3COO)_4(LC8)_2].3H_2O$).

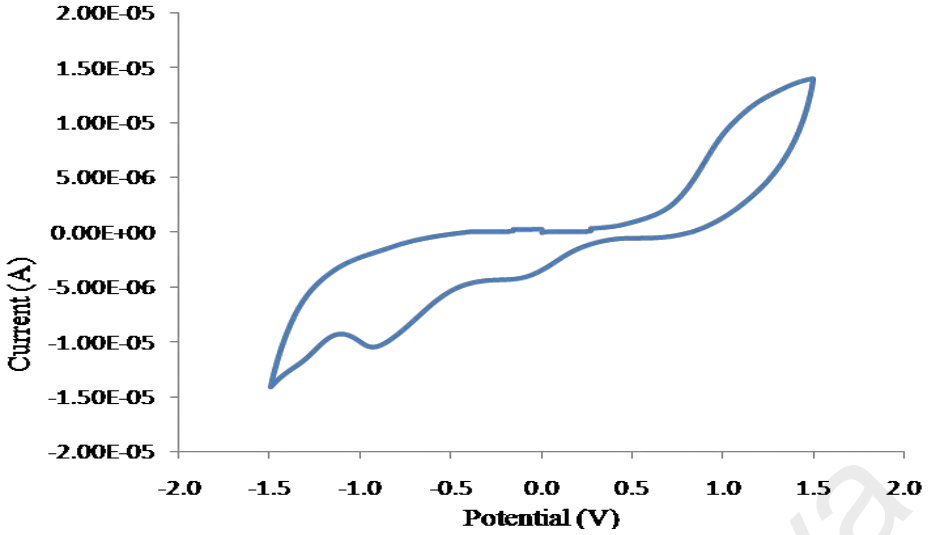

Figure 4.73 Cyclic voltammetry of **Complex 13**

Its E_e value, similarly calculated as previously done from the onset potentials for oxidation (+0.75 V) and reduction (+0.20 V), the values for E_{HOMO} (5.15 eV) and E_{LUMO} (4.60 eV), was 0.55 eV. This was similar with **Complex 9** ($[Co_2(CH_3COO)_4(LC12)_2].2H_2O$; E_e = 0.50 eV).

(c) Magnetic properties

Its $\chi_M T$ value, similarly calculated as before from its proposed chemical formula (FW = 2809.9 g mol^{-1}), χ_g (4.01 x 10^{-6} cm^3 g^{-1}), χ_M (1.13 x 10^{-2} cm^3 mol^{-1}), χ_D (-1.91 x 10^{-3} cm^3 mol^{-1}) and χ_M^{corr} (1.25 x 10^{-2} cm^3 mol^{-1}), was 3.96 cm^3 K mol^{-1} at 298 K. Accordingly, both of its Co(II) atoms were HS at this temperature. This result was similar with **Complexes 1** ($[Co_2(CH_3COO)_4(LC8)_2].3H_2O$), **5** ($[Co_2(CH_3COO)_4(LC10)_2].H_2O$) and **9** ($[Co_2(CH_3COO)_4(LC12)_2].2H_2O$).

(*d) Thermal properties*

The **TGA** trace for **Complex 13** (**Figure 4.74**) shows a total mass loss of 94.1% from 179 ^oC to 670 ^oC due to the decomposition of CH_3COO^- ion and LC14 (calculated, 94.6%). The amount of residue was 6.0% at temperatures above 670 ^oC. This was in good agreement with the calculated value of 5.4%, assuming pure CoO [30]. Hence, its

decomposition temperature was 179 ^{o}C, which was similar with **Complex 9** ($[Co_2(CH_3COO)_4(LC12)_2].2H_2O$; T_{dec} = 182 ^{o}C).

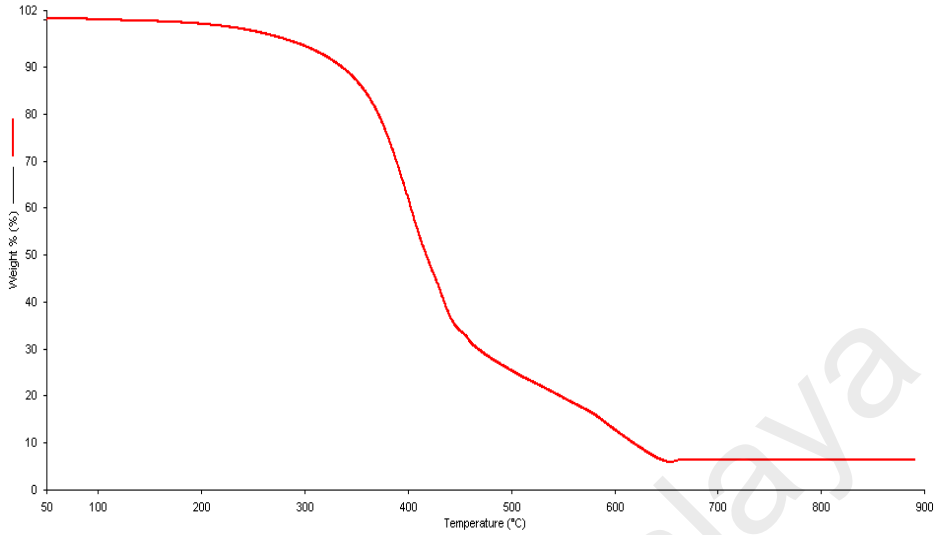

Figure 4.74 TGA trace of **Complex 13**

(e) Thermoelectric properties

Graphs of ΔV *versus* ΔT for **Complex 13 (Figure 4.75)** were linear up to ΔT of about 28 K, indicating a good thermoelectric behaviour. Its mean S_e value was -0.60 ± 0.02 mV K^{-1}, which was similar to **Complex 1** ($[Co_2(CH_3COO)_4(LC8)_2].3H_2O$; S_e = -0.58 ± 0.03 mV K^{-1}), **Complex 5** ($[Co_2(CH_3COO)_4(LC10)_2].H_2O$; S_e = -0.58 ± 0.03 mV K^{-1} for the cooling cycles only), and **Complex 9** ($[Co_2(CH_3COO)_4(LC12)_2].2H_2O$; S_e = -0.53 ± 0.01 mV K^{-1} for the second and third heating cycles only), in agreement with the similarity in their structures and same spin states (100% HS Co(II) atoms).

However, **Complex 13** showed better thermoelectric behaviour compared to its analogs with shorter alkyloxy chains in the bipyridyl ligands. It is noted earlier that dimeric molecular complexes with long alkyloxy chains formed less stable micelle-like structures, which dissociated more readily to the monomers in $CHCl_3$. Thus, it is likely that the good thermoelectric behaviour observed for this complex was that of its monomer.

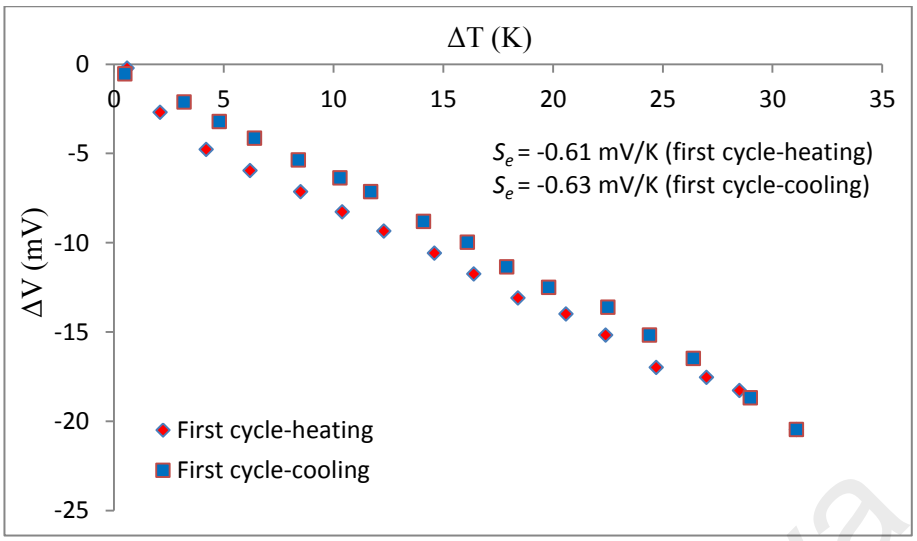

(a)

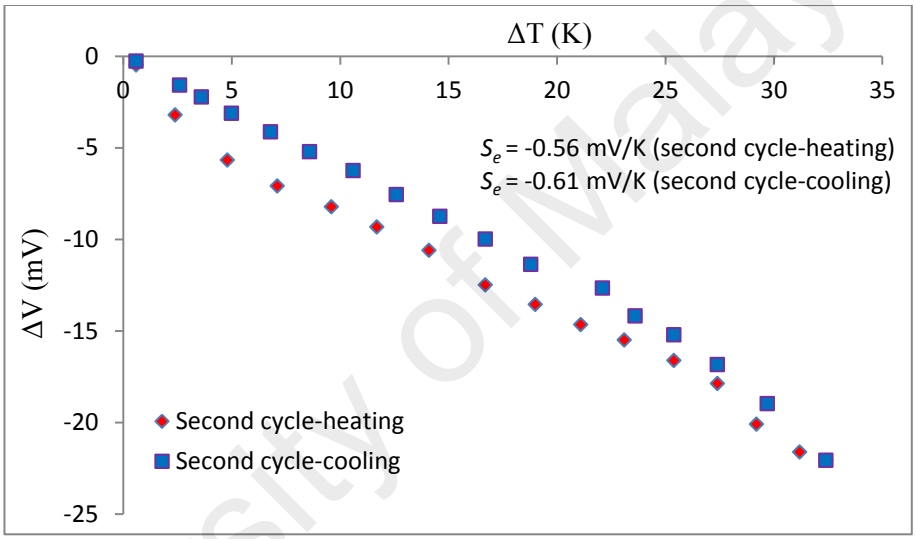

(b)

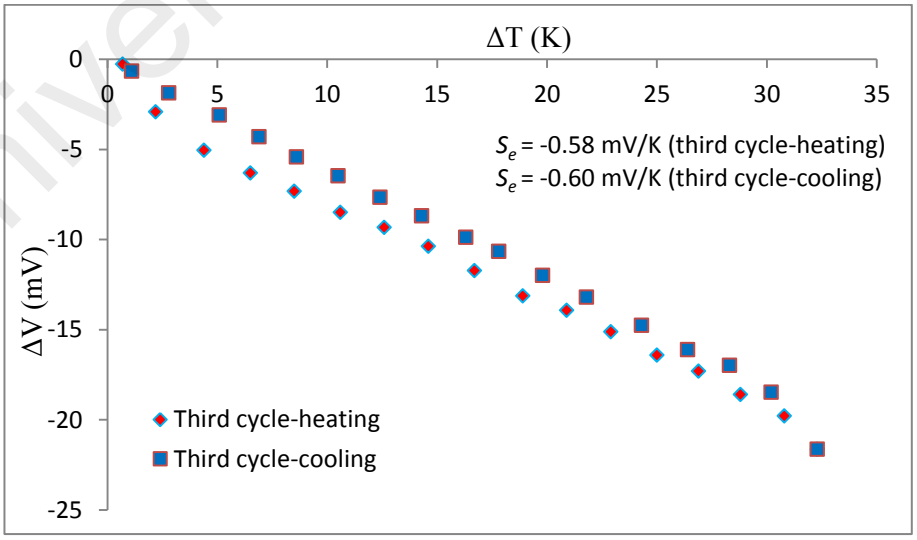

(c)

Figure 4.75 Graphs of ΔV *versus* ΔT for **Complex 13**: (a) first; (b) second; and (c) third heating-and-cooling cycles

4.5.3 $[Fe_2(CH_3COO)_4(LC14)_2].4H_2O$

Ligand **LC14** reacted with iron(II) acetate, $Fe(CH_3COO)_2$in a mole ratio of 1:1 to form a black powder **(Complex 14)**, and its yield was 77.8%. Its solubility was similar to the previously discussed complexes.

(a) Deduction of structural formula

From combined instrumental data discussed below, it is proposed that **Complex 14 (**$[Fe_2(CH_3COO)_4(LC14)_2].4H_2O$) has similar structure as **Complex 1** ($[Co_2(CH_3COO)_4(LC8)_2].3H_2O$; **Figure 4.3**).

The results of the **elemental analyses** (72.58% C, 10.07% H, 1.70% N) were in good agreement with those calculated for the chemical formula $C_{172}H_{284}Fe_2N_4O_{20}$ (72.75% C, 10.08% H, 1.97% N; formula weight, 2839.8 g mol^{-1}).

Its **FTIR** spectrum **(Figure 4.76)** shows shows peaks (in cm^{-1}) for the expected functional groups and bonds at 2918, 2850, 1672, 1610, 1594, 1510, 1467, 1389, 1266, 531 and 481 **(Table 4.11)**. These peaks may be similarly assigned as for **Complex 1** ($[Co_2(CH_3COO)_4(LC8)_2].3H_2O$). The Δ values for CH_3COO^-ligand were 205 cm^{-1} and 121 cm^{-1}, suggesting monodentate bridging and bidentate chelating binding modes [15, 49], respectively.

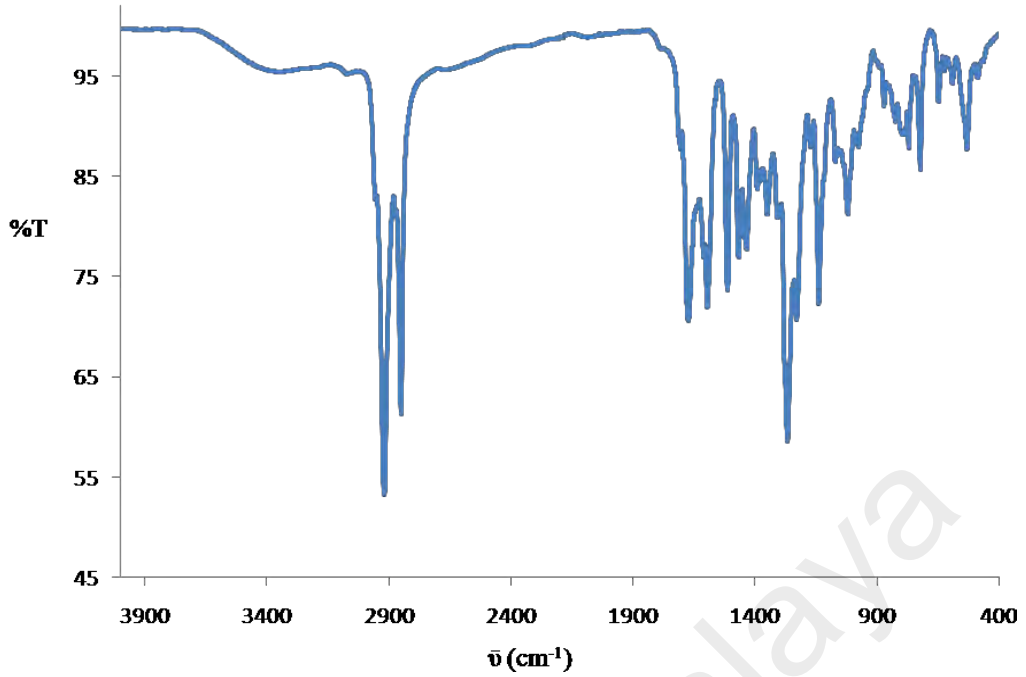

Figure 4.76 FTIR spectrum of **Complex 14**

Its **UV-vis** spectrum recorded in $CHCl_3$ **(Figure 4.77**; 1.4 x 10^{-4} mol dm^{-3}) shows a weak *d-d* band which appeared as a shoulder at about 630 nm (ε, 4.3 x 10^2 M^{-1} cm^{-1}), and strong MLCT bands at 546 nm (ε_{max}, 1.1 x 10^3 M^{-1} cm^{-1}), 360 nm (ε_{max}, 6.3 x 10^3 M^{-1} cm^{-1}), 301 nm (ε_{max}, 7.9 x 10^3 M^{-1} cm^{-1}) and 263 nm (ε_{max}, 8.3 x 10^3 M^{-1} cm^{-1}). The *d-d* electronic transition is similarly assigned as for **Complex 6** ($[Fe_2(CH_3COO)_4(LC10)_2].3H_2O$) and **Complex 10** ($[Fe_2(CH_3COO)_4(LC12)_2].2H_2O$).

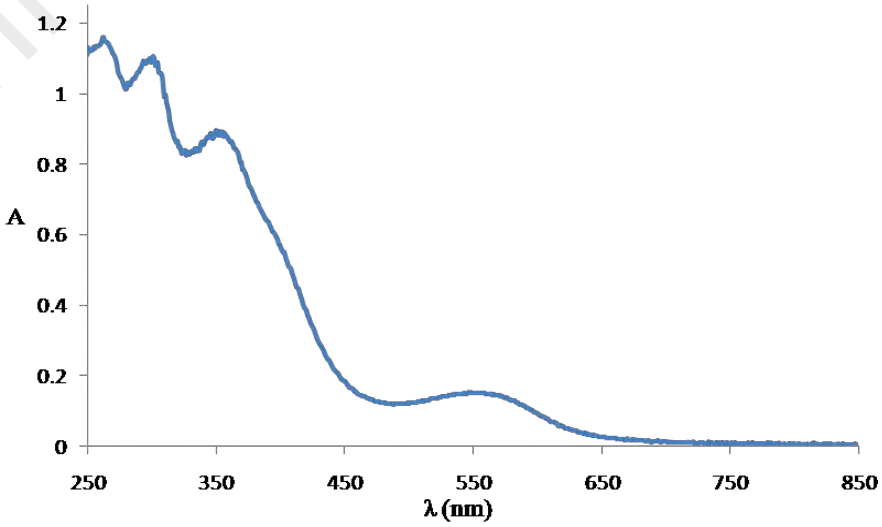

Figure 4.77 UV-vis spectrum of **Complex 14**

(b) Band gap

Its E_o, calculated as before, was 1.93 eV (λ_{onset} = 640 nm). This was slightly higher than **Complex 10** ($[Fe_2(CH_3COO)_4(LC12)_2].2H_2O$; E_o = 1.85 eV).

Its **CV** scan **(Figure 4.78)** shows two overlapping anodic peaks at +0.80 V and +1.10 V assigned to oxidation of [Fe(II)Fe(II)] to [Fe(II)Fe(III)] and LC14 to $LC14^+$, respectively, and two corresponding cathodic peaks at +0.10 V and -0.90 V assigned to reduction of [Fe(II)Fe(III)] to [Fe(II)Fe(II)] and $LC14^+$ to LC14. Accordingly, the metal-based ΔE_p was 700 mV, indicating a quasireversible redox reaction [68]. Hence, its redox behaviour was similar with **Complex 2** ($[Fe_2(CH_3COO)_4(LC8)_2]$).

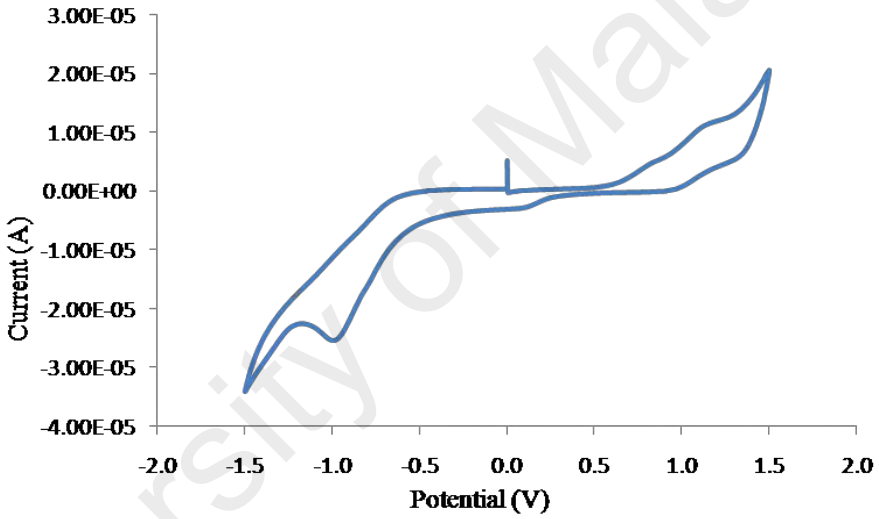

Figure 4.78 Cyclic voltammetry of **Complex 14**

Its E_e value, similarly calculated as previously done from the onset potentials for oxidation (+0.66 V) and reduction (+0.20 eV), the values for E_{HOMO} (5.06 eV) and E_{LUMO} (4.60 eV), was 0.46 eV. This value was similar with **Complex 6** ($[Fe_2(CH_3COO)_4(LC10)_2].3H_2O$; E_e = 0.49 eV) and **Complex 10** ($[Fe_2(CH_3COO)_4(LC12)_2].2H_2O$; E_e = 0.48 eV).

(c) Magnetic properties

The value of $\chi_M T$ for **Complex 14,** calculated as before from its proposed chemical formula (FW = 2839.8 g mol^{-1}), χ_g (3.73 x 10^{-6} cm^3 g^{-1}), χ_M (1.06 x 10^{-2} cm^3 mol^{-1}),

χ_D (-1.93 x 10^{-3} cm^3 mol^{-1}) and χ_M^{corr} (1.25 x 10^{-2} cm^3 mol^{-1}), was 5.46 cm^3 K mol^{-1} at 298 K. Hence, the complex was made up of 62.5% HS and 37.5% LS Fe(II) atoms. This suggests that it has stronger Fe-O and Fe-N bonds compared to **Complex 10** (100% HS).

(d) Thermal properties

Its **TGA** trace for **Complex 14 (Figure 4.79)** shows a total mass loss of 93.8% from 171 ^oC to 730 ^oC due to the decomposition of CH_3COO^- ions and LC14 (calculated, 94.8%). The amount of residue at temperatures above 730 ^oC was 6.2%, which was in good agreement with the calculated value of 5.2%, assuming pure FeO. Therefore, its decomposition temperature was 171 ^oC, which was similar with **Complex 10** ($[Fe_2(CH_3COO)_4(LC12)_2].2H_2O$; T_{dec} = 170 ^oC).

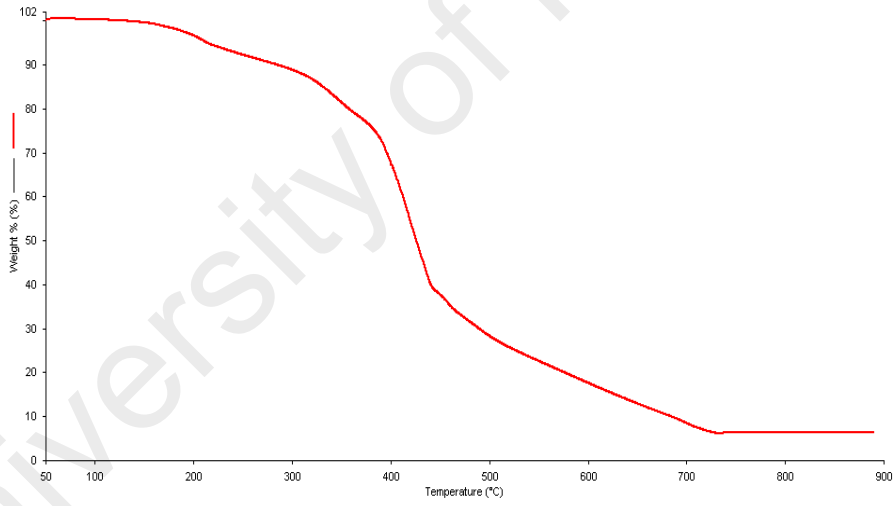

Figure 4.79 TGA trace of **Complex 14**

(e) Thermoelectric properties

Graphs of ΔV *versus* ΔT for **Complex 14** (**Figure 4.80**) were linear, indicating a good thermoelectric behaviour. However, its mean S_e value of -0.44 ± 0.01 mV K^{-1}, which was lower compared to **Complex 2** ($[Fe_2(CH_3COO)_4(LC8)_2]$; S_e = -0.51 ± 0.01 mV K^{-1}), **Complex 6** ($[Fe_2(CH_3COO)_4(LC10)_2].3H_2O$; S_e = -0.56 ± 0.02 mV K^{-1}), and **Complex 10** ($[Fe_2(CH_3COO)_4(LC12)_2].2H_2O$; S_e = -0.61 ± 0.02 mV K^{-1}), and may be

due to the lower percentage of HS Fe(II) atoms in this complex (62.5%) compared to **Complex 2** (68.5% HS), **Complex 6** (91.0% HS), and **Complex 10** (100% HS). Accordingly, there were more molecules in **Complex 14** with stronger Fe-N and Fe-O bonds (lower entropy).

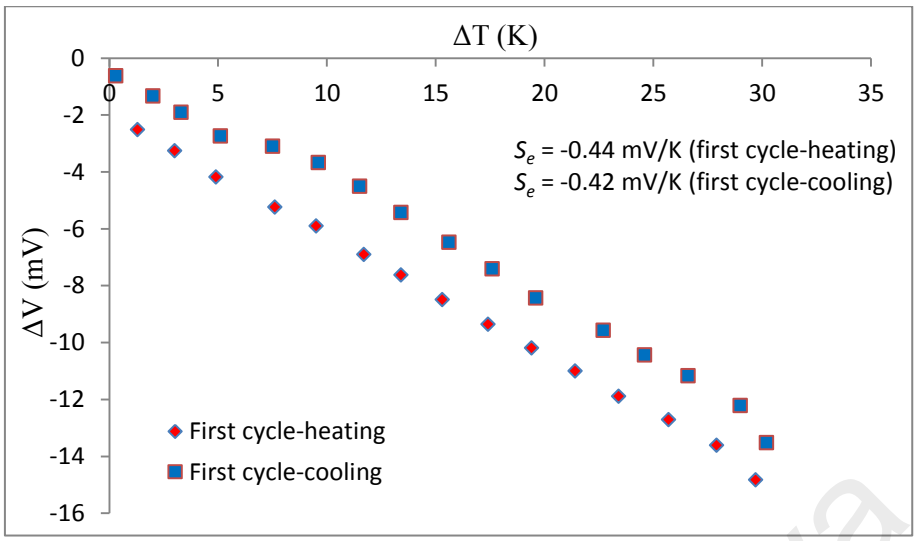

(a)

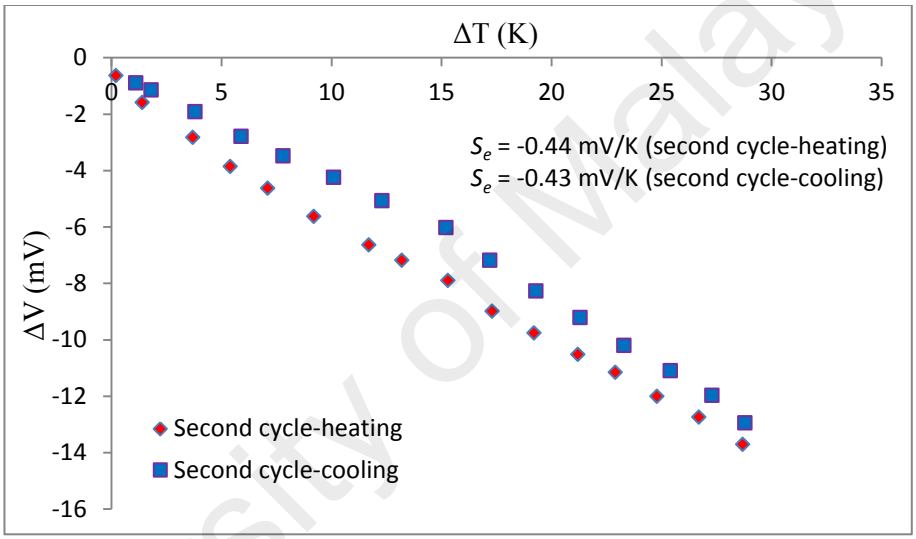

(b)

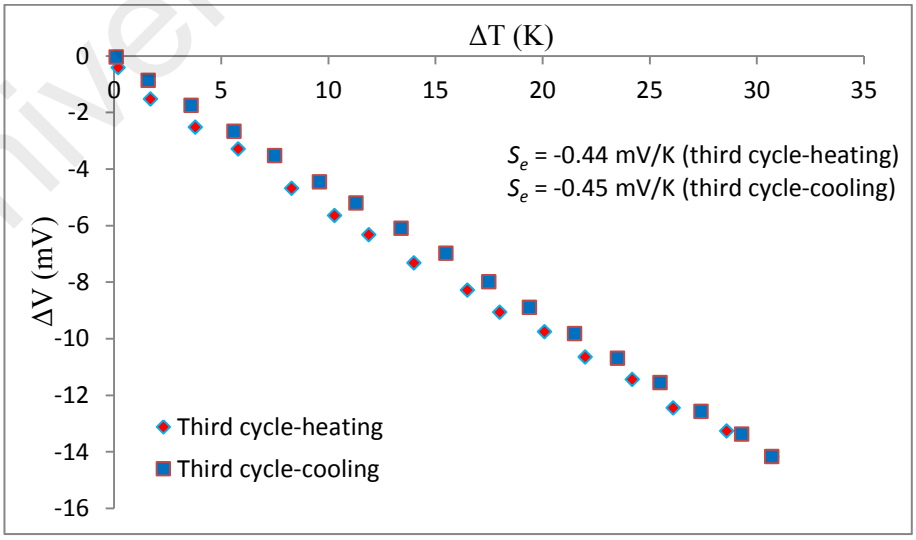

(c)

Figure 4.80 Graphs of ΔV *versus* ΔT for **Complex 14**: (a) first; (b) second; and (c) third heating-and-cooling cycles

4.5.4 $[Co(LC14)_3](BF_4)_2.4H_2O$

Cobalt(II) tetrafluoroborate hexahydrate, $Co(BF_4)_2.6H_2O$, reacted with **LC14** in a mole ratio of 1:3 to form a dark red powder **(Complex 15)**, and its yield was 71.4%. Its solubility was similar to the previously discussed complexes.

(a) Deduction of structural formula

Based on combined instrumental data discussed below, it is proposed that the structural formula for **Complex 15** was $[Co(LC14)_3](BF_4)_2.4H_2O$), which was similar with **Complex 3** ($[Co(LC8)_3](BF_4)_2.2H_2O$; **Figure 4.14**).

The results of the **elemental analyses** (74.99% C, 10.72% H, 1.94% N) were in good agreement with those calculated for the chemical formula $C_{246}H_{404}B_2CoF_8N_6O_{16}$ (75.10% C, 10.35% H, 2.14% N; formula weight: 3934.4 g mol^{-1}).

Its **FTIR** spectrum (**Figure 4.81**) shows peaks (in cm^{-1}) for the expected functional groups and bonds at 2918, 2849, 1609, 1590, 1056 and 592 (**Table 4.11**). These peaks may be similarly assigned as for **Complex 3**.

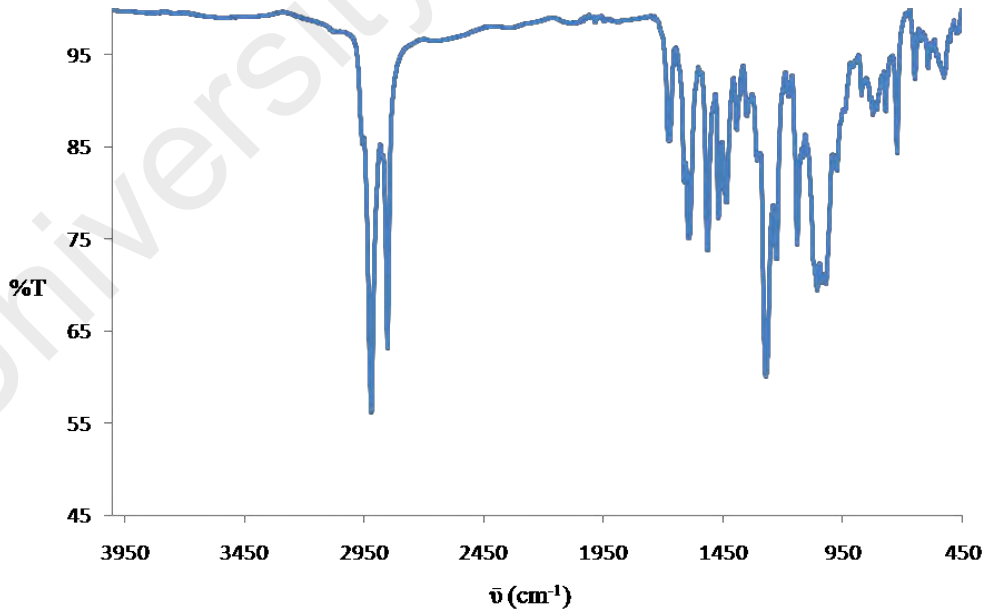

Figure 4.81 FTIR spectrum of **Complex 15**

Its **UV-vis** spectrum in $CHCl_3$ **(Figure 4.82**; 1.3 x 10^{-4} mol dm^{-3}) shows a weak *d-d* band which appeared as a shoulder at about 550 nm (ε_{max}, 4.6 x 10^2 M^{-1} cm^{-1}) and a

strong MLCT band at 413 nm (ε_{max}, 6.0 x 10^3 M^{-1} cm^{-1}). The *d-d* band is assigned to $^2A_{1g} \rightarrow {}^2T_{1g}$ electronic transition for a LS Co(II) complex [28].

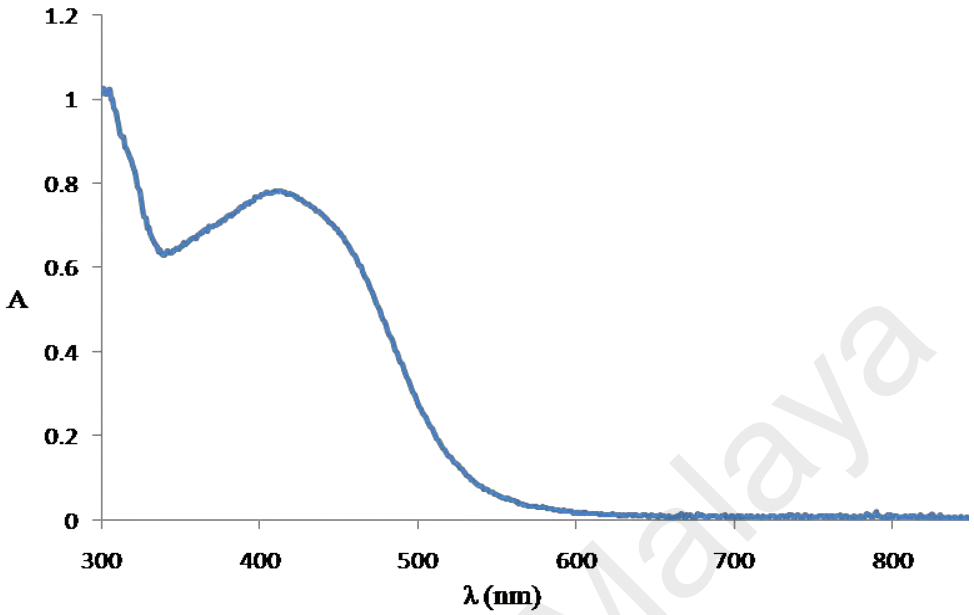

Figure 4.82 UV-vis spectrum of **Complex 15**

(b) Band gap

The E_o for **Complex 15**, calculated as before, was 2.31 eV (λ_{onset} = 535 nm). This value was similar to **Complex 11** ($[Co(LC12)_3](BF_4)_2.3H_2O$; E_o = 2.25 eV).

Its **CV** scan **(Figure 4.83)** shows two overlapping anodic peaks at +0.76 V and +1.00 V assigned to oxidation of [Co(II)] to [Co(III)] and LC14 to $LC14^+$, respectively, and two corresponding cathodic peaks at +0.15 V and -0.85 V assigned to reduction of [Co(III)] to [Co(II)] and $LC14^+$ to LC14, respectively. Thus, the metal-based ΔE_p was 610 mV, indicating a quasireversible redox reaction [68]. Hence, its redox behaviour was similar with **Complex 3** ($[Co(LC8)_3](BF_4)_2.2H_2O$).

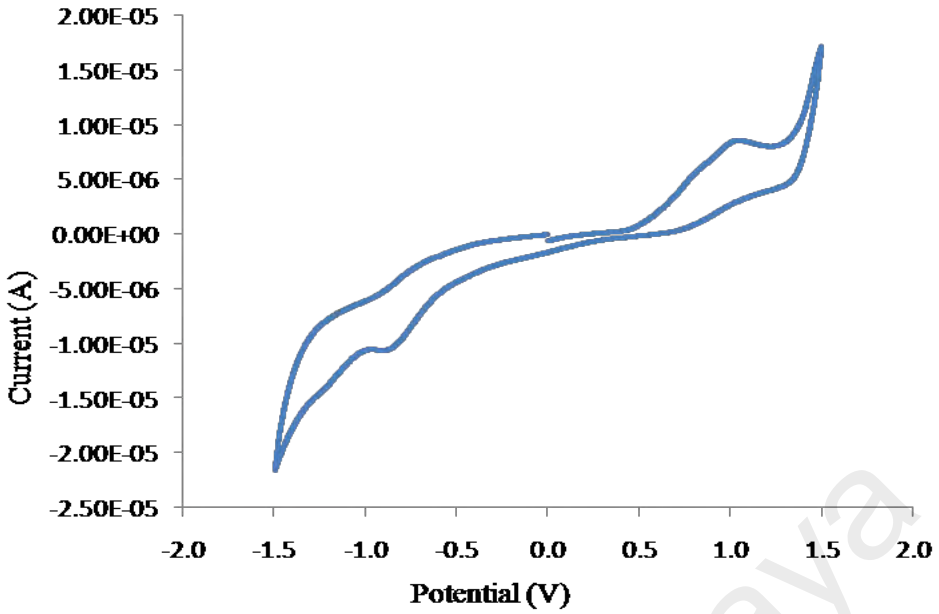

Figure 4.83 Cyclic voltammetry of **Complex 15**

Its E_e value, similarly calculated as previously done from the onset potentials for oxidation (+0.62 V) and reduction (+0.30 eV), the values for E_{HOMO} (5.02 eV) and E_{LUMO} (4.70 eV), was 0.32 eV. The value was similar with **Complex 11** ($[Co(LC12)_3](BF_4)_2.3H_2O$; E_e = 0.35 eV).

(c) Magnetic properties

The $\chi_M T$ value for **Complex 15**, calculated above before from its proposed chemical formula (FW = 3934.4 g mol^{-1}), χ_g (0.51 x 10^{-6} cm^3 g^{-1}), χ_M (2.01 x 10^{-3} cm^3 mol^{-1}), χ_D (-2.87 x 10^{-3} cm^3 mol^{-1}) and χ_M^{corr} (4.87 x 10^{-3} cm^3 mol^{-1}), was 1.45 cm^3 K mol^{-1} at 298 K. Hence, it may be concluded that this complex was made up of 71.8% HS and 28.2% LS Co(II) atoms at this temperature. Thus, the Co-N bonds in this complex was stronger than **Complex 11** (100% HS).

(d) Thermal properties

The **TGA** trace for **Complex 15 (Figure 4.84)** shows a total mass loss of 97.9% from 258 ^oC to 865 ^oC due to loss of BF_3 (from BF_4^- ions) and decomposition of LC14 (calculated, 97.5%). The amount of residue at temperatures above 865 ^oC was 2.1%

(calculated 2.5%, assuming pure CoF_2 [73]). Hence, its decomposition temperature was 258 ^oC, which was similar with **Complex 11** ($[Co(LC12)_3](BF_4)_2.3H_2O$; T_{dec} = 260 ^oC).

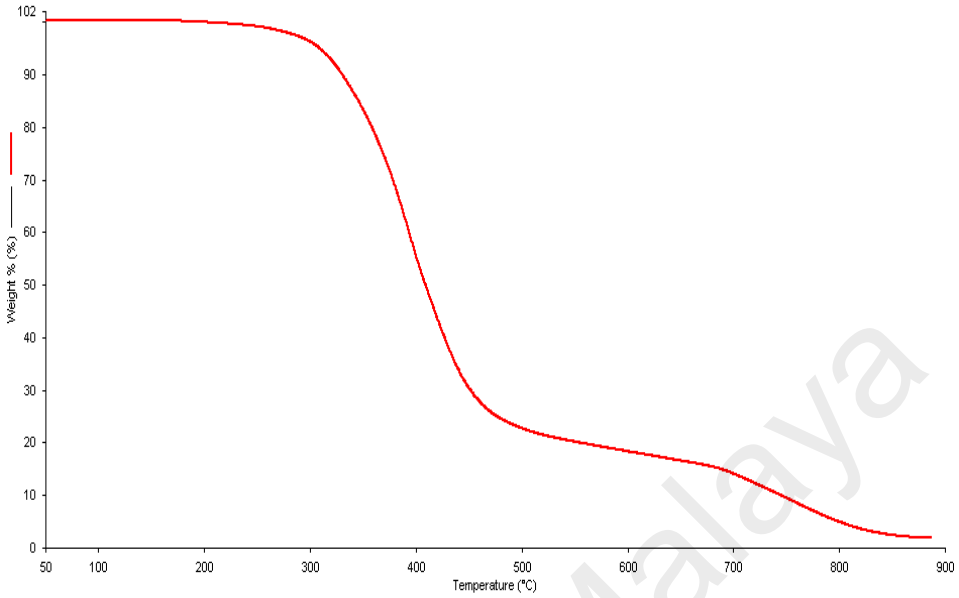

Figure 4.84 TGA trace of **Complex 15**

(e) Thermoelectric properties

Graphs of ΔV *versus* ΔT for **Complex 15 (Figure 4.85)** were satisfactory only in the cooling cycles, indicating good thermoelectric behaviour. This behaviour was similar to its shorter alkyoxy chains analogs, ligands, namely $[Co(LC8)_3](BF_4)_2.2H_2O$ **(Complex 3)** and $[Co(LC10)_3](BF_4)_2.4H_2O$ **(Complex 7)**, but not to $[Co(LC12)_3](BF_4)_2.3H_2O$ **(Complex 11)**, which showed good thermoelectric behaviours in all three heating-and-cooling cycles.

The mean S_e values for **Complex 15** in the cooling cycles was -0.35 ± 0.02 mV K^{-1}. This was lower compared to **Complex 3** (-0.45 ± 0.01 mV K^{-1}), **Complex 7** (-0.40 ± 0.01 mV K^{-1}) and **Complex 11** (-0.44 ± 0.01 mV K^{-1}) under similar conditions. It is postulated that the latter complex formed more stable micelle-like structures in $CHCl_3$ due to the longer alkyoxy chains, which more effectively trapped the charge carriers.

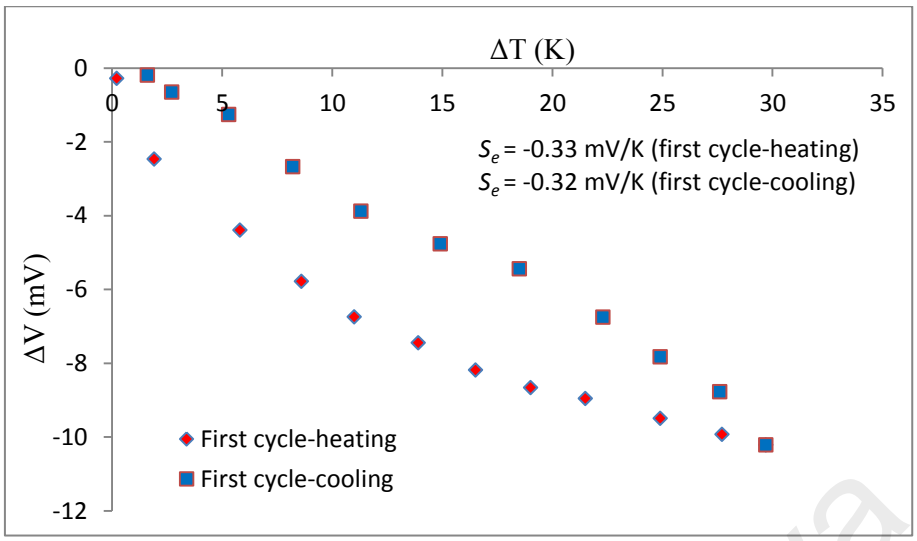

(a)

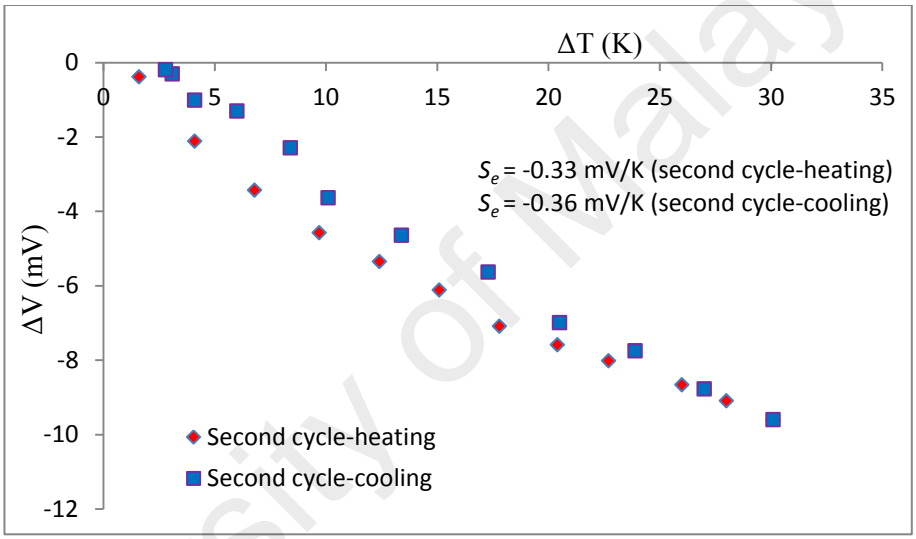

(b)

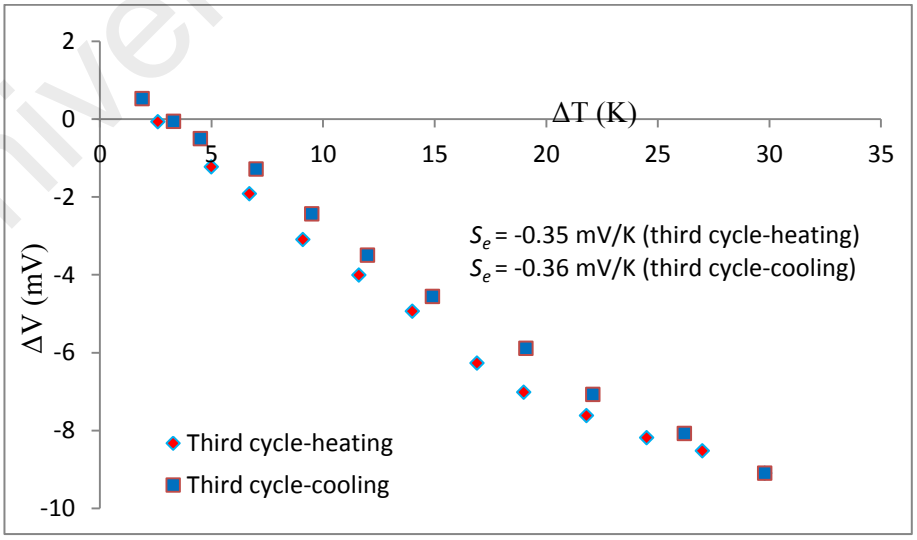

(c)

Figure 4.85 Graphs of ΔV versus ΔT for **Complex 15**: (a) first; (b) second; and (c) third heating-and-cooling cycles

4.5.5 [Fe(LC14)$_3$](BF$_4$)$_2$.4H$_2$O

Iron(II) tetrafluoroborate hexahydrate, $Fe(BF_4)_2.6H_2O$, reacted with LC14 in a mole ratio of 1:3 to form a black powder **(Complex 16)**, and its yield was 80.1%. Its solubility was similar to the previously discussed complexes.

(a) Deduction of structural formula

Based on combined instrumental data discussed below, it is proposed that the structural formula for **Complex 16** was $[Fe(LC14)_3](BF_4)_2.4H_2O$, which was similar with **Complex 3** ($[Co(LC8)_3](BF_4)_2.2H_2O$; **Figure 4.14**).

The results of the **elemental analyses** (75.06% C, 10.49% H, 2.21% N) were in good agreement with those calculated for the chemical formula $C_{246}H_{404}B_2F_8FeN_6O_{16}$ (75.16% C, 10.36% H, 2.14% N; formula weight: 3931.3 g mol^{-1}).

Its **FTIR** spectrum **(Figure 4.86)** shows peaks (in cm^{-1}) for the expected functional groups and bonds at 2917, 2849, 1610, 1594, 1054 and 589 (**Table 4.11**). These peaks may be similarly assigned as for **Complex 3**.

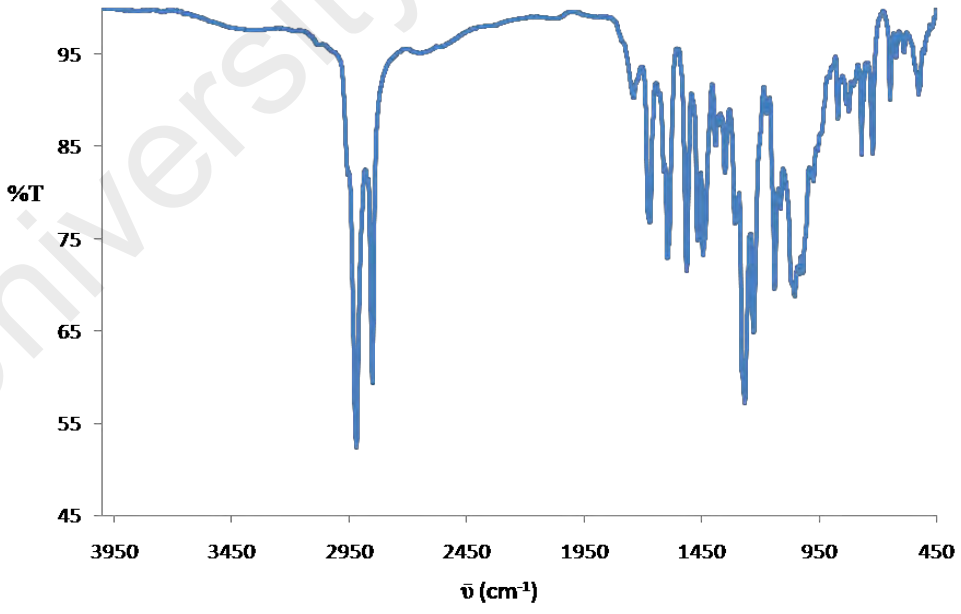

Figure 4.86 FTIR spectrum of **Complex 16**

Its **UV-vis** spectrum recorded in $CHCl_3$ **(Figure 4.87;** 2.5 x 10^{-4} mol dm^{-3}), shows a weak *d-d* band which appeared as a shoulder at about 630 nm

(ε_{max}, 6.0 x 10^2 M^{-1} cm^{-1}), and three strong MLCT bands at 561 nm (ε_{max}, 1.3 x 10^3 M^{-1} cm^{-1}), 392 nm (ε_{max}, 4.0 x 10^3 M^{-1} cm^{-1}) and 301 nm (ε_{max}, 4.4 x 10^3 M^{-1} cm^{-1}). The *d-d* electronic transition may be similarly assigned as for **Complex 6** ($[Fe_2(CH_3COO)_4(LC10)_2].3H_2O$) and **Complex 10** ($[Fe_2(CH_3COO)_4(LC12)_2].2H_2O$).

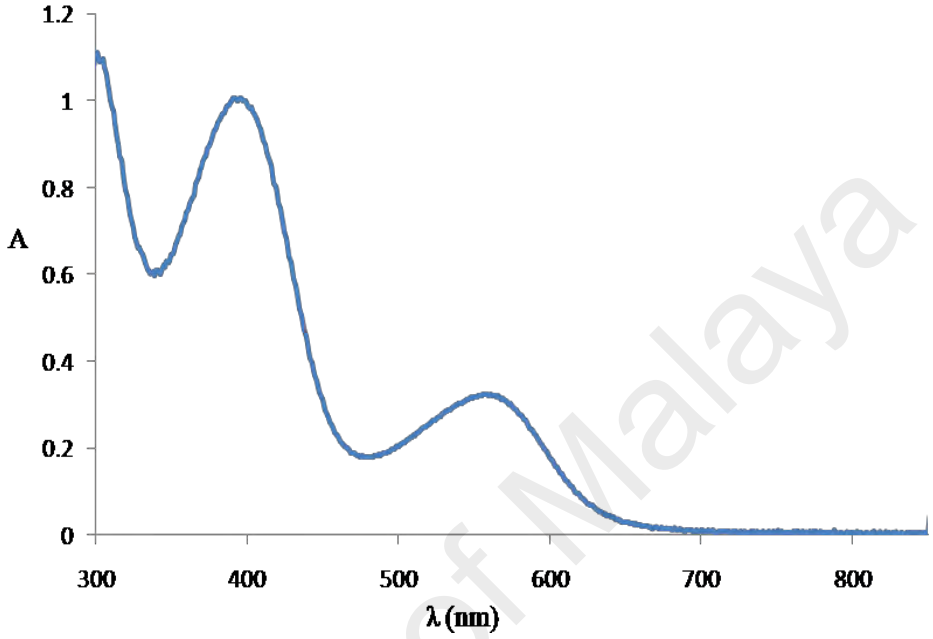

Figure 4.87 UV-vis spectrum for **Complex 16**

(b) Band gap

The E_o value for **Complex 16**, calculated as for previous complexes, was 1.93 eV (λ_{onset} = 640 nm). This was similar with **Complex 12** ($[Fe(LC12)_3](BF_4)_2.3H_2O$; E_o = 1.93 eV).

The **CV** scan for **Complex 16 (Figure 4.88)** shows two anodic peaks at +0.75 V and +1.25 V assigned to oxidation of [Fe(II)] to [Fe(III)] and LC14 to $LC14^+$, respectively, and two corresponding cathodic peaks at +0.15 V and -0.95 V assigned to reduction of [Fe(III)] to [Fe(II)] and $LC14^+$ to LC14, respectively. The metal-based ΔE_p was 600 mV, suggesting a quasireversible redox reaction [68]. Hence, its behaviour was similar with **Complex 4** ($[Fe(LC8)_3](BF_4)_2.H_2O$).

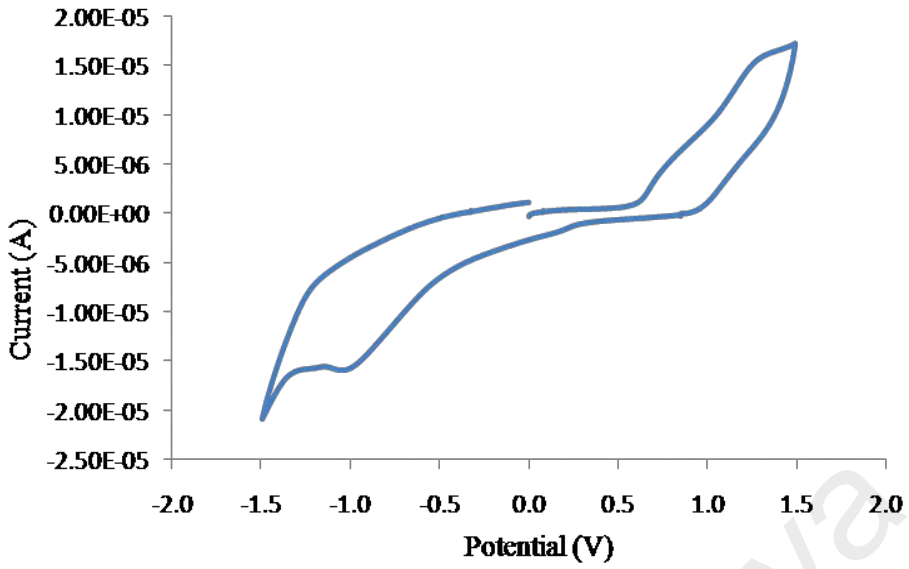

Figure 4.88 Cyclic voltammetry of **Complex 16**

Its E_e value, similarly calculated as previously done from the onset potentials for oxidation (+0.65 V) and reduction (+0.30 eV), the values for E_{HOMO} (5.05 eV) and E_{LUMO} (4.70 eV), was 0.35 eV. This value was similar to **Complex 12** ($[Fe(LC12)_3](BF_4)_2.3H_2O$; E_e = 0.36 eV).

(c) Magnetic properties

The $\chi_M T$ value for **Complex 16**, calculated as before from its proposed chemical formula (FW = 3931.30 g mol^{-1}), χ_g (0.05 x 10^{-6} cm^3 g^{-1}), χ_M (1.96 x 10^{-4} cm^3 mol^{-1}), χ_D (-2.79 x 10^{-3} cm^3 mol^{-1}) and χ_M^{corr} (2.98 x 10^{-3} cm^3 mol^{-1}), was 0.89 cm^3 K mol^{-1} at 298 K. Thus, the **Complex 16** was made up of 29.6% HS Fe(II) and 70.4% LS Fe(II) atoms at this temperature, indicating weaker Fe-N bonds compared to **Complex 12** (100% LS Fe(II) atom).

(d) Thermal properties

TGA trace for **Complex 16** (**Figure 4.89**) shows a total mass loss of 96.7% from 256 ^oC to 750 ^oC due to loss of BF_3 (from BF_4^- ions) and decomposition of LC14 (calculated, 97.6%). The amount of residue at temperatures above 750 ^oC was 3.3% (calculated, 2.4% assuming pure FeF_2 [73]). Therefore, its decomposition temperature

was 256 °C, which was similar to **Complex 12** ($[Fe(LC12)_3](BF_4)_2.3H_2O$; T_{dec} = 262 °C).

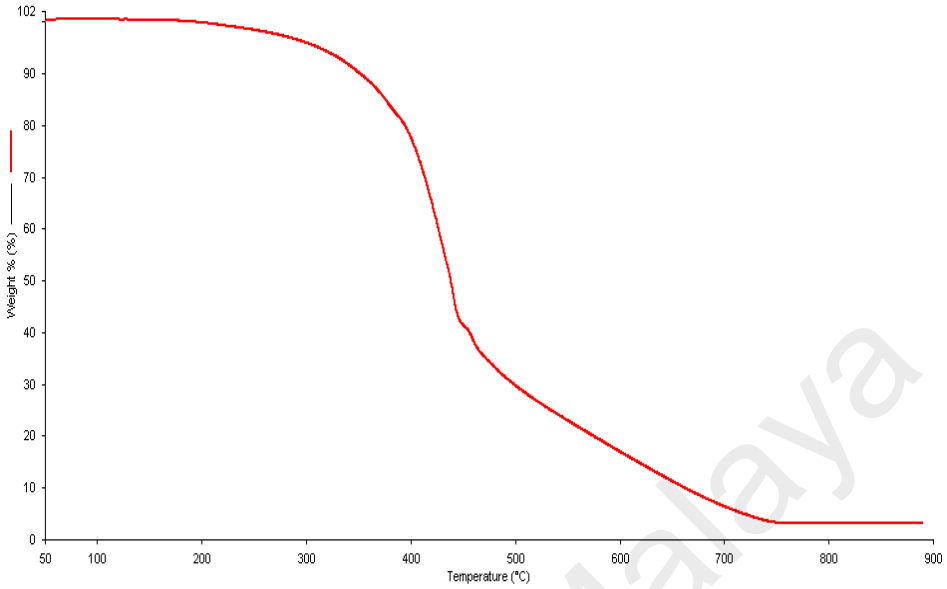

Figure 4.89 TGA trace of **Complex 16**

(e) Thermoelectric properties

Graphs of ΔV *versus* ΔT for **Complex 16 (Figure 4.90)** were linear for all three heating-and-cooling cycles, indicating good thermoelectric behaviour. Its mean S_e value was -0.54 ± 0.02 mV K^{-1}. Hence, its S_e value and thermoelectric behaviour were similar with its shorter chain analogs, namely $[Fe(LC8)_3](BF_4)_2.H_2O$ (**Complex 4**; S_e = -0.55 ± 0.03 mV K^{-1}), $[Fe(LC10)_3](BF_4)_2.3H_2O$ (**Complex 8**; S_e = -0.51 ± 0.01 mV K^{-1}), and $[Fe(LC12)_3](BF_4)_2.3H_2O$ (**Complex 12**; S_e = -0.52 ± 0.01 mV K^{-1}). Since these complexes have similar structural formulas and same spin states (100% LS Fe(II) atoms, it may be concluded that the thermoelectric behaviours of these complexes were independent of the alkyloxy chain lengths in the bipyridyl ligands.

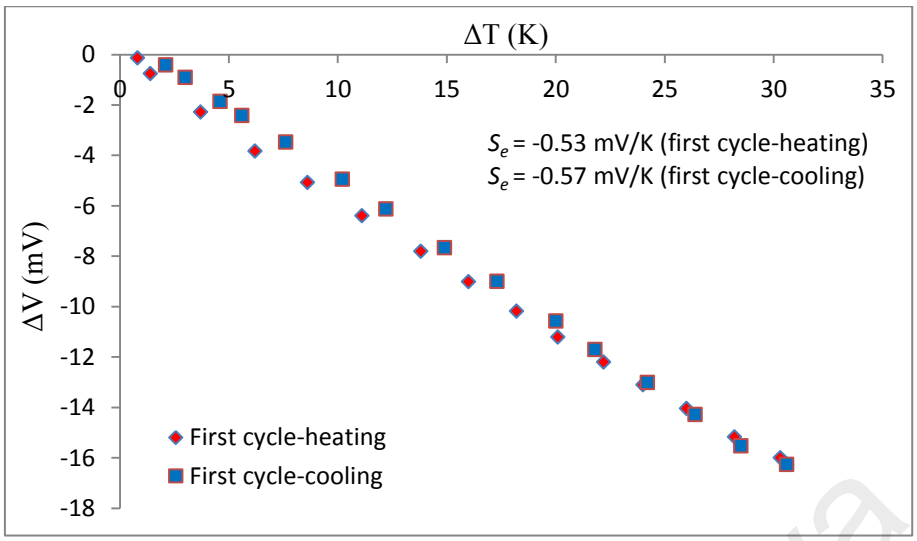

(a)

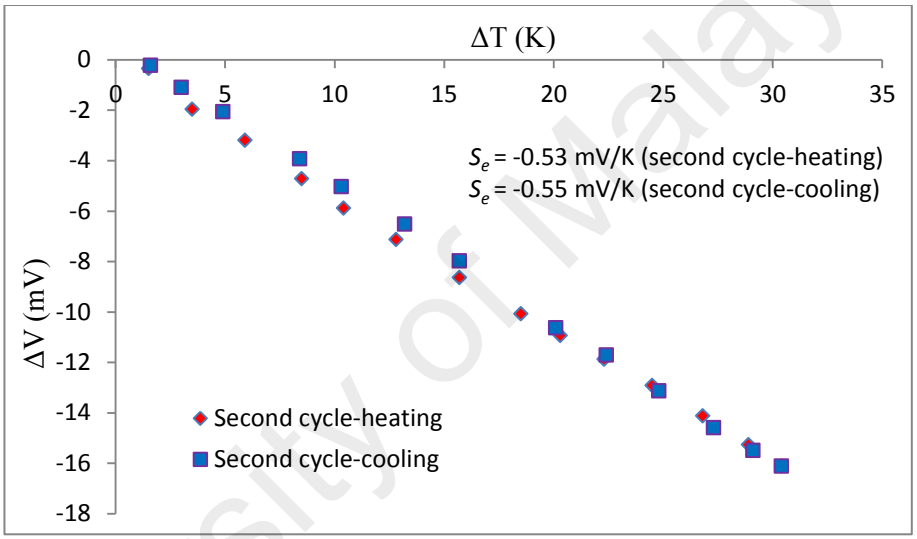

(b)

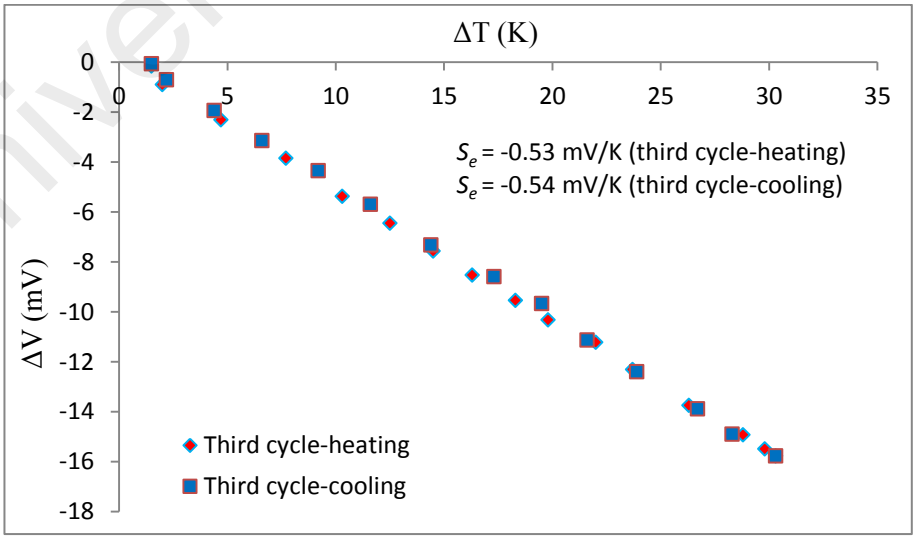

(c)

Figure 4.90 Graphs of ΔV *versus* ΔT for **Complex 16**: (a) first; (b) second; and (c) third heating-and-cooling cycles

4.5.6 Summary

The results for **Complexes 13 - 16** are summarised in **Table 4.12**. Except for the thermoelectric behaviour (S_e values), these results were similar with those for **Complexes 1 - 4** (**Table 4.3**), **Complexes 5 - 8** (**Table 4.6**) and **Complexes 9 - 12** (**Table 4.9**), and may be similarly explained.

Complexes 13, **14** and **16** showed better thermoelectric behaviour in all three heating-and-cooling cycles compared to their shorter chain analogs, while **Complex 15** showed good thermoelectric behaviour only in the cooling cycles.

Table 4.12 Summary of results for **Complexes 13 - 16**

Chemical Formula	**Band gap (eV)**		**$\chi_M^{corr}T$ (cm^3 K mol^{-1})**	**T_{dec} C**	**S_e (mV K^{-1})**
	E_o	***E_e***			
$[Co_2(CH_3COO)_4(LC14)_2].2H_2O$ **(Complex 13)**	2.75	0.55	3.96 (100% HS)	179	-0.62 ± 0.01
$[Fe_2(CH_3COO)_4(LC14)_2].4H_2O$ **(Complex 14)**	1.93	0.46	5.46 (62.5% HS)	171	-0.44 ± 0.01
$[Co(LC14)_3](BF_4)_2.4H_2O$ **(Complex 15)**	2.31	0.32	1.45 (71.8% HS)	258	-0.35 ± 0.02 (Cool)
$[Fe(LC14)_3](BF_4)_2.4H_2O$ **(Complex 16)**	1.93	0.35	0.89 (29.6% HS)	256	-0.54 ± 0.02

CHAPTER 5: CONCLUSIONS AND SUGGESTIONS FOR FUTURE WORKS

5.1 Conclusions

A total of 16 complexes of Co(II) and Fe(II) with four bipyridyl ligands (LC8, LC10, LC12, LC14) and two counterions (CH_3COO^-, BF_4^-) were successfully obtained in good yields (59.1 – 96.2%) by the step-wise method. The structural formulae of these complexes **(Table 5.1)** were proposed based on combined analytical data.

Table 5.1 Structural formulae of Co(II) and Fe(II) complexes

Co(II) complexes	Fe(II) complexes
$[Co_2(CH_3COO)_4(LC8)_2].3H_2O$ **(Complex 1)**	$[Fe_2(CH_3COO)_4(LC8)_2]$ **(Complex 2)**
$[Co(LC8)_3](BF_4)_2.2H_2O$ **(Complex 3)**	$[Fe(LC8)_3](BF_4)_2.H_2O$ **(Complex 4)**
$[Co_2(CH_3COO)_4(LC10)_2].H_2O$ **(Complex 5)**	$[Fe_2(CH_3COO)_4(LC10)_2].3H_2O$ **(Complex 6)**
$[Co(LC10)_3](BF_4)_2.4H_2O$ **(Complex 7)**	$[Fe(LC10)_3](BF_4)_2.3H_2O$ **(Complex 8)**
$[Co_2(CH_3COO)_4(LC12)_2].2H_2O$ **(Complex 9)**	$[Fe_2(CH_3COO)_4(LC12)_2].2H_2O$ **(Complex 10)**
$[Co(LC12)_3](BF_4)_2.3H_2O$ **(Complex 11)**	$[Fe(LC12)_3](BF_4)_2.3H_2O$ **(Complex 12)**
$[Co_2(CH_3COO)_4(LC12)_2].2H_2O$ **(Complex 13)**	$[Fe_2(CH_3COO)_4(LC12)_2].4H_2O$ **(Complex 14)**
$[Co(LC12)_3](BF_4)_2.4H_2O$ **(Complex 15)**	$[Fe(LC12)_3](BF_4)_2.4H_2O$ **(Complex 16)**

All complexes have octahedral Co(II) and Fe(II) atoms. Complexes with CH_3COO^-as ligand were dinuclear, while complexes with BF_4^- ion were mononuclear. These complexes were only soluble in lipophilic solvents, such as chloroform and dicholoromethane.

The optical bandgaps (E_o) for Co(II) complexes (2.25 – 2.75 eV) were higher compared to Fe(II) complexes (1.85 – 1.93 eV), while, the electrochemical bandgaps (E_e) for monomer complexes (0.32 – 0.37 eV) were slightly lower compared to the

dinuclear complexes (0.45 – 0.55 eV). However, the E_e values for all complexes were within the semiconductor band.

At room temperature, **Complexes 1**, **3**, **5**, **9**, **10**, **11** and **13** were 100% high spin (HS), **Complexes 4**, **8** and **12** were 100% low spin (LS), while all other complexes have a mixture of HS and LS metal(II) atoms.

The ionic complexes have higher thermal stability (T_{dec} = 256 – 265 ^{o}C) compared to the molecular complexes (T_{dec} = 170 – 182 ^{o}C). The most thermally stable complex was **Complexes 3** and **4** (T_{dec} = 265 ^{o}C), while the least thermally stable complex was **Complex 10** (T_{dec} = 170 ^{o}C).

Finally, the S_e values for all complexes were in the range of -0.35 ± 0.02 – -0.62 ± 0.02 mV K^{-1}. The negative values suggest the anions (I^- from KI-KI_3 redox couple) as the majority charge carriers in solution. The HS molecular complexes (**1**, **5**, **9**, **10**, **13**) and LS ionic complexes (**4**, **8**, **12**) have higher Seebeck coefficient (S_e) values than the other complexes. Hence, these complexes are potential thermoelectric materials.

5.2 Suggestions for Future Works

In order to confirm the proposed structure of all complexes, it is suggested to try to obtain crystals using different solvents and techniques (such as solvothermal), or use of a shorter linear alkyloxy or alkyl chains. Alternatively, their structures can be ascertained by molecular modelling, such as was reported for $[Fe_2(CH_3COO)_4(L1)_2]$, where L1= (4,4-bis[3,4-bis(tetradecyloxy)styryl]-2,2‟-bipyridine) [49].

It would also be exciting to study the effect of other ions, especially coordinating ones, such as SCN^-, ClO_4^-, SO_4^{2-}, $Cl^-$and $C_6H_5COO^-$ ions, the alkyloxy chain with odd numbers of carbon atoms, other multi N-donor neutral ligands, such as 2,2‟-bipyrimidine and 2,2‟:6‟,2”-terpyridine, on the structures, band gaps (optical and

electrochemical), magnetic, thermal and thermoelectric performance (Seebeck coefficient).

Moreover, similar complexes with long alkyl chains were found to have mesomorphic (liquid crystal) properties [46]. In addition, Co(II) and Fe(II) complexes are extensively studied as spin-crossover (SCO) materials for potential applications in information storage (memory device), and as sensors and molecular switches [77]. Hence, the study of mesomorphic (using polarising optical microscopy, differential scanning microscopy, and power X-ray diffractography) and SCO properties (using SQUID magnetometry) may also be performed for complexes **1** – **16**.

The study of thermoelectric properties is closely related to thermal and electrical conductivities. An example is figure of merit (ZT). Theoretically, in order to obtain high ZT, the Seebeck coefficient and electrical conductivity need to be high, whilst thermal conductivity need to be low, so that the temperature difference producing Seebeck coefficient can be maintained in the system [78]. Other useful parameters that can be studied include ionic conductance, voltage, power and current.

Finally, the study of thermoelectric properties (Seebeck coefficient) may be extended to mixed valence complexes, such as $[Co(II)Co(III)(CH_3COO_4)_5(LC8)_2]$ and $[Fe(II)Fe(III)(CH_3COO)_5(LC8)_2]$. This is based on the results found for $[Co(L^{12})2](BF_4)_{2/3}$ and $[Co(L^{14})_2](BF_4)_{2/3}.H_2O$, where $L^{12,14}$ = N_3-Schiff bases appended with linear $C_{12,14}$ carbon chains at the nitrogen atoms, reported to give high S_e values which were +1.89 ± 0.02 mV K^{-1} and +1.92 ± 0.08 mV K^{-1} [10]. Furthermore, it is advantages to design the complexes which are soluble in high boiling point of solvents, such as DMSO or aromatic solvents, so that data can be obtained at higher temperatures.

REFERENCES

[1] Tritt, T. M. (2011) Thermoelectric Phenomena, Materials, and Applications. *Annual Review of Materials Research*, **41**, 433-448.

[2] Koerver, R., MacFarlane, D. R., Pringle, J. M. (2015) Evaluation of Electrochemical Methods for Determination of the Seebeck Coefficient of Redox Couple. *Electrochimica Acta*, **184**, 186-192.

[3] Kang, T. J., Fang, S., Kozlov, M. E., Haines, C. S., Li, N., Kim, Y. H., Chen, Y., Baughman, R. H. (2012) Electrical Power From Nanotube and Graphene Electrochemical Thermal Energy Harvesters. *Advanced Functional Materials*, **22**, 477-489.

[4] Abraham, T. J., Tachikawa, N., MacFarlane, D. R., Pringle, J. M. (2014) Investigation of the Kinetic and Mass Transport Limitations in Thermoelectrochemicals Cells with Different Electrode Materials. *Physical Chemistry Chemical Physics*, **16**, 2527-2532.

[5] Kaes, C., Katz, A., Hosseini, M. W. (2000) Bipyridine: The Most Widely Used Ligand. A Review of Molecules Comprising at Least Two 2,2‟-Bipyridine Units. *Chemical Reviews*, **100**, 3553-3590.

[6] Sasse, W. H. F. (1966) 2,2‟-Bipyridine. *Organic Syntheses*, 46, **5**, 102-106.

[7] Damrauer, N. H., Boussie, T. R., Devenney, M., McCusker. J. K. (1997) Effects of Intraligand Electron Delocalization, Steric Tuning, and Excited-State Vibronic Coupling on the Photophysics of Aryl-Substituted Bipyridyl Complexes of Ru(II). *Journal of the American Chemical Society*, **119**, 8253-8268.

[8] Arun Kumar, K., Amuthaselvi, M., Dayalan, A. (2011) cis-Bis(2,2‟-Bipyridine-k_2N,N‟)dichloridocobalt(II) Trihydrate. *Acta Crystallographica Section E: Structure Reports Online*, **67**(4), m468-m468.

[9] Petkova, E. G., Lampeka, R. D., Gorichko, M. V., Palamarchuk, G., Dyakonenko, V. V., Zubatyuk, R. I., Shishkin, O. V. (2008) Copper(II), Nickel(II), Cobalt(II), and Chromium(III) Complexes Based on 6,6‟-Bis{[methyl(oxido)imino]methyl}-2,2‟-bipyridine. *Zeitschrift für Naturforschung B*, **63b**, 841-847.

[10] Abdullah, N., Md. Noor, N. L., Nordin, A. R., Halcrow, M. A., MacFarlane, D. R., Lazar, M. A., Pringle, J. M., Bruce, D. W., Donnio, B., Heinrich, B. (2015) Spin-crossover, Mesomorphic and Thermoelectrical Properties of Cobalt(II) Complexes with Alkylated N_3-Schiff Bases. *Journal of Materials Chemistry C*, **3**, 2491-2499.

[11] Thompson, M. (2008) CHNS elemental analysers, *AMCTB of The Royal Society of Chemistry*, No. 29, **4**, 1-2.

[12] Agrawa, M. O., Ndifon, P. T., Ndosiri, N. B., Paboudam, A. G., Yufanyi, D. M., Mohamadou, A. (2010). Synthesis, Characterization and Antimicrobial Activities of Cobalt(II), Copper(II) and Zinc(II) Mixed-Ligand Complexes Containing 1,10-Phenanthroline and 2,2‟-Bipyridine, *Bulletin of the Chemical Society of Ethiopia*, **24**(3), 383-389.

[13] Stuart, B. H. (2005) *Introduction in Infrared Spectroscopy: Fundamental and Applications*, John Wiley & Sons Ltd., London, 1-13.

[14] Banwell, C. N., McCash, E. M. (1983) *Fundamental of Molecular Spectroscopy*, McGraw-Hill, London.

[15] Deacon, G. B., Phillips, R. J. (1980) Relationships Between The Carbon-Oxygen Stretching Frequencies of Carboxylato Complexes and the Type of Carboxylate Coordination. *Coordination Chemistry Reviews*, **33**, 227-250.

[16] Ye, B.-H., Chen, X.-M., Xue, F., Ji, L.-N., Mak, T. C. W. (2000) Reaction of Divalent Metal Acetate and 2,2‟-Bipyridine. Syntheses and Structural Characterization of Mono-, Bi- and Tri-nuclear Complexes. *Inorganica Chimica Acta*, **299**, 1-8.

[17] Siddiqi, Z. A., Ansari, I. A., Sama, F., Shahid, M., (2014) Synthesis and Characterization of Carboxylate Bridged Homodinuclear Co(II) Complex: Crystal Structure of $[Co_2(Pda)_2(H_2O)_5].2H_2O$ (H_2Pda = pyridine-2,6-dicarboxylic acid), *International Journal of Innovative Research in Science, Engineering and Technology*, **3**, 8673-8679.

[18] Paris, J. P., Brandt, W. W. (1959) Charge Transfer Luminescence of a Ruthenium(II) Chelate. *Journal of the American Chemical Society*, **81**(18), 5001-5002.

[19] Wang, Y. (1992) Photophysical Properties of Fullerenes and Fullerene/N,N-diethylaniline Charge-Transfer Complexes. *The Journal of Physical Chemistry*, **96**(2), 764-767.

[20] Atkins, P., Overton, T., Rourke, J., Weller, M., Armstrong, F., (2010), *in: Inorganic Chemistry*, W. H. Freeman and Company, New York.

[21] www.rsc.org/learn-chemistry/resource/res00000282/spectroscopy-in-a-suitcase-uv-vis-student-resources?cmpid=CMP00001304 retrieved on 25 June 2015.

[22] O'Brien, M. C. M., Chancey, C. C. (1993) The Jahn-Teller Effect: An Introduction and Current Review. *American Journal of Physics*, **61**(8), 688-697.

[23] http://wwwchem.uwimona.edu.jm/courses/JahnTeller.html retrieved on 4 April 2016.

[24] Lehleh, A., Beghidja, A., Beghidja, C., Mentré, O., Welter, R. (2011) Synthesis, Crystal Structure and Thermal Decomposition of Cu(II), Co(II), Mn(II) Complexes with Hetero-ligands containing Cysteic Acid, 4,4'-Dimethyl-2,2'-Bipyridine and Azide. *Comptes Rendus Chimie*, **14**, 462-470.

[25] Cortes, P., Atria, A. M., Garland, M. T., Baggio, R., Pena, O., Corsini, G. (2006) Crystal Structure and Antimicrobial Activity of a High Spin Cobalt(II) Dimer: $[Co_2(OH)_2(Ac)_3(bipy)_2].K.2H_2O$, *Journal of the Chilean Chemical Society*, **51**, N^o 2, 843-847.

[26] Hill, H. A. O., Day, P. (1968) *Physical Methods in Advanced Inorganic Chemistry*, Interscience Publishers, a division of John Wiley and Sons, London-New York-Sydney.

[27] Santra, B. K., Lahiri, G. K. (1998) Low-spin Octahedral Cobalt(II) Complexes of CoN_6 and CoN_4P_2 Chromophores. Synthesis, Spectroscopic Characterization and Electron-Transfer Properties. *Journal of the Chemical Society*, *Dalton Transactions*, 139-145.

[28] Enachesu, C., Krivokapic, I., Zerara, M., Real, J. A., Amstutz, N., Hauser, A. (2007) Optical Investigation of Spin-crossover in Cobalt(II) Bis-terpy Complexes. *Inorganica Chimica Acta*, **360**, 3945-3950.

[29] Sasaki, Y. (1980) Electronic Spectra of Octahedral Nickel(II) and Cobalt(II) Complexes with 2-(2-Pyridyl)imidazole and 2-(2-Pyridyl)benzimidazole. *Bulletin of the Institute for Chemical Research, Kyoto University*, **58**(2), 187-192.

[30] Czakis-Sulikowska, D., Czylkowska, A. (2003) Thermal and Other Properties of Complexes of Mn(II), Co(II) and Ni(II) with 2,2‟-Bipyridine and Trichloroacetates. *Journal of Thermal Analysis and Calorimetry*, **74**, 349-360.

[31] http://www.tpub.com/neets/book7/24c.htm retrieved on 13 September 2015.

[32] http://www.chem.ucla.edu/~bacher/CHEM174/equipment/CV1.html retrieved on 5 April 2016.

[33] Toledo. I., Arancibia, M., Andrade, C., Crivelli, I. (1998) Redox Chemistry of Copper Acetate Binuclear Complexes in Acetic Acid-Methanol Mixture as Solvent. *Polyhedron*, **17**, 1, 173-178.

[34] Scholz, F. (2010) *Electroanalytical Methods: Guide to Experiments and Applications*, Springer, Heidelberg, Germany.

[35] Heinze, J. (1984) Cyclic Voltammetry-“Electrochemical Spectroscopy”. *Angewandte Chemie International Edition in England*, **23**, 831-847.

[36] Mabbott, G. A. (1983) An Introduction to Cyclic Voltammetry. *Journal of Chemical Education*, **60**, 697-702.

[37] Cabral, D., Howlett, P. C., Pringle, J. M., Zhang, X., MacFarlane, D. (2015) Electrochemistry of Tris(2,2‟-bipyridyl) Cobalt(II) in Ionic Liquids and Aprotic Molecular Solvents on Glassy Carbon and Platinum Electrodes. *Electrochimica Acta*, **180**, 419-426.

[38] de Leeuw, D. M., Simenon, M. M. J., Brown, A. R., Einerhand, R. E. F. (1997) Stability of n-type Doped Conducting Polymers and Consequences for Polymeric Microelectronic Devices. *Synthetic Metals*, **87**, 53-59.

[39] Kaya, I. Koyuncu, S. (2007) Thermal Stability, Conductivity, and Band Gaps of Oligo-2-[(phenylimino)methyl]phenol and Oligomer-metal Complexes. *Iranian Polymer Journal*, **16**(4), 261-270.

[40] Zhang, L., Wei, Y., Wang, C., Guo, H., Wang, P. (2004) Hexatungstate Subunit as Building Block in the Hydrothermal Synthesis of Organic-Inorganic Hybrid Materials: Synthesis, Structure and Optical Properties of $[Co_2(bpy)_6(W_6O_{19})_2]$ (bpy = 4,4‟-bipyridine). *Journal of Solid State Chemistry*, **177**, 3433-3438.

[41] Krivokapic, I., Zerara, M., Daku, M. L., Vargas, A., Enachescu, C., Ambrus, C., Tregenna-Piggott, P., Amstutz, N., Krausz, E., Hauser, A. (2007) Spin-crossover in Cobalt(II) Imine Complexes. *Coordination Chemistry Reviews*, **251**(3), 364-378.

[42] Kahn, O. (1993) *Molecular Magnetism*, VCS Publishers Inc, New York.

[43] http://www.itc.tu-bs.de/Abteilungen/Makro/Methods/dsc.pdf retrieved on 6 April 2016.

[44] Tao, B., Lei, W., Cheng, F., Xia, H. (2012) One-Pot Synthesis, Crystal Structures and Thermal Properties of Two Three-Dimensional Cobalt(II) Complexes. *Bulletin of the Korean Chemical Society*, **33**, 6, 1929-1933.

[45] Abraham, T. J., MacFarlane, D. R., Pringle, J. M. (2013) High Seebeck Coefficient Redox Ionic Liquid Electrolytes for Thermal Energy Harvesting. *Energy & Environmental Science*, **6**, 2639-2645.

[46] Abdullah, N., Elsheikh, M. H., Nik Ibrahim, N. M. J., Mohd Said, S., Mohd Sabri, M. F., Haji Hassan, M., Marlina, A. (2015) Magnetic, Thermal, Mesomorphic and Thermoelectric Properties of Mononuclear, Dimeric and Polymeric Iron(II) Complexes with Conjugated Ligands. *RSC Advances*, **5**, 50999-51007.

[47] Abdullah, N., Hashim, R., Ozair, L. N., Al-Hakem, Y., Samsudin, H., Marlina, A., Salim, M., Mohd Said, S., Subramanian, B., Nordin, A. R. (2015) Structural, Mesomorphic, Photoluminescence and Thermoelectric Studies of Mononuclear and Polymeric Complexes of Copper(II) with 2-Hexyldecanoato and 4,4‟-Bipyridine Ligands. *Journal of Materials Chemistry C*, **3**, 11036-11045.

[48] Pomeranc, D., Heitz, V., Chambron, J.-C., Sauvage, J.-P. (2001) Octahedral Fe(II) and Ru(II) Complexes Based on a New Bis 1,10-Phenanthroline Ligand That Imposes a Well Defined Axis. *Journal of the American Chemical Society*, **123**, 12215-12221.

[49] Abdullah, N., Mohd Said, S., Marlina, A., Roslan, M. F., Azil, A., Nordin, A. R. (2015), Photophysical and Electrochemical Studies of Multinuclear Complexes of Iron(II) with Acetate and Extended Conjugated N-Donor Ligands. *Scientific World Journal*, **2015**, Article ID 860537, 8 pages.

[50] Braterman, P. S., Song, J.-I., Peacock, R. D. (1992) Electronic Absorption Spectra of the Iron(II) Complexes of 2,2‟-Bipyridine, 2,2‟-Bipyrimidine, 1,10-Phenanthroline and 2,2‟:6‟,2”-Terpyridine and Their Reduction Products. *Inorganic Chemistry*, **31**, 4, 555-559.

[51] Bushuev, M. B., Krivopalov, V. P., Nikolaenkova, E. B., Daletsky, V. A., Berezovskii, G. A., Sheludyakova, L. A., Varnek, V. A. (2012) Spin Crossover Complex $[FeL_2^1](ClO_4)_2.H_2O$ (L^1 = 4-methyl-2,6-bis(1*H*-pyrazol-1-yl)pyrimidine): Synthesis and Properties. *Polyhedron*, **43**, 81-88.

[52] Ferrere, S. (2002) New Photosensitizers Based Upon $[Fe^{II}(L)_2(CN)_2]$ and $[Fe^{II}L_3]$, where L is Subsituted 2,2‟-Bipyridine. *Inorganica Chimica Acta*, **329**, 79-92.

[53] Osowole, A. A., Ekennia, A. C., Osukwe, A. E. (2014) Synthesis, Spectroscopies and Antibacterial Properties of Some Metal(II) Mixed Ligand Complexes of Riboflavin and 2,2‟-Bipyridine. *Research and Reviews: Journal of Chemistry*, **3**(1), 32-37.

[54] Czakis-Sulikowska, D., Ka użna-Czapli ska, J. (2000) Thermal Properties of Complexes of Mn(II), Fe(II), Co(II), Ni(II) with 2,2‟-Bipyridine or 4,4‟-Bipyridine and Thiocyanate. *Journal of Thermal Analysis and Calorimetry*, **62**(3), 821-830.

[55] Lawandy, M. A., Huang, X., Wang, R.-J, Li, J., Lu, J. Y, Yuen, T., Lin, C. L. (1999) Two-Dimensional Coordination Polymers with One-Dimensional Magnetic Chains: Hydrothermal Synthesis, Crystal Structure, and Magnetic and Thermal Properties of $[MCl_2(4,4‟\text{-bipyridine})]$ (M = Fe, Co, Ni, Co/Ni). *Inorganic Chemistry*, **38**, 5410-5414.

[56] Gütlich, P., Goodwin, H. A. (2004) *Spin Crossover in Transition Metal Compounds I*, Springer-Verlag Berlin Heidelberg, Volume 233.

[57] Gaspar, A. B., Seredyuk, M. (2014) Spin Crossover in Soft Matter. *Coordination Chemistry Reviews*, **268**, 41-58.

[58] Seredyuk, M. (2012) Iron(II) Metallomesogens Based on Symmetrical Tripod Ligands. *Inorganica Chimica Acta*, **380**, 1, 65-71.

[59] Abraham, T. J., MacFarlane, D. R., Pringle, J. M. (2011) Seebeck Coefficient in Ionic Liquids – Prospects For Thermo-Electrochemicals Cells. *Chemical Communications*, **47**, 6260-6262.

[60] Lambert, Joseph B. (1987) *Introduction to Organic Spectroscopy*. Macmillan, New York.

[61] Al-Obaidi, F. N., Al-Diwan, T. A., Mahdi, A. S. (2010) Study of the Coordination Tendency of [N,N‟-Ethylenebis(salicylidenimine)] Toward Transition Metal Ions, *International Journal of Pure & Applied Chemistry*, **5**(2), 131-134.

[62] Imran, M., Iqbal, J., Iqbal, S., Ijaz, N. (2007) In Vitro Antibacterial Studies of Ciprofloxacin-Imines and Their Complexes with Cu(II), Ni(II), Co(II) and Zn(II). *Turkish Journal of Biology*, **31**, 67-72.

[63] Xinde, Z., Chenggang, W., Zhiping, L., Zhifeng, L., Zishen, W. (1996) Synthesis and Reactivity in Inorganic and Metal-Organic Chemistry Synthesis and Biological Acvitity of the Schiff Base N,N‟-bis(Salicylidene) thiourea and Its Complexes of Copper(II), Nickel(II) and Zinc(II). *Synthesis and Reactivity in Inorganic Metal-Organic Chemistry*, **26**(6), 955-966.

[64] Ejidike, I. P, Ajibade, P. A. (2015) Synthesis, Characterization and Biological Studies of Metal(II) Complexes of (3E)-3-[(2-{(E)-[1-(2,4-Dihydroxyphenyl)ethylidene]amino}ethyl)imino]-1-phenylbutan-1-one Schiff Base. *Molecules*, **20**, 9788-9802.

[65] Wang, Y., Ramos, I., Santiago-Avilés, J. J. (2007) Optical Bandgap and Photoconductance of Electrospun Tin Oxide Nanofibers. *Journal of Applied Physics*, **102**, 093517(1)-093517(5).

[66] Ilenikhena, P. A. (2008) Optical Characterization and Possible Solar Energy Applications of Improved Solution Grown Cobalt Oxide (CoO) Thin Films at 300 K. *African Physical Review*, **2**:0008, 68-77.

[67] Das, N. (1998) Reversible Formation of Binuclear Complexes Between Pyridine-2-Carboxylato (Tetraethylenepentamine) Cobalt(III) and Nickel(II)/ Cobalt(II) in Aqueous Solution. Anomalous Behaviour in the Dissociation of Binuclear Complexes. *Transition Metal Chemistry*, **23**, 455-459.

[68] Zanello, P. (2003) *Inorganic Chemistry; Theory, Practise, Application*, Royal Society of Chemistry, United Kingdom.

[69] Leonat, L., Sbârcea, G., Braňzoi. (2013) Cyclic Voltammogram for Energy Levels Estimation of Organic Materials. *UPB Scientific Bulletin*, *Series B,* **75**(3), 111-118.

[70] Tynan, E., Jensen, P., Kelly, N. R., Kruger, P. E., Lees, A. C., Moubaraki, B., Murray, K. S. (2004) The Ligand, the Metal and the „Holey"-host: Synthesis, Structural and Magnetic Characterization of Co(II), Ni(II) and Mn(II) Metal-Organic Frameworks Incorporating 4,4"-dicarboxy-2,2"-bipyridine. *Dalton Transactions*, **21**, 3440-3447.

[71] Abdullah, N., Azil, A., Marlina, A., Md. Noor, N. L. (2015) Magnetic, Photophysical and Thermal Properties of Complexes of Iron(II) with Structurally Different Schiff Bases. *Asian Journal of Chemistry*, **27**(7), 2359-2364.

[72] Seo, J., Moon, S,-T., Kim, J., Lee, S. S., Park, K.-M. (2003) Assembly of a Cyclic Dimer Silver(I) Complex Encapsulating Two BF_4^- Ions. *Bulletin of the Korean Chemical Society*, **24**, 1393-1395.

[73] Md. Noor, N. L. (2014) *Spin-Crossover and Mesogenic Properties of Cobalt(II) and Iron(II) Complexes With Ligands Derived From 2,6-Pyridinedicarboxaldehyde and 1-Aminoalkanes*, MSc. Thesis, Faculty of Science, University of Malaya, Kuala Lumpur.

[74] Abdullah, N., Sharmin, N., Ozair, L. N., Nordin, A. R., Mohd. Nasir, W. S. N., Mohamadin, M. I. (2015) Structures and Mesomorphism of Complexes of Tetrakis(4-chlorobenzoate-μ-O,O‟)bis(ethanol)dicopper(II) with Different N-Donor Ligands. *Journal of Coordination Chemistry*, **68**(8), 1347-1360.

[75] Ozair, L. N. (2012) *Synthesis and Characterization of Ionic Mixed Copper(II) Carboxylate Complexes, $K_n[Cu_2(p\text{-}OC_6H_4COO)_n(RCOO)_{4-n}]$ as Thermally Stable Solar Cell Materials*, MSc. Thesis, Faculty of Science, University of Malaya, Kuala Lumpur.

[76] Gütlich, P., Hauser, A., Spiering, H. (1994) Thermal and Optical Switching of Iron(II) Complexes. *Angewandte Chemie International Edition in England*, **33**, 2024-2054.

[77] Gural‟skiy, I. A., Quintero, C. M., Costa, J. S. Demont, P., Molnar, G., Salmon, L., Shepherd, H. J., Bousseksou, A. (2014) Spin Crossover Composite Materials for Electrothermomechanical Actuators. *Journal of Materials Chemistry C*, **2**, 2949-2955.

[78] Zhang, X., Zhao, L.-D., (2015) Thermoelectric Materials: Energy Conversion Between Heat and Electricity. *Journal of Materiomics*, **1**, 92-105.